41st IGS ANNUAL LECTURE

Characterisation, Modelling and Engineering of Rocks and Rockmasses

Presented by

Prof. K. Seshagiri Rao

Professor

Department of Civil Engineering

Indian Institute of Technology Delhi

Hauz Khas, New Delhi – 110016

raoks@civil.iitd.ac.in

Presented at

INDIAN GEOTECHNICAL CONFERENCE

IGC – 2019

19th – 21st, December, 2019

Prof. K.S. Rao,
Department of Civil Engineering
Indian Institute of Technology Delhi
Hauz Khas, New Delhi – 110016
Phones: +91 11 26591206, +91 9818222563
E-mail: raoks@civil.iitd.ac.in

Dr. K. S. Rao, Professor in the Department of Civil Engineering at IIT Delhi has obtained his M.Sc. (Andhra Univ), M.Tech. (IIT Kanpur) and Ph.D. (IIT Delhi) in 1978, 80 and 84 respectively. His research spanning over 39 years has been on engineering behaviour of rockmass, stability of slopes, underground structures, foundations, site characterization, numerical modeling and seismic hazard and microzonation of mega cities. An established teacher, researcher and active consultant, **Prof. Rao** has supervised 26 Ph.D. and 170 M.Tech thesis. Presently, 16 doctoral students are working with him. He is the recipient of IGS-Prof Leonard's best Ph.D. thesis award and 19 other IGS and ISRMTT best research awards. A prolific writer, **Prof. Rao** published 370 technical papers in national and international journals and conferences. Some of his articles are best-referred category and included in text books. He has been the Principal investigator of 13 sponsored research projects and carried out more than 350 consultancies in the areas of Soil, Rock, Mining and Earthquake Geotechnical Engineering.

Prof. Rao travelled extensively and has collaborative research with several universities. He is member of several technical committees and academic boards. He delivered several keynotes and special lectures in India and abroad and was a guest Editor for "Defence Science Journal". **Prof. Rao** is a regular peer reviewer for several International journals.

Prof. Rao designed and developed a large-scale Polyaxial (σ_1, σ_2, σ_3) testing facility, Impact testing facility, Direct shear apparatus under CNL and CNS loading in static and cyclic modes, Large Profilometer for 3D joint mapping, Creep testing equipment, High temperature rock chamber and Rainfall impact analyzer. **Prof. Rao,** establishing a large-scale direct shear facility for mine dump material at CMPDI, Ranchi.

Prof Rao is the Fellow of Indian Geotechnical Society and contributed extensively to the growth of IGS for more than 25 years in various capacities. He was the Honorary Secretary of the IGS for 10 yrs and managed very professionally. **Prof Rao** has been the Editor of the IGJ and IGS News. He was the Joint Organizing Secretary and Organizing Secretary for highly successful 13th ICSMFE, New Delhi (1994) and 13thARC, Kolkata (2008) conferences. He edited 6 vols of 13th ICSMFE and several IGC proceedings. He was the President of Indian Geotechnical Society for the term 2011-12. Presently, he is the President of Indian Society of Engineering Geology.

Prof. Rao provided solutions for many projects executed by Delhi Metro, NTPC, NHPC, GMR, GVK, L&T, Power Grid, KRCL, Mott Mec, JP, Gati, Energy Infratech, NWDA, Reliance, Stup, Vedanta, IRCON, Northern Railway, DLF, Feedback Infra, etc. His recent Geotechnical modeling work for assessing the stability of Chenab and Anjikhad bridge abutments has cleared the way for the construction of Jammu – Baramula Rail link of National importance.

Characterisation, Modelling and Engineering of Rocks and Rockmasses

K. Seshagiri Rao

Indian Institute of Technology Delhi
raoks@civil.iitd.ac.in

Abstract: Rocks are heterogeneous materials usually associated with geological discontinuities making them weak for sustaining the loads due to civil and mining engineering structures. Characterization details of different isotropic, anisotropic and weathered rocks are presented along with the newly formulated classification system for weathered rockmass.

Physical modelling of jointed rockmass under uniaxial, biaxial and polyaxial stress state through newly designed polyaxial system yielded significant results. Critical role of intermediate principal stress on strength and deformation for jointed rockmass is highlighted. A new polyaxial failure criteria is proposed and compared. New observations on brittle fracture propagation and interlocking phenomena in crystalline rocks are modelled under polyaxial stress state. Extensive large scale test results on rock joints under constant normal load (CNL) and constant normal stiffness (CNS) in static and cyclic modes were presented along with new predictive models. A new closed form analytical solution is provided for circular openings in isotropic, homogeneous and elasto-plastic rockmass for assessing the wellbore stability and openings. Results of physical modelling tests conducted on shallow tunnels subjected to impact loads and new predictive models developed for squeezing behavior are also included in this paper.

Understanding gained from the extensive characterization and physical modelling of materials in appropriate stress regime, used effectively to solve real time cases. The case studies included are: Stability analysis of jointed rock slopes of Chenab bridge abutments, Subansri power house slope stability, Tindharia landslide in Darjeeling, Evaluation of bored tunneling practices in rocks for Delhi metro and Coupled hydro-mechanical modelling for the slopes in Beas catchment .

Keywords: *Strength and deformation, rockmass, polyaxial stress, physical and numerical modelling, strength criteria, rock joints, closed-form solution, creep and swelling, cyclic loads, impact loads, landslide, rock weathering, rocksalt rheology, case studies*.

1 Introduction

Approximately four decades of my teaching, research and consulting career, I have dedicated my life in understanding loading and unloading processes in the most abundant material in nature that is silicates. Almost every Civil engineering infrastructure is either built on it or under it. William Blake (1863) in his poem Auguries of Innocence, wrote the first line “To see a World in a Grain of Sand” and yes, I saw the world in the grain of sand and beyond.

Construction of infrastructure either cause loading or unloading. Material behavior under these loading or unloading condition is very fundamental for civil engineering design. Yes, it is the simplest way to define the Civil engineering problem but comprehending of this loading and unloading processes require fundamental understanding of the material, environment and nature of the loading and unloading itself.

Laboratory experiments have shown that the strength of geomaterials are dependent on various conditions like confinement, temperature, pore-fluid, rate of loading and many more. During the design life of any civil engineering structure, material will be subjected to various combinations of these conditions. The condition under which the material response is weakest, that value is required to be obtained from laboratory investigations and used in the design of that section.

This motivates the researchers to study the geomaterial under various conditions in laboratory. We at IIT Delhi, have explored these avenues of research and developed several models, which help in defining the material behavior under creep, quasi-static loading, impact loading, cyclic loading under various stress paths. Some of these aspects will be discussed in this article.

Rock itself has heterogeneity, during the formation and under in-situ geological conditions various micro-mechanical processes are active. Some of these are thermo-hydro-mechanical-chemical (THMC) coupled processes. The long-term pressure solutions and sediment transportations cause anisotropy in some rocks and alters its mechanical characteristic in different directions. Extensive work in understanding the mechanical response of anisotropic rock with thermal effects has been investigated and the results are shared in this article.

In-situ THMC coupled processes effect the strength and one of the outcomes of these processes is weathering. Weathering studies showed that the rocks with high strength tend to become weak and fragile under the coupled attack, classical example is the mineral feldspar into clay minerals such as illite and kaolinite. In nature we find various forms of weathered rock and we tried to address various weathering related strength issues in our research work.

Till now, I have just discussed about the rocks, but we find something more complex than rock, that is the rockmass. Rockmass is rock plus the geological features. These geological features can cause anisotropy in an isotropic rock. Understanding the behavior of rock joints is one of the biggest achievements at IIT Delhi. We designed and performed experiments on jointed as well as single joint system. Joints in actual rocks are tested under both CNL, CNS in static and cyclic modes. On top of this, the complete complex rockmass system is also tested in uniaxial, complex polyaxial loading conditions. These results helped us to understand the joint system and we will share some of these results in this article.

Mechanical behavior of rocks and joints is an input for design, and we at IIT Delhi used our laboratory understanding of the material in developing the close-formed solutions to see the effects of the phenomenon on large scale engineering design. We have also adopted numerical techniques such as FE (finite element), FD (finite difference) and DE (discrete element) to

solve some of the real-life problems. In the end of this article, I will share theoretical and numerical implementations of the laboratory ideas into real life case studies.

2 Strength and Deformation Behaviour of Intact Rocks

All rocks are an assemblage of a mineral or several minerals primarily silicates, of shapes differing in size and arranged in certain patterns. The mechanical behavior of rocks is the mechanical response of minerals or grains and the interaction taking place among the grains due to their shape and spatial distributions in relation to the applied force field. The rocks which are not having any preferred orientation of grains are normally considered as isotropic, homogeneous display similar mechanical behavior in all the directions, not having any cracks could be called intact rocks. Strength of intact rock is influenced mainly by geological, lithological, physical, mechanical end environmental factors as shown in Fig. 1.

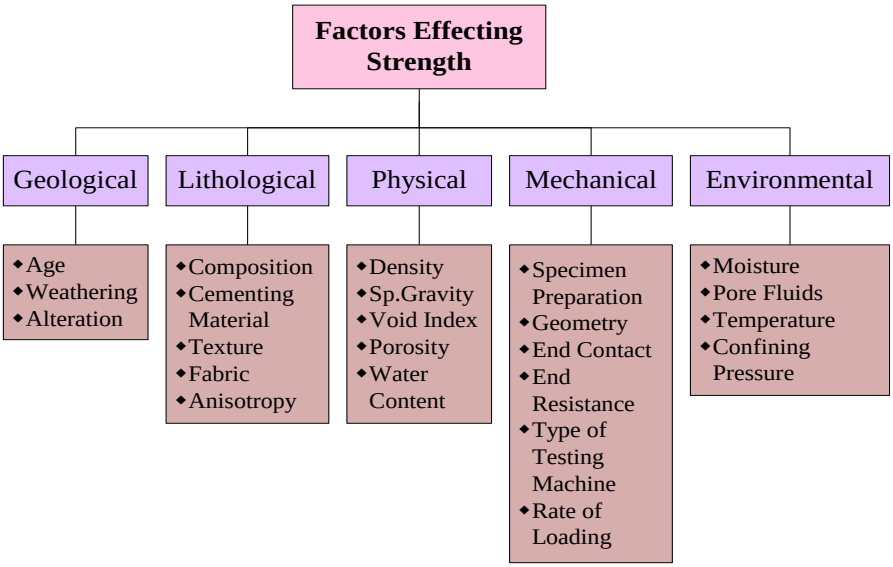

Fig. 1. Factors affecting the strength of rocks (Rao, 1984)

The strength of rocks is more influenced by the mechanical factors e.g. mode of testing, size and shape of specimen and the environmental factors such as nature of pore fluids, moisture content and temperature. Rao (1984) and Rao et al. (1988) conducted a comprehensive study on four sandstones from geologically different provinces to illustrate how the environmental factors influence compressive, tensile and shear behaviors. The list of different laboratory tests conducted as per the ISRM (1979) standards on intact rock specimens is shown in Fig. 2.

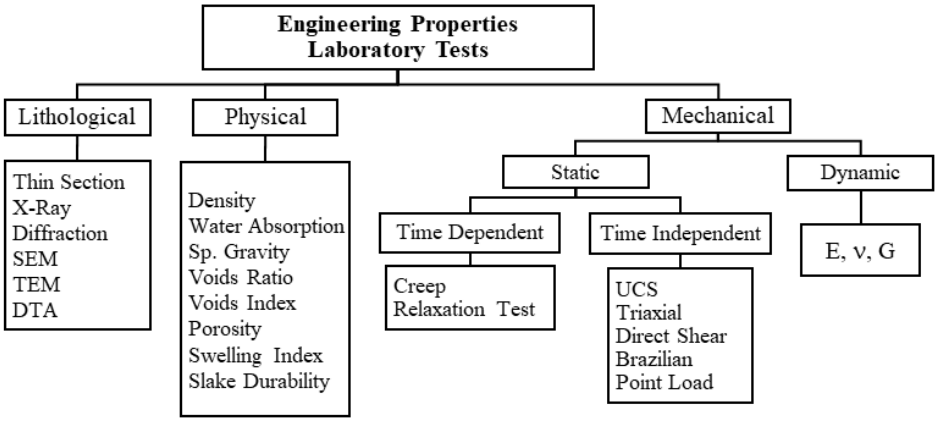

Fig. 2. Laboratory tests for engineering properties of rocks (Rao, 1984)

2.1 Uniaxial compressive strength (σ_c)

Unconfined compressive strength is the most important index property obtained from the tests conducted on L/D ratio of 2.0 specimens as per the ISRM (1979) test procedure (Rao, 1984; Behrastaghi et al., 1996; Gupta and Rao, 2000). To achieve the uniform stress distribution and to minimize end friction, the teflon sheets of 0.5 mm thickness are placed between the loading platen and specimen at both ends. Both axial and diametral strains were measured by fixing electrical strain gauges to the specimens. Extensive tests in dry and saturated conditions were conducted on different rocks which includes sandstones, limestones, quartzites, granites and basalts.

The typical stress-strain response of different rocks under uniaxial is shown in Fig. 3 (a). From these curves, Modulus of elasticity, $E_{t\,(50\%)}$ and Poisson's ratio at 50% of failure load were obtained for the rocks tested. The uniaxial compressive strength is very sensitive to the moisture, causing more than 50% reduction in strength for some sandstones. Rao (1984) found that the compressive strength of sandstones tested at different relative humidities, decreases with increase of the moisture content. Point load (Is_{50}) and Brazilian (σ_t) strengths have strong dependency on degree of moisture content at the time of testing (Rao et al., 1981).

2.2 Triaxial compressive strength

Strength under triaxial conditions is affected by a number of factors viz. confining pressure, pore fluid pressure, strain rate etc. If one keeps the mechanical, physical and environmental conditions constant, the isotropic rock strength mainly depends on confining pressure.

The effect of confining pressure on rock strength has been studied by many investigators in the past. von Karman (1911) conducted pioneering experiments on specimens of Carrara marble in copper jackets and observed that the strength increased non linearly with increasing confining pressure. After von Karman, many researchers improved the triaxial test apparatus. A summary by Vutukuri et al. (1974) of these works confirms the trends observed by von Karman.

Extensive triaxial tests were carried out on sandstones as per the ISRM (1978, 1983) at different confining pressures using high pressure triaxial cell at IITD. The typical stress strain curves are shown in Fig. 3 (b) for Jhingurda sandsone. The variation of σ_1 with σ_3 for Kota, Jamrani, Singrauli and Jhingurda sandstones is shown in Fig. 4. Systematic variation of elastic and shear strength parameters, c and ϕ with σ_3 was observed for sandstones tested.

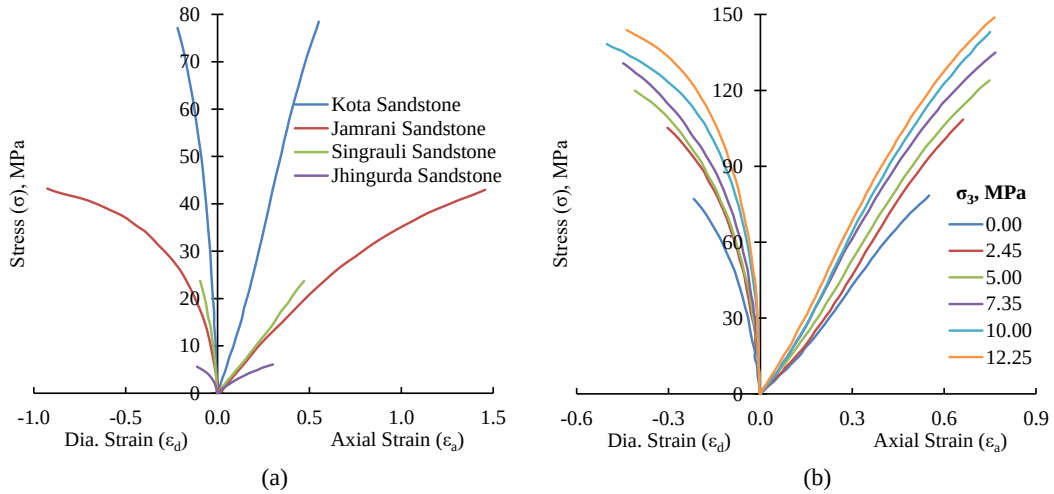

Fig. 3. Stress -strain curves under (a) UCS mode for sandstones and (b) Triaxial mode for Jhingurda sandstone at different confining pressures

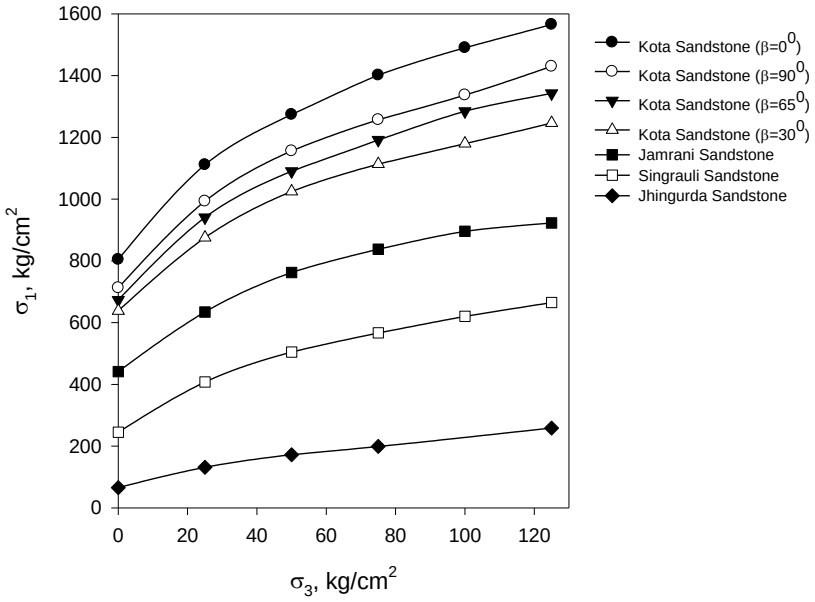

Fig. 4. Variation of σ_1 with σ_3 for sandstones (Rao, 1984)

2.3 Deere and Miller classification

The two parameter classification proposed by Deere and Miller (1966) based on UCS and modulus ratio is very useful to classify the rocks as shown in Fig. 5. Originally proposed for intact rocks, extended its limits to use for weathered and jointed rockmass as well.

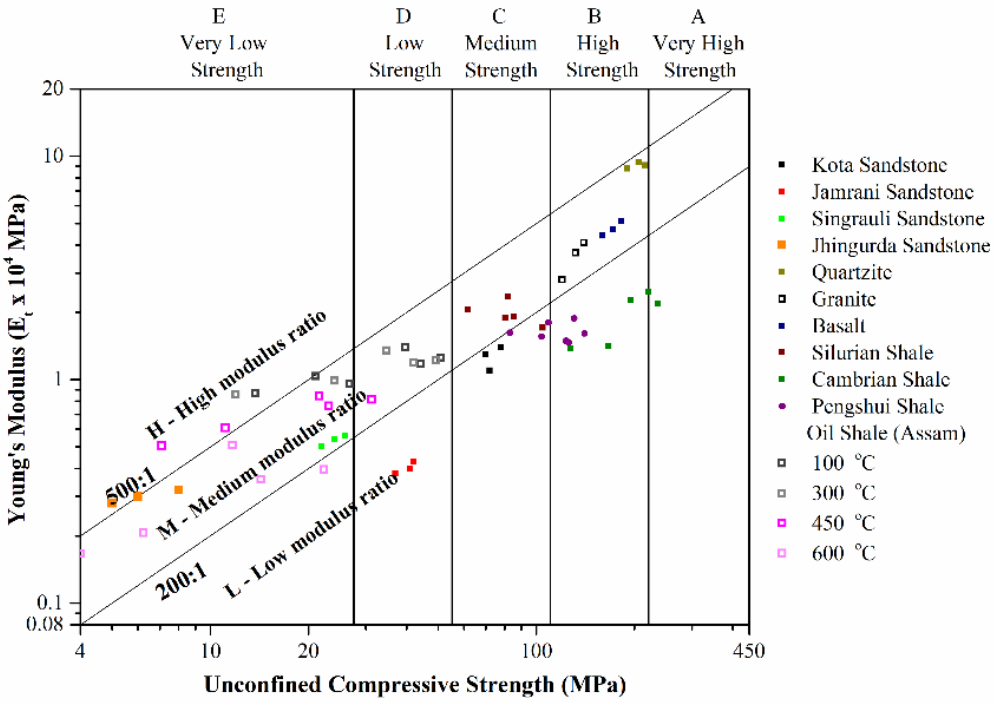

Fig. 5. Deere and Miller's classification for rocks (Kumar, 2019a)

2.4 Strength Criteria

Rock behaviour under triaxial stress is non linear and many researchers proposed failure criteria. After relising the limitations in the applicability of the existing strength criteria in one way or other, Rao (1984) and Rao et al. (1986), proposed a new strength criterion based on Mohr- Coulomb equation to account for the non-linear strength response of intact rocks. The criterion is expressed as:

$$\frac{\sigma_1-\sigma_3}{\sigma_3} = B\left(\frac{\sigma_c}{\sigma_3}\right)^{\alpha} \qquad (1)$$

Where, σ_c is the uniaxial compressive strength of intact rock, σ_1 and σ_3 are the principal stresses, α is the slope of the plot between $\left(\frac{\sigma_1-\sigma_3}{\sigma_3}\right)$ and $\left(\frac{\sigma_c}{\sigma_3}\right)$ on log–log scale and B = $\left(\frac{\sigma_1-\sigma_3}{\sigma_3}\right)$ when $\left(\frac{\sigma_c}{\sigma_3}\right)$ = 1; and B is a material constant and function of rock type. The plots are straight lines nearly parallel to each other, which indicates the narrow range of α for different rocks. Analysis of triaxial test data for more than 80 different rocks, Rao (1984) suggested a constant value of α as 0.8 and B values for different rocks as shown in the Table 1. In comparison with existing failure criteria, including Hoek and Brown (1980), this criterion predicts well. Further, the criterion is modified for weathered and rockmass. Further, predictive relations with classification ratings with respective material parameters were proposed to facilitate predictions.

Triaxial strength at any confining pressure can be estimated if UCS value of the rock is known by selecting the B from the above table and considering α value as 0.8.

Table 1. Suggested B values for different rocks (Rao, 1984; Ramamurthy et al., 1985)

	Sedimentary and Metamorphic Rocks						Igneous Rocks	
	Argillaceous		Arenaceous		Chemical Rocks			
Rock Type	Silt-stone	Shale	Sandstone	Quartzite	Limestone	Marble	Andesite	Granite
	Clays	Slate			Anhydrite	Dolomite	Diorite	Charnockite
	Tuffs	Mud-stone			Rock salt		Norite	
	Loess	Clay-stone					Liprite Basalt	
B	1.8	2.2	2.2	2.6	2.4	2.8	2.6	3.0

2.5 Strength in Partially and Fully Saturated States

The variation of strength with moisture content of four Indian sandstones in different test modes, including uniaxial compression, Brazilian, axial and diametral point load tests has been investigated. Test results in all modes shown decreasing trend with increasing moisture content (Rao, 1984; Rao et al., 1987). These changes in the engineering properties due to changes in moisture content was explained from the physico-chemical view point using the principle of effective stress (Terzaghi, 1936; Lambe, 1960; Sridharan, 1968):

$$\bar{\sigma}_c = \bar{\bar{\sigma}}\, a_m = \sigma - \bar{u}_w - \bar{u}_a - R + A \qquad (2)$$

$\bar{\sigma}_c$= effective contact stress
$\bar{\bar{\sigma}}$ = mineral to mineral contact stress,
a_m= mineral-to-mineral unit contact area,
σ = externally applied pressure on unit area,
$\bar{u}_w$ = effective pore water pressure,
$\bar{u}_a$ = effective pore air pressure,
R and A = effective inter-particle repulsive and attractive pressures, respectively.

The principle takes in to consideration of inter particle electrical attractive (A) and repulsive force (R), pore water pressure ($\bar{u}_w$)and pore air pressure ($\bar{u}_a$). This concept has been adopted to demonstrate the unification of the existing strength reduction mechanisms. The major changes which occur in rock due to moisture increase are:

i) Negative pore pressure, $\bar{u}_w$
ii) Inter-particle forces/surface energy

Using the adsorption isotherms, the pore size distributions have been estimated for four sandstones (Fig. 6). The method has conveniently brought out changes in pore size ranging from 0.005 to 0.4 μm for sandstones.

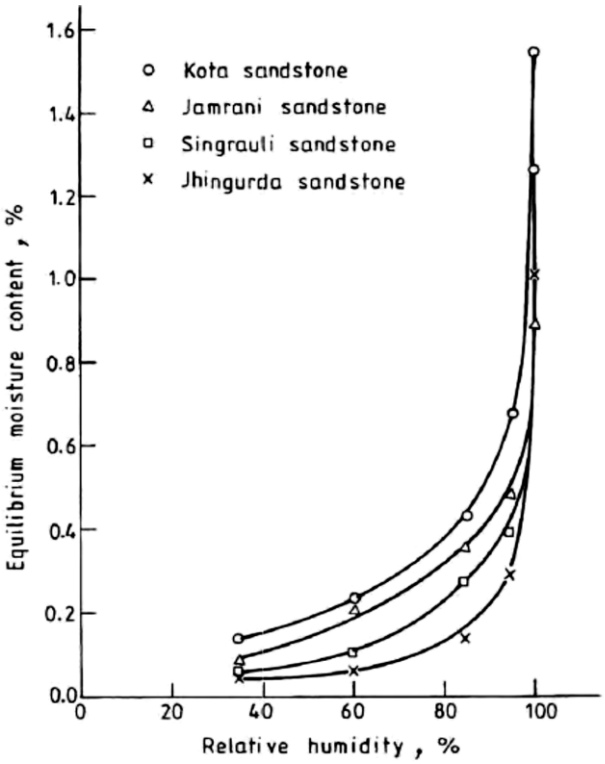

Fig. 6. Water vapour sorption isotherms (Rao et al., 1987)

Based on these pore size distributions and assuming cylindrical pores, the effective negative pore water pressures have been computed. The maximum negative pore water pressures were noticed around an equilibrium moisture content of 0.2 to 0.4% for all sandstones (Fig. 7).

The other factor which contributes to strength reduction on saturation is the reduction in inter particle attractive force or surface energy. A review of literature revealed the significant influence of these forces on rock strength. Thus, with an increase in moisture content, the $\bar{u}_w$ initially exhibits a peak and then shows a drastic reduction, whereas the surface energy steadily decreases. Accordingly the strength variation is the result of the combined effect of these two micro effects, though the relative magnitude is difficult to decipher. However, a careful scrutiny of the variation of $\bar{u}_w$ and strength with moisture content has clearly revealed the zones wherein the $\bar{u}_w$ does seem to have played a positive role.

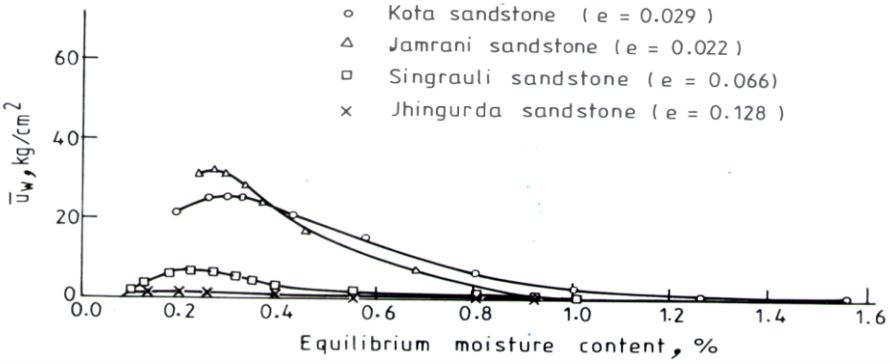

Fig. 7. Variation of negative pore water pressure with moisture content (Rao et al., 1987)

Furthermore, as per the Griffith's crack theory, strength is expected to be a function of $(E\ \gamma)^{½}$ where E is modulus of elasticity and γ is surface energy. Assuming that the reduction in surface energy is proportional to change in relative humidity, a computation has been made of the variation of $(E\ \gamma)^{½}$. The variation of $(\gamma/\gamma_{dry})^{½}$ and and $(E\ \gamma/E_{dry}\ \gamma_{dry})^{½}$ with equilibrium moisture content, along with the variations in the relative strength indices (σ_c/σ_{dry}), $(\sigma_{tb}/\sigma_{tb\ dry})$, $(\sigma_{ta}/\sigma_{ta\ dry})$ and $(\sigma_{td}/\sigma_{td\ dry})$ as shown in Fig. 8.

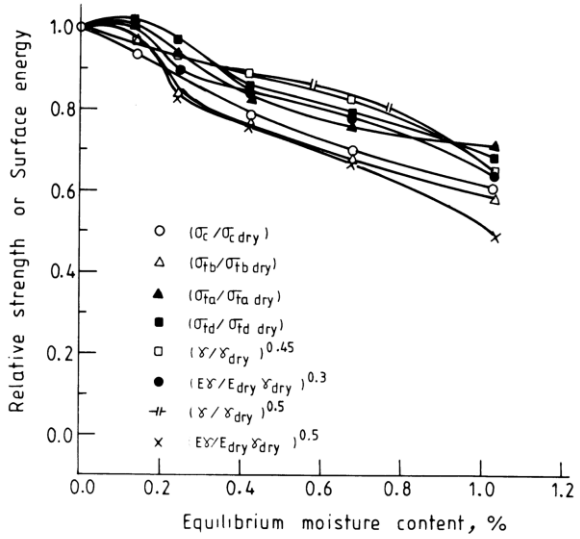

Fig. 8. Variation of relative strength or surface energy with moisture content for Kota sandstone (Rao, 1984; Rao et al., 1987)

Table 2. Optimal exponents for sandstones tested (Rao et al., 1987)

Exponent 'n' value	Rock type			
	Jamrani sand-stone	Jhingurda sandstone	Kota sand-stone	Singrauli sandstone
$(\gamma/\gamma_{dry})^n$	0.71	0.70	0.45	0.30
$(E\ \gamma/E_{dry}\ \gamma_{dry})^n$	0.25	0.41	0.30	0.17
$(\sigma_{c\ sat}/\sigma_{c\ dry})$, %	52	48	37	33

Though there is a broad agreement, the matching has been poor. On the other hand, by changing the exponent to other values, a better correlation has been obtained (Table 2). Interestingly these exponents differ from rock to rock but are found to be a function of rock type and related to strength reduction which one observe on saturation. Though the comparisons are qualitative in nature, the results have brought to focus the factors responsible for the strength reduction. Results from the cyclic tests on intact rock samples from Himalayas will be discussed in the following section.

3 Cyclic Behaviour of Intact Rocks

Weakening of rock under cyclic loading is termed as rock fatigue. Repeated loading causes rupture. The phenomena of premature failure due to cyclic or repetitive loading leaves a significant scope for research in the field of rock mechanics due to growing evidence that such strength weakening is found in the underground excavation as well as in dam reservoir, bridge abutments, dam foundations, open cut benches and structures subjected to earthquake motions. This consideration of time dependence in the form of static and cyclic behavior of rocks is essential for judicious design of surface and subsurface

engineering structures in the mountainous terrain like Himalayas. Keeping this in view a comprehensive study on three isotropic sandstones from Himalayas is carried out and brief highlights of the same is presented here.

3.1 Mechanism of Damage

Fatigue indicators are derived to analyse and interpret mechanism of damage evolution under cyclic loading. Different fatigue indicators proposed by several authors are as follows:

a) Secant modulus (Loading and Unloading)
b) Young's modulus
c) Cyclic energy dissipated
d) Residual axial/diametral deformation
e) Poisson's ratio
f) Acoustic emission count
g) Permeability

Secant modulus is a direct measure of damage of the material. The secant modulus values provides an insight into the relationship between grain size and stress induced fracturing. Young's modulus reflects the susceptibility of rock to crack initiation, propagation and coalescence. Stress/ Hysteresis energy is utilized to cause rock failure. Stress energy released by the rock is a potential indicator of rock burst. Residual/ Irreversible axial strain method is one of the most reliable damage variable because unlike secant/Young's modulus, it has a distinct physical meaning and can describe the initial fatigue damage and degradation process of rock subjected to fatigue loading (Liu et al., 2012). Permeability evolution is another indirect means of assessing damage in rock samples.

3.2 Cyclic Experimentation

Extensive cyclic experiments were carried out on Disang, Barail and Katra sandstones in the servo controlled cyclic compression machine of IIT Delhi. The basic difference in machine behavior for static and cyclic controlled tests is that there is a constant loading rate (kN/s) in static loading and a sinusoidal load path having constant loading frequency (Hz),load amplitude, σ_a (kN) and mean load, σ_m in cyclic loading as shown in Fig. 9 and Fig. 10. Results are discussed briefly below.

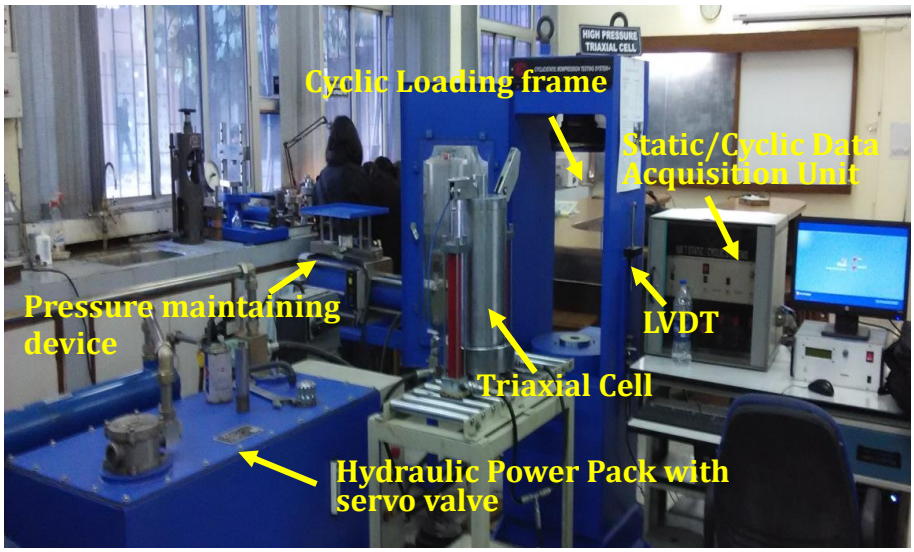

Fig. 9. Servo controlled cyclic triaxial system with data acquisition unit

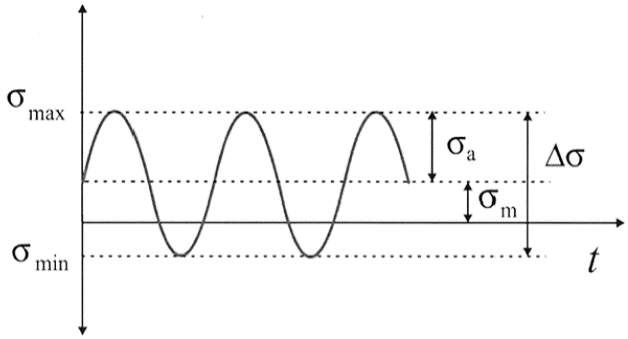

Fig. 10. Sinusoidal compression loading

3.3 Influence of Amplitude, Frequency and Stress

Damage behaviour of the rock under the influence of amplitude, show a sharp drop in elastic parameters (secant modulus, unloading modulus and Young's modulus) with increase in amplitude and marked increase in deformation parameters like residual axial and diametral strain and Poisson's ratio (Fig. 11). The time during which the stress acts in the plastic region increases leading to potential decrease in strength of the rock. Whereas, all the three elastic properties of the rock viz. Secant modulus, Unloading modulus and Young's modulus increase with frequency. This trend may be a result of the fact that at high frequencies, maximum stress is not being applied for long enough to create a failure surface.

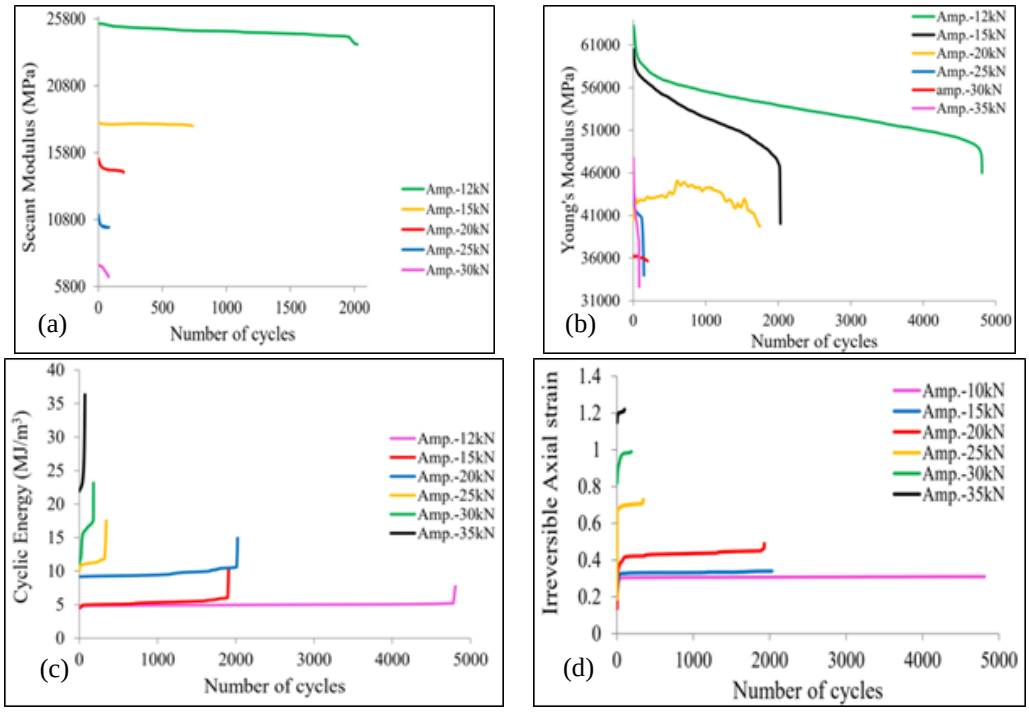

Fig. 11. Evolution of dynamic mechanical properties under cyclic loading (GhoshRoy, 2019)

The fatigue life of a material is represented by S-N (Stress vs. number of cycles) curves (Fig. 12). Damage behaviour of the rock under the influence of peak stress result shows degradation of elastic properties. This may be due to the fact that at higher peak stress, rock undergoes low cycle fatigue in the plastic region with rapid development of irreversible axial and lateral strain resulting in rapid extension and unstable propagation of cracks with sudden breakdown (GhoshRoy, 2019; Zaei, 2019). Fatigue life can be related with the number of cycles by a power law of the form: $S = aN^{-b}$ for the sandstones.

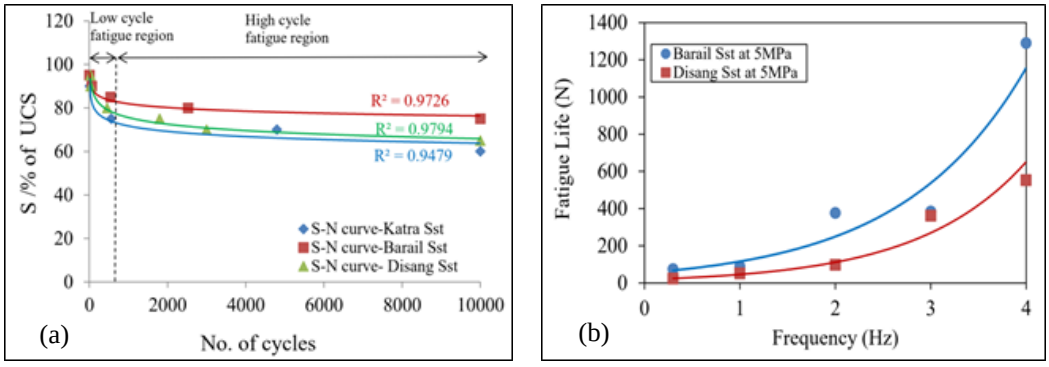

Fig. 12. (a) S-N curve (b) Influence of frequency on the fatigue life

3.4 Cyclic Hardening Behaviour

Cyclic hardening is the increase in static strength of the rock if it is subjected to predetermined number of cycle below its fatigue limit under confinement. With increase in amplitude and number of cycles, cyclic hardening increases. A comparative analysis of the evolution curve obtained from cyclic damage and cyclic hardening tests shows that under cyclic damage test, elastic properties of the rock show rapid decline while Hysteresis energy, axial and lateral strain show a sharp increase (Fig. 13). On the other hand during cyclic hardening test under triaxial compression, elastic parameters shows a gradual decline, hysteresis energy decreases and axial and lateral strain curve becomes asymptotic with no. of cycles (Fig. 14).

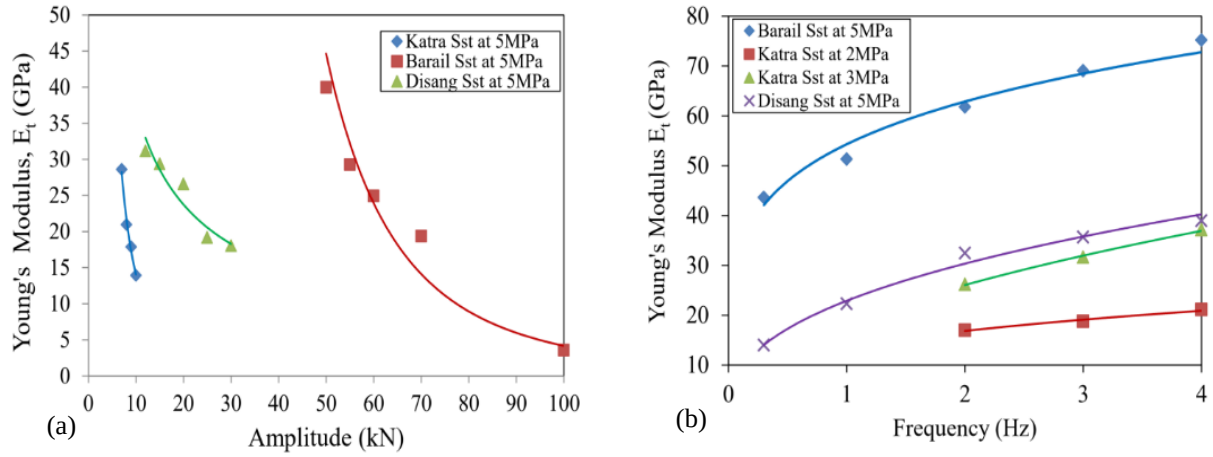

Fig. 13. Relation between dynamic mechanical properties of sandstone with (a) Amplitude and (b) Frequency (GhoshRoy, 2019)

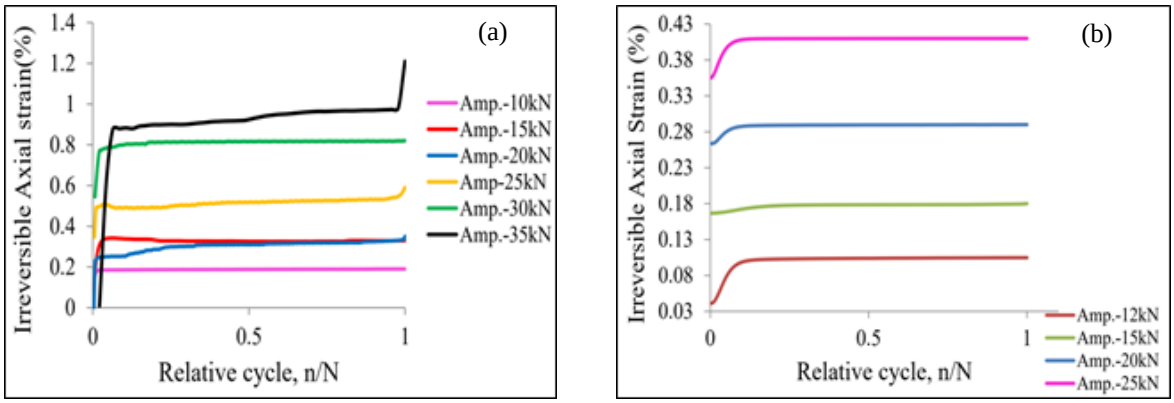

Fig. 14. Evolution of deformation under (a) Cyclic damage and (b) Cyclic hardening test (GhoshRoy, 2019)

Hardening (R) of sandstone can be related through a linear equation of the form $R = a\,\frac{\sigma_a}{\sigma_1} - b$ with normalized amplitude ($\frac{\sigma_a}{\sigma_1}$) and a logarithmic equation of the form $R = a\ln(N) - b$ with number of cycles (N) under triaxial conditions where σ_1 is the static strength and a, b are the material parameters.

3.5 New Fatigue Damage Model

Based on the experimental results, two constitutive models are proposed by modifying generalized Voigt-Kelvin and Lomnitz model to describe the three stages of deformation behaviour under cyclic loading (GhoshRoy, 2019).

Model-I*;* when the applied stress $\sigma_{max} \leq 0.7$UCS i.e. during incomplete cyclic loading test below the fatigue limit of the rock

$$\varepsilon_{irr} = \frac{\sigma_{max}}{E_1} + \frac{\sigma_{max}}{E_2}\left(1 - e^{-\frac{E_2}{\eta}N}\right) \qquad (3)$$

where E_1, E_2 and η are the material constants. N in the proposed model is the number of cycles. This model is applicable to primary and secondary stages of cyclic deformation.

Model-II; when the applied stress σ_{max} >0.7UCS i.e. during complete cyclic loading test above the fatigue limit of the rock

$$\varepsilon_{irr} = A + B\log(n) + C(n^2) + D(n^3) \qquad (4)$$

Where A, B, C and D are material constants, n is the number of cycles. The model is applicable to all stages of cyclic deformation leading to failure.

3.6 Numerical Validation

A deformation analysis through finite element model ABAQUS (Abaqus, 2011) was carried out to simulate ground borne vibration due to noise generated by high speed moving train or heavy traffic in a rail or road tunnel. It is observed that amplitude value in the range of 30-40 kN in a tunnel of length 1km and width 10m under overburden cover of 10m, is capable of producing 90dB sound. Results of the numerical modelling show that deformation increases with amplitude irrespective of nature of bedrock. Deformation vs. number of cycle plot deduced from the model shows a three stage deformation behaviour similar to the experimental results (Fig. 15).

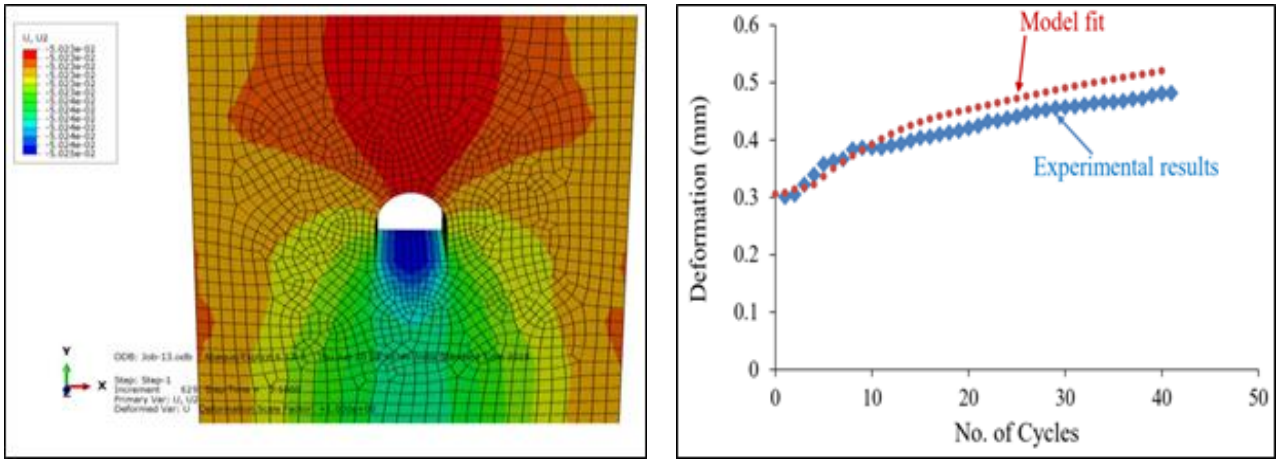

(a) (b)

Fig. 15. (a) Model simulating noise induced vibration in a tunnel (b) Relation between experimental results and numerical model.

As seen above, the major cyclic parameters controlling damage in the rocks are frequency, amplitude, peak stress and number of cycles. Through the extensive cyclic experiments on Disang, Barail and Katra sandstones, it is found that while increase in frequency enhances the fatigue strength of rocks, peak stress and amplitude drastically reduces the fatigue strength. Increase in cycles increases plasticity and progressive degradation of rock strength.

Microstructural analysis of damage shows the intense crushing, micro fracturing, de-cohesion and distinct inter granular crack growth are the dominant mechanisms governing failure during cyclic loading.

4 Engineering Behaviour of Anisotropic Rocks

Anisotropy is one of the most distinct features that must be considered in rock engineering whether it is applied in civil, mining, geo-environmental, or petroleum engineering. Many rocks have anisotropic characteristics, i.e., their mechanical, thermal, and hydraulic properties vary with direction, and engineering applications that do not consider the anisotropic behavior of rock produce errors of differing magnitudes, depending on the extent of rock anisotropy. Anisotropic characteristics generally originate from the mineral foliation in metamorphic rocks, stratification in sedimentary rocks, and discontinuities in the rockmass. The presence of bedding planes and schistosity make the rock weaker and dictate its overall behaviour. If the rock is anisotropic in nature i.e. strength and deformation behaviour changes with orientation. Therefore, exhaustive studies are carried out at IIT Delhi on different type of anisotropic rocks (sandstone, schist, phyllite, gneiss, slate and shale) to understand the behaviour of intrinsically anisotropic rocks. Further, the strength prediction models are developed and subsequently modified by considering different environmental parameters (Rao, 1984; Behrestaghi et al. 1996; 1997).

4.1 Effect of Inclination Angle

The type of anisotropy is defined by the shape of curve between uniaxial compressive strength and the orientation angle β, where β angle is the angle between weak plane and the major principal stress (Fig. 16 and Fig. 17). The three possible features which define the concept of strength anisotropy in rocks are: (i) the location of maximum and minimum compressive strength in a range of β varying from 0° to 90°, (ii) the respective value of uniaxial compressive strength (σ_c) at those orientation, and (iii) the general shape of the anisotropic curve between σ_c and β. The anisotropy in rocks is governed by systematic set of weak planes, their nature and formation (induced or inherent). Based on extensive testing, Singh (1988) and Behrestaghi (1992) modified the classification as U-type, undulatory type and shoulder type. The U-type anisotropy is mostly observed in metamorphic rocks due to oriented crystalized grains.

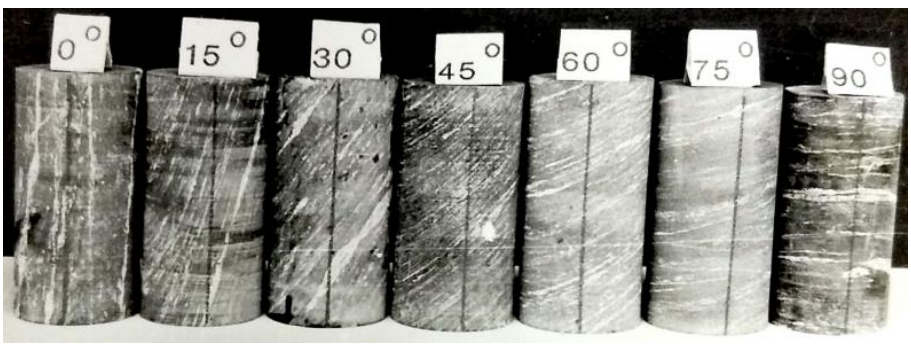

Fig. 16. Anisotropic quartzitic schist (Behrestaghi et al. 2003)

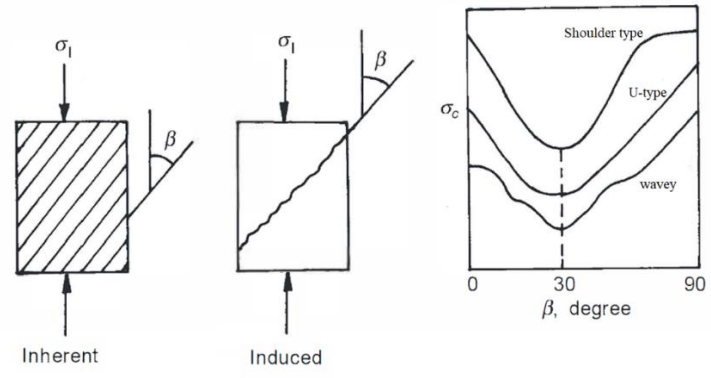

Fig. 17. Key diagram with possible variation of σ_c with β angle for inherent anisotropy

The Undulating or wavy anisotropy curve is a typical form of cleavage anisotropy, which is due to presence of more than one set of cleavage plane in rocks. Further, the shoulder type anisotropy curve is observed due to the bedding plane. This type of anisotropy curve is U-shape and restricted in narrow range of β and tend to generate a "shoulder" near β = 90°. This type of anisotropy is characteristic of sedimentary rocks such as sandstone and shale (Rao et al. 1986).

4.2 Tensile Strength

The experimental investigations suggest that the tensile strength of anisotropic rocks depends on the lamination orientation. It is observed that the tensile strength obtained from Brazilian tests, increases as the angle between tensile loading direction and bedding plane changes from 0° to 90° (Rao, 1984; Singh, 1988; Behrestaghi et al., 1996 and Kumar 2019a). The minimum strength observed at 0° angle is due to the low cohesion existing between the lamination and neighboring rock material. The results of the tensile testing on anisotropic rocks are shown in Fig**.** 18. It is observed that the tensile strength is the maximum for foliation angle (Ψ) of 90°. The minimum strength is observed at 30° loading angle (β) and foliation angle (Ψ).

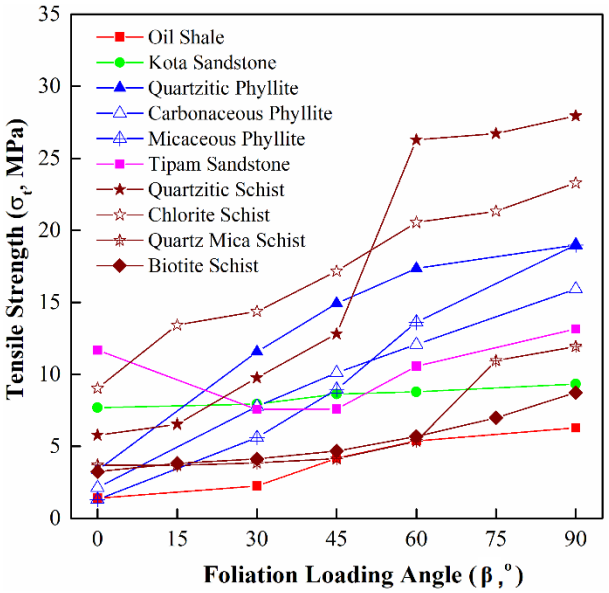

Fig. 18. Variation of tensile strength with foliation loading angle

The fracture pattern of quartzitic schist under Brazilian test for different loading conditions is shown in Fig. 19. The failure modes observed in the study are as follows: (1) tensile failure, (2) mixed mode failure (combination of tensile and shear failure) and (3) shear failure.

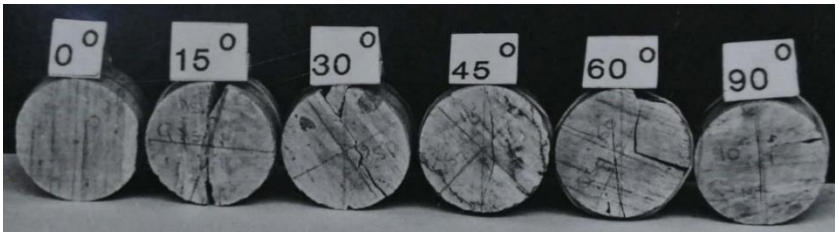

Fig. 19. Failure patterns exhibited by quartzitic schist under Brazilian test mode at different foliation angle (ψ) and loading angle (β) (Kumar, 2019a)

4.3 Stress-Strain Behaviour

The stress-strain behavior of anisotropic rock under uniaxial and triaxial stress state for different anisotropic angles is shown in Fig. 20 (a), (b) (c) and Fig. 21 (a). Further, the effect of anisotropy angle and confinement on the Young's modulus and Poisson's ratio is shown in Fig. 21. It is observed that the failure stress of anisotropic rocks is maximum at 90° and minimum at 30°. Whereas, the deformation modulus at β = 0° is higher than at other orientation angles. At this orientation there is less deformation, as a result of interlocking of the vertically oriented foliation planes when they are subjected to compression, whereas the values of deformation modulus at β = 90° are less than those at β = 0°, due to the compression of foliation planes.

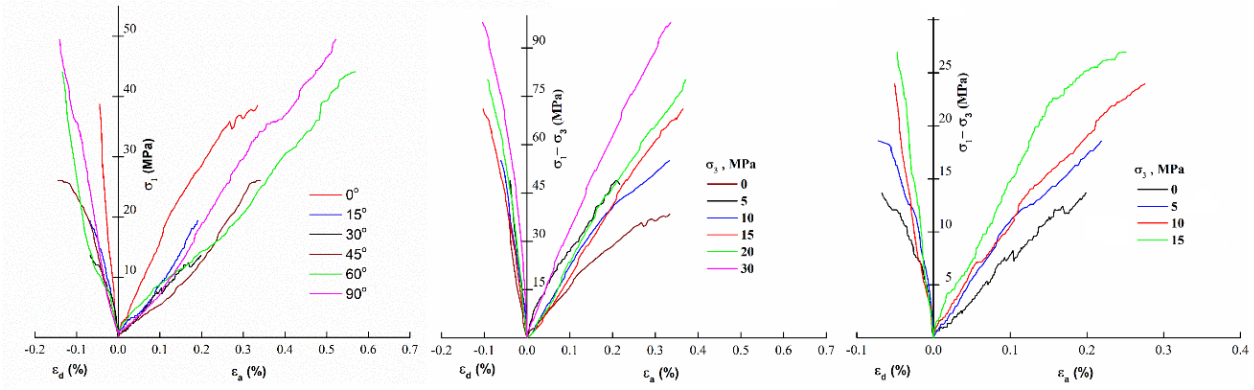

(a) (b) (c)

Fig. 20. Stress-strain response of oil shale under (a) Uniaxial compression, (b) and (c) Triaxial stress state at β = 0° and 30°

The variation observed for $E_{t(50)}$ with respect to β is similar to that of compressive strength variation as a function of β angle. Generally, the stress-strain response of anisotropic rock at β = 90° is plastic-elastic-plastic nature, due to the compression of the foliations. It is also observed that the axial deformation is maximum at β = 90° due to the same reason. Whereas, the failure strain is minimum at β = 30°. It is also observed that the Poisson's ratio is minimum at β = 30°. The behaviour observed in the study can be attributed to the effect of weak laminated nature of the anisotropic rock, due to which the failure takes place along the laminations at lower strength in the region 15° ≤ β ≤ 60°.

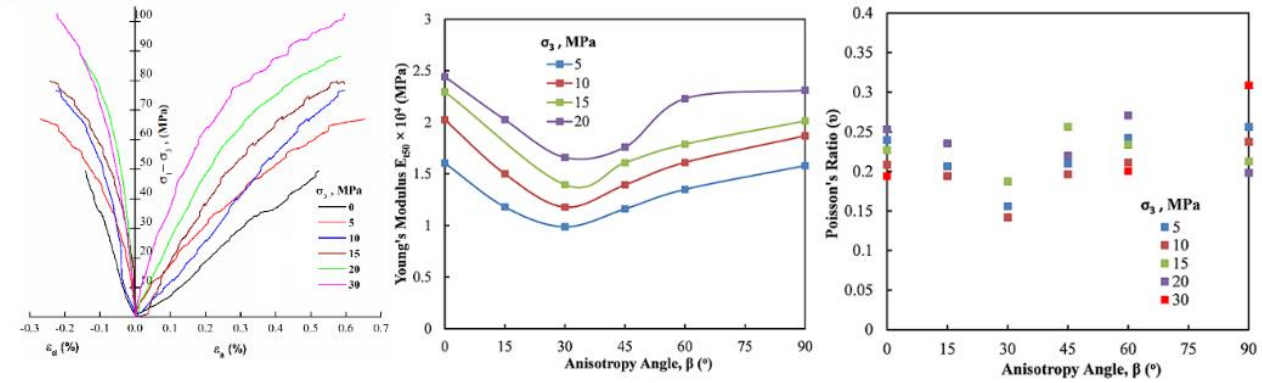

(a) (b) (c)

Fig. 21. (a) Stress-strain response at β = 90°, effect of confinement and anisotropy angle on (b) Young's modulus and (c) Poisson's ratio

4.4 Anisotropy Ratio

The anisotropic rocks are classified on the basis of anisotropy ratio (Rc). It is defined as the ratio of maximum uniaxial compressive strength to the minimum strength ($\sigma_{c(90)}/\sigma_{c(min)}$). As per the literature, generally the maximum compressive strength is obtained at 90° angle. Table 3 shows the anisotropy ratio of different rocks. The maximum value of anisotropy ratio is observed for oil shale and the minimum value is observed for sandstone.

4.5 Influence of Pressure and Temperature

4.5.1 Strength Behaviour in Triaxial Compression

The variation of failure stress (σ_1) with confining pressure for different anisotropic angles is reported in Fig. 22. It is observed from the figures that the curves between σ_1 and σ_3 show nonlinear behaviour for all the cases. It is also noted that the failure strength at β = 90° is higher than that at other orientation angles. The variation of failure stress (σ_1) with anisotropy angle at different confining pressure is shown in Fig. 22 (b). It is observed that the strength of rock is minimum for β between 30° and 45°. The lower strength is due to the lower shear strength along the laminations.

Table 3. Strength anisotropy of different rocks tested

Rock Type	$\sigma_{cmax}(\beta)$	Anisotropy Ratio	Source
Kota sandstone	0	1.12	Rao, (1984)
Quartzitic phyllite	90	2.19	Ramamurthy et al., (1993)
Carbonaceous phyllite	90	2.19	Ramamurthy et al., (1993)
Micaceous phyllite	90	6.00	Ramamurthy et al., (1993)
Quartzitic schist	90	2.7	Behrestaghi et al., (1996)
Chlorite schist	90	2.24	Behrestaghi et al., (1996)
Quartz mica schist	90	2.20	Behrestaghi et al., (1996)
Biotite schist	90	1.60	Behrestaghi et al., (1996)
Barail oil shale (100°C)	90	3.71	Kumar, (2019a)
Barail oil shale (300°C)	90	4.14	Kumar, (2019a)
Barail oil shale (450°C)	90	4.37	Kumar, (2019a)
Barail oil shale (600°C)	90	5.55	Kumar, (2019a)
Tipam sandstone (100°C)	90	1.62	Zaei, (2019)
Tipam sandstone (400°C)	90	1.72	Zaei, (2019)
Tipam sandstone (600°C)	90	1.64	Zaei, (2019)
Tipam sandstone (800°C)	90	1.81	Zaei, (2019)

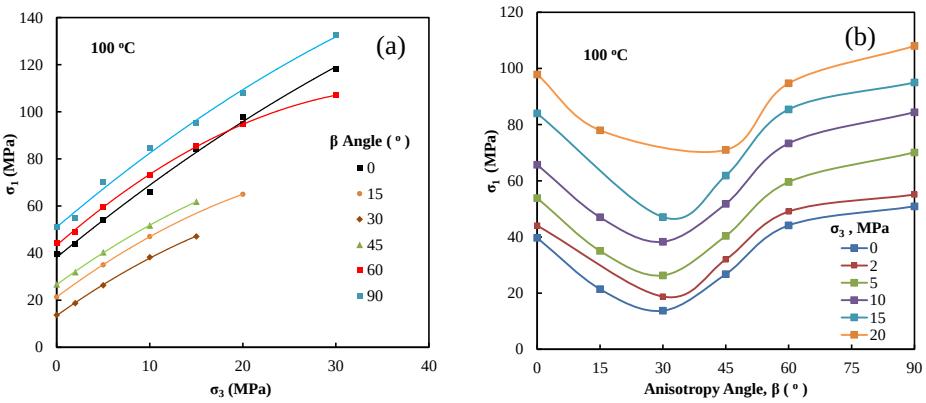

Fig. 22. Variation of σ_1 with σ_3 at different β angle for Oil shale rock

4.5.2 Shear Strength Parameters

The effect of anisotropy angle on cohesion (c) and friction angle (ϕ) are shown in Fig. 23 (a) and (b). The maximum value of cohesion (c) is obtained at β = 90°, whereas the minimum value is observed at β = 30°. The shape of envelop depends on the type of interlocking between two laminations. Further, the value of friction angle (ϕ) is minimum at 30° angle in most of the anisotropic rocks. The shoulder type variation of cohesion (c) and friction angle (ϕ) with orientation angle is observed for oil shale rock (Behrestaghi et al. 2003).

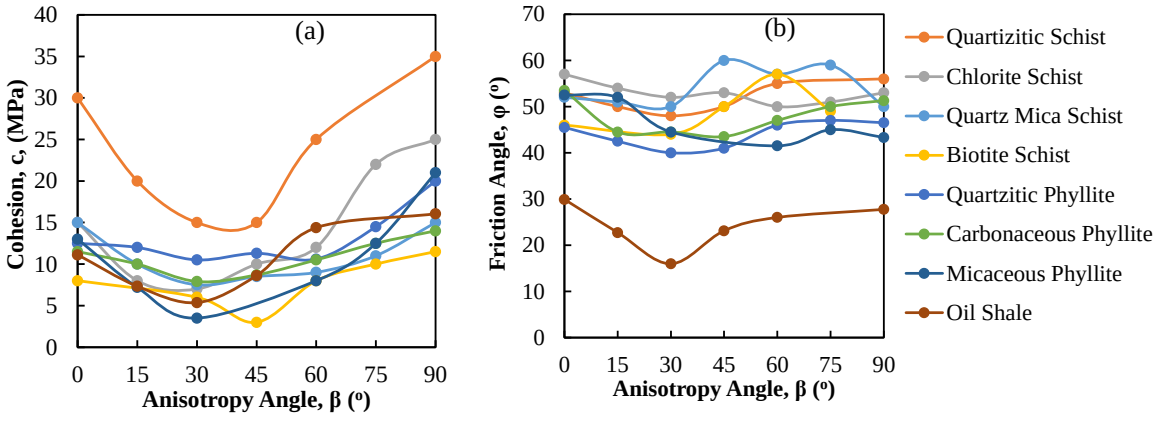

Fig. 23. Effect of anisotropy angle on (a) Cohesion and (b) Friction angle

4.5.3 Effect of Confinement

The effect of confining pressure on the strength of anisotropic rocks is studied by Ramamurthy et al. (1993) for phyllite and Behrestaghi et al. (2003) for schists. Rao et al. (1986) studied the variation of stress ratio with the anisotropy angle for different sandstones. Fig. 24 shows the plot between stress ratio (σ_1/σ_3) and anisotropic angle (β) under varying confining pressure (σ_3).

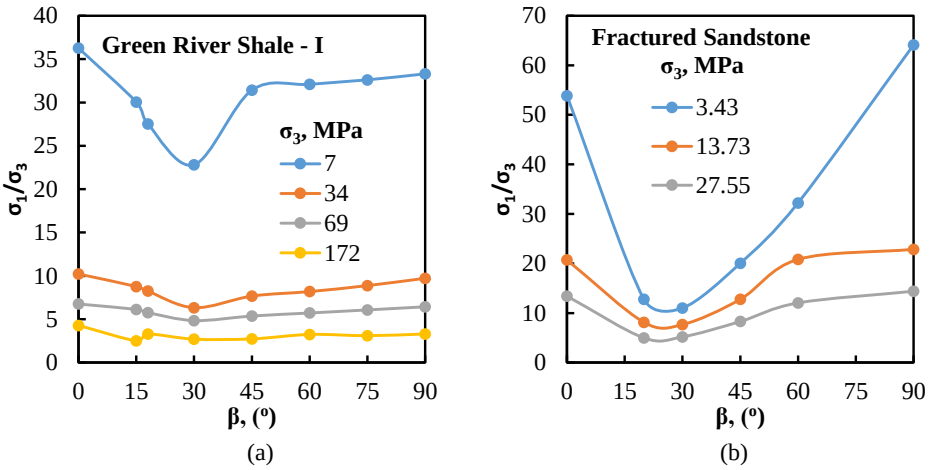

Fig. 24. Variation of stress ratio with orientation angle (β) for (a) Green river shale, (b) Fractured sandstone (Rao, 1984)

It is interpreted from the figures that the values of stress ratio decrease with increase in confining pressure, which shows that the effect of anisotropy reduces with rise in confining pressure. It is also observed that the strength anisotropy reduces faster below σ_c/σ_3 ratio of 5 and anisotropy almost vanishes in most of the rocks at $\sigma_c/\sigma_3 = 1$, where the anisotropy does not play a significant role for practical purposes.

4.5.4 Effect of Thermal Treatment

The temperature plays a crucial role in most of the civil engineering activities, such as deep well bores, underground caverns, or sudden fire outburst etc. Therefore, the effect of different heating temperatures on the strength of the oil shale is extensively investigated (Fig. 25). The stress-strain response of thermally treated oil shale rock shows that the plastic-elastic-plastic behaviour increase as thermal treatment temperature increases, this is due to the increase in the porosity and thermally induced cracks. Further, the concept of thermal degradation ratio introduced and investigated, which is the ratio of uniaxial compressive strength at β angle after thermal treatment at T°C ($\sigma_{c\beta T}$) with uniaxial compressive strength at β angle after thermal treatment at 100°C ($\sigma_{c\beta 100}$). The results are shown in Fig. 26. It is observed that with increase in temperature the thermal degradation ratio decreases for all β angles. The strength reduction is minimum at β = 90° and maximum at β = 45°. This variation in ratio is due to the generation of thermal cracks along the foliation plane. It is also found that the cohesion and friction angle also decrease with increase in thermal treatment temperature.

4.6 Dependency of Permeability

The stress-dependent permeability of different Indian rocks is measured by using permeability apparatus at IIT Delhi. The stress depencent permeability of different Indian rocks is investigated by Rao (1984), Behrestaghi (1992), Kumar (2019a), Singh (2019) and Zaei (2019). It is found that the permeability of these rocks decreases with increase in effective stress. Further, the effect of β on coefficient of permeability is observed due to the laminations. The weak laminations are allowing the water to permeate at a higher rate through them. Fig. 27 shows the stress dependent permeability of oil shale at different anisotropy angles.

4.6.1 Models for Stress Dependent Permeability

The stress sensitive models are modified by incorporating the effect of anisotropy of rocks. The exponential model is modified as:

$$k_\beta = (k_o)_\beta e^{-\gamma_\beta \Delta\sigma} \quad (5)$$

and power law model is modified as:

$$k_\beta = (k_o)_\beta \left(\frac{\Delta\sigma}{\sigma_o}\right)^{-p_\beta} \quad (6)$$

where, k_β is permeability at β angle in m^2, $(k_o)_\beta$ is permeability at atmospheric pressure for β angle in m^2, γ_β is pore compressibility dependent material constent at β angle in MPa^{-1}, p_β is material constent at β angle, $\Delta\sigma$ is change in effective stress in MPa and σ_o is the initial stress in MPa.

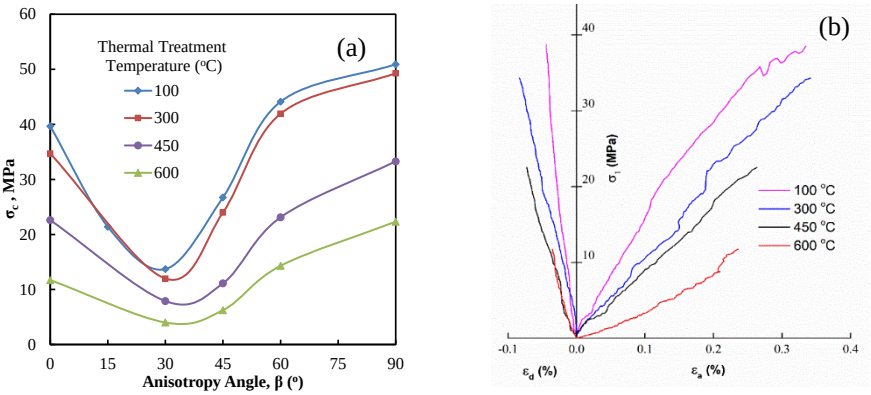

Fig. 25. (a) Variation of unconfined compressive strength (UCS) of oil shale with β for oil shale rock after thermal treatment, (b) Stress-strain response of thermally treated oil shale rock

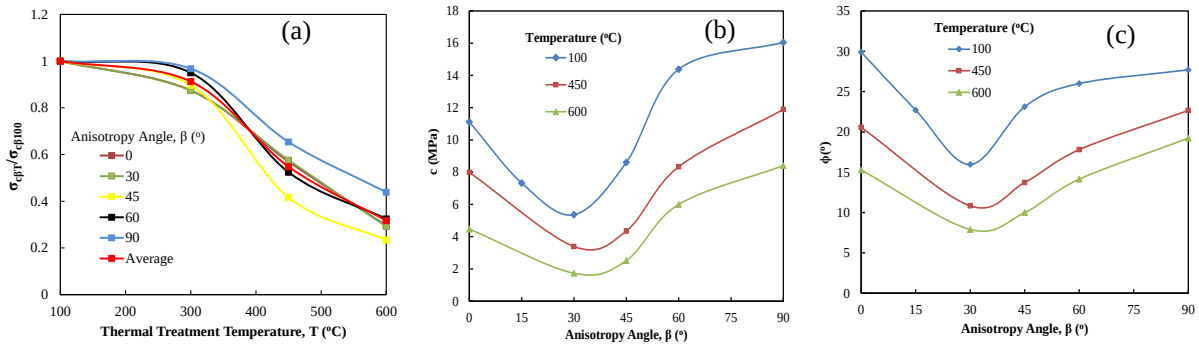

Fig. 26. Effect of thermal treatment temperature and anisotropy angle on (a) Thermal degradation ratio, (b) Cohesion, and (c) Friction angle

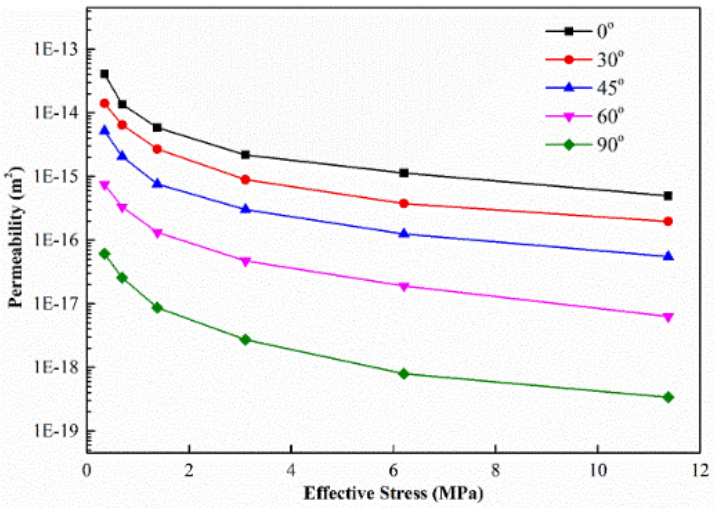

Fig. 27. Variation of permeability with effective stress at different β angle for Oil shale

The value of $(k_o)_\beta$ for both the models can be calculated from the following equation:

$$\frac{(k_o)_0}{(k_o)_\beta} = a\beta^2 + b\beta + 1 \quad (7)$$

Where, a, b are material constants (a = 0.0002 and b = -0.0277 for upper Assam oil shale rock) and β is anisotropy angle (°)

The value of material constant $\gamma\beta$ for exponential model can be defined as:

$$\gamma_\beta = m\beta + n \quad (8)$$

The material constant p_β can be found empirically as:

$$p_\beta = g\beta + h \quad (9)$$

Where, m and n are constants for exponential model (m = 0.001 and n = 0.221 for upper Assam oil shale rock) and g, h are constants for power law model (g = 0.0032 and h = 1.18 for upper Assam oil shale rock).

4.7 Failure Criteria

4.7.1 Strength Criteria for Anisotropic Rocks

The strength criterion proposed by Ramamurthy et al. (1988) for anisotropic rock is given by:

$$\frac{\sigma_1-\sigma_3}{\sigma_3} = B_j \left(\frac{\sigma_{cj}}{\sigma_3}\right)^{\alpha_j} \quad (10)$$

Further, two equations have been developed for the evaluation of αj and B_j; the strength parameters at any orientation other than β=90°; with σ_{cj} as the compressive strength at the corresponding orientation,

$$\frac{\alpha_j}{\alpha_{90}} = \left(\frac{\sigma_{ci}}{\sigma_{c90}}\right)^{1-\alpha_{90}} \quad (11)$$

$$\frac{B_j}{B_{90}} = \left(\frac{\alpha_{90}}{\alpha_j}\right)^{0.5} \quad (12)$$

where, σ_{c90} is the compressive strength at β=90°; α and B are the strength parameters σ_j ; and B_j ; at β=90° obtained by a minimum of two triaxial tests at this orientation.

Kumar (2019a), based on the test results on the oil shale, modified the criterion to incorporate the temperature effect. The modified equations are represented as:

$$\frac{\sigma_1-\sigma_3}{\sigma_3} = R_{cT} B_j \left(\frac{\sigma_{cj}}{\sigma_3}\right)^{\alpha_j} \quad (13)$$

Except R_{cT}, all the other parameters have the same significance as mentioned in the previous section. This is very useful to predict strength of rocks at any confinement and temperature.

5 Engineering Behavior of Weathered Rocks

Weathering is an inevitable process of nature, gradually alters a rock from its original hard state (fresh) to residual (soil) material and as a consequence, changes its engineering behavior. Most of the rocks encountered are weathered to some extent and it is universally recognized that this process will have affected many of the engineering properties. Although a progressive deterioration of strength is generally found, to-date no attempt has been made to compare the index properties of different rocks in different weathering conditions.

Extensive field and laboratory studies on three major geological outcrops viz. granite (Precambrian) from Malanjkhand copper pit mines, basalt (Deccan traps) exposed at Nagpur and quartzite (Precambrian) from Delhi were conducted (Gupta, 1997). In the second phase a detailed study carried out in the field on natural out corps, road cuts and quarry wall exposures at and nearby Mumbai-Pune-Satara-Koyna at six locations, by investigating 23 weathered profiles of different volcanic rocks. For each rock, six grades of weathered materials e.g.W_0, W_1, W_2, W_3, W_4 and W_5 were collected for laboratory investigations (Chala, 2018).

5.1 Elemental Mobility

The relative mobility of elements determined by XRF studies in each weathering sequence shows the stability or differential movement of cations with respect to the cations present in the parent material. The following mobility orders for the three rock weathering sequences have been established based on extensive studies (Gupta and Rao, 2001; Chala, 2018).

Granite:	Na > Ca > K > Mn > Mg > Si > Fe > Al > Ti
Basalt/Pyroclasts:	Na > Ca > Mg >K > Si > Al > Fe > Mn > Ti
Quartzite:	Na > Ca > Si > Fe > Ti > Al > K

5.2 Weathering Indices

The physical appearance of volcanic rocks investigated are shown in Fig. 28. For quantification of weathering several petro-physico-mechanical indices e.g. UCS, $I_{s(50)}$, σ_t, RN, V_p ,γ and QAI along with two petrographic DI and MI have been worked out for these rocks. The UCS values gradually decrease with increase of degree of weathering for all rocks tested as shown in Fig. 29. Such variances are found with other physical and strength properties also (Gupta and Rao, 1996; 1998).

A new strength index 'strength ratio' R_s has been proposed.

$$R_s = \frac{\sigma_{cw}}{\sigma_{cf}} 100 \quad (14)$$

where, σ_{cw} and σ_{cf} are the unconfined compressive strength values of the weathered and corresponding fresh rock respectively. The degree of weathering can be expressed using the Rs index successfully. Similarly, the indices have been correlated with degree of weathering as shown in Table 4. These indices with high r^2 are very useful.

Typical peak strength variation with σ_3 for different grade basalts are shown in Fig. 30. It is observed that all the engineering parameters decrease with increase in the weathering grade of the rock, except Poisson's ratio.

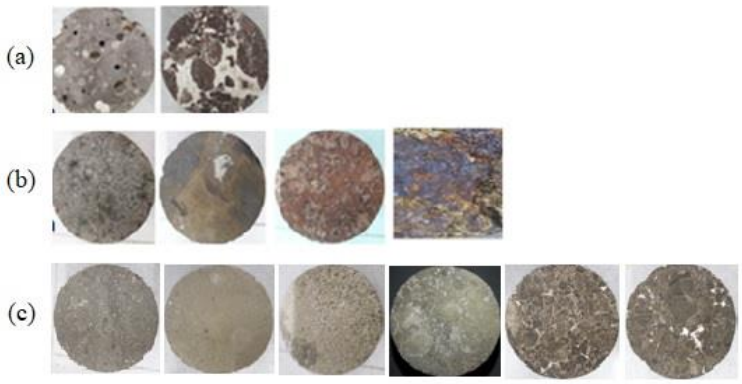

Fig. 28. Appearance of various weathered basaltic and pyroclastic volcanic rocks studied (a) Vesicular and amygdaloidal basalt (b) Basaltic specimens with various weathering grade (c) Different varieties of pyroclastic volcanic rocks from Deccan Trap (Chala and Rao, 2017)

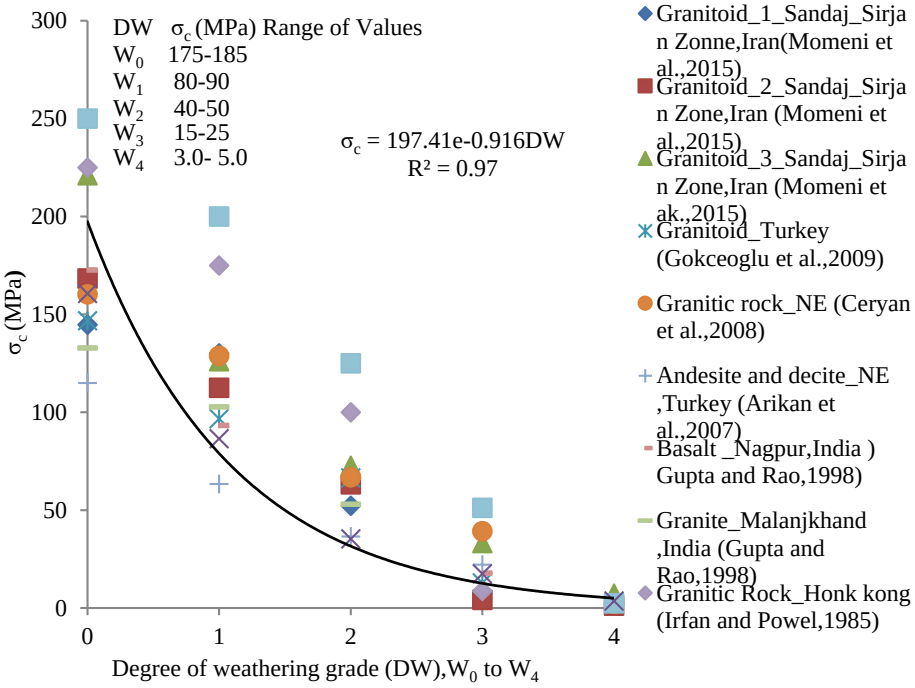

Fig. 29. UCS as a function of weathering grade

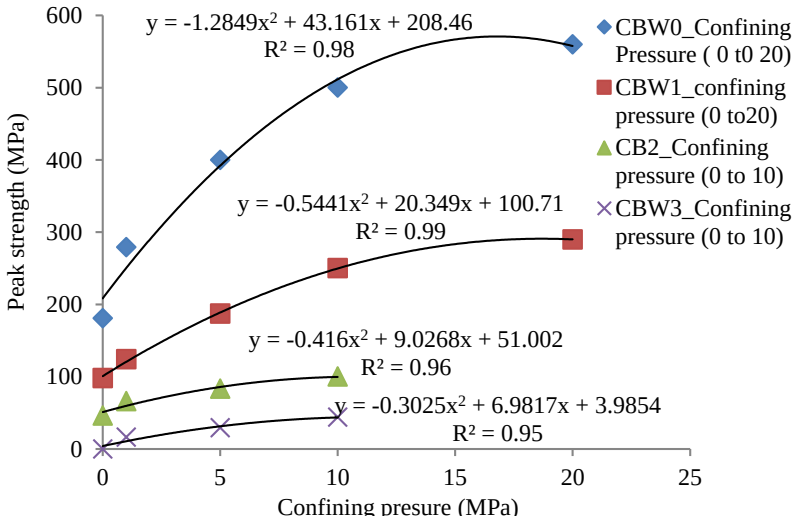

Fig. 30. Peak strength variations with confining pressure for weathered basaltic rocks

Table 4. Summary of developed physico-mechanical indices as a function of weathering grade

Developed Correlations	r^2	Remark
n(%) = 0.4659e0.9174DW	0.93	n = Porosity
ɣ (kN/m^3) = -1.43DW + 30.02	0.90	ɣ = density
QAI (%) = 0.6556e$^{0.609DW}$	0.78	QAI = Quick absorption Index
V_p (m/s) =-856.85DW+5409.3	0.90	V_p = Sonic wave velocity
σ_c (MPa) = 19741e$^{-0.916DW}$	0.96	σ_c = Unconfined compressive strength
$I_{s(50)}$ (MPa) = 10.9e 0.656DW	0.99	$I_{s(50)}$ = Point load strength,
E(GPa)=88.057e-$^{1.89DW}$	0.94	E = Young's Modulus
υ = 0.198e0.1282DW	0.98	υ = Poisson ratio

5.3 Failure Modes

The following failure modes are observed for different grades of weathered rocks,

W_0 Fresh grade : Splitting + tensile
W_1 Slightly weathered : Tensile + shear
W_2 Moderately weathered : Shear + tensile
W_3 Highly weathered : Shear
W_4 Completely weathered : Shear + bulging

5.4 New Weathering Rockmass Classification System

The classification system that is specifically useful for weathered rockmass is initially proposed by Gupta and Rao (2001) and further modified by Chala and Rao (2018) incorporating the weathering indices chart proposed (Fig. 31) on the bases of Total Core Recovery and Rebound hammer values for assessing strength of various chemically weathered rockmass. This quantitative weathering classification system is developed on the basis of field study of more than 30 weathered profiles and laboratory testing for index and material properties. The material and mass parameters used for the classification are:

- Strength Ratio, R_s
- State of Joint Weathering, J_{wt}
- Number of Joints, J_n
- Joint Width, J_{wd}

All the important elements of rockmass, affected by weathering, have been considered by using a rating system (Table 5). Not all the parameters are of equal importance in the assessment of rockmass strength thus, it is necessary to assign a numerical weightage to each parameter according to influence of weathering on it. Summing up the weighted values determined for the individual parameter in each zone marked the final rating for the rockmass. Higher value of final rating, R_w reflects less weathering. The recommended rating for each parameter and each class is presented in Table 5. Based on final rating the zones of profile may be classified according to the range of total ratings suggested in Table 6 (Rao and Gupta, 2003; Chala and Rao, 2018). The developed classification systems can be used along with strength criterion for prediction of rockmass strength.

Table 5. Rock weathering classification based on rating system

Weathered Material Grade	Symbol	Fresh	Slightly Weathered	Moderately Weathered	Highly Weathered	Completely Weathered
Strength Ratio	R_s	80-100	50-80	25-50	10-25	<10
Rating		30	25	15	7	3
State of Joint Weathering	J_{wt}	Fresh	Slightly Weathered	Moderately Weathered	Highly Weathered	Completely Weathered
Rating		35	28	17	8	3
Number of Joints per meter	J_n	<2	2..4	4-8	8-16	>16
Rating		25	20	13	6	3
Joint Width (mm)	J_{wd}	<1.0	1-2	2-5	5-20	>20
Rating		10	8	5	2	1

Table 6. Classified range of final rating

Symbol	Zone	Final Rating, Rw
Z0	Fresh Rock	100-81
Z1	Slightly Weathered	80-51
Z2	Moderately Weathered	50-26
Z3	Highly Weathered	25-11
Z4	Completely Weathered	10-1
Z5	Residual Soil	0

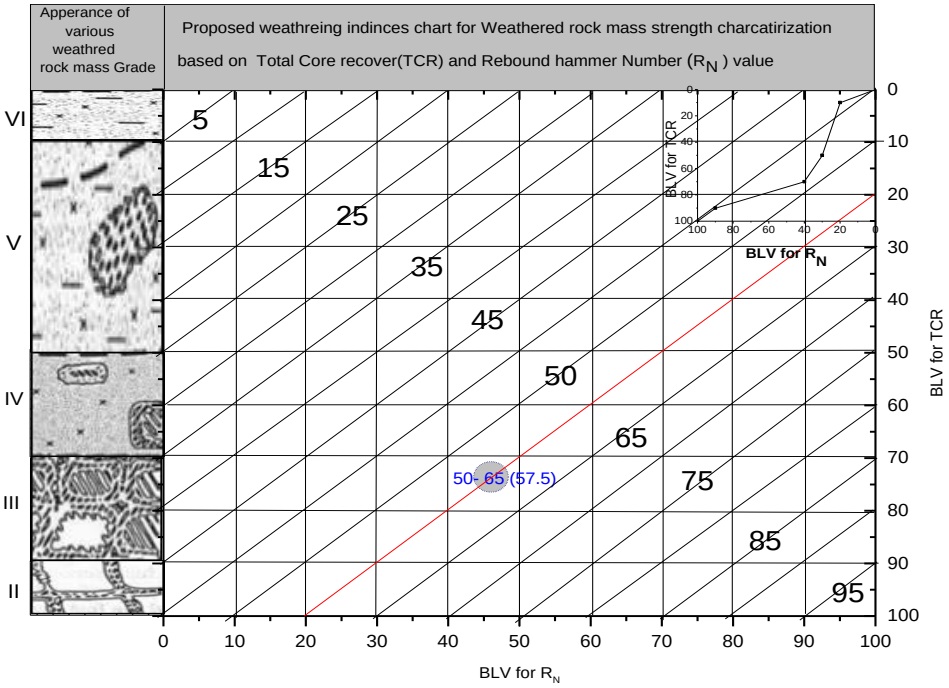

Fig. 31. Proposed weathering indices chart (WI Chart) by R_N values and TCR (Chala, 2018)

As per this classification 65% weightage is allotted for chemical weathering and 35% for physical weathering. Parameters in RMR and Q classifications have more bias towards for physically weathering.

5.5 Strength and Deformation Prediction

The strength criterion proposed by Rao (1984) in the following form may be used for predicting the strength of weathered rocks:

$$\frac{(\sigma_1-\sigma_3)}{(\sigma_3)} = B_w\left(\frac{\sigma_c}{\sigma_3}\right)^{\alpha_w} \quad (15)$$

Where, B_w and α_w are weathered material constants. Based on the available data and test results, the following equations are suggested for evaluating material constants:

$$\frac{B_w}{B_i} = e^{\left[\frac{R_w-100}{30}\right]} \quad (16)$$

$$\frac{\alpha_w}{\alpha_i} = e^{\left[\frac{R_w-100}{140}\right]} \quad (17)$$

Where, R_w= rating through weathering classification, rest defined already.

Based on triaxial tests on fresh rock and UCS tests on fresh (σ_{ci}) and weathered (σ_{cw}) rock using the 'R_s', the following correlations also could be used for estimating the material constants B_w and $\dot{\alpha}_w$ for the strength prediction at any σ_3.

$$B_w/B_i = 0.0089R_s + 0.09 \text{ for granite} \quad (18)$$

$$B_w/B_i = 0.0073R_s + 0.28 \text{ for quartzite} \quad (19)$$

$$B_w/B_i = 0.0083R_s + 0.17 \text{ for basalt} \quad (20)$$

$$\alpha_w/\alpha_i = 0.002R_s + 0.81 \text{ for quartzite and granite} \quad (21)$$

$$\alpha_w/\alpha_i = 0.003R_s + 0.72 \text{ for basalt} \quad (22)$$

In-situ deformability can be estimated using the following relationship:

$$E_{t(in-situ)}\ \text{GPa} = e^{\left[\frac{R_W-27}{16}\right]} \quad (23)$$

The R_w classification is more suitable for the tropical and subtropical regions like India where weathering profiles have considerable thickness developed due to severe chemical weathering. The classification and the strength predictions through the strength criterion are very useful for rapid and preliminary investigation of any rock engineering project. The new classification (R_w) has been successfully adopted in bored tunnel and station works of Delhi metro and several foundation and slope works in Mumbai and Pune (Rao and Gupta, 1997; Chala and Rao, 2017 and Malik et al., 2017). The newly proposed weathering indices chart is very promising and useful in estimating strength properties of various weathered rockmass zones for numerical modelling.

6 Jointed Rockmass Behaviour under Uniaxial Compression

A proper assessment of strength and deformational behaviour of jointed rockmass is necessary for the design of slopes, foundations, underground openings and anchoring systems. Both the intact rock and the properties of the joints govern the mass response. If the mass is not highly fractured and the joint system has only few sets, then the mass usually behaves anisotropically. Most of the civil and mining projects are on surface or near surface activities in rockmass occur under low confining pressure. In such cases the influence of joints is quite decisive. The uncertainty in predicting the behaviour of a jointed mass under uniaxial stress is essentially caused by scale effects and the unpredictable nature of the modes of failure. Extensive field tests are often required to assess the strength and deformability of the ground making the exercise quite expensive. To minimise this uncertainty an extensive experimental study has been carefully planned and executed to develop a more reliable link between the strength and modulus of jointed rockmasses and those of the intact rock.

6.1 Experimental Program

The experiments were conducted on specimens of a jointed block mass (Singh, 1997) formed of saw cut blocks of a model material. The joint configuration was varied to achieve the possible modes of failure commonly occurring in the field. For reproducibility of results and ease of working, a model material called sand-lime brick was used in this study. The material has a uniaxial compressive strength (UCS) of 17.13 MPa and represents a weak rock belonging to the ‘‘EM’’ group on the Deere-Miller (1966) classification chart.

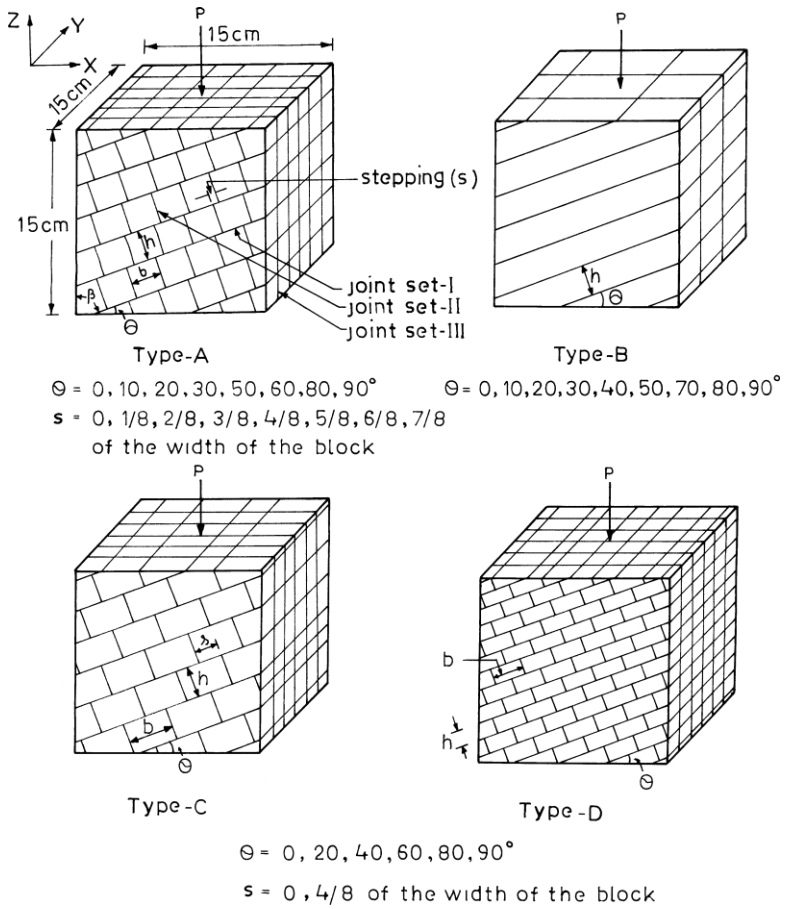

Fig. 32. Configuration of joints tested (Singh et al., 2002)

6.1.1 Description of Specimens of Jointed Block Mass

The jointed specimens can be grouped into two main categories (Fig. 32). The first category belongs to Type-A specimens in which the specimens were formed from cubical blocks. The major part of the experimental program belongs to Type-A specimens. A few additional tests were conducted by varying the geometry of the elemental blocks forming the specimens (Types-B, C and D).

Type-A Specimens

A typical configuration of the specimens is shown in Fig. 32. To have a reasonably scale free jointed block mass, it was decided to have at least six elements in each direction. The size of each of the specimens was 15cm*15cm*15cm and on an average there were more than 260 cubes, each of 2.5 cm side length. The jointed mass consisted of three sets of joints. The joints in Set-I were continuous and inclined at a variable angle y, with the horizontal. The values of y adopted were 0°, 10°, 20°, 30°, 40°, 50°, 70°, 80° and 90°. The joints in Set-II were orthogonal to Set-I and were staggered at variable stepping ‘s’. For each orientation θ, the values of ‘s’ used were 0, 1/8, 2/8, 3/8, 4/8, 5/8, 6/8 and 7/8 of the width of the block. The joint Set-III remained vertical. A total of 55 specimens were tested in this category (Singh et al., 2002).

Types-B, C and D Specimens

Few selected tests were also conducted with changed geometry of the elemental blocks forming the specimens. Three more geometries were investigated (Fig. 32). In Type-B, plates of 2.5 cm thickness (h) were used. The values of θ adopted for Type-B specimens were 0°, 10°, 20°, 30°, 40°, 50°, 70°, 80° and 90°. A total of nine specimens were tested in this category.

The Type-C specimens had block width, b = 3.75 cm and height, h = 2.5 cm h/b 0.67. The Type-D specimens had blocks with dimensions as b = 2.5 cm and h = 1.25 cm (h/b = 0.5). For both Types-C and D, the orientation θ was adopted as 0, 20, 40, 60, 80 and 90○. For each orientation only two stepping i.e. zero and 4/8 (half of the width of the block) were used. For Types-C and D, 12 specimens of each were tested.

6.1.2 Preparation of the Specimens and Testing Program

Model bricks were cut into plates and bars and then into blocks or cubes as per the requirement of the specimen. These blocks or cubes were then arranged on a perspex sheet with required orientation and stepping ‘s’. All four sides were cut to obtain one vertical segment of the jointed specimen (separated by joint Set-III). All the six segments were prepared using the same method and oven dried at 105°C for 24hours. After this, the blocks were kept in air for 7 days and on the eighth day they were assembled to form the specimen for testing. To minimize end friction two sandwiches of Teflon sheets smeared with silicon grease were used at the top and the bottom of the specimen. Eight rubber bands of low stiffness were placed around the specimen to hold the blocks in place. Four LVDTs were used to measure the vertical deformation between the upper and lower loading platens (Fig. 33).

Horizontal deformations were measured at the center of all the four vertical faces of the specimen using LVDTs. The tests were conducted under uniaxial stress conditions. Load was applied through a hydraulic jack under controlled rate of deformation. The rate of loading was so adjusted that the failure took place within 20 minutes from starting of the experiment. The deformations were continued till the load decreased to about half to one third of the peak load. The mode initiating the failure was recorded.

6.2 Results and Discussion

6.2.1 Modes of Failure

The modes of failure of the jointed block specimens are complex and multiple failure mechanisms occur. It was however possible to identify the most dominant mode initiating the failure. Out of all the combinations available, four distinct modes of failure were identified viz.: Splitting of intact material, shearing of intact material, rotation of blocks and sliding along critical joints. Modes of failures observed are shown in Fig. 34 (Singh and Rao, 2005).

Splitting

The term splitting implies failure of material due to tensile stresses developed within it. The failed specimens show large number of minute tensile cracks, roughly vertical in direction and without any sign of shearing. The crushing of material is also considered under this mode.

Shearing

The specimen fails due to one or more shearing planes, which are inclined and pass through the intact material and the pre-existing joints. Signs of displacement along the shearing plane are shown by the specimen. Powder gouge material is also formed due to shearing.

Rotation

Under this mode of failure rotation of blocks takes place right from the loading. The specimen as a whole translates and large relative displacement in the transverse direction is observed. The individual elements remain intact.

Sliding

The specimen failure was initiated due to sliding on the continuous joints. The mode is associated with large deformations, stick-slip phenomena and a poorly defined peak in the stress-strain curves. At large deformations the mode is mostly associated with either rotation or material failure or any other complex combination of modes. A summary of the modes of failure observed for Type-A specimens is presented in Table 7. The table shows distinctly different regions in terms of orientation of joints and steppings conditions (a measure of interlocking), in which a particular mode of failure lies. This was also confirmed by modes of failure obtained for other types of specimens. The observations from this table can be used later to suggest guidelines for assessing the mode of failure in the field.

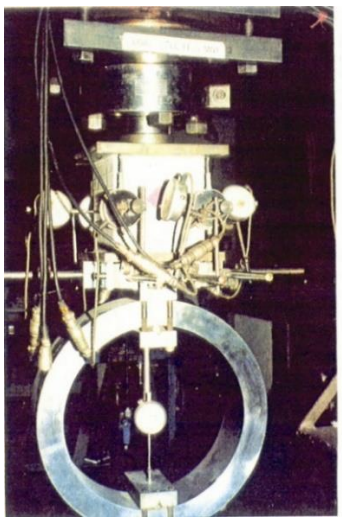

Fig. 33. Experimental arrangement for model tests (Singh, 1997)

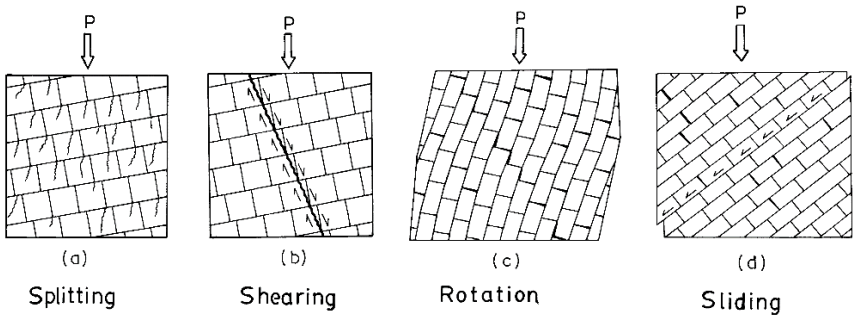

Fig. 34. Modes of failures observed in the modelling (Singh and Rao, 2005)

Table 7. Zones of modes of failure for Type-A specimens (Singh et al., 2002)

90	***Shearing***							
80	***Rotation***							
70	***Sliding***							
50								
40								
30					***Shearing***			
20								
10								
0	***Splitting***							
θ° ↑ s→	0	1/8	2/8	3/8	4/8	5/8	6/8	7/8
	Nil	Low		Medium		High		V. high
	Extent of Interlocking →							

6.2.2 Stress-Strain Behaviour

The axial stress has been computed by applying corrections for changes in the cross-sectional area due to lateral expansion during loading. Axial strains were corrected for the compression of the teflon sandwiches. The compressive stress and strains

are considered positive. Most of the stress-strain curves are S-shaped and some of them are presented in Fig. 35. Out of the two deformations measured in the transverse directions, the deformation in the direction X (Fig. 32) is generally larger due to dipping of joints. Near the origin, the axial stress-strain curve is concave upward, which indicates closure of joints and an initial seating effect. The middle portion of all the curves is linear, exhibiting elastic deformations. The failure of the specimens was progressive, and near the peak did not show a sudden stress decrease. For almost all cases of splitting, shearing and rotational mode of failure, smooth stress-strain curves were obtained. In the sliding mode, the specimens failed exhibiting stick-slip phenomena along the joints.

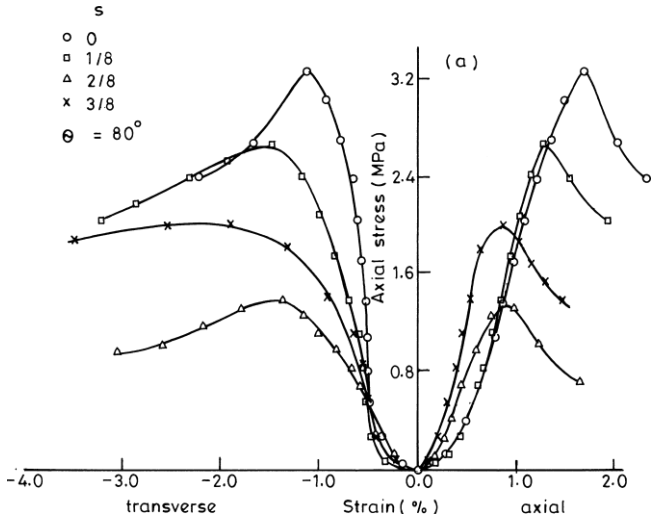

Fig. 35. Typical stress-strain curves for Type-A specimens (Singh and Rao, 2005).

6.2.3 Effect of Interlocking on Strength and Deformational Behaviour

The strength and deformational characteristics are found to change with different combinations of inclination of joints, θ, and interlocking 's'. The effect of stepping 's' on strength and tangent modulus for Type-A specimens is shown in Fig. 36 (a and b). These values are shown in terms of ratios as defined below:

$$\sigma_{cr} = \sigma_{cj}/\sigma_{ci} \quad (24)$$

$$E_r = E_j/\sigma E_i \quad (25)$$

Where, σ_c and E refer to the uniaxial compressive strength and tangent modulus respectively; the subscripts i and j refer to intact and jointed specimens respectively. From the observations of the test results, it is clear that the stepping has little effect on the strength when the continuous joints are horizontal or vertical (θ = 0° and 90°). The specimens fail either due to splitting or shearing through intact material, giving upper bound values of strength and tangent modulus. There is no systematic influence of stepping and the properties are thus primarily influenced by joint frequency.

6.3 Anisotropic Behaviour

One of the most important features of the joints in rock is that they introduce anisotropy in strength and deformability of rocks. β is orientation of continuous joints relative to the loading direction (90°-θ°). It is observed that the value drops sharply between β = 0° and 30° with minimum at β = 30°. The shape of the curve is 'U' with flat base.

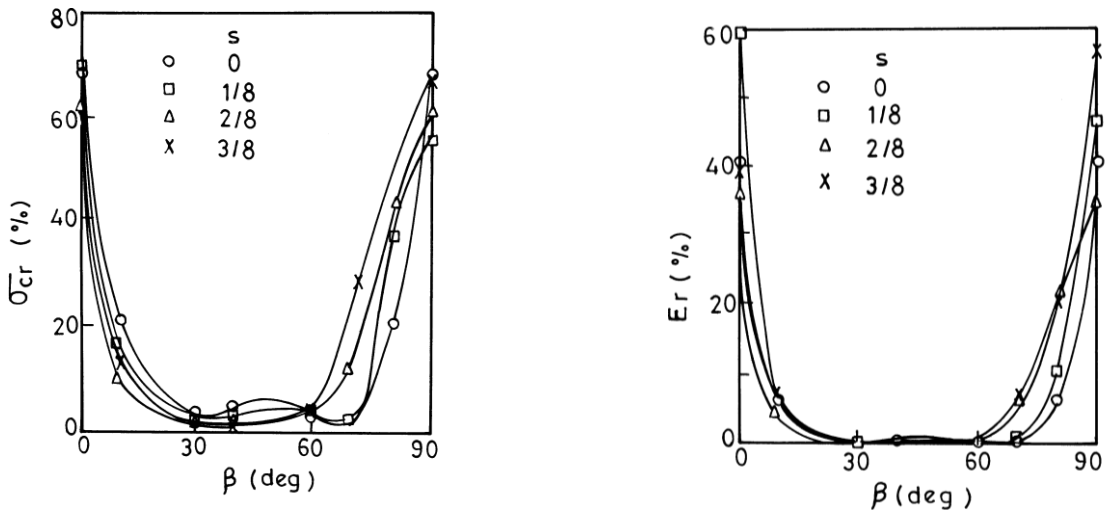

Fig. 36. Anisotropic behaviour in strength and tangent modulus (Type-A specimens) (Singh et al. 2002)

6.4 Concept of Joint Factor

The influence of jointing on the response of intact rock can be studied through a weakness coefficient called Joint factor (Ramamurthy, 1993; Ramamurthy and Arora, 1994). This coefficient reveals the 'weakness' brought in to the intact rock through jointing and takes into account the combined effect of frequency of joints, their inclination and roughness along the critical joints. The higher the Joint factor, the greater is the 'weakness'. It is represented as $J_f = \frac{J_n}{nr}$.

where J_f = joint factor; J_n = number of joints/m depth in the direction of loading; n = critical joint inclination parameter; r = sliding joint strength parameter tan(ϕ_i); ϕ_i is friction angle along the critical joint at sufficiently low normal stress so that the initial roughness of the surface is reflected through this value.

For this study, the value of ϕ_i was computed by conducting direct shear tests on the joint surface between the two blocks. The experimental data were sub-divided based on the failure mode, and the following methods were used to compute the parameters J_n and n and hence J_f . Computed J_f values for different modes of failure specimens were used to correlate with their respective strength and modulus values.

6.5 Prediction of Strength and Modulus of Deformation

A rough estimate of the probable mode of failure in the field is made based on the test results reported in Table 7. Once the probable mode of failure is assigned based on the guidelines suggested above, the value of Joint factor, J_f can be computed for each meter depth of the jointed mass. The maximum value of J_f should be considered as this will represent the weakest zone in the section. The following expressions reproduced from previous sections can be used for computing the average strength and tangent modulus for a mass with two sets of joints:

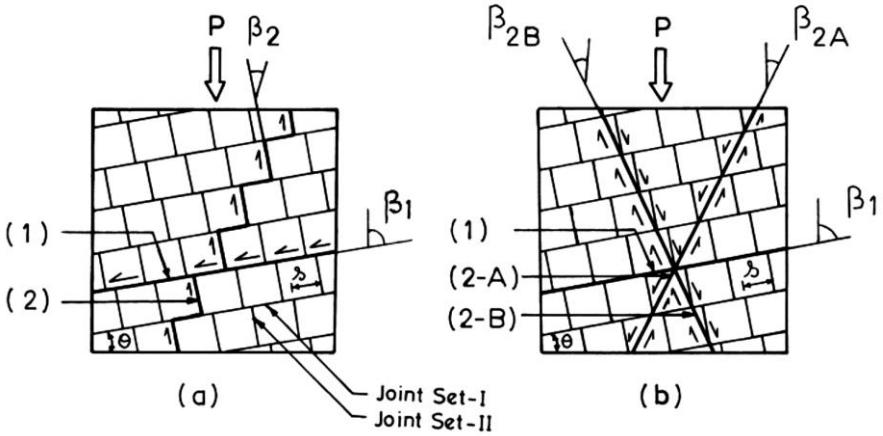

Fig. 37. Potential failure surfaces to compute J_f (Singh et al., 2002)

$$\sigma_{cj} = \sigma_{cj}\, e^{(a.J_f)} \qquad (26)$$

$$E_j = E_i\, e^{(b.J_f)} \qquad (27)$$

where σ_{cj} and E_i are the uniaxial compressive strength and tangent modulus of the intact rock respectively. The values of the coefficients, 'a' and 'b' for different modes of failure are presented in Table 8.

Table 8. Coefficients 'a' and 'b' for predicting σ_{cj} and E_j

Failure mode	a	b
Splitting	0.0123	0.020
Shearing	0.0110	0.020
Rotation	0.0250	0.040
Sliding	0.0180	0.035

6.6 Conclusions

The following major conclusions can be drawn from the study.

i. The study established four distinct modes of failure namely splitting of intact material, shearing of intact material, rotation of blocks and sliding along the critical joints. These modes of failure are dependent on the configuration of joints and interlocking conditions.
ii. Guidelines are suggested to assess the probable modes of failure in the field based on the mapping of joints.
iii. A weakness coefficient called Joint factor is used to describe the effect of jointing introduced in the intact rock.
iv. Expressions are suggested to compute the strength and tangent modulus of the jointed mass through the Joint factor.

7 Behaviour of Rockmass under Polyaxial Stress State

Structures such as rock slopes, tunnel faces near the surface experience only two dimensional (σ_1 and σ_2) stress state whereas at deep depths slopes, foundations and tunnel openings or caverns experience all the three sets of stresses i.e. triaxial or polyaxial condition is prominent. The strength and deformation response of rockmass is of great importance in rock engineering and the same can be estimated through in-situ and laboratory large-scale testing, physical and numerical modeling studies.

The strength and deformability behaviour of rockmass was studied in polyaxial stress state by Tiwari (2004), Tiwari and Rao (2004, 2006a, 2007). To study the effect of intermediate principle stress, σ_2 and angle of critical discontinuity in rockmass on its stress-strain, failure mechanism and failure strength, an extensive rockmass model testing was carried out in true triaxial stress state ($\sigma_1 > \sigma_2 > \sigma_3$). Rao and Tiwari (2008) developed a polyaxial loading system at Indian Institute of Technology Delhi for laboratory testing of mechanical behaviour of rockmass. The large-scale rockmass models of different joint geometry can be tested under true triaxial stress state simulating with field stress conditions using this true triaxial system (TTS). Based on the results a new strength criterion was developed. Further, Tiwari and Rao (2006c) used the test data to explain the post failure behaviour of rockmass. Salient features of the study are highlighted in this section.

7.1 Design and Development of Polyaxial System

Few researchers developed biaxial and polyaxial testing equipment (Bobet and Einstein, 1998; Haimson and Chang, 2000) with several limitations. Rao (2006) developed polyaxial system with which jointed rocks tests were conducted. The Polyaxial or True Triaxial System (TTS) system developed by Rao and Tiwari (2008) works on the principle of general stress system, and three principal stresses are applied through rigid platens independently.

7.1.1 The Equipment

Vertical and Horizontal Loading Frames.

The new True Triaxial System (TTS) of 1000kN capacity was designed and fabricated to carry out the experimental study on rockmass models. The 5000kN capacity loading frame is available rock mechanics laboratory was modified as vertical loading frame by equipping it with load cell (1000kN, sensitivity 0.1kN) and LVDTs (± 20 mm, least count 0.01 mm) for measuring load and axial deformation respectively. The application of vertical load is strain controlled and can be applied through the existing hydraulic pumping unit (Fig. 38).

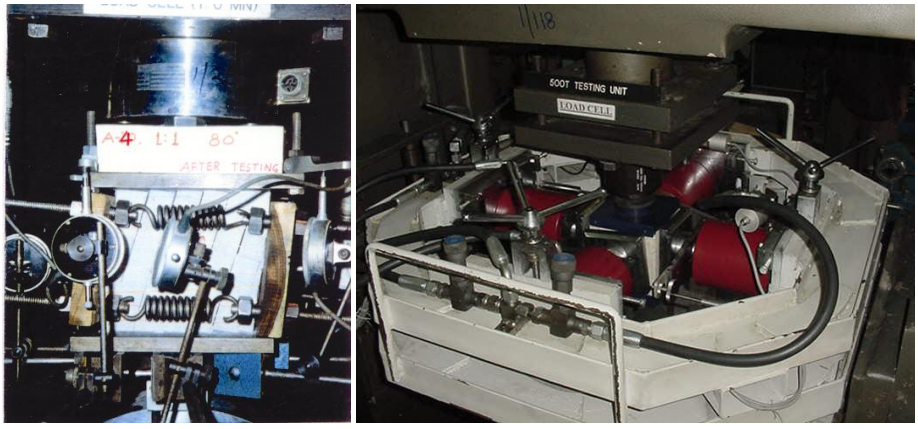

(a) (b)

Fig. 38. (a) Initial polyaxial system (Rao, 2006) (b) Biaxial frame of TTF with accessories (Rao and Tiwari, 2008)

The horizontal irregular octagonal shape rigid frame of capacity 300kN having external dimensions 490 mm and 400 mm was designed and fabricated. This shape was achieved by welding eight pieces of I-beam sections of ISLB125. The internal clearance in x and y directions was kept at 623 mm.

Two pairs of identical hydraulic jacks 300kN capacities were fitted on the face of octagonal frame to apply σ_2 and σ_3 independently upto 15.0 MPa on a specimen of size 150mm x 150 mm x 150 mm. Both sets of plates were having 140mm x 140mm size as to provide small gaps of 5mm on either side of the vertical edge of the cubical specimen. The jacks placed on the opposite faces were inter-connected with load sensor and in turn connected to the accumulator and a constant confining pressure unit for measuring and maintaining constant pressure over the specimen faces during the testing. The deformations on all faces of specimen are measured by LVDTs fitted on platen faces (Rao, 2011).

7.1.2 Constant Confining Pressure and Data Acquisition Systems

The unit is equipped with a pair of booster pistons and an oil tank for applying hydraulic pressure in jacks. The air compressor is connected to piston for maintaining required pressure in confining unit. Three load cells/sensors and five LVDTs coming

out from true triaxial system are connected to data acquisition system. This eight-channel system converts the mechanical and electrical signals into digital data. The output signal is connected to CPU where the load and deformation data can be stored at desired intervals. Appropriate calibrations were done for all measurements (Rao and Tiwari, 2008).

7.2 Strength Behaviour of Rockmass

7.2.1 Rockmass Testing

The different joint geometries were formed in rockmass specimens with the help of model rock and testing were performed under triaxial and true triaxial stress conditions.

Model Material Characterization

Due to reproducibility of results and ease of working, the sand lime brick a substitute for rock, model material that was reported in section earlier was used for this study as well.

Geometry of Specimens Tested

Most frequently occurring joint geometries in rockmass at site was created in model rock. The specimens were prepared by cutting model rock into small cubes of size 2.5 cm and arranging the small cubes to form the test specimen of size 15 cm x 15 cm x 15 cm having three sets of orthogonal joints as explained in section 5.1 three sets of joints were created with varying θ and β (Fig. 39). Type-A specimen of θ = 60° and is acted by principal stresses, σ_3 = 0.31 MPa and σ_2 = 1.62 MPa along y and x-axis respectively.

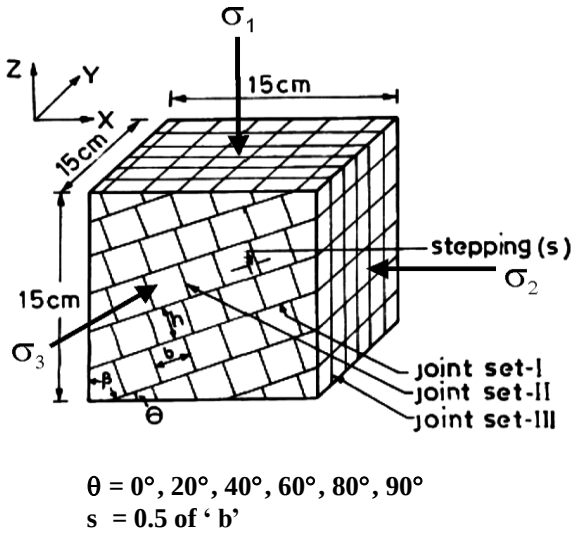

θ = 0°, 20°, 40°, 60°, 80°, 90°
s = 0.5 of ' b'

Fig. 39. Key sketch of model tested (Tiwari, 2004; Tiwari and Rao, 2006a)

The vertical and lateral deformations in σ_1, σ_2 and σ_3 directions were corrected for deformation in teflon sheet and platens. The axial stress σ_1 in z direction at any level of strain was determined by dividing corresponding axial load with corrected area of specimen. The corrected area A_f of specimen at any axial strain level ε_1 was estimated using following expression:

$$A_f = \frac{A_0(1\pm\varepsilon_v)}{(1-\varepsilon_1)} \qquad (28)$$

where, A_0 is original cross-sectional area of specimen and is equal to xyz.

7.2.2 Mechanical Behaviour

Stress and Strain Behaviour

The typical stress-strain curves are plotted from the results of rockmass testing and are shown in Fig. 40 (a) and (b). The curve shows the deviotric stress (σ_1-σ_3) plot against axial strain (ε_1), lateral strain along σ_2 (ε_2), lateral strain along σ_3 (ε_3), and volumetric strain (ε_v). Fig. 40 (a) shows strain softening behaviour for samples with θ = 0°, 20°, 80° and 90° showing steep elastic portion up to almost the peak and gradual fall in stress after failure. The steepness of curve increases in both regions with increase in σ_2/ σ_3 ratio. Fig. 40 (b) shows the ductile behaviour for Type-A (θ = 40°, 60°) showing short elastic range followed by a continuous increase in stress and decrease in tangent modulus with increasing strain up to failure. After peak, stress increase is continued showing strain hardening in most specimens whereas stress remains constant exhibiting elastic-plastic nature in few specimens depending upon joint configuration and confinement levels.

Failure Modes

The specimens also have shown different failure pattern depending upon joint configuration, stress ratio, and stress orientation. Shearing of intact material and joints was observed in case of specimens with θ = 0°, 20°, 80° and 90°. The shear

planes developed on YZ or σ_2 face dips along σ_3 directions and fracture dip increases with increasing σ_2. In rockmass specimen with $\theta = 40°$, joint dilation and shearing of some blocks occurred whereas sliding of small blocks along joint mixed with shearing was seen in $\theta = 60°$. The shifting of failure mode from sliding and dilation along joint to shearing of intact material with increasing σ_2/σ_3 ratio was also observed.

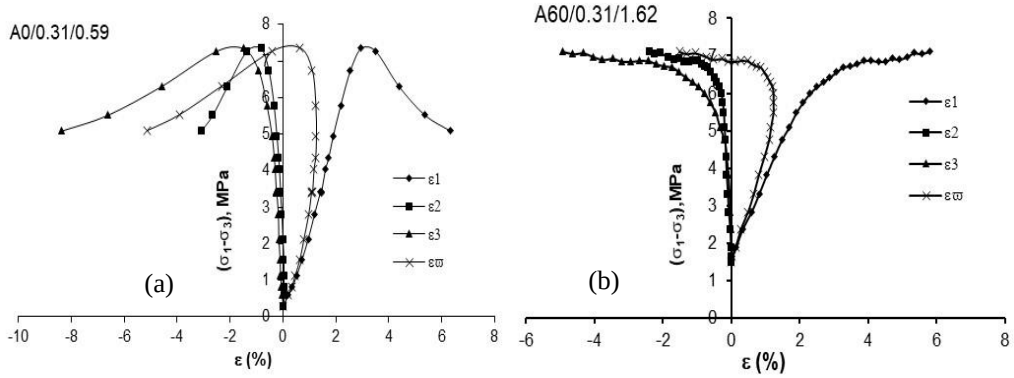

Fig. 40. Stress- strain curves for rockmass specimens showing (a) Strain softening and (b) Strain hardening behaviour (Tiwari and Rao, 2007)

Strength Enhancement

The strength and modulus enhancement are expected in polyaxial stress state. The strength enhancement may be defined as $(\sigma_{1ttr} - \sigma_{1tr}) / \sigma_{1tr}$, where σ_{1ttr} and σ_{1tr} are true-triaxial and triaxial compressive strength respectively. Similarly, modulus enhancement will be equal to as $(E_{ttr} - E_{tr}) / E_{tr}$, where E_{ttr} and E_{tr} are deformation modulus in true-triaxial and triaxial stress state respectively. Similar expression for modulus ratio can also be written by replacing E_{ttr} and E_{tr} in equation of modulus enhancement with M_{rj} (ttr) and M_{rj} (tr) respectively.

Failure Strength

The rockmass with $\theta = 90°$ exhibits highest uniaxial compressive strength (UCS) value and minimum at $\theta = 60°$. The strength at failure in triaxial compression further increases, when σ_2/σ_3 is increased keeping $\sigma_3 = 0.31$ MPa of constant value. This percentage increase over triaxial strength is termed as strength enhancement. This enhancement varying with θ° found to be highest (309.2%) at $\theta = 60°$ and minimum (26.1%) at $\theta = 90°$. Thus, rocks with high uniaxial compressive strength are subjected to low strength enhancement than weak rocks when they are subjected to increase in intermediate principal stress σ_2. Haimson and Chang (2000) have also reported maximum 20% of enhancement in strength of westerly granite due to increase in σ_2/σ_3 ratios. Singh et al. (1998) reported similar strength enhancement in rockmass at site based on their experience on tunnels and other underground structures.

Deformation Modulus

The deformation modulus also gets enhanced when subjected to true triaxial compression. In rockmass, the maximum enhancement is observed to be at $\theta = 60°$ and the minimum at $\theta = 90°$. The percentage of maximum enhancement in modulus value is always higher than the enhancement in their respective failure strengths.

Modulus Ratio

Modulus ratio combines the effect of both failure strength and deformability characteristics of rock material. Enhancement of modulus ratio is found to be varying with joint dip θ. Further, the enhancement is maximum (186.4%) at $\theta = 60°$ and minimum (4.9%) at $\theta = 90°$. If all the three engineering parameters e.g strength, deformation modulus and modulus ratio are compared, it can be seen that the σ_2 has the maximum influence on modulus enhancement and the minimum on modulus ratio.

Influence of Horizontal Stress Ratio

The failure strength increases with increasing σ_2/σ_3 ratio at each joint inclination θ of rockmass. The rate of increase is maximum for $\theta = 60°$ and strength reaches 7.53 MPa corresponding to $\sigma_2/\sigma_3 = 5.2$. In case of $\theta = 90°$, rate of increase is the lowest i.e. from 7.28 to 9.18 MPa only. In all joint inclinations, the rate of increase in strength at failure is higher initially which declines gradually with increasing σ_2/σ_3 but in no case lower than the strength corresponding to triaxial stress state.

Influence of Joint Geometry

The failure strength, deformation modulus and modulus ratio of rockmass are significantly influenced by joint configuration or inclination of critical joint set-I. The variation of engineering parameters with β (= 90°-θ) is known as anisotropy. The anisotropy ratio R_c is defined by the following equation:

$$R_c = \frac{\sigma_{1(90)}}{\sigma_{1(\min)}} \qquad (29)$$

where, $\sigma_{1(90)}$ is strength value corresponding to $\beta = 90°$. The $\sigma_{1(min)}$ is the minimum values of strength near $\beta = 30°$ to $50°$. The anisotropy ratio R_c for engineering parameters reduces with increase in σ_2/σ_3 value. Fig. 41 (a) and (b) show the variation of strength with change in joint inclination, θ at different σ_2/σ_3 ratio. Anisotropy in strength is high at lower confinement and diminishes (low anisotropy value) with increase in σ_2/σ_3 value.

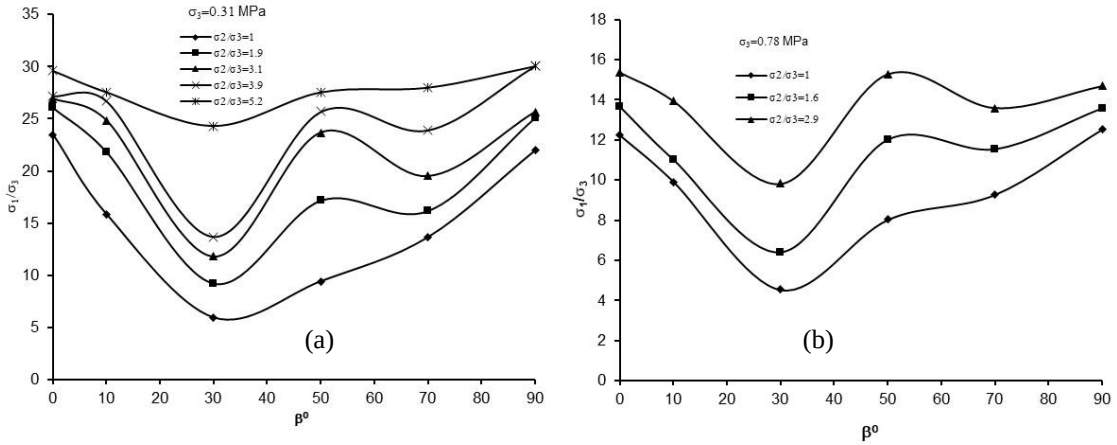

Fig. 41. Strength anisotropy in rockmass under polyaxial compression at (a) σ_3 = 0.31 MPa and (b) σ_3 = 0.78 MPa (Tiwari and Rao, 2007)

7.3 Suggested Strength Criterion

The rockmass specimens failed due to both brittle failure and plastic yielding of specimens. The results were used to develop the following true triaxial strength criterion in the pattern of generalized von Mises theory (Mogi, 1971).

$$\tau_{oct} = f(\sigma_{oct}) \quad (30)$$

where, τ_{oct} is the octahedral shear stress i.e $\left\{\frac{1}{3}[(\sigma_1 - \sigma_2)^2 + (\sigma_2 - \sigma_3)^2 + (\sigma_3 - \sigma_1)^2]\right\}^{1/2}$ at the point when σ_1 attains its peak value σ_1, peak and σ_{oct} is the mean normal stress acting on failure plane and f is monotonically increasing function. It is based on the assumption that yielding occurs in the entire body of specimen and such behaviour in most of the specimens of the study may be assumed. Further, the octahedral shear stress is a function of the full octahedral normal stress, σ_{oct}. The σ_{oct} is taken equal to $(\sigma_1+\sigma_2+\sigma_3)/3$. Based on the results of laboratory testing, τ_{oct} and σ_{oct} were calculated for each θ values. The strength criterion developed is presented in Eqn. (31)

$$\tau_{oct} = D_m \sigma_{ci} \sigma_{oct}^{e_m} \quad (31)$$

The D_m and e_m are true triaxial parameters and are function of joint geometry. D_m and e_m systematically vary with joint configuration for rockmass specimens. The σ_{ci} is the uniaxial compressive strength of intact model material. The criteria have been derived based on the assumption that joints are smooth (ϕ_j =36.8°) and the extent of interlocking level (s = 0.5) is medium.

The strength envelopes for all specimens are plotted from the results of rockmass testing under polyaxial compression. Strength parameters D_m and e_m at different inclination (θ) are estimated through these envelopes. The data of D_m and e_m were plotted against (40°-θ) or (2π/9-θ). The equation of curve between D_m and (40°-θ) is represented by Eqn. (32). Similarly curve between em and (40°-θ) is represented by Eqn. (33) using curve fitting method of least square.

$$D_m = 0.08\left[\cos\left(\frac{2\pi}{9} - \theta\right)\right]^{-0.8} \quad (32)$$

$$e_m = 0.59 \exp\left[0.40 \cos\left(\frac{2\pi}{9} - \theta\right)\right] \quad (33)$$

The parameters Dm and em can be interrelated by the following equation:

$$e_m = 0.32 {D_m}^{-0.41} \quad (34)$$

The Eqn. (31) can be applied in field with good accuracy for prediction of strength of rockmass by making input of relevant parameters. The parameters needed are uniaxial compressive strength, σ_{ci} of intact cylindrical rock core; insitu stresses (σ_1, σ_2 and σ_3 state and joint geometry (θ° and s) of rockmass obtained from field scan line survey.

7.3.1 Prediction of Model Parameters.

The proposed strength model along with Mohr-Coulomb and Drucker-Prager models is presented in terms of stress invariants in principal stress space. The strength parameters of these models are estimated for rockmass geometries used in the study. The variation of model parameters with joint inclination θ is interpreted here.

Mohr-Coulomb Model

Mohr-Coulomb yield surface in principal stress state is irregular hexagonal pyramid with its axis coinciding with hydrostatic stress axis (i.e. $\sigma_1 = \sigma_2 = \sigma_3 = 0$). The deviatoric stress section on π-plane is an irregular hexagon (Tiwari and Rao, 2006a).

The parameters c_m and ϕ_m are calculated from triaxial test on rockmass specimens. They vary systematically with inclination, θ and are the minimum corresponding to inclination ranges $\theta = 40°$ to $60°$.

Drucker-Prager Model

The Drucker-Prager model is modification over Mohr-Coulomb's model. The failure surface is a right circular cone. The cone will circumscribe the hexagonal pyramid of Mohr-Coulomb criterion. Drucker-Prager model parameters α and k are calculated (Tiwari and Rao, 2006a).

Proposed Model

The proposed model is an important modification over Drucker-Prager model. The results of true triaxial tests were plotted between octahedral normal and octahedral shear stress. The meridian section plot revealed that the failure surface is non-linear in contrast to linear surface of Ducker-Prager model. Thus, in this study a model was proposed as shown in Eqn. (35), which incorporates non-linearity parameters (also known as true triaxial strength parameters) D_m, and e_m when represented in terms of stress invariants in principal stress space.

$$F = \sqrt{\frac{2J_2}{3}} - D_m \left(\frac{I_1}{3}\right)^{e_m} \sigma_{ci} \qquad (35)$$

The strength parameters D_m and e_m for different joint inclinations θ are estimated using the strength envelopes for rockmass. In the above Eqn. (35), stress invariants J_2 and I_1 can be estimated from insitu stress values and parameters D_m and e_m from joint pattern of rockmass at site. The σ_{ci} is obtained through laboratory tests. Thus, this equation can be effectively used for estimation of rockmass strength at site under polyaxial stress compression.

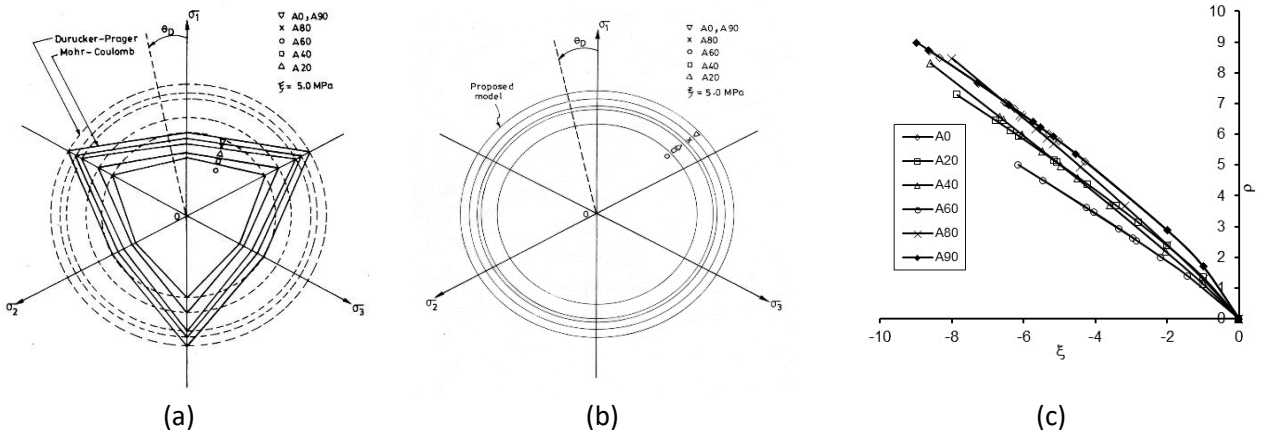

Fig. 42. (a) Deviatoric section of M-C and D-P failure envelopes (b) Deviatoric sections and (c) Meridian section of Tiwari and Rao criterion (2006a, 2007)

Strength Model Plots

The failure envelope plots of polyaxial rockmass testing results are made using all three strength models. The shape of strength envelope can be clearly visualized by plotting meridian section and deviatoric section in octahedral plane. All the three models are pressure dependent and are two parametric models (Fig. 42). For plotting the sections of failure envelopes, the two parameters needed are radius, ρ of deviatoric section and different levels of hydrostatic stress, ξ. The radius, ρ of deviatoric section increases linearly or non-linearly with increase in hydrostatic stress, ξ depending upon the specific strength model used.

Proposed Failure Surface

In this case also the section is circular so radius ρ will be same in tensile and compressive meridians and can be expressed as:

$$\rho_t = \rho_c = \sqrt{3}.D_m.\left(\frac{\xi}{\sqrt{3}}\right)^{e_m}.\sigma_{ci} \qquad (36)$$

Thus, failure surface plots can be made for all three models at each joint inclination, θ of rockmass specimens using ρ and ξ values.

Model Comparison

The radius of failure envelope is calculated using the strength models and is compared with the experimental results. The radius, ρ estimated at inclination $\theta = 0°$, $20°$, $40°$, $60°$, $80°$ and $90°$. The lode angle θ_D for experimental values is lying near

to 60° i.e. in compression meridian. It is very clear from computed ρ values that in comparison to Mohr-Coulomb and Drucker-Prager models, the proposed model back predicts the results more closer to the experimental values at all joint inclinations, θ. If one sees the deviatoric section in Fig. 42 (a), it can be observed that Mohr-Coulomb and Drucker-Prager failure surfaces are irregular hexagonal pyramid and circular cone respectively. The Tiwari and Rao (2006) model is represented by a failure surface, which is circular cone with curvilinear surface (Fig. 42 (b)). Further, it can be seen from the Fig. 42 (a) and (b) that the radius of deviatoric section is the minimum for joint inclination θ = 60° and the maximum at θ = 0°, 90° in all strength models (Tiwari and Rao, 2006b).

7.4 Post Failure Behaviour of Rockmass

Bieniawski (1967) showed that knowledge of the strength and deformation behaviour of fractured rock is particularly important in determining the stability of underground excavations. These structures most of the time are stable even though they are in fractured rock. To understand this problem one should evaluate the behavior beyond peak. Since the complete stress-strain curves are rarely available, an extensive testing on 54 simulated rockmass specimens was conducted with different joint geometries and stress states. The vertical deviatoric stress vs axial strain is plotted for the simulated rockmass specimens and are grouped separately for different joint inclinations, θ. Plot of Line-A, Line-B and Line-C with respect to σ_2/σ_3 ratio were made for all joint inclinations similar to Bieniawski et al. (1969). These lines are almost straight lines and the slopes vary with joint geometry (Fig. 43). Based on this, suitable equations are developed to predict the post peak behaviour for UCS, triaxial and true triaxial stress conditions (Tiwari and Rao, 2006b).

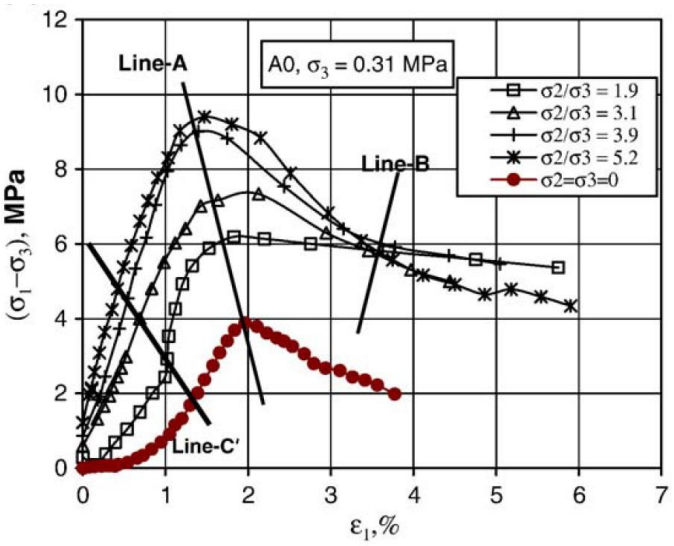

Fig. 43. Deviatoric stress-strain curves and locus of points A, B and C for A0 specimens

7.5 Failure mechanism

The deviatoric stress-strain curves showed an increase in strain softening rate with increase in σ_3 and σ_2/σ_3 ratio at all inclinations of joint set-I. It is interesting to see that this behaviour is apparently different from the mechanical behaviour of intact rocks as observed by Bieniawski et al. (1969). When the confining pressure is low, sliding predominantly on the joint surface causes the deformation of jointed rocks. As the confining pressure increases, sliding on the joint surface is more restrained and the deformation is controlled mainly by the fracture of intact rocks, which results in an increased strain-softening rate. When dip angle of joint set-I is low the restraint against sliding along joints is higher as compared to steeper dips. In general dilation of joints leading to shearing of intact blocks causes failure of specimens. Distinct shear planes are also seen in several failed specimens (Fig. 44). Hence, strain softening is greater for lower dip angles. In the case of specimens with θ = 40° and 60° the deformation is due to joint sliding up to σ_2/σ_3 = 5.2 and plastic behaviour is seen in the post peak region. At a lower σ_2/σ_3 ratio, some specimens failed due to joint dilation and block rotation resulting in bulking and plastic deformation. At higher σ_2/σ_3 ratio bulging diminishes and shear cracking dominates as shown in Fig. 44.

7.5.1 Zonation map for post peak behaviour of rockmass

Based on the above observations it is suggested that the post peak response is dependent on the joint configuration of the rockmass and the surrounding stress state in a systematic manner. The material may behave as strain softening, strain hardening and plastic in the field depending upon the joint geometry and stress state. The behaviour is summarized and represented in a tabular form indicating different zones viz. strain softening, strain hardening and elastic perfectly plastic. The proposed zonation table is shown in Table 9 and may be used for identifying possible behaviour of material in situ.

The scan line survey may provide detailed information on rockmass geometry at site and gauge instruments can be used to determine in-situ stresses. Based on joint pattern and in-situ stress state, rockmass behaviour can hence be predicted. The

zonation table is applicable for a rockmass with smooth joints and medium interlocking (s = 0.5) under low stress levels. The predicted material behaviour can be used for proper selection of stress-strain models in analytical and numerical modeling of rockmass problems dealing with excavation, long wall mining and designing of mine pillars.

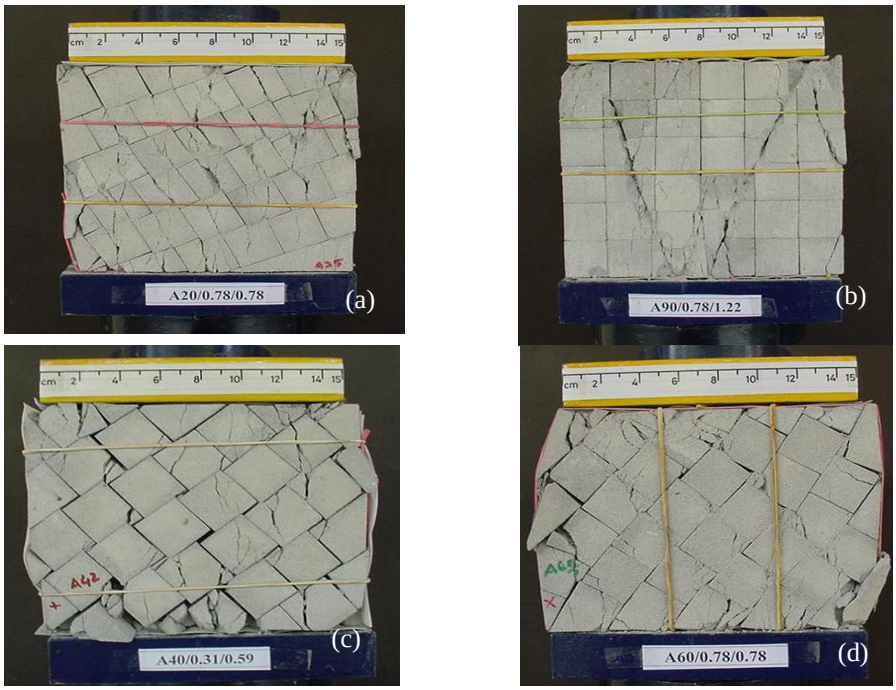

Fig. 44. Shearing of (a) intact blocks and joints (b) planes developed on the face at which is σ_2 is applied (c) intact material and joint dilation (d) Bulging and rotation of blocks (after Tiwari and Rao, 2007)

Table 9. Zonation table showing different post peak zones (s = 0.5, ϕ_f = 38.8)

$\frac{\sigma_3}{\sigma_2}$ (MPa) θ (°)	$\frac{0.31}{0.31}$	$\frac{0.31}{0.59}$	$\frac{0.31}{0.95}$	$\frac{0.31}{1.22}$	$\frac{0.31}{1.62}$	$\frac{0.31}{0.31}$	$\frac{0.78}{0.78}$	$\frac{0.78}{2.24}$
0								
20	SS							
40	SH		PL	SS		SH	PL	SS
60	PL		SH					
80	SS							
90	SS							

SS: Strain softening SH: Strain hardening PL: Elastic plastic

7.6 Conclusions

i. A high capacity (1000kN) polyaxial testing system was developed.
ii. Using the developed True-Triaxial System (TTS) tests are conducted on the jointed rockmass under uniaxial, biaxial, triaxial, and polyaxial compression.
iii. The stress strain curves exhibit strain softening, strain hardening behaviour depending upon joint geometry and σ_2/σ_3 ratios.
iv. The different failure modes viz. splitting, shearing, sliding and rotation failure modes are observed.
v. The influence of intermediate principal stress is established on strength, modulus behaviour of rockmass. The σ_2 enhance the strength, modulus and modulus ratio values.
vi. The strength values show anisotropy with joint inclination, θ (= 90°-β) with minimum value at 60°. This anisotropy reduces with increase in σ_2/σ_3 ratios.
vii. A new polyaxial strength criterion is developed which incorporates UCS of intact rock, Joint inclination θ and surrounding stresses σ_1, σ_2 , and σ_3.

8 Brittle Failure and Interlocking in Crystalline Rocks

Brittle failure is a familiar phenomenon in rock mechanics, which occurs at zero or low confining pressures. Despite the remarkable development of rock mechanics in the recent past, sufficient insight into the real mechanism of this failure type

has not been achieved. Even in a homogeneous, isotropic solid, treating the problem is very hard; cracks form at the atomic scale, extend to the macroscopic level, are irreversible and travel far from equilibrium. Experimental studies of intact rock behaviour under compressive stresses started with early fundamental researches using direct examination of the failure process under stiff testing machines such as Cook (1965) and Bieniawski (1967). Subsequent researchers focused on crack growth and interactions. Observations of the crack initiation, propagation and coalescence in the rock specimens, loaded to different points along their stress-strain curve under high-resolution optical or SEM or indirectly through the acoustic emission method (Noferesti, 2007).

To achieve a closer view of the actual brittle failure phenomenon, an elaborate testing program has been executed to simulate the heterogeneous and interlocked nature of rock. Using dental plaster mixed with different distilled water ratios, it was tried to create the sharp differences between the mechanical properties of the small brick-like elements. These elements were then put together to make the large blocky specimens that were nearly heterogeneous and interlocked as observed in crystalline rocks. A detailed coverage of unique micro to macro physical modelling and results of the new observations on brittle failure and interlocking coefficient, K studies are presented in this sections.

8.1 Characteristics of the Crystalline Rocks

Crystalline rocks include mostly igneous and metamorphic rock types that expose a structure of interlocked crystals (Fig. 45). Microscopic observations have proved that no chemical bond exists among the crystals and that the overall strength of these rocks is only due to their very intricate and three-dimensional interlocking. Regarding igneous rocks, many mechanisms are suggested by geologists responsible for the mineral crystallization from original magma. However, the most recognized mechanisms are crystal settling (Bowen, 1915) and magma convection (Martin et al., 1987). But as discussed by Philpotts (1990), a combination of these mechanisms is more likely to cause igneous crystallization.

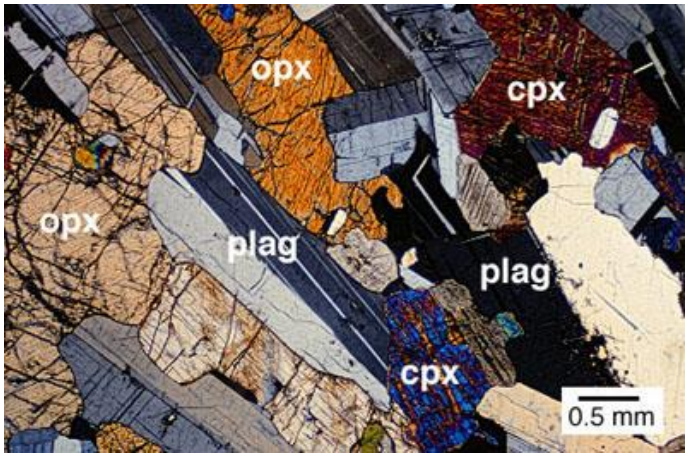

Fig. 45. Interlocking textures of an igneous rock (Granite)

Metamorphic rocks, on the other hand, usually display a banded or foliated texture with platy or elongated crystals as a result of extreme pressure and temperature applied to them. However, metamorphic rocks such as quartzite and marble have granular texture. In addition, some of the sedimentary rocks derived from chemical precipitation (e.g. limestone, rock salt, and dolomite) may be considered as crystalline materials. These rocks are generally single-mineral with a compacted texture.

In view of the fact that most of the crystalline rocks are igneous, the focus is more to find compatible model materials for physical modelling of crystalline rocks.

8.2 Selection and Characterisation of the Model Material

Instead of directly working with crystalline rocks, use of suitable alternative that exposes strongly similar behaviour in the area of concern is tried. To select a proper model material many factors are considered, i.e. behaving in a brittle fashion against applied stresses, easy adjustment of the mechanical properties of the model material so as to adjust for different rock forming minerals, and the ease of preparation and curing in the laboratory. Regarding the mechanical properties, uniaxial compressive strength, σ_c, and the elastic modulus, E, are taken into account because the first summarises the strength properties and the latter deformational behaviour of the minerals. The ratio between σ_c and E of the minerals is considered as the simulation parameter in the study Rao and Noferesti (2009).

According to Barth (1952) in almost all igneous rocks, five major minerals i.e. quartz, feldspar, mica, pyroxene and olivine are always present; the percentage of the other minerals is negligible.

8.3 Dental Plaster as a Model Material

To find out a suitable set of compositions for simulating the major minerals of igneous rocks, a variety of materials and additives were considered. After several trials, three varieties of dental plaster, commercially named as Kaldent, Kalstone and Ultrarock were selected as the base powders to make four different model materials.

8.4 Physical and Mechanical Properties

Specific gravity (SG), dry density (γd) and porosity (n) as physical properties and uniaxial compressive strength (σ_c), Brazilian strength (σ_t), cohesion (c), angle of internal friction (ϕ), and Poisson's ratio (υ) as mechanical properties are determined for all model materials according to the procedures given by ISRM (1978, 1979).

8.5 Experimental Set-up

Using four systematic interlocking patterns, i.e. patterns A, B, C and D, real interlocking textures of crystalline rocks at micro-level were simulated as shown in Fig. 46. Enlargement of the microscopic texture to a macroscopic systematic pattern is an unconventional way of modelling adopted here, making the model similar to a masonry wall. Using this macro-model, direct observation over sequence of events that occur during a failure process is possible. Every step in the failure process is closely monitored and recorded.

For all systematic patterns, the overall size of the specimen was 180 x 180 x 76 mm. It was made of two layers, each having 38 mm thickness. Each layer was made of dissimilar element sizes interlocked together. In total, 18 different element sizes were used. To give a heterogeneous nature to the specimens, different element materials were used.

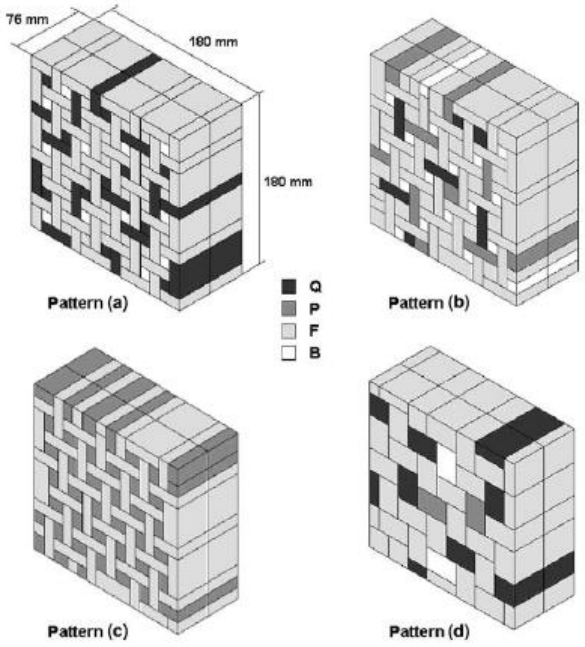

Fig. 46. Perspectives of four systematic patterns used to simulate the natural textures. Black Q, dark grey P, light grey F, white B (Noferesti and Rao, 2010)

The building elements of the specimens were prepared by mixing the dental plaster with different distilled water ratios and then pouring the paste into split moulds. After curing, the individual elements were assembled, according to the necessary pattern, into large specimens. The specimens were tested in biaxial loading conditions. To perform biaxial testing the 1,000kN True Triaxial System (TTS) developed at IIT Delhi by Rao and Tiwari (2004) was used. Very low strain rates were selected to provide sufficient time to observe and record cracking processes in the sample faces and to take proper photographs. Each test took around 30-45 min to complete the failure process.

Altogether 66 specimens were tested at four lateral pressures i.e. 0.08, 0.15, 0.88, 3.10 MPa, four interlocking patterns and with different configurations of the element types. After completion of each test, the specimen was carefully removed from the loading section and induced cracks on all six faces of the specimens were mapped.

8.6 New Observations on the Brittle Failure Mechanism

A detailed description of the experimental programme and results are given by Noferesti and Rao (2010). Here a brief summary of major observations and conclusions is presented.

a) Crack initiation observed starting about 20% of failure load. They formed due to local bending forces applied on crystal-like elements extended perpendicular to the maxi-mum principal stress (Fig. 47 (a)). After initiation, cracks grow as the load increases but the growth is conversely stable. Most of cracks were observed to stop at element boundaries and few cracks that cross the boundaries stopped after two or three elements.

b) As a new observation, there exists the phenomenon of systematic crack propagation rather than random crack growth or propagation, i.e. after limited growth of one crack, new cracks kick off parallel and close to the first crack (Fig. 47 (b)). The small gap between parallel cracks decreases as load increases.

c) The micro-buckling of small columns of material left among closely located tensile cracks, as depicted in Fig. 47 (c), is the major observation in the study. This phenomenon is responsible for the key task of connecting stable tensile micro-cracking to the unstable macroscopic shear fracturing. Just upon occurrence of micro-buckling about 90-95% of peak load, a shear force builds up in the rock and drives the adjacent columns to cut off. By col-lapsing each column the shear force backed by the applied axial load increases and shear movements accelerate. Consequently, in a very short time, the instability appears in the form of a macroscopic failure plane.

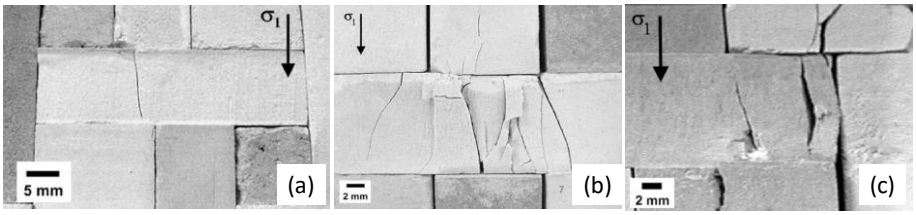

Fig. 47. (a) First tensile cracks observed in an element extended perpendicular to σ_1 direction (b) Intense parallel cracking in an element extended perpendicular to σ_1 direction (c) Micro-buckling of a very thin column formed amid a tensile crack and an element boundary

In summary, the brittle failure is primarily a continuous process of tensile micro-cracking inside the rock. These cracks are formed essentially due to bending forces applied to the favourably oriented crystals, perpendicular to the maximum principal stress. At a critical density of parallel tensile cracks, the very slender columns collapse due to buckling (Noferesti 2007). This begins a series of unstable shear activities that leads to the final collapse of rock.

8.7 Developing a Simple Form of the New Criterion

An envelope criterion has been formulated based on Timoshenko beam theory that allows for analysing short beam behaviour as relevant to the study. However, the error caused by use of simple Euler-Bernoulli beam theory might be negligible for practical purposes. Applying the Euler-Bernoulli beam theory, a more simplified criterion is proposed as presented below:

$$\sigma_x = \frac{M_c}{I} = \frac{3Pl}{16} * \frac{\frac{h}{2}}{\frac{bh^3}{12}} = \frac{9Pl}{8bh^2} \quad (37)$$

$$\frac{9PL}{8bh^2} = \sigma_t \quad (38)$$

$$P = \frac{8bh^2\sigma_t}{9l}$$

$$\sigma_b = \frac{P}{A}$$

$$\frac{K\pi^2 El^2}{12h^2} = \frac{8bh^2\sigma_t}{bl(9l)} \quad (39)$$

$$l^4 = \frac{96\sigma_t h^4}{9K\pi^2 E}$$

$$l_{cr} = 2h\left(\sqrt[4]{\frac{2\sigma_t}{3K\pi^2 E}}\right)$$

$$\sigma_{cr} = \left(\frac{K\pi^2 El_{cr}^2}{12h^2}\right) = \left(\frac{K\pi^2 E}{12h^2}\right) * 4h^2\left(\sqrt{\frac{2\sigma_t}{3K\pi^2 E}}\right) \quad (40)$$

$$\sigma_{cr} = \sqrt{\left(\frac{2}{27}\right) * K\pi^2 E\sigma_t}$$

K is a constant that represents the degree of crystal interlocking. Using of E_m and σ_{tm} symbols to refer to microstructural properties and by defining a new interlocking factor, i.e. Km = (2*π^2/27)* K, Eqn. 40 can be more simplified as follows:

$$\sigma_c = \sqrt{K_m E_m \sigma_{tm}} \quad (41)$$

Where, σ_c is the uniaxial compressive strength of rock, Km is the degree of crystal interlocking, Em is the average Young modulus of crystals, and σ_{tm} is the average tensile strength of crystals.

For any rock specimen, the interlocking factor is easily calculated as follows:

$$K_m = (\sigma_c^2/E_m\sigma_{tm}) \quad (42)$$

Using Eqn. 42, Km values are smaller than K values discussed in the previous section. For the same example discussed in Sect. 4 having E_m = 100GPa, σ_{tm} = 100 MPa and σ_c = 182.2MPa, the K factor obtained 0.01 while Km factor according to Eqn. 42 is obtained 0.003 (Noferesti and Rao, 2011).

8.8 Results

Based on the new experimental observations, occurrence of micro-bending and micro-buckling phenomena during brittle failure inside the solid, intact rock is proved. Considering geometry of the problem, the classical beam and buckling theories

were applied and a new failure criterion was derived for compressive strength of crystalline rocks. Macroscopic compressive strength, as suggested by the new criterion, is dependent on three basic microstructural properties, i.e. E_m and σ_{tm} and a new K factor that is related to the support conditions of an arbitrary crystal inside the rock. K factor is therefore interpreted in the brittle failure context as the interlocking factor.

Having E_m, σ_{tm} and σ_c values for different rocks, and using the new strength criterion, the degree of crystal interlocking, K, for each rock type is calculated. The estimated values are given in Table 10. Fig. 48 shows the variation of compressive strength for different rocks and estimated k values for different rocks. K factors for different rocks are compared together and some interesting conclusions are made as follows:

a) The K increases for plutonic rocks in contrast to volcanic rocks,
b) The interlocking factor for carbonates is generally higher than silicate rocks with the marble having highest K factor amongst carbonates.
c) The rock salt possesses a very large interlocking factor comparing with other crystalline rocks.
d) While interlocking factor increases for a rock the ratios of its macro-to micromechanical properties increases as well.

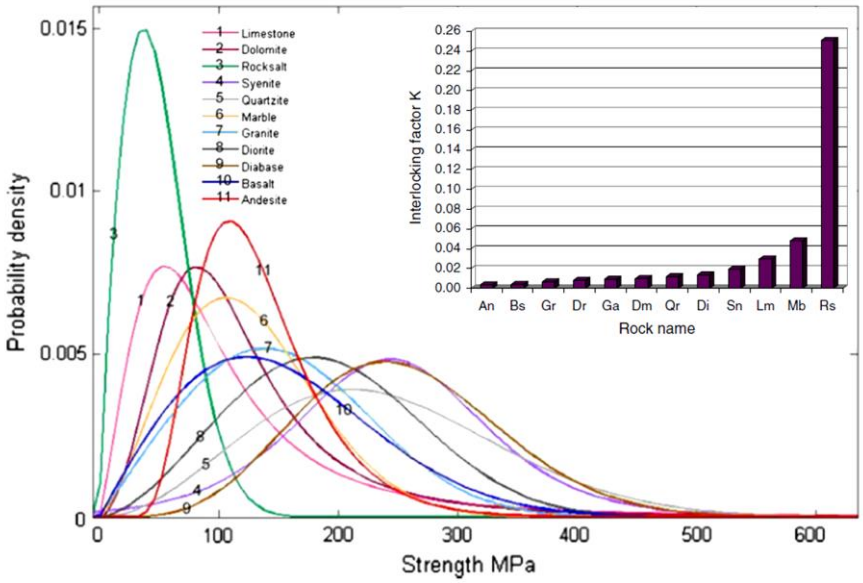

Fig. 48. Variations of uniaxial compressive strength for different crystalline rocks and Variation of interlocking factor K amongst crystalline rocks; An andesite, Bs basalt, Gr granite, Dr diorite, Ga gabbro, Dm dolomite, Qr quartzite, Di diabase, Sn syenite, Lm limestone, Mb marble, Rs rock salt (Noferesti, 2007)

Higher interlocking of carbonate rocks than the silicates explains their comparable strength even though they are made of weak calcite mineral. For any crystalline rock E_m and σ_{tm} values are intrinsic properties that do not change much unless the compositional changes occur in rock, i.e. due to severe changes in environmental factors such as weathering, metamorphism, etc. But the interlocking factor, K, will change easily due to moderate variations of some environmental parameters like confining pressure. It is interesting to see that the interlocking effect on σ_c is quite similar to the effect of conventional confining pressure on rock strength. This implies that the actual role of confining pressure is reinforcing the rock microstructure and thereby strengthening the rock

Table 10. Ratios of macro to micromechanical properties against interlocking factor for some crystalline rocks

Rock	E/E_m	σ_t/σ_{tm}	K
Granite	0.51	0.10	0.0067
Syenite	0.61	0.15	0.0193
Diorite	0.57	0.33	0.0081
Gabbro	0.87	0.13	0.0092
Diabase	0.69	0.34	0.0136
Andesite	0.32	0.07	0.0036
Basalt	0.36	0.11	0.0041
Quartzite	0.61	0.15	0.0119
Rock Salt	0.66	0.60	0.2510
Dolomite	0.50	0.11	0.0099
Limestone	0.50	0.67	0.0297
Marble	0.67	0.56	0.0481

9 Closed-form Solution for Circular Opening

Wellbore and tunnel problems are of true triaxial stress state, even if the ground is under axisymmetric loading condition. We worked on the analytical approach to develop the closed-form solution considering elastoplastic (Singh et al., 2019a, b) and visco-elastoplastic (Singh et al., 2018a) models for circular opening under plane strain using the 3D criterion. In elasto-plasticity both elastic perfectly plastic and elastic brittle plastic behaviours are considered. The study was based on the out-come of the investigation that the intact rock and rockmass show higher strength in the influence of the intermediate principal stress as discussed in the previous section.

9.1 Assumptions, advantages and disadvantages

The study is focused on the criterion, which uses triaxial tests data for predicting the strength in true-triaxial stress state. The detail comparison of the various criterion showed that the Mogi-Coulomb criterion (Al-Ajmi and Zimmerman, 2005) perfor-mance on an average was satisfactory. The criterion was simple and uses the explicit function. These two important qualities made us use Mogi-Coulomb criterion for the analytical solution. The solution developed was derived considering the two assumptions: first plain strain condition, second plastic strain magnitude is also assumed to be equal to zero in out-of plane direction. The former assumption helped in the converting the 3D problem into 2D, later helped in making the function relationship between the intermediate principal stress with the minor and major principal stresses. The limitation of this solution was it provided solution for break out shear problem (out-of the plane stress is intermediate principal stress). The solution uses non-associative flow rule for plastic strain calculations. The advantage of this solution was the pure analytical nature of the solution, which makes it highly computationally efficient; this makes it extremely useful when large set of computations are to be run. Such analytical solutions play a very important role in the reliability-based studies when numerous sets of runs are required to obtain reliable statistical results (Singh et al., 2017).

9.2 Validations

To obtain the analytical solution for Mogi-Coulomb (Al-Ajmi and Zimmerman, 2005), a completely new mathematical al-gorithm was developed, the algorithm is robust and can be adopted for any mathematically explicit criterion. To validate the solution, two types of checks were employed in the study: first one is from the experimental data and the second one was using FE-analysis. The results for the experimental validation are taken from the thick cylinder tests performed by Papanasta-siou and Durban (1996). It does not represent the actual problem (circular hole in infinite media) but it is considered very close experimental simulation. Papanastasiou and Durban (1996) performed the experiments on the Castlegate sandstone. The outcome of the comparison between experimental results and closed-form solution is shown in Fig. 49. Results show the very high degree of agreement with the experimental results.

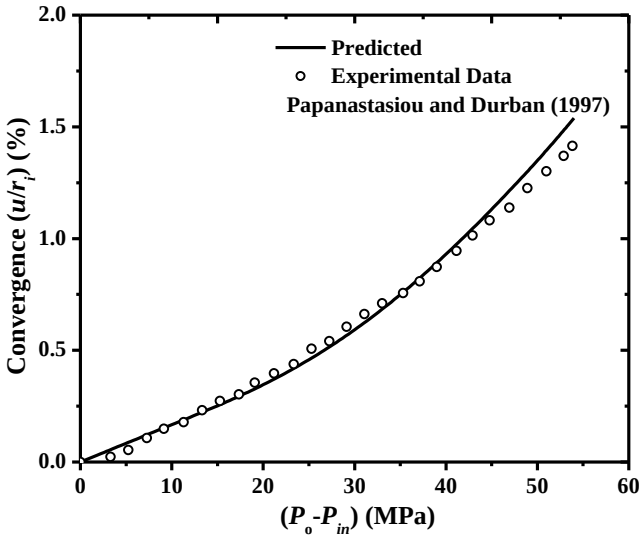

Fig. 49. Comparison of experimentally determined convergence of thick cylinder with the proposed solution (Singh, 2019a)

In the second case, since the mathematical algorithm used to derive the solution could be used for any explicit function, the solution methodology was used on the Drucker-Prager criterion (1952). The advantage of Drucker-Prager criterion is that the numerical solution could be found in any commercially available FE package, hence results of comparison could be used for the validation of solution procedure.

Refer to the Singh et al. (2019b) for more details. The comparison of results are shown in Fig. 50 and Fig. 51 for both elastic-perfectly plastic and elastic-brittle-plastic model with FE results generated from *phase*^{2} (rocscience software). These figures show that the results are very close match with the FE results even though we employed a gross approximation that out of plane plastic strain is assumed to be zero in the analytical solution.

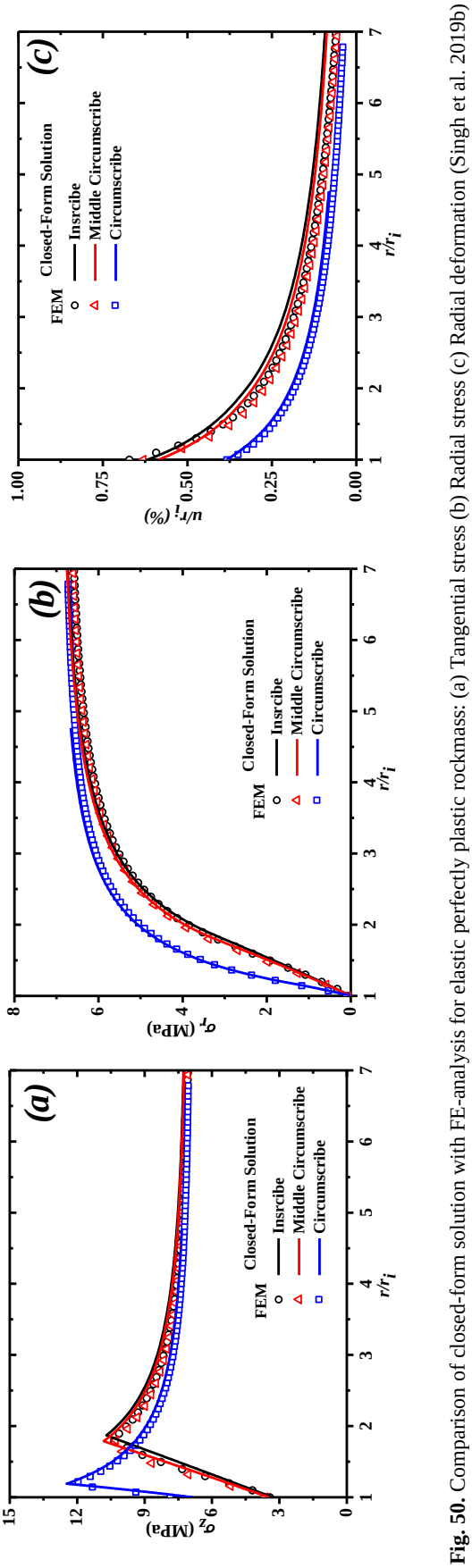

Fig. 50. Comparison of closed-form solution with FE-analysis for elastic perfectly plastic rockmass: (a) Tangential stress (b) Radial stress (c) Radial deformation (Singh et al. 2019b)

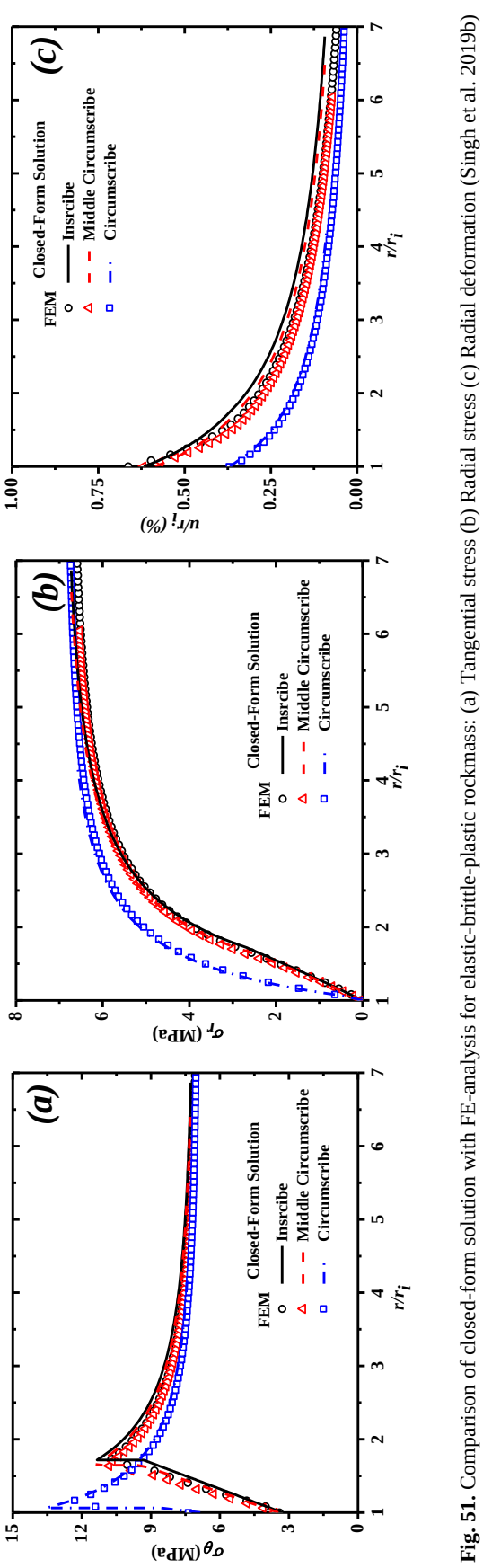

Fig. 51. Comparison of closed-form solution with FE-analysis for elastic-brittle-plastic rockmass: (a) Tangential stress (b) Radial stress (c) Radial deformation (Singh et al. 2019b)

9.3 Observations

Most interesting outcome of the work was the result of comparison of Mogi-Coulomb model with Mohr-Coulomb model. The results of comparison are shown in Fig. 52 and Fig. 53. For more detail please refer to Singh et al. (2019a). Fig. 52 shows the comparison for elastic-perfectly plastic model and Fig. 53 shows the comparison for elastic-brittle-plastic model.

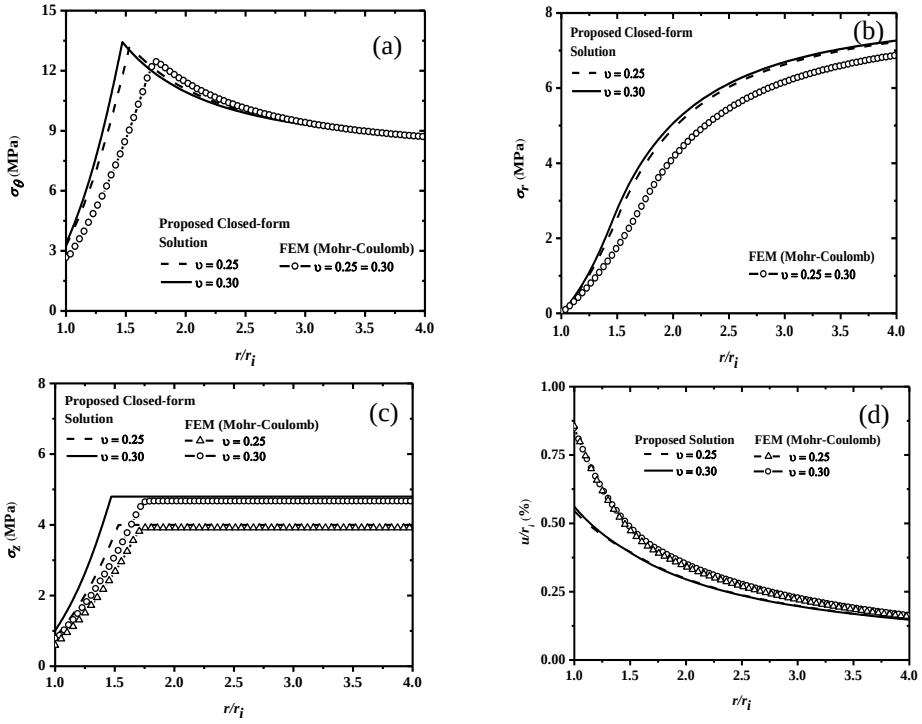

Fig. 52. Comparison of closed-form solution with FE based (Mohr-Coulomb solution) for elastic perfectly plastic rockmass:(a) Tangential stress along radial distance (b) Radial stress along radial distance (c) Out-of plane stress along radial distance (d) Radial deformation along radial distance (Singh et al, 2019a)

It was observed from the figures that the Mogi-Coulomb solution was sensitive to the Poisson's ratio were as Mohr-Coulomb results are not. The radius of plastic zone was observed to shrink for the case of the Mogi-Coulomb model about 14-19% of Mohr-Coulomb results. These outcomes reflect that the parameter Poisson's ratio which is often consider as insensitive for plasticity shows its influence when the 3D criterion is consider in analysis. Similar observation was also derived by the Zhou et al. (2010).

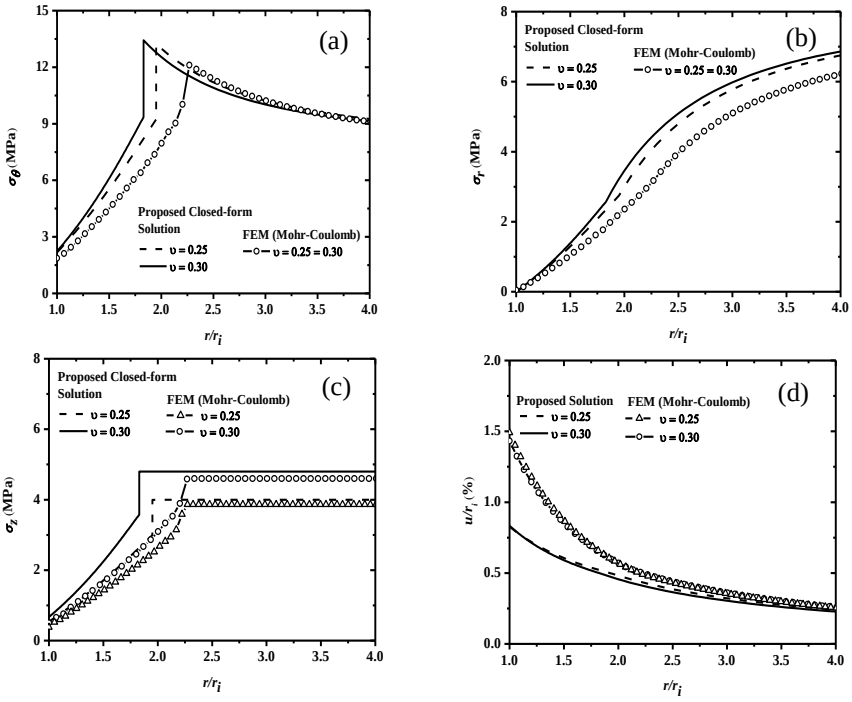

Fig. 53. Comparison of closed-form solution with FE based (Mohr-Coulomb solution) for elastic-brittle-plastic rockmass:(c) Out-of plane stress along radial distance (d) Radial deformation along radial distance (Singh et al, 2019a)

9.4 Introduction of creep for rock salts

To extend the solution for the material like rock salts the solution was extended with the help of Maxwell rheological model. The elaborate details of the solution developed, can be found in Singh et al. (2018a). The parameters calculated from the

laboratory experiments for Khewra rock salt and the viscosity estimated by the Singh et al. (2018b) are used as an input for the solution. The results for the borehole deformation with the time lapse were calculated from the solution as shown in Fig. 54. The figure shows that the solution successfully handles the time dependent deformation problem.

The advantage of the solution is that, it is very simple to use and take in account the intermediate principal stress effect. The simplistic nature of the solution is because of its simplistic assumptions, they are: the material is considered to follow the simple rheological model and it is assumed that the Poisson's ratio is close to 0.5 for material like rock salts. Various experimental and theoretical reasonings are provided for these assumptions (Singh et al., 2018a).

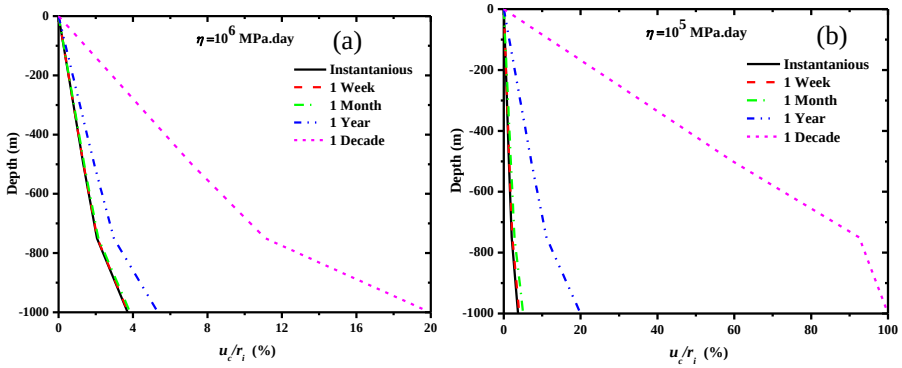

Fig. 54. Deformation of wellbore for the viscosity (a) 10^6 MPa. day (b) 10^5 MPa. day (Singh et al. 2018a)

Thus, a new closed form analytical solution is provided for circular openings in isotropic, homogeneous elastoplastic rockmass exhibiting elastic-perfectly plastic and elastic-brittle-plastic behaviour using Drucker-Prager failure criterion under axisymmetric loading.

Singh (2018b) successfully showed the application of the 3D strength criterion in various engineering problems using analytical techniques. This work is just a tip of the iceberg and one can extend this work by considering more complicated plasticity models or extending it to FE based numerical solution such as recent attempts made by the Feng et al. (2019) in this area.

10 Shear Behaviour of Rock Joints

In general, strength and deformability properties of discontinuities are quite different from those of intact rock, and in many cases, the discontinuities completely dominate the performance of the in situ rockmass. The presence of joints, fractures and other planes of weakness reduce the shear strength. Correct evaluation of shear strength of the rock joints play an important role in the design of underground openings, slopes, foundations, rock socketed piles and risk assessment of underground waste disposal.

Rock joints are normally filled up with varying thickness of the fine sediments resulting from weathering of the joint walls (gouge) mixed with transported sediments. Most of the infill materials transported by the water are either cohesive i.e. clay, silty clay or frictional i.e. silty, silty sand. This infill forms the weakest planes, from where sliding or shearing of the rock joints initiate and reduce the overall shear strength of the joint.

In the past numerous studies were carried out to investigate the shear behaviour of unfilled and in filled rock joints under constant normal load (CNL). The shearing under CNL conditions are suitable for situations where the surrounding rocks freely allow the joints to shear without restricting the dilation, thereby keeping normal stress constant during shearing. Planar joints and non-reinforced rock slopes, as shown in Fig. 55 (a) can be considered under CNL. However, shearing of non-planar joints result in dilation as one asperity overrides another, and if the surrounding rockmass is unable to deform sufficiently, an inevitable increase in the normal stress occurs. The increase in normal stress on the shearing plane depends upon the stiffness of the surrounding rockmass and dilation resisted at any time; hence shearing of rough joints takes place under variable normal load but constant normal stiffness (CNS) boundary conditions, as depicted in Fig. 55 (b).

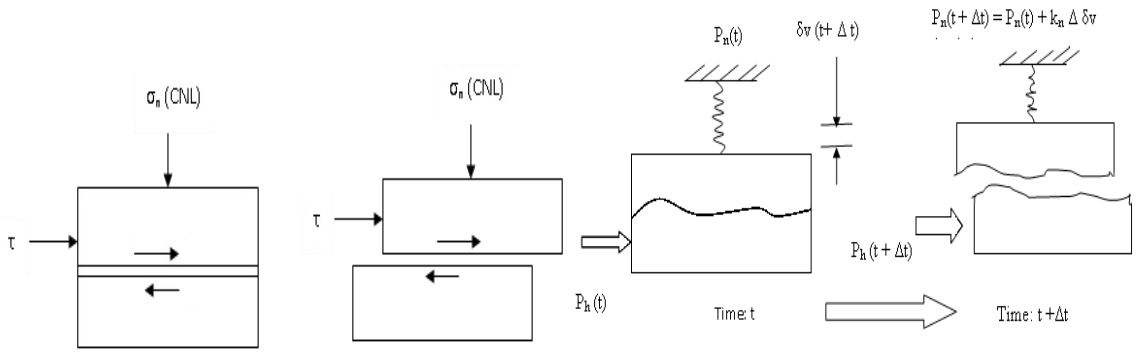

Fig. 55. Behaviour of planar and non planar rock joints

10.1 Earlier Attempts in CNL and CNS Conditions

Most of the conventional equipment used in the past by different researchers like Patton (1966), Goodman (1974), Ladanyi and Archambault (1970), Barton (1971 and 1973), Barton and Choubey (1977), Bandis et al. (1981) and Hoek (1983) to predict the shear behavior of rock joints fail to correctly determine the shear behavior because of the limitation of boundary conditions. Conventional equipment work under CNL condition.

To overcome this limitation, conventional equipment were modified (Obert et al. 1976, Ooi and Carter,1987) or new equipment developed (Indraratna et al.1998, Jiang et al.2004 and Kim et al. 2006) to conduct tests under CNS boundary conditions. The equipment developed by Indraratna et al. (1998) have difficulties to change stiffness plate to simulate different stiffness conditions of the surrounding rockmass. Though this difficulty was overcome by using servo-controlled equipment by Jiang et al. (2004), but still this is suitable for the comparatively smaller size of sample testing. The equipment developed by Kim et al. (2006) can test the samples only under two extreme conditions of the stiffness of the boundary i.e. CNL (normal stiffness, $k_n = 0$) and infinite normal stiffness condition ($k_n = \infty$).

Hence, it is important to use the equipment for the study where boundary conditions can be changed easily and without disturbing the sample. Hence, a servo control large-scale direct shear testing machine designed and developed which is capable of conducting tests on large, jointed prismatic specimens through friction free rigid platens under CNL and CNS boundary conditions.

10.2 Design and Development of Direct Shear Facility

The servo controlled large-scale direct shear apparatus designed and developed by Shrivastava and Rao (2013) as shown in Fig. 56, is used for testing rock joint under CNL and CNS boundary conditions. The apparatus can perform the test on a sample of size up to 300mm, the normal and shear loads are applied through the actuator having the capacity of 500kN and 1000kN respectively. Six LVDTs are used to measure displacements.

Fig. 56. Photograph of direct shear testing machine

The CNL and CNS conditions are achieved by an electro-hydraulic servo-valve, which controls the application of hydraulic power to linear actuator to provide the programmed force to test specimens. The programmed force is calculated from Eqn.43 and the equation is made part of the direct shear software. The programmed force keeps changing depending upon the stiffness of the surrounding rock joint entered as input data in the direct shear software and the dilation and horizontal displacement data collected through sixteen channel data acquisition system (Rao et al., 2009; Shrivastava and Rao, 2013; Bhardwaj, 2019).

The change in load during the progress of testing is calculated by the following equation:

$$P_{n_{(t+\Delta t)}} = P_{n(t)} + k_n(Y - Y') \qquad (43)$$

where, $P_{n\,(t+\Delta t)}$ = normal load at any time interval $t+\Delta t$
$P_{n(t)}$ = normal load at any time interval t
k_n = stiffness of the surrounding rockmass

Y-Y' = dilation resisted by the surrounding rockmass

The typical calculation for (Y-Y') for a given asperity angle (i) can be explained with the help of Fig. 57 and process of change in applied force is presented in Fig. 58, Y is the free dilation of the joint at any shear displacement, which can be calculated from Y = X tan(i), if the JRC values are known for the joint than, i can be calculated by the method suggested by Xie and Pariseau (1992) and Maksimovic (1996), X = horizontal displacement measured as the average of two horizontal LVDTs readings placed near the sample, Y'= dilation measured as the average of readings of four normal LVDTs placed on the top of the sample.

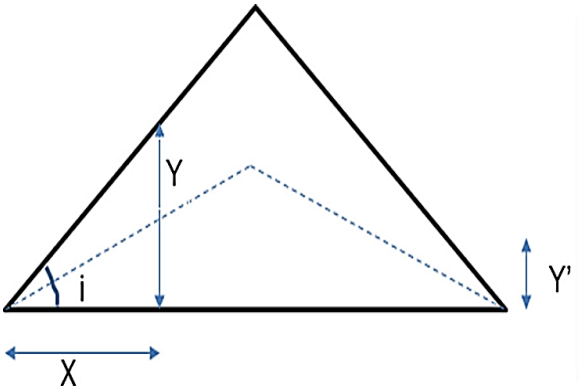

Fig. 57. Asperity angle

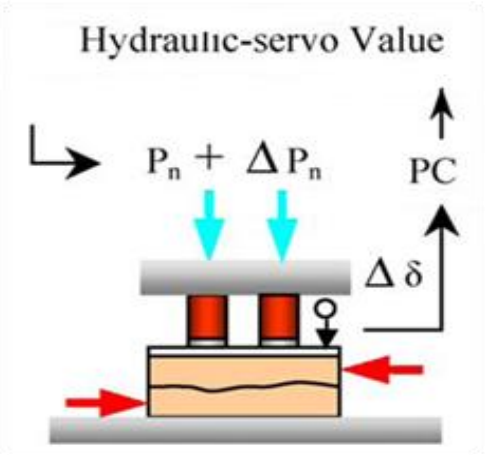

Fig. 58. Mechanism of application of changed force

10.3 Physical Modelling

Plaster of Paris (PoP) is selected as the model material for conducting a series of physical and mechanical tests. The water PoP ratio is finally selected as 0.60. The infill material is selected to simulate the field conditions (Shrivastav, 2012). The asperity plates of different angles like 0˚-0˚,15˚-15˚ and 30˚-30˚ etc., have been designed and fabricated to produce desired asperity in the sample (Rao et al., 2009) as shown in Fig. 59.

A series of tests were performed on the physically modeled rock joints with asperity angles 30°-30°, 15°-15° and varying the thickness of infilled from 0 to 10mm making thickness (t) to asperity (a) ratio 0 to 2 (Fig. 60). In the study 0.50 mm/ min rate of shearing is adopted. The normal stiffness of the joint under CNS condition is selected as 8kN/mm. The tests were performed at different initial normal stress (P_i) ranging from 0.05 to 2.04 MPa, by keeping normal stiffness of the joint at 0 for CNL and 8kN/mm for CNS condition.

10.3.1 Unfilled and Infilled Joint Behaviour

Shear stress vs displacement characteristics of infill joints under CNL and CNS conditions are presented by Shrivastava and Rao (2018) for infill material thickness 0, 5, 7 and 10mm respectively, making t/a ratio of 0, 1, 1.4 and 2. The results indicate that the shear strength reduces due to the presence of the infilled material. The change in dilation with shear displacement for infill thickness 0, 5, 7 and 10mm for different P_i under CNL and CNS conditions also discussed. The test result indicates that infill material causes positive dilation i.e. compression for all range of P_i except at very low P_i under small horizontal displacement, and it increases with increase in infill material thickness. The increase in infill thickness causes a reduction in participation of the asperity and shearing takes place predominantly through infill material which is more compressible. Hence, mostly positive dilation i.e. compression of the sample takes place instead of dilation (negative) with shear displacement. It is also observed that the dilation is more for CNL than CNS boundary conditions.

The reduction in shear strength is higher for CNL conditions compared to CNS. During the shearing process, the normal stress on the shearing plane increases with shear displacement under CNS condition, whereas it is constant for CNL condition for a given Pi. This increase in normal stress causes, increase in the compression of the infilled joint for CNS condition as compared to CNL at a given Pi. As the shear strength of the infilled material is less than that of joints, increase in the participation of joints will result into increase of shear strength of the infilled joint. However, for CNL condition the participation of joint is less than that of CNS condition, hence reduction of shear strength will be higher for CNL condition than CNS condition as shown in Fig. 61. A close visual examination of the surface of the sheared joints also revealed that the asperities were subject to moderate to low-grade damage for an infill t/a =1.4 i.e. thickness up to 7 mm, whereas no sign of asperity damage was observed for t/a=2.0. The CNL conditions reflect only shearing of the infill material whereas for CNS conditions, for the same P_i = 0.10 MPa and t/a=1 the participations of the peak of joint surface can be seen easily.

Similar to the unfilled joint for infilled joint also peak shear stress under CNS boundary condition occurs at greater shear displacement than CNL boundary condition (Shrivastava and Rao, 2010; 2011; 2015). It is observed that there is no change in the normal stress with shear displacement for CNL condition whereas normal stress changes with shear displacement for CNS condition.

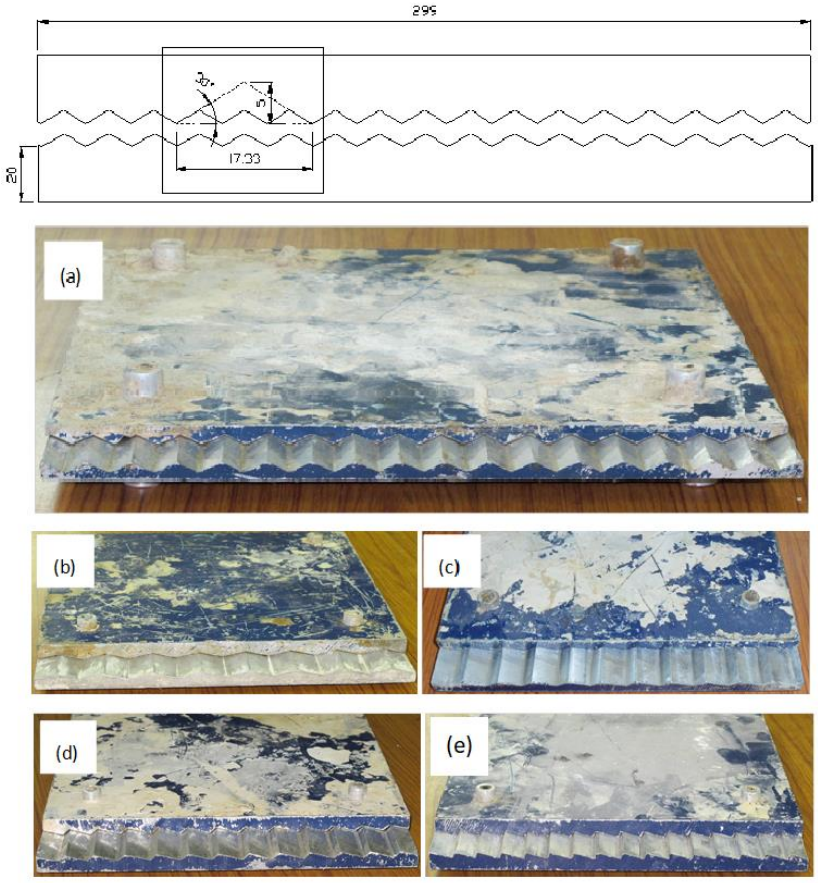

Fig. 59. Asperity plates (a) 30^0-30^0, (b) 15^0-15^0, (c) 15^0-30^0, (d) 15^0-60^0, (e) 15^0-90^0.

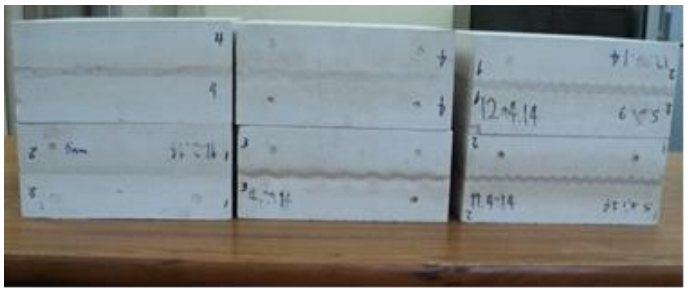

Fig. 60. Samples of unfilled and infilled with asperity angles 0˚-0˚,15˚-15˚, 30˚-30˚

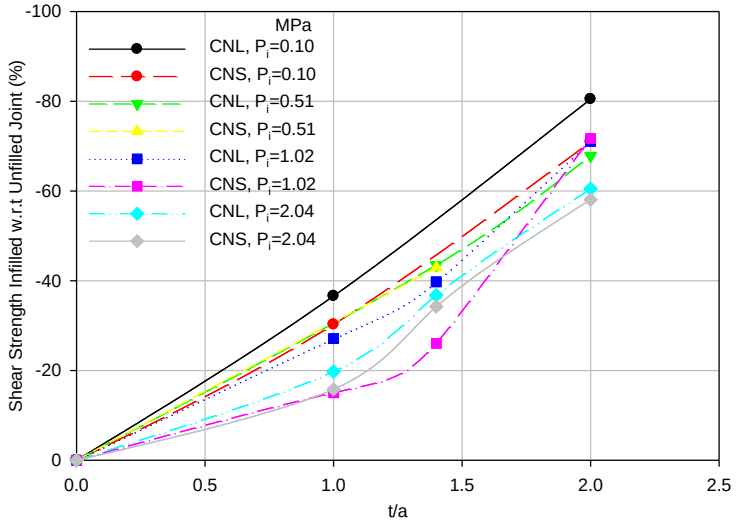

Fig. 61. Reduction in shear strength of infilled joint w.r.t. unfilled joint for 30°-30° joint

10.4 New Shear Strength Criteria

10.4.1 Unfilled Joints

Based on experimental observations and results, a new shear strength model is developed. Bilinear shear strength model proposed by Patton (1966) is used as a basic equation, for the development of the model. As discussed above the Patton's equation has two limitations:

i) Unable to use correct value of Pi for CNS conditions and

ii) Effect of asperity degradation is not considered due to increase in normal stress.

Hence, Patton's (1966) equation is modified to overcome the above limitations. It is developed by assuming that at peak shear stress under CNS condition, the normal stress momentarily remains constant. The equation is as given below:

$$\tau_p = P_n \tan(\phi_b + i') \quad (44)$$

where, τ_p = peak shear stress in MPa

P_n = normal stress corresponding to peak shear stress in MPa for CNL/CNS condition

ϕ_b = basic friction angle

i' = effective asperity angle in degree

Linear relationship between the normal stress corresponding to peak shear stress and P_i is observed as shown in Fig. 62.

$$P_n = aP_i + b \quad (45)$$

where, P_n is normal stress corresponding to peak shear stress, P_i is initial normal stress in MPa, a and b are constants which depend upon the asperity angle (i) and normal stiffness (k_n).

The statistical analysis of the result reflects that constant a is almost insensitive to k_n and asperity angle and hence a=1 is used for all the conditions, but the coefficient b is sensitive to both k_n and i. The constant, b decreases with increase in asperity angle and linear relationship exist between coefficient, b and k_n. The increase in asperity angle causes increase in dilation and reduction in dilation resisted which in turn reduces the increase in normal stress. Hence the generalized coefficients are:

$$a = 1 \text{ and } b = 0.6\left(\frac{k_n}{i}\right) \quad (46)$$

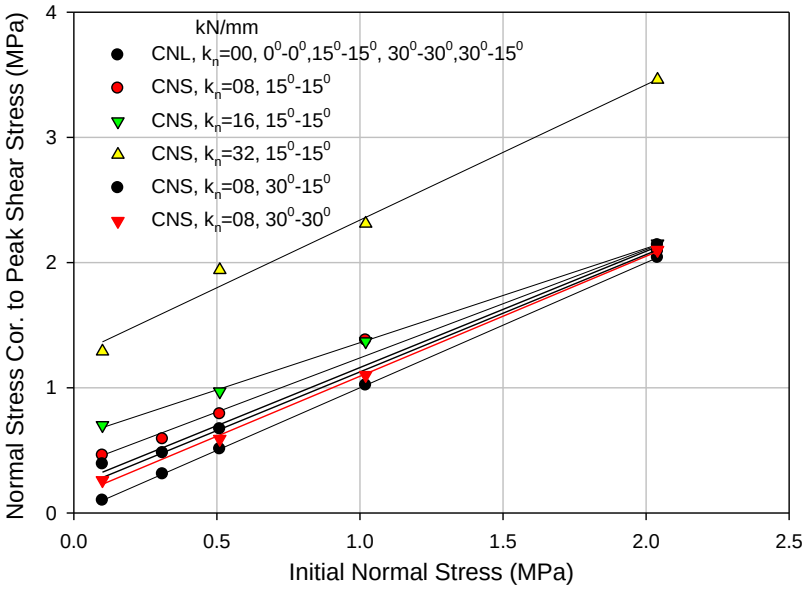

Fig. 62. Variation of normal stress for different CNL and CNS conditions

The rate of asperity degradation depends upon the ratio of P_n/σ_c. Increase in this ratio causes flattening of the asperity and the reduction in the effective asperity angle. The decay rate of asperity angle is exponential as shown in Fig. 63, the figure shows that most of the experimental data falls within the 95% confidence band. This can be represented by the following equation:

$$\frac{i'}{i} = 1.25e^{-9.86\frac{P_n}{\sigma_c}} \quad (47)$$

where, i' = effective asperity angle, i = initial asperity angle

Now, P_n and i' are calculated from the Eqns. (45) and (47) respectively. These values are substituted in the Eqn. (44) to predict the shear strength under CNL and CNS conditions. To predict the basic parameters like ϕ_b, σ_c, k_n and asperity angle (i) are required for any rock joint, which can be easily determined by simple testing facility. The proposed model is validated with some of the available experimental. The detail account of this is presented by Shrivastava and Rao (2015).

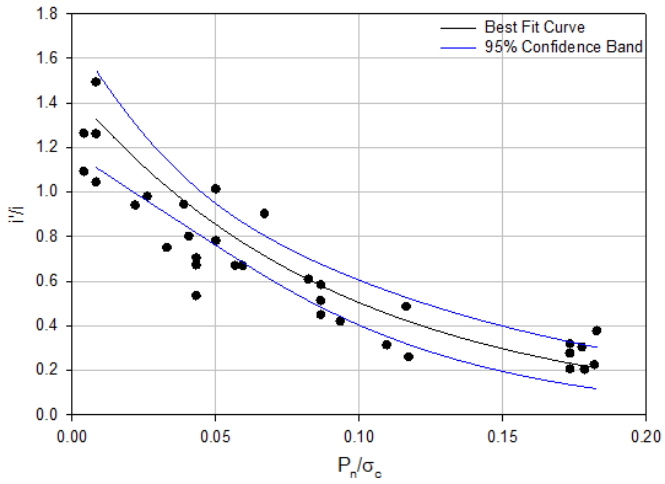

Fig. 63. Asperity decay with increase in normal stress for asperity angle

10.4.2 Infilled Joints

The Eqn. (44) is modified to suite infilled joint conditions:

$$\tau_{pinfil} = P_n \tan(\phi_b + i'_{infill}) \quad (48)$$

where, $\tau_{pinfilled}$ = peak shear stress of infilled joint in MPa

$i'_{infilled}$ = effective infilled asperity angle in degree

The statistical analysis of experimental results presented by Shrivastava and Rao (2018) reflect that the decay rate of infilled asperity angle is logarithmic as compared to exponential in case of unfilled joints and it is given by:

$$\frac{i'_{infill}}{i} = x \ln(P_n/\sigma_c) + y \quad (49)$$

where, $i'_{infilled}$ = effective asperity angle of infilled joint, i = initial asperity angle

x and y = coefficients which depend upon t/a ratio and asperity angle

It can be seen that at t/a=2 i.e. at t/a= $(t/a)_{cr}$ the value of R^2 is low which will not result in a better prediction because shear strength for this case will completely depend on the shear strength of the infill alone. Hence, Eqn. (49) will be valid for t/a < $(t/a)_{cr}$ and for t/a ≥.$(t/a)_{cr}$ shear strength must be calculated from the shear strength of the infill only.

The above model is not valid for planar infilled joint where asperity angle (i) =0. The effect of infill material on the planar joint is to reduce friction angle (ϕ) in comparison to basic friction angle (ϕ_b). Hence, the Eqn. (44) is modified as given below:

$$\tau_p = P_n \tan\phi \quad (50)$$

The decay rate is logarithmic and best represented by the Eqn.(51):

$$\frac{\phi}{\phi_b} = x \ln\left(\frac{P_n}{\sigma_c}\right) + y \quad (51)$$

where, ϕ = friction angle of infilled joint, ϕ_b = basic friction angle

10.5 Cyclic Shear Testing

Existing large scale direct shear system designed and developed by Rao et al. (2009 a, b) and Shrivastava and Rao (2013) is able to conduct tests under static condition on jointed rock. New design to test under cyclic condition is made and modification in existing equipment is done by Niktabar et al. (2018). It can work under varying normal stiffness, frequency, and amplitude of cyclic shear loads. The horizontal load is modified in such a way that it can move under cyclic load with the following four stages: forward advance (FA), forward return (FR), backward advance (BA), and backward return (BR), as shown in Fig. 64.

The shear apparatus developed is capable of conducting tests under both static and dynamic loads at different boundary condition on natural and synthetic rock joints. This shear testing machine can work under different normal stiffness by feeding value of normal stiffness as input parameter in the software of apparatus.

Existing direct shear software is installed on the PC. In this, software can select two type of shear mode, static or dynamic (or cyclic) shear condition. The parameters initially feed as input data to shear software. Under cyclic loads the parameters are wave type, frequency, amplitude, total cycles, normal stiffness and initial normal stress.

10.5.1 Design of Large Scale Profilometer

Natural jointed rocks have very variable and irregular roughness surfaces. Large scale profilometer is designed and fabricated to quantify roughness of natural rock joints as shown in Fig. 65 (a). The maximum size of the sample for quantifying

joint roughness is 600×600 mm. This apparatus is composed of two main units which include frame and LVDTs, and data acquisition and processing unit. Coordinates such as X, Y and Z are loaded into the surfer software and 3D view of joint surface are plotted by digitizing of the data (Fig. 65 (b)) (Niktabar, 2016).

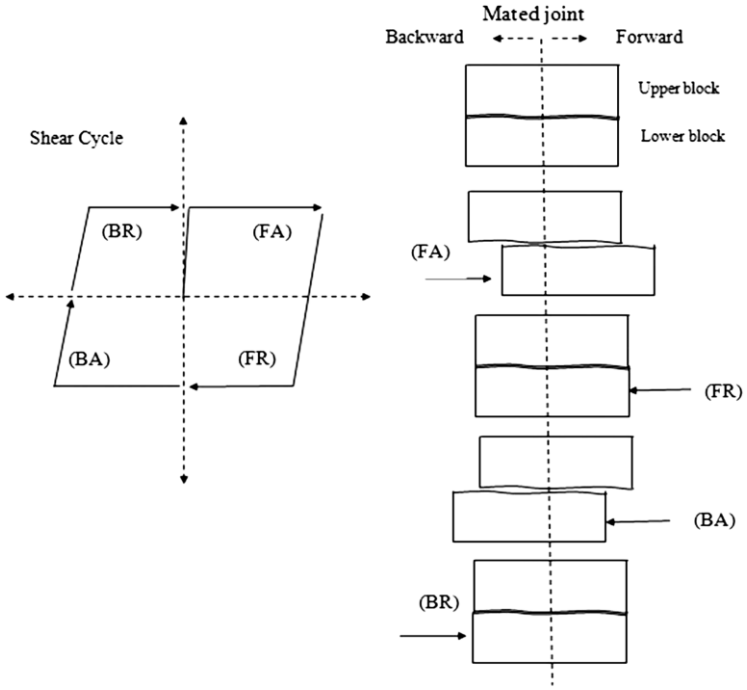

Fig. 64. Load directions and joint movements under shear cyclic condition. FA, forward advance; FR, forward return; BA, backward advance; BR, backward return.

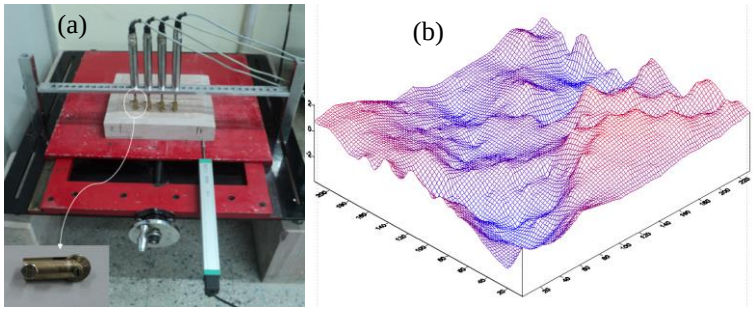

Fig. 65. (a) Large scale Profilometer with LVDTs and (b) 3D measured joint roughness profile

10.5.2 Preparation of the Sample

Unfilled and infilled synthetic rock and natural rock samples are prepared as per procedures explained by Shrivastava and Rao (2013, 2015 and 2018) and Niktabar (2016). The representative samples of synthetic and natural rock joints are presented in Fig. 66 (a), (b) and (c).

10.5.3 Shear Behaviour

Shear test performed on each sample under thirty cyclic loads. Shear loads, normal loads and deformations data captured by the software automatically during the test. Interpretation of results is implemented based on loads and deformations with increasing number of cycles. Failure mechanism on joint and asperities degradation is recorded and observed after cyclic shear test to compare with results. Cyclic shear behavior of one of the joints presented in Fig. 67.

10.6 New Cyclic Shear Model

Based on the experimental results and Patton (1966) model, shear strength model is developed to predict peak shear strength of the joint under CNL and CNS boundary conditions for different regular asperities under cyclic shear loads. The proposed model is compared with experimental results for 30°-30° asperity at P_i = 0.1 MPa for both CNL and CNS (K_n= 8kN/mm) boundary conditions for different cycle of shearing at presented in Fig. 68. A close agreement between proposed model and experimental results observed. In this model if both of initial normal stress and asperity angle increase to 0.17 and 300 respectively, shear strength of the joint is same as intact sample for first cycle and it is planar joint for subsequent cycles.

$$\tau_{P_N} = \tan(\phi_b + i') \quad (52)$$

$$i' = i \times e^{-j_\alpha\left[4(N-1)\left(\frac{(P_n)^2}{\sigma_c}\right)\right]} \quad (53)$$

$$j_\alpha = \frac{2i}{\lambda}$$

$$P_n = P_i + K_n \Delta y) \quad (54)$$

If $P_i \geq 0.17\sigma_c$ and $j_\alpha \geq 3.53$, $(i \geq 30^0)$

First cycle $\tau_{P_1} = c + P_n \tan(\phi_i)$ (55)

Subsequent cycles $\tau_{P_N} = P_n \tan(\phi_b)$ (56)

where, N= no. of cycles, i= asperity angle in degree, λ= asperity base length in mm
j_α = Interlocking factor, i' = Change of asperity angle by the shear cycles in degree,
P_n = Normal stress in MPa, P_i = Initial normal stress in MPa
k_n= Normal stiffness in MPa/mm, Δ y = Peak dilation in mm
σ_c = UCS of intact sample, MPa; $\tau_{(PN)}$ = Shear stress peak at cycle N in MPa
ϕ_b = Basic friction angle, ϕ_i =Intact friction angle

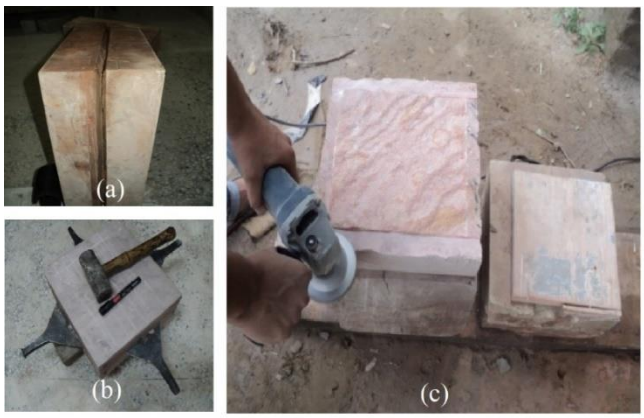

Fig. 66. Photograph of rock joint preparation (a) Grooving in block (b) Hammering chisel for splitting(c) Polishing for proper dimension

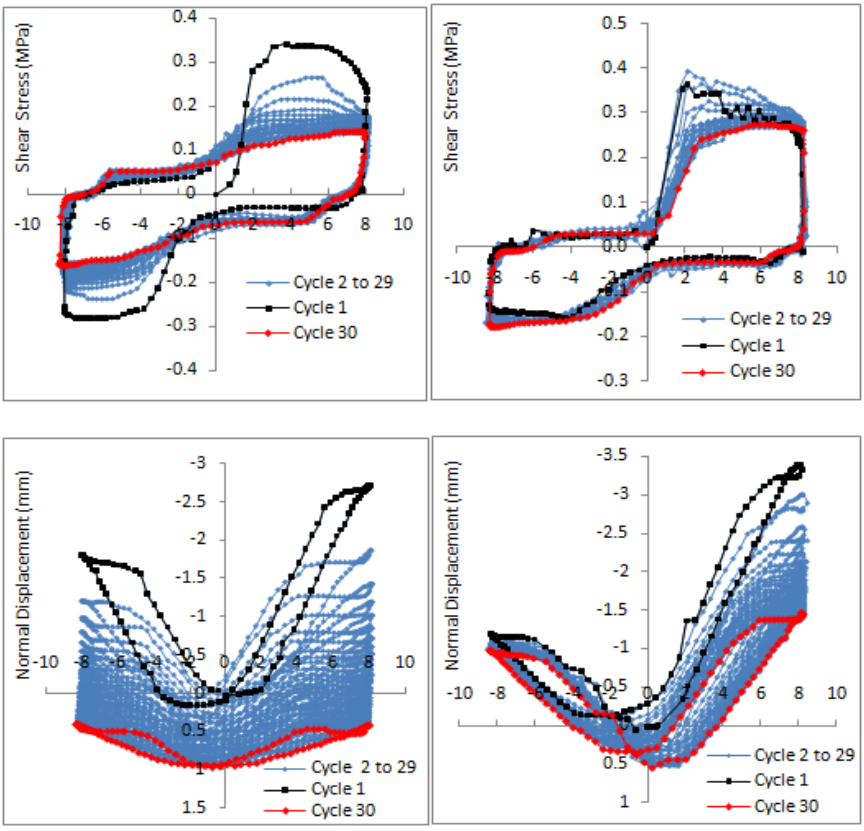

Fig. 67. Shear stress and normal displacement versus horizontal displacement of unfilled synthetic rock joints with 30°-30° asperity (a and b) as regular joint and 15°-30° asperity (c and d) as irregular joint at P_i =0.1 MPa under CNL and cyclic loads (Niktabar, 2016)

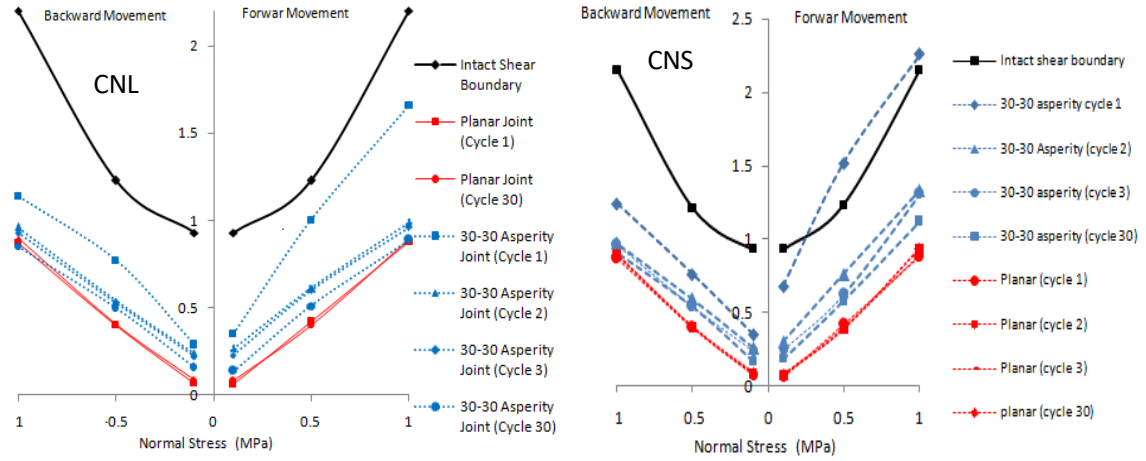

Fig. 68. Shear strength envelope for regular and irregular joint under CNL and CNS condition for 30°-30° asperity (Niktabar, 2016 and Niktabar et al., 2018)

10.6.1 Numerical Modelling

It is very difficult to simulate all the factors influencing the shear behaviour of the rock joints by constitutive modelling and experimental study. A constitutive model has to consider the large number of assumptions and uncertainties or requires the input of complex parameters for analysis. The experimental studies require very good testing facilities. The availability of sophisticated software's and high speed computer has made numerical approaches of analysis popular and easy. Numerical method can be used to model large scale projects as well as for the physical model studies conducted on jointed rockmass in the laboratory.

Now an attempt has been made to model the shear behaviour under both CNL and CNS conditions using UDEC. The behaviour of simulated rock joints (Plaster of Paris) with asperity angle 0^0-0^0,15^0-15^0 and 30^0-30^0 has been modelled in UDEC and the predicted shear strength is compared with the experimental results (Shrivastava and Rao, 2010 and 2011).

10.6.2 Modification in the Joint Model

The deformability of the discontinuities between the blocks and their frictional characteristics in UDEC are modelled by spring slider system with prescribed force displacement relations enabling the normal and shear forces between the blocks to be calculated. The UDEC contains different constitutive models for the joint. Coulomb slip model which provides a linear representation of joint stiffness and yield limit. It is based upon elastic stiffness, frictional, cohesive, tensile strength properties and dilation characteristics common to rock joint. Second, continuously yielding model which is more realistic than the Coulomb joint model as it accounts for nonlinear behaviour observed in physical tests. This joint model, displays a continuous accumulation of plastic displacement from the onset of shearing.

The bounding strength is given by

$$\tau_m = \sigma_n \tan \phi_{eff} \qquad (57)$$

Where σ_n and ϕ_{eff} are the normal stress and effective friction angle respectively. During the shearing process ϕ_{eff} is continuously reduced from $\phi_b + i_0$ to ϕ_b, where, ϕ_b and i_0 are the basic friction angle and initial angle of the dilatancy respectively. In practice the factor F and the law of reduction of effective friction angle is determined empirically. The third joint model i.e. Barton-Bandis model is also a nonlinear joint model that directly utilizes index properties from laboratory tests on joints.

In this work, initially coulomb joint model was used for the prediction of the shear behaviour of planar and nonplanar rock joints. The result showed that it is suitable only for the planar joints. Then, continuous yielding joint model was used for the analysis, it gives better prediction than coulomb joint model for the nonplanar joints, but it has limitation in predicting the peak shear stress at higher initial normal stress. This is due to improper law of reduction of effective friction angle used in continuous yielding joint model. Hence, continuously yielding model is modified to consider the effect of the CNS boundary conditions and the law of reduction of effective friction angle, for this the models proposed by Shrivastava (2012) is used.

The numerical code of the continuous yielding model is modified by writing FISH (Itasca, 2004) function to incorporate the new shear strength proposed from these investigations. The new code is capable of predicting the shear behaviour of the rock joints under CNL and CNS boundary conditions for static and cyclic conditions.

10.6.3 Modelling of Direct Shear Test in UDEC

Model geometry of size 297 mm X 297 mm X 125 mm is created in the UDEC software. The desired asperity of planar rock joint and nonplanar rock joint with asperity 150-150 and 300-300 of thickness 5mm is created. Initial boundary condition is applied on the sample in such a way that the lower shear box is only allowed to move in X direction and movement in Y direction is restricted by imposing Y velocity at the bottom of the lower shear box as zero. The upper shear box is allowed to

move only in the Y direction and movement in the X direction is restricted by imposing X velocity at the sides of the upper shear box as zero. The boundary conditions are similar to the conditions used during laboratory testing. The average normal and shear stresses and normal and shear displacements along the joints are measured. The UDEC results are compared with the experimental results (Shrivastava and Rao; 2010, 2011, 2015, 2018). It is observed that the predicted peak shear stress based on UDEC is in close agreement with the experimental results, although the pre peak shear stress response is under estimated.

10.7 Conclusions

A new servo-controlled large scale direct shear facility was designed and developed to conduct tests in CNL and CNS conditions in static mode further modified to cyclic mode. A new Profilometer was also designed to capture 3D roughness profiles of natural rock joints.

The influence of boundary conditions and thickness of the infill material on shear behavior of modeled joint with different asperities (30^0 - 30^0, 15^0 - 15^0, and 0^0 0^0) were systematically observed and a new shear strength model is proposed based on experimental results for infilled joints with different infill thickness and asperity angle under CNL and CNS conditions. The study is further advanced to capture the cyclic shear bevaiour of unfilled and infilled jonts for natural and synthetic rock joints.

A new shear strength model for cyclic conditions is proposed. The proposed model is compared with the results in the literature and a close aggreement for different conditions is observed. Numerical modelling is also done and necessary modification in exiting numerical code is carried out to find shear behaviour under CNL and CNS boundary conditions for the unfilled and infilled jonts subjected to static and cyclic loading.

11 Creep Experiments on Rock Salt for Underground Structures

Another interesting aspect of the engineering behaviour of rock and rockmass is the study of time-dependent behaviour. Most of the rocks respond to the applied time-dependent short-term response while performing the quasi-static tests in terms of different strain rate to which the load is applied on the specimen and long-term response, with respect to deviatoric stress the material is subjected to during its course of engineering application in its intrinsic way. In most of the cases, the long-term effects due to applied engineering loads are too small and are normally ignored. In rock such as rock salt, this viscoelastic behaviour is prominently identified and has been a concentrated area of research in IIT Delhi. Important aspects of the rheological behaviour of rock and its engineering applications through the study of rock salt are briefly discussed.

11.1 Physico-Mechanical Behaviour

Rock salt or halite is an evaporite deposit formed directly precipitated from the concentrated seawater and buried in sedimentary formations all over the world including India since the Pre-Cambrian times. The evaporite deposits are found in the form of extensive bedded deposits or dome and plugs of hundreds of meters thick and underlie broad areas of several kilometers. Rock salt is an isotropic coarsely crystalline, mono-mineralic (NaCl) rock and is found typically colorless as shown in Fig. 69 (a). However, a natural rock salt looks to be as shown in Fig. 69 (b) with some pinch of impurities such as calcite, dolomite, anhydrite, and gypsum.

Rock salt is delicate and physically weak compared to other rocks. So delicate that it flows much like ice under quite moderate deviatoric pressure. However, due to its unique physical and mechanical behaviour, its engineering application has increased manifold. These properties are to remain always unjointed due to high viscosity, homogeneous, isotropic, and impermeable rock (Baar, 1977). Utilizing these unique properties, thousands of caverns and tunnels have been constructed worldwide in rock salt for the storage of hydrocarbons and the disposal of most hazardous nuclear waste.

In India, known salt deposits are restricted to a small but highly tectonized Lower Shali formation exposed around Guma, District Mandi, and the extensive bedded formation of marine evaporates in north-western Rajasthan of the so-called Nagaur-Ganganagar Basin. Rock salt in Mandi is highly tectonized and deformed while the deep-seated natural rock salt formations of Nagaur-Ganganagar spread over the surface area of more than 50,000 sq. km which covers much of northwestern Rajasthan, India. The salt of this area is pure (around 95%) and offers an ideal medium to its multipurpose needs. So far, very limited studies on rock salt in India have been studied and thus incited IIT Delhi to take up the comprehensive research in pursuit to examine its engineering behaviour in more detail. Summary of the physical properties of rock salt based on XRD, SEM, XRF and other standard tests is given in Table 11.

11.2 Stress-Strain Behaviour

A typical stress-strain curve of rock salt specimen applied at a strain rate 0.01mm/sec or $1.3x\ E^{-4}$ is presented in Fig. 70. The failure strength observed is 29.88 MPa and failure strain is 4.8%. The specimen exhibits non-linear deformation even at very low stress and the stress-strain curve is found to vary as a function of applied loading rates.

The initial part of the stress-strain curve is slightly concave upwards with an increased strain rate (Fig. 70). The initial higher increase in strain rate at low stress could probably due to the closure of inherent crack, pore space, voids, and interface. Because rock salt has a low porosity of around 4% and falls under the non-fissured to a slightly fissured class of degree of fissuring (IQ), this convexity is less prominent and is restricted in a very low strain range of less than 4% of the total failure

strain. With further increase in stress, the rock salt specimen exhibiting strain hardening behaviour and the stress-strain curve becomes concave towards abscissa. This strain hardening remains more prominent in around 75% of the total failure stress, however, within this stress range, only 50-60% of total failure strain occurs. The rest of40 to 50% of failure strain occurs in the only remaining 25% stress range when the strain hardening began to gradually reduce, and the strain steadily increases with a very small increment in the stress.

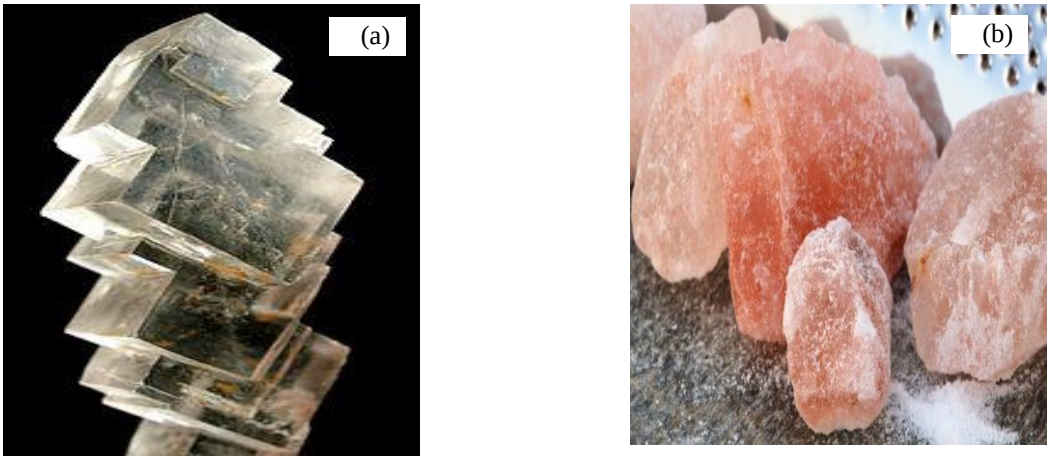

Fig. 69. Rock salt (a) Pure (b) Natural with impurities

Table 11. Physical properties of rock salt

Characteristics of rock salt	Typical value
Chemical Classification	Halite, NaCl
Cleavage	Perfect, cubic, 3-directions at right angles
Mohs hardness	2.5
Crystal system	Isometric, Galena(PbS) class
Density	2.13g/cc
Specific gravity	2.20
Average porosity	3.5%
Sonic velocity	4000 m/sec
Point load index ,$I_{s\,(50)}$	1.15 MPa
Tensile strength	2.85MPa

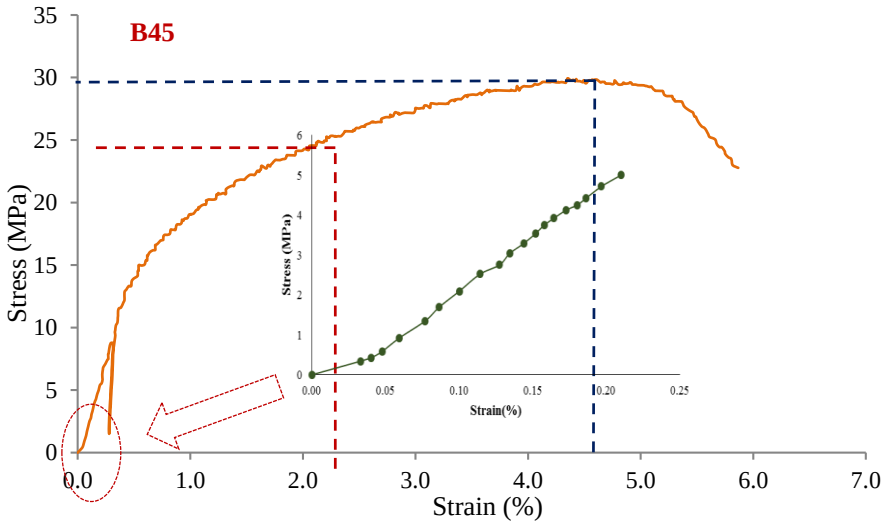

Fig. 70. A typical stress-strain plot of rock salt

Kaiser Effect: The behaviour of unloading and reloading excursion cycle was time-independent and the specimens were unresponsive i.e. when held at constant stress lower than 90% of the previous peak stress. The stress-strain curve remains linear during the entire unloading and reloading cycle until it reaches around 90% of the previous cycle peak. This phenomenon is also known as the breakage of the Kaiser effect which is defined as the absence of local failures such as micro-cracking or pores collapsing in rock until the load imposed on the specimen exceeds the previous maximum applied stress during unloading and reloading cycle. To observe this critical stress in terms of felicity ratio (FR) in rock salt for the safe loading, a multiple unloading and reloading excursion cycle were made at different stress percentage of peak stress as shown in Fig. 71 for the entire stress-strain curve. Seven unloading and reloading were carried out at around every 5 kN interval before failure and one unloading and reloading was done post-failure. The slope of the unloading and reloading cycle remains almost constant in the entire stress range during the UCS condition which depicts a constant elastic constant. It remains constant even after the post-failure.

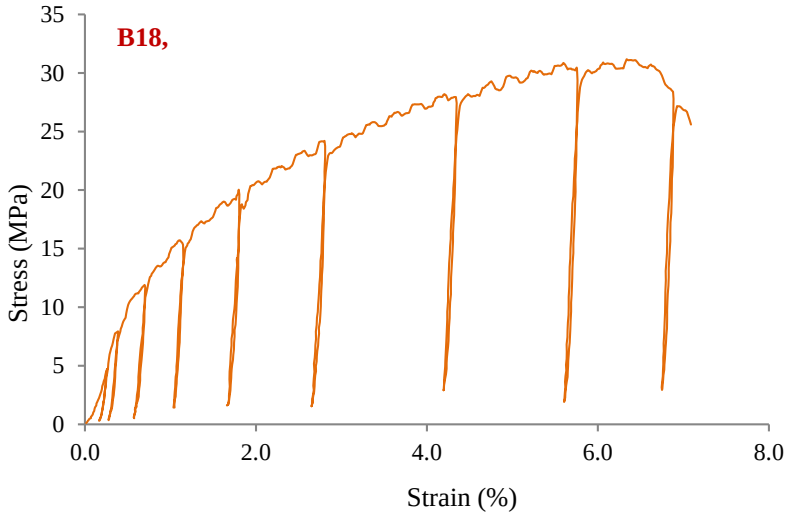

Fig. 71. Multiple unloading and reloading excursion cycle

11.2.1 Felicity Ratio

Results show that the rock salt has an exceptional high felicity ratio of around 0.9 rarely found in most other rocks during the entire unloading and reloading excursion cycle up to failure, means that if the salt is subjected to stress less than 90% of its uniaxial strength, the specimen probably can sustain this load for a long time without failure. With this critical stress, the stress-strain response of rock salt up to failure, including the zone of cyclic unloading and reloading can be expressed by a proposed constitutive model. The governing equation for strain in uniaxial compression test is given as:

$$\varepsilon(t_n) = \left(\frac{\sigma_0(t_n)}{E}\right) + \sum \frac{\sigma_0(t_{n-1})}{\eta}(t_n - t_{n-1}) + \left(\frac{\sigma_0(t_n)+\sigma_0(t_{n-1})}{2\eta}\right)(t_n - t_{n-1}) \qquad (58)$$

$$\text{if } \left[\frac{d\sigma_o}{dt} \geq 0,\ \sigma_0 \geq \sigma_{cri}\right]$$

$$\text{and, } \varepsilon(t_n) = \varepsilon(t_{n-1}) + \frac{\sigma_0(t_n)-\sigma_0(t_{n-1})}{E} \qquad (59)$$

$$\text{if } \left[\frac{d\sigma_o}{dt} < 0\,, \sigma_0 < \sigma_{cri} \text{ and } \frac{d\sigma_o}{dt} > 0\,, \sigma_0 < \sigma_{cri}\right]$$

The creep parameters of rock salt are estimated from the UCS testing in terms of viscosity η and strain rate $\dot{\varepsilon}$ through a nonlinear regression analysis and are expressed as:

$$\eta = 37\ /\dot{\varepsilon}^{\,0.96} \qquad (60)$$

For a soft rock like salt, the deformation up to failure is dependent not only on the confining pressure but also on the strain rate since the specimen has more time to deform in the slow tests than the fast one. The salt can deform and continue to deform up to more than 10%.

11.3 Effect of Confining Pressure and Temperature

The data reveal that, confining pressure has a significant effect on strength, deformation and other mechanical parameters of rock salt as shown in the Fig. 72. The figure shows that with increase in confining pressure, deformation becomes less discrete, and more distributed. At confining pressure of 8MPa, the average failure stress increased up to 56MPa from the average UCS of 27.85 MPa and the salt underwent about 9% shortening before it failed to hold increasing loads. Compared to linear Mohr-Coulomb criterion, the non-linear IIT Delhi criterion (Rao, 1984) fits better.

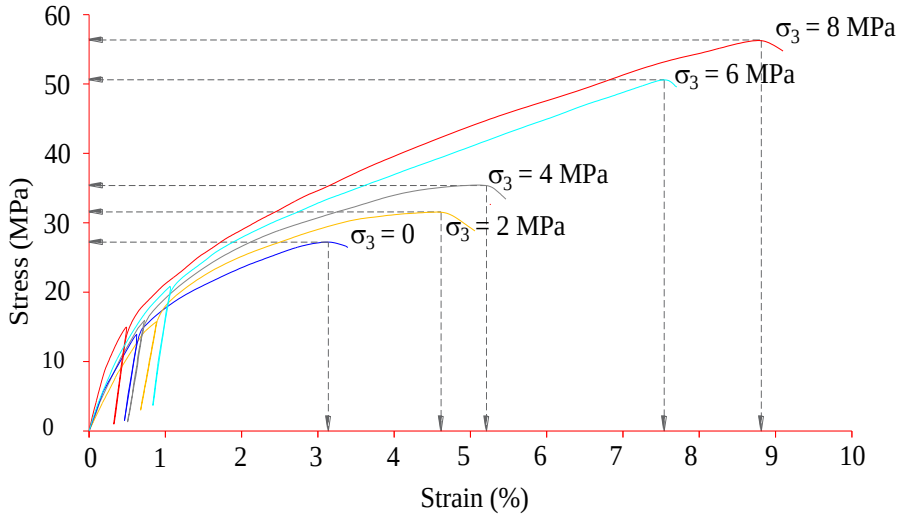

Fig. 72. Stress-strain plot at different confining pressure

The strength of rock salt is not restricted by the stresses and by the failure strain but also by the dilatation. At higher confining pressure, shear causing dilation are large enough to cause dilatancy damage. Stress state that led to dilatancy is defined in terms of the traditional Cauchy stress tensor which is also term as of mean stress invariant I1 and the square root of the stress deviator invariant $\sqrt{J_2}$ which is a measure of the overall deviatoric or dilatant shear stress. $I_1$is the first invariant of stress tensor and is defined as $I_1 = 3\sigma_m = \sigma_1 + \sigma_2 + \sigma_3$ and, $J_2$is the second invariant of the deviatoric stress tensor which is defined as

$$\sqrt{J_2}=\left\{\frac{1}{6}[(\sigma_1 - \sigma_2)^2 + (\sigma_2 - \sigma_3)^2 + (\sigma_3 - \sigma_1)^2]\right\}^{1/2}$$

Damage due to excessive dilatancy is likely to happen when the deviatoric stress tensor exceeds the mean or confining stress. The damage zone in the study with the set of experimental results is defined as a blue line as shown in Fig. 73. The results show that in few cases, the shear stress (J_2) in the rock salt is large compared to the mean stress (I_1) and the dilatancy damage is expected which is more pronounced at higher confining pressure (Kumar, 2019b).

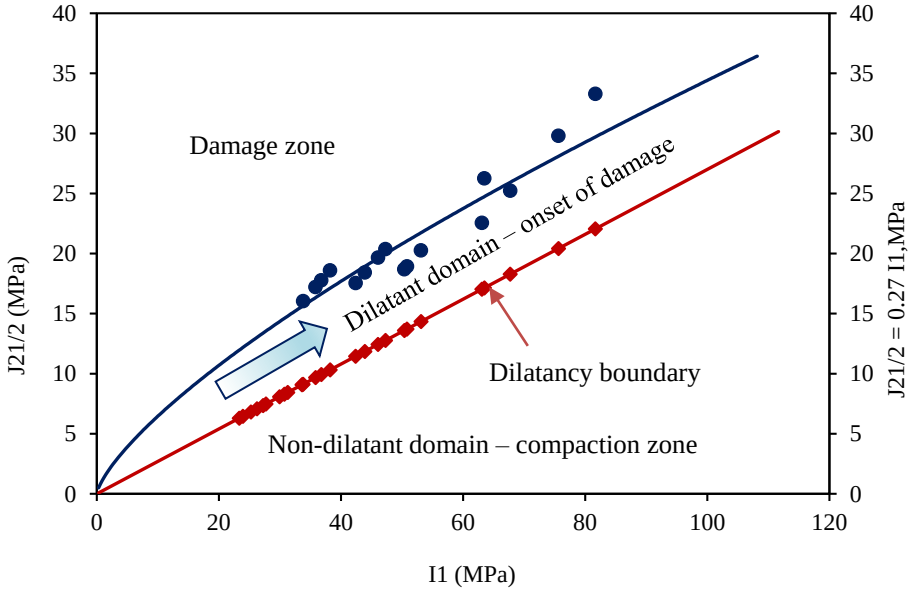

Fig. 73. Comparison of experimental test results with dilatancy criteria

The dilatancy boundary also known as an important long-term safety boundary in which creep and increasing permeability above this line are inevitable is rather a band than a line. This dilatancy boundary varying from about one half or one-third of the short-term failure and have used it for the safety assessment of nuclear waste repositories in rock salt. Between this band of lower dilation boundary (red line) and upper damage zone (blue line), the salt expects an onset of dilatancy and an increase in volume change, though, but not to the extent of substantial damage or failure. Below this dilatation boundary, marked red in colour, the shear stresses are small compared to the mean stress, wherein the volume of the specimen decreases until all microcracks are closed and dilatancy is not expected.

Of all other parameters, temperature has the maximum effect on the mechanical behaviour of rock salt. A testing facility of performing UCS up to 400°C is made available in the IIT laboratory through a temperature controller device are shown in Fig. 74. UCS tests on 54mm dia specimens of rock salt were performed up to a temperature of 250°C. The specimens were loaded in compression by an automatic compression testing machine of 3000kN capacity as shown in the Fig. 74.

Figure 75shows the overall decrease of around 20% in strength for the entire range of testing temperature. The decrease in failure strength, however, is more pronounced at temperatures greater than 100°C. The stiffness (Young's modulus) of salt decrease at a rate of around 0.025 GPa/K as temperature increases.

Ductility of salt on the other hand increases very rapidly as the temperature increases. Increase in ductility with an increased temperature could be attributed to the dominance of crystalline plasticity over the crystalline micro cracking. Result of the tests performed with elevated temperature are shown in Fig. 75.

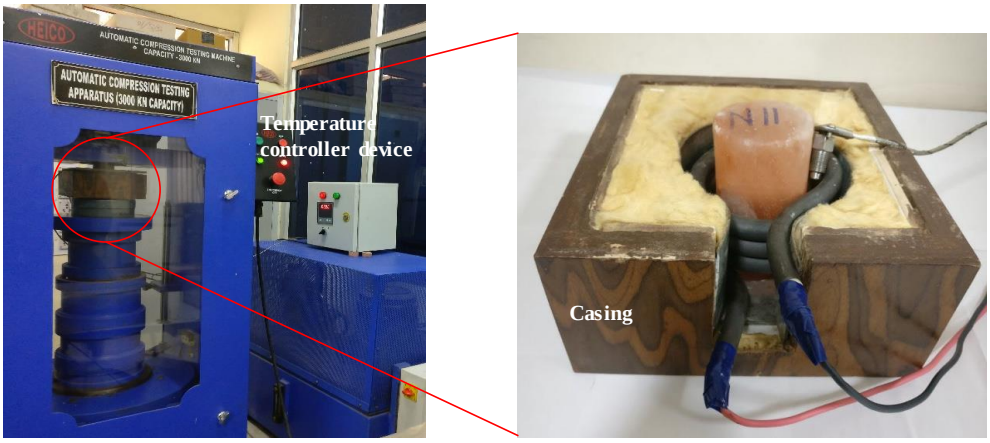

Fig. 74. Setup for uniaxial compressive strength testing at high temperature

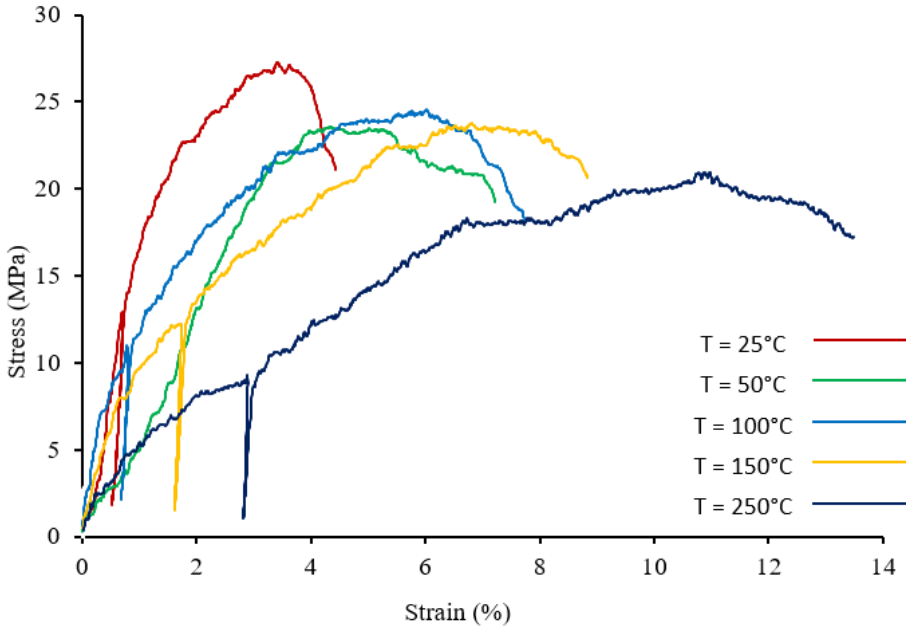

Fig. 75. Stress-strain curves of the salt at RT, 50°C, 100°C, 150°C and 200°C

11.4 Design and Development of Creep Facility (CF)

Viscous behaviour of rock salt also known as creep, is defined as a slow plastic deformation over a prolonged period at essentially constant load. Creep plays a key role in the development of underground spaces for their stability and simulation of its long-term behaviour constructed in it. To observe the creep behaviour of rock salt, a new cantilever type creep testing machine has been designed and installed at IITD as shown in Fig. 76 which can perform a long-term uniaxial creep test on a cylindrical rock sample.

11.5 Creep Experiments on Rock Salt

Uniaxial compression creep tests on a 38mm dia specimen with constant vertical stress, ranging from 5 to 9.5 MPa were performed shown in Fig. 77. As the applied stress was less than the uniaxial strength of 28MPa, a long-term deformation was

expected. The tests comprised of both single stage creep tests as well as multistage creep tests with step-wise load increment. A typical test duration of around 30 days for each step of loading was taken. One typical plot obtained from the multistage creep test as shown on Fig. 78 is commonly represented by the instantaneous elastic deformation followed by the sequence of specific time dependent plastic deformations.

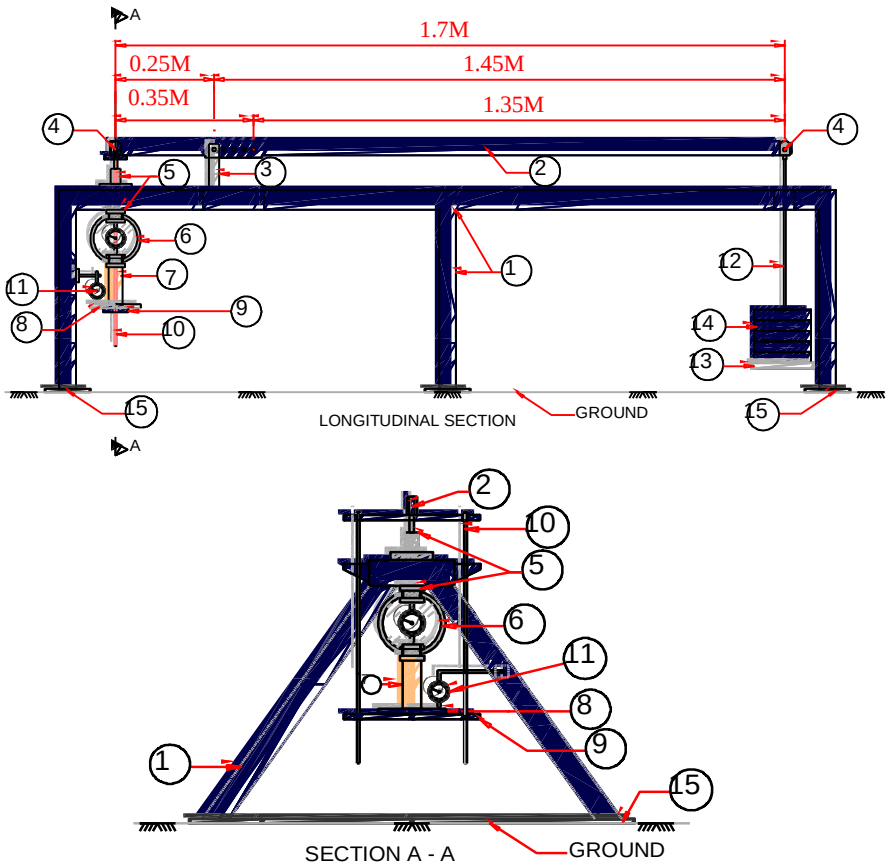

1. Frame with leg support
2. Lever arm
3. Fulcrum
4. Bearing
5. Proving ring coupling
6. Proving ring
7. Specimen
8. Platen
9. Base support
10. Threaded rods
11. Dial gauge
12. Load hanger
13. Load plate
14. Dead weights
15. Rubber pads

Fig. 76. Uniaxial creep testing equipment schematic layout

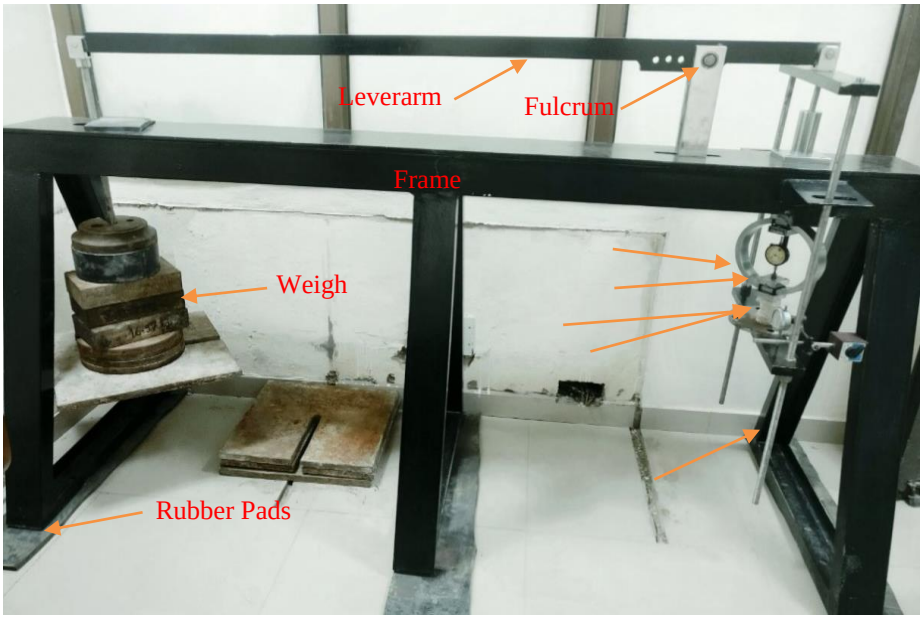

Fig. 77. Creep testing equipment

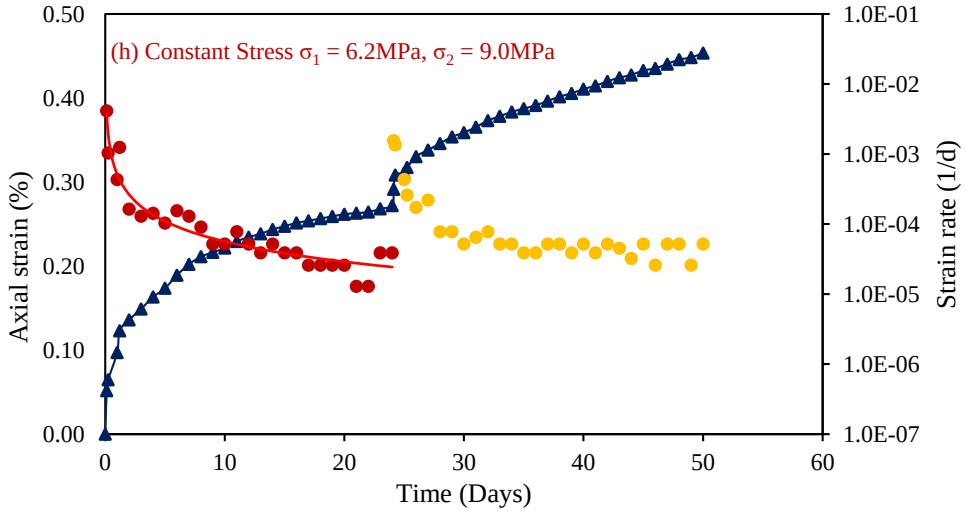

Fig. 78. Typical multi-stage creep plot of a rock salt

After each load step, the deformation starts with a high deformation rate i.e. the primary transient creep which decreases continuously until it reached the secondary creep rate (also called steady-state creep) where the strain rate remains constant. Time to reach steady state creep rate in most curves is around 8 to 10 days. The typical plot also shows the effects of stepwise loading during the tests in order to create phases with constant conditions. This phase of loading resembles the operating state of salt cavern filled with oil/gas where multiple withdrawal and filling of product takes place. The results show that as the deviatoric stress was increased it results in another instantaneous elastic deformation and another transient creep phase followed by another steady-state creep.

The steady-state creep rate increases with an increase in deviatoric stress and can be approximated by a power function, $\dot{\varepsilon}^{cr} = A \times \sigma^{n}$, where a pre-factor A and stress component, n is estimated as 7 x 10^{-7} MPa^{-n} d^{-1} and 1.41 (Kumar, 2019b and Singh et al., 2018b). The test results show that the creep behaviour as described by the proposed constitutive model approximated by power function can satisfactorily describe the creep strain measured over the operational period of a salt cavity. The creep parameter such as viscosity obtained from the proposed relationship based on UCS testing as expressed by Eqn. 60 is found to be in good agreement with the measured values obtained from the creep test.

11.6 Engineering in Rock Salt

As discussed, rock salt has a unique combination of material characteristics, making it the ideal host rock for various storage purposes including nuclear waste. Caverns built in rock salt are deep (from 300m to 2000m) and are larger (average dia of 80m and the height of 160m) than cavities made in hard rock (average width of 20 to 30m and height of 30 to 50m). Some salt caverns are large enough measuring 80 m diameter and 400m high for the Eifel Tower in Paris (324m) to fit inside. At these depths, the surrounding salt is under such pressure that any cracks that may occur will close almost instantly. This "self-healing" phenomenon makes the deep salt caverns geologically very stable.

Design fundamentals of such large salt cavities and the modes of instabilities associated to it are local fracture, creep closure, pillar collapse, surface subsidence, subsurface subsidence, and deep fracturing. Engineering aspects of these caverns and tunnels in the vast expanse of the bedded salt formation near Bikaner, Rajasthan, for creating a large inventory of crude oil and nuclear waste repository are discussed in brief.

11.6.1 Storage of Crude Oil in Salt Caverns

Fig. 79 illustrates a typical rock mechanical envelope of project. Caverns are located at a depth of around 600m with an average diameter of 120 m, height of 150m and a net storage volume of about 0.55 Million m^3. A total of ten such large caverns of volume around 0.55 Mm^3 each is proposed under the Phase 2 strategic storage program of Government of India. The construction time of large caverns of this size through solution mining leaching process would typically take four years.

The geomechanical analysis performed in the Abaqus FEA software through visco-elastic model, suggest a moderate displacement and stress state field with some minor damage but predict no large-scale regions of concern. Fig. 80 compares the cavern at the end of construction that is at t = 0 and predicted cavern shapes into the future after 25 years. The net closure rate for the cavern due to creep under the normal operating condition with a constant minimum pressure inside is expected to be around 0.40% per year, resulting in a volumetric loss of around 10.08 % in its service span of 25years.

11.6.2 Nuclear Waste Repository

As an alternative to the country's disposal of both hazardous and non-hazardous waste generated from the nuclear power, which is still being pursued, a generic conceptual layout of a nuclear waste repository is proposed as shown in Fig. 81. The conceptual layout demonstrates the technical viability of a nuclear waste disposal program for the storage of all kinds of

waste including the heat-generating high-level waste in rock salt near Bikaner. The model illustrates the broad lithology of the project area in sequence from the top (not in scale). The repository is located at a depth of around 600m from the ground and built in the thickest halite layer H6.

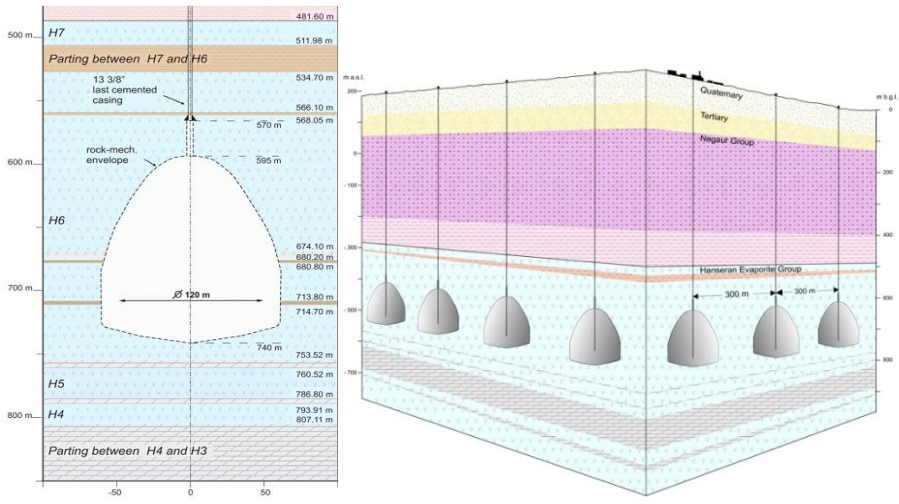

Fig. 79. Proposed rock mechanical envelope and typical project layout

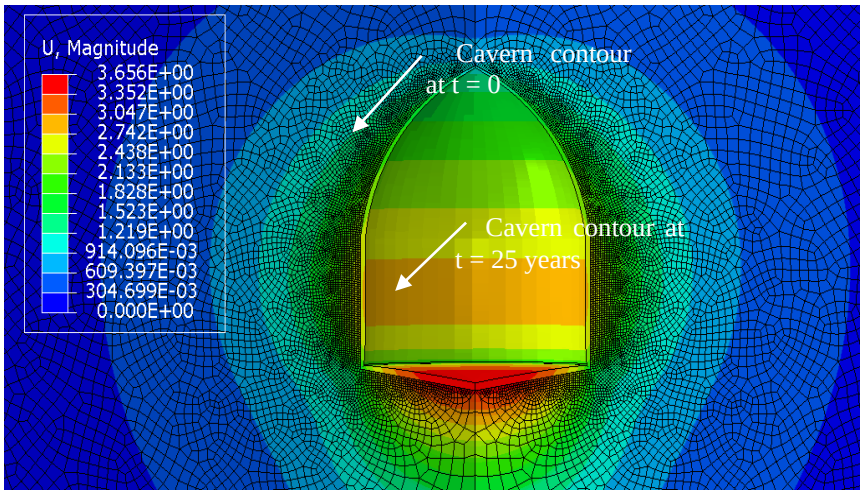

Fig. 80. Contour plot of cavern at the onset of creep and after 25years of run

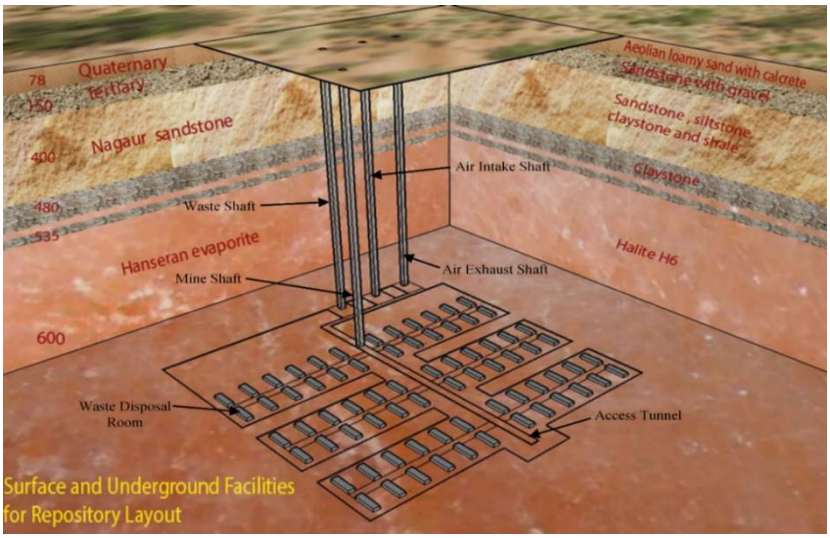

Fig. 81. Proposed nuclear waste repository in 3D model

As shown in Fig. 81, the proposed mine layout mainly consists of shafts, a network of access tunnel and waste disposal room, and other underground facility rooms. Four shafts connect the underground facilities. Two smaller shafts of 4m x 4m

shall be used for air intake and exhaust and two larger shafts of 6m x 6m for waste handling and to haul salt mine. The larger shaft shall also be used for the movement of personnel. Shaft and underground facilities are connected with the main access tunnel of 6m x 10m which further joins the network of waste disposal room as shown in figure. The size of each waste disposal room is 3m (width) x 4m (height). Length of the room would vary from 50 to 100m. Size of disposal room is kept narrow enough to improve mining efficiency and structural stability and convenience of waste handling. These rooms would be excavated keeping in mind stand-up time due to creep and excavation would take place by mechanical means of roof and pillar methods with minimum rock support. The mining of the access tunnel and waste disposal room shall remain a continuous process in a lateral direction depending on the current and future requirement. The repository room would be separated by 50m that would be enough for inconsequential of all possible modes of interference.

After staking the shielded container of non-heat generating intermediate-level waste in the disposal room floor, the surrounding space shall be filled with mine-run crushed salt for radiological shielding and to avoid any generation of heat. The geomechanical creep in salt may be considered disadvantageous to the storage industries as it results in the convergence of cavern and volume loss, however, has long been recognized as favorable for nuclear waste isolation. High pressure on salt from surrounding causes the salt to gradually creep filling the voids created by mine and the waste inside it will be permanently encapsulated that may remain radioactive for thousands of years. Thus, the plasticity and impermeability assure that once emplaced with salt disposal rooms, radioactive waste will be isolated for the accessible environment essentially forever.

Fig. 82 shows the room closure of disposal room with waste placed inside due to creep of a geomechanical model run in ABAQUS FEA. In isothermal calculation, room closure will nearly complete in 50 to 60 years. On an average, room size of 3m width and 4m height experiences 10 mm of closure per year. Disturbed rock zone (DRZ) is limited to the extent of around 2m near the waste disposal and as the stress drives towards equilibrium, the waste is expected to be entombed in the rock salt forever.

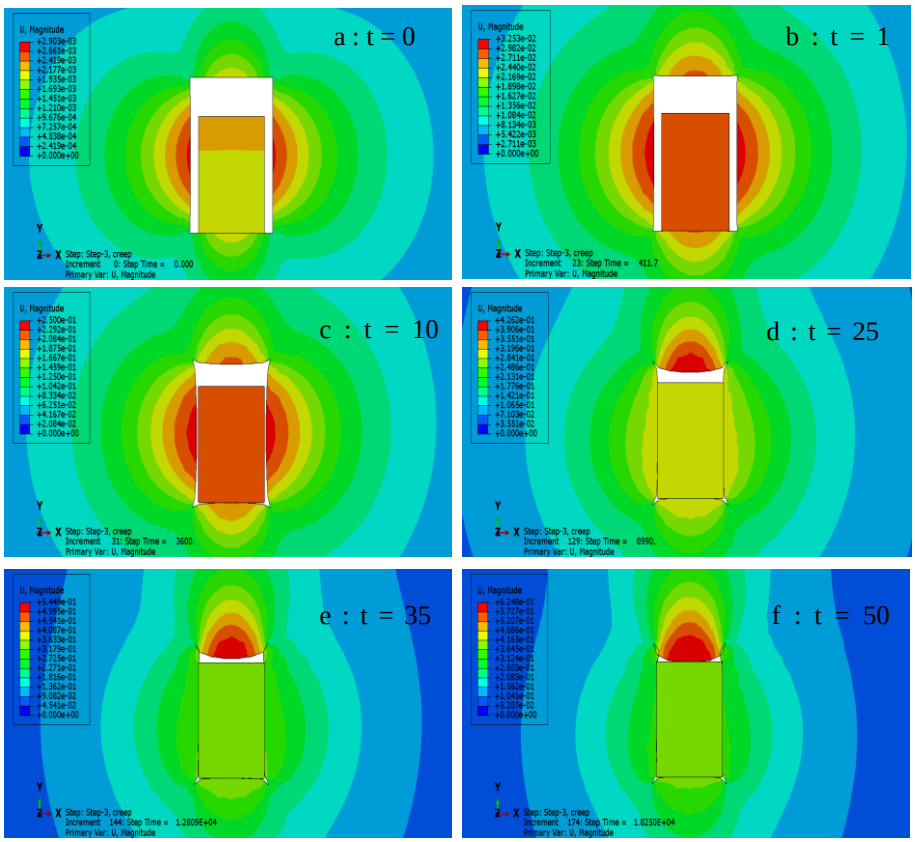

Fig. 82. Creep closure around disposal room at time (a) t = 0 (b) t = 1 year (c) t = 10 years (d) t = 25 years (e) t = 35 years and (f) t = 50 years

12 Analysis of Underground Structures under Squeezing Rock Conditions

The term 'squeezing rock' originates from the pioneering days of tunnelling in the Alps during the excavation of railway tunnels between 1860 and 1910 (Kovari, 2000). Karl Terzaghi defined rock squeezing in 1946. In 1995, the International Society for Rock Mechanics (ISRM) Commission defined rock squeezing as: "Squeezing of the rock is the time dependent large deformation, which occurs around the tunnel, and is essentially associated with creep caused by exceeding a limiting shear stress. Deformation may terminate during construction or continue over a long time period".

Squeezing is considered as a convergence phenomenon caused by overstressing and deformation characteristics of the rockmass. The physical and mechanical properties of rockmass play a significant role in determining the stress condition, squeezing and swelling phenomenon. The Himalayas are young and still under complex building processes with varying

geology and high-stress condition (Heidback et al. 2009). These heterogeneous metamorphosed mountains due to high overburden pressure, tectonic activity and high in situ stresses are highly weathered, weak and fractured and deformable in nature.

More than 200 tunnels from 62 Projects are experiencing squeezing phenomena due to several factors e.g. rock stresses, overburden, shape and size of tunnel and saturated rockmass condition in different ways (Aydan et al., 1996; Kovari and Staus, 1996; Gioda and Cividini, 1996; Brantmark and Stille, 1996; Goel, 1994; Singh et al., 1992; Aydan et al., 1993; Duncan Fama, 1993; Kovari, 1998 and Hoek and Marinos, 2000).

Thus the assessment of squeezing phenomenon, evaluation of stability of the tunnel and support pressure estimation is very necessary before construction of any underground structure (Rao and Jain, 2015; Rao and GhoshRoy, 2015).

12.1 Field and Lab Investigations

The Rohtang tunnel connecting Leh and Manali is selected for the investigations (Fig. 83 and Fig. 84). The tunnel passes through an average overburden of > 600m and maximum overburden about 1900m with an entry point at an elevation of EL.3060M in South and runs towards North and end at elevation of EL.3071M. Rohtang traverses through uniformly dipping alternate sequence of quartzitic schist, intermixing of quartzitic phyllite (QP)/ phyllitic quartzite (PQ) and phyllite from south portal whereas the North portal starts with sequence of biotite mica schist (BMS) and migmatitic gneiss (MG) (Fig. 85).The rock samples of four type of rocks encountered in squeezing portions of tunnel were collected and tested for their physical and mechanical properties in dry and saturated states.

A comprehensive study has been undertaken for determining physico-mechanical behavior of these rocks through laboratory test (Table 12) and its impact during tunnel excavation.

Fig. 83. Location of the Rohtang tunnel

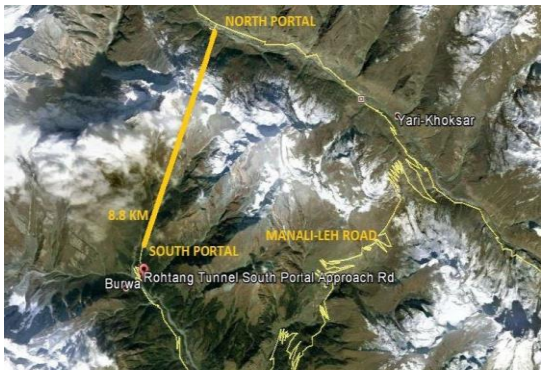

Fig. 84. Satellite image of the project area showing proposed tunnel

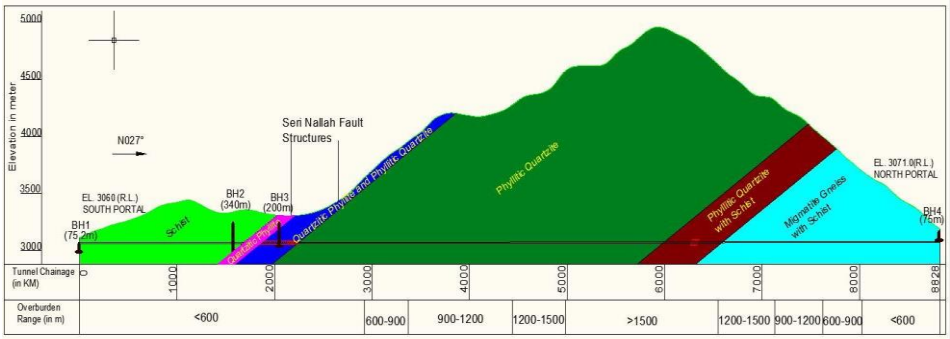

Fig. 85. Geological section of the Rohtang tunnel

12.2 Support Measures and Measurements

The tunnel has been supported by fibre reinforced shotcrete, one to two layer of wiremesh, swellex type rock bolt varying in length from 4 m to 12 m, lattice girder or steel sets of ISHB 250 type. Apart from this regular support the tunnel has been excavated at various sections using fore polling of diameter 32mm to 76mm with length varying from 6 m to 12 m. The detail description of support with rock class has been collected and documented for support analysis. Recorded instrumentation data were also collected and analyzed to use in this study.

12.3 Evaluation of Squeezing in Rohtang Tunnel

Squeezing assessment has been done using empirical, semi-analytical, analytical and numerical approaches and the results are compared. A total of 64 tunnel sections were evaluated through aforesaid criteria's. Above approaches were compared and possible reasons for variations in results by different approaches have been documented. In addition an attempt has been made to proposed new criteria's (Jain, 2019) for squeezing predictions through comparative and parametric study and compared with the existing correlation.

Table 12. Physical and mechanical properties of PQ, QP, MG and BMS rocks

Name of Test	PQ	QP	MG	BMS
Bulk Density (gm/cc) Dry	2.70	2.73	2.68	2.66
Bulk Density (gm/cc) Saturated	2.71	2.74	2.69	2.68
Specific Gravity	2.77	2.74	2.81	2.83
Resistivity (Ω m) Dry	2.77E+07	6.85E+08	2.97E+06	1.72E+06
Resistivity (Ω m) Saturated	6.51E+03	7.80E+03	5.39E+03	4.63E+03
Wave velocity (km/s) Dry	3.65	3.99	2.52	3.26
Wave velocity (km/s) Saturated	4.23	4.55	3.28	4.22
Modulus (GPa) Dry	35.97	43.48	17.09	28.44
Modulus (GPa) Saturated	48.37	56.73	29.01	47.71
Index Quality (%) Dry	60.76	66.47	42.07	54.39
Index Quality (%) Saturated	70.45	75.84	54.75	70.34
Water Content (%)	0.18	0.21	0.28	0.56
Porosity (%)	0.49	0.57	0.74	1.50
Slake Durability Index Id_1(%)	99.35	99.33	98.78	98.18
Slake Durability Index Id_2 (%)	98.93	98.78	98.04	97.32
Permeability (m/s)	$3.00*10^{-9}$	$2.04*10^{-9}$	$7.19*10^{-9}$	$2.08*10^{-9}$
Tensile strength (MPa) Dry	11.91	12.03	6.01	8.19
Tensile strength (MPa) Saturated	9.79	11.13	5.49	6.85
Unconfined compressive strength (MPa) Dry	105.96	112.18	46.36	67.64
Unconfined compressive strength (MPa) Saturated	94.49	83.26	44.22	60.43
Modulus of Elasticity (GPa) Dry	42.91	43.57	23.19	49.32
Modulus of Elasticity (GPa) Saturated	41.10	43.28	15.05	48.05
Poisson's ratio (%) Dry	0.26	0.24	0.24	0.25
Poisson's ratio (%) Saturated	0.23	0.30	0.26	0.21
Material constant Hoek-Brown (mi) Dry	17.33	15.04	27.49	10.02
Material constant Hoek-Brown (mi) Saturated	20.60	19.12	30.04	13.60
Cohesion c (MPa) Dry	20.72	23.37	8.51	15.40
Cohesion c (MPa) Saturated	16.46	18.27	6.49	12.22
Angle of internal friction ϕ (°) Dry	48.88	46.27	47.58	41.40
Angle of internal friction ϕ (°) Saturated	48.40	45.56	47.26	38.80

In empirical approach Jethwa et al. (1984) criteria predicted that out of 64 tunnel sections 51 tunnel sections are under squeezing condition, whereas as per Singh et al. (1992) criteria only 55 tunnel sections are under squeezing condition and according to Goel (1994) criteria 61 tunnel sections are under squeezing condition whereas as per observed tunnel deformation there are only 33 tunnel sections under squeezing condition. The details of non-squeezing and squeezing sections (using 1% strain criteria) determined through semi-analytical, analytical and numerical approaches are tabulated in Table 13.

Table 13. Comparison of number of squeezing sections through semi-analytical and analytical approaches

Approaches	Number of sections				
	Non-Squeezing	Minor Squeezing	Severe Squeezing	Very Severe Squeezing	Extremely Squeezing
Kovari (1998)	33	15	12	4	0
Hoek and Marinos (2000)	44	10	10	0	0
Salencon (1969)	49	13	2	0	0
Duncan-Fama (1993)	50	13	1	0	0
Carranza-Torres and Fairhurst (2000)	45	19	0	0	0
Numerical analysis	64	0	0	0	0
Measured convergence	31	21	12	0	0

The convergent confinement analysis of all 64 sections was also carried out using Hoek-Brown criterion. The analysis shows that 45 number of tunnel sections have encountered support failure with safety coefficient less than 1. Few tunnel

sections up to RD 2380m passing through Seri nalah despite having safety coefficient more than 1 have shown higher convergence, this may be due to water pressure which was not considered during analysis.

12.3.1 Prediction of Squeezing

Attempt was made to develop new correlations through comparative and parametric study. In comparative study a new linear classification with Q and N value was developed to enhance the classification given by Singh et al. (1992) and Goel (1994) by using 172 number squeezing and non-squeezing cases.

The linear equations (Eqns.61 and 62), (Fig. 86 and Fig. 87) developed through comparative study using Q and N as main parameters is:

For squeezing $H > 390Q^{0.29}$ (61)

For squeezing $H > 253N^{0.32}$ (62)

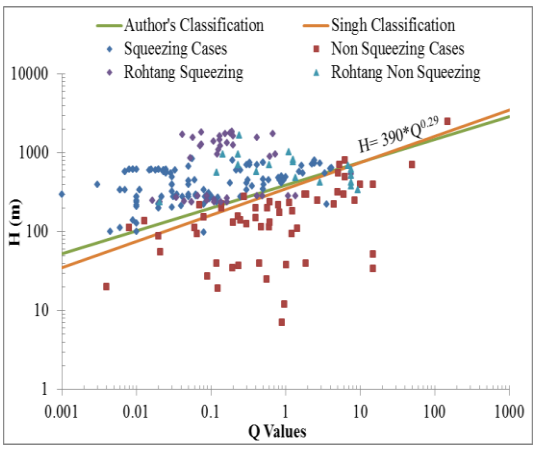

Fig. 86. Squeezing prediction criteria using rock quality index Q

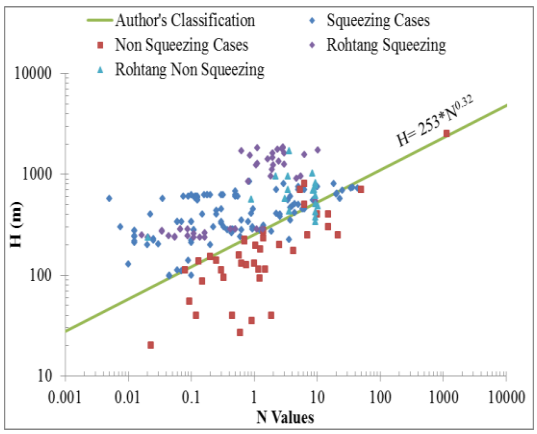

Fig. 87. Squeezing prediction criteria using rock quality index N

The parametric study is also done using 122 tunnel cases. Empirical correlations are derived using the regression analysis on the available data for the prediction of tunnel strain. The dimensionally correct empirical correlations (Eqns. 63, 64 and 65) and (Fig. 88, Fig. 89 and Fig. 90) developed through parametric study using J_f, Q and N as main parameters and with regression correlation factors of 0.88, 0.80 and 0.80 are

$$\frac{U_p}{a} = \frac{1x10^{-12}\sigma_v J_f^{4.01} K_0^{1.5}}{K+2.2} + 0.005 \quad (63)$$

$$\frac{U_p}{a} = \frac{0.011\sigma_v Q^{-0.3} K_0^{1.25}}{K+4} + 0.005 \quad (64)$$

$$\frac{U_p}{a} = \frac{0.023\sigma_v N^{-0.3} K_0^{1.2}}{K+5.2} + 0.005 \quad (65)$$

An index called Coefficient of Accordance (COA) (Dwivedi et al., 2014) is computed for values of deformation estimated from correlations given by Dwivedi et al. (2013) and Goel (1994) and Eqns. 63, 64 and 63).

Lower value of COA indicates a better correlation. Values of deformation estimated from the developed correlation in this study Eqns. (63), (64) and (65) give the COA 0.19, 0.51 and 0.44 respectively as compared to existing correlations of Dwivedi et al. (2013) and Goel (1994) (Fig. 91, Fig. 92 and Fig. 93) which give the COA 0.66, 0.80 and 6.33 respectively. It can therefore be concluded that the proposed correlations are definitely an improvement over the existing correlations. In addition estimated values of deformation obtained through developed equation and existing correlations of Dwivedi et al. (2013) and Goel (1994) were also plotted with observed deformation in Fig. 94, Fig. 95 and Fig. 96 for comparison.

The plot also shows a linear line with 1:1 gradient. If predictions by a given approach are better, the points should lie close to the linear line. It is seen that the predictions made by the proposed approach lie closer to the linear line as compared to the other approaches.

12.4 Results

i. In general the empirical and semi-analytical approaches can be used primarily to determine the extent of squeezing phenomenon. However, empirical approaches are found to be conservative for squeezing prediction analysis when compared with actual deformations calculated from monitoring instrumentation data.

ii. Both the semi-analytical approaches Kovari (1998) and Hoek and Marinos (2000) provides information regarding tunnel deformation and radius of plastic zone but Hoek and Marinos (2000) approach considers the support pressure and also gives the squeezing grade on basis of tunnel strain percentage. Therefore, the later approach can be considered in the beginning of tunnel analysis.

iii. Goel's (1994) approach can be used to estimate support pressure in preliminary stages of investigation as it does not required laboratory investigation whereas Carranza-Torres and Fairhurst (2000) approach can be used for measuring convergence, radius of plastic zone and support pressure once rockmass properties are available.

iv. The analytical approaches can be used indirectly for detailed tunnel analysis. The analytical method (convergence confine method) can be used significantly to gather information regarding allowable deformation, yielding of different types of support with safety coefficient.

v. Although the numerical modeling cannot be used directly to analyze the squeezing phenomenon in the tunnels, its application can be utilized to find the deformation of the tunnel in squeezing environment and the results can be compared with other approaches.

vi. Two dimensionally correct correlation to predict tunnel squeezing were proposed through comparative study using the parameters rock quality index Q, rockmass number N (Q with SRF=1), overburden height (H), and observed deformation (U_{obs}).

vii. Out of three dimensionally correct empirical correlations (Eqns. 63, 64 and 65) the Eqn. (63) developed using joint factor (J_f) as main parameter with correlation factor 0.88 and COA 0.19 is the best correlations for prediction of squeezing followed by Eqns. (64) and (65) having correlation factor 0.8 and 0.8 with COA 0.44 and 0.51respectively for tunnels excavated through drill and blast method in Himalayan region.

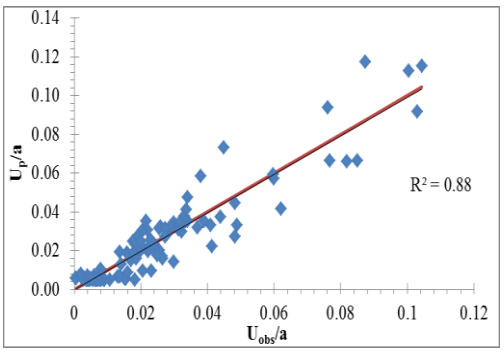

Fig. 88. Comparison between predicted (Up/a) by J_f approach and observed (U_{obs}/a) in squeezing ground condition

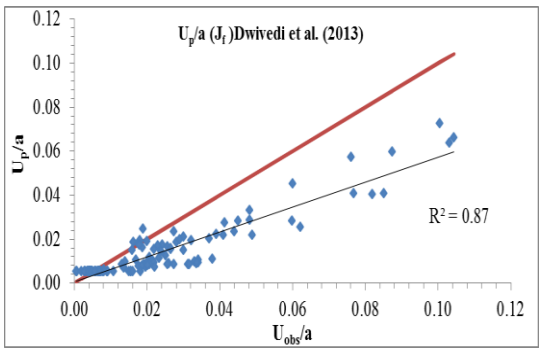

Fig. 89. Comparison between predicted (U_p/a) by J_f approach (Dwivedi et al., 2013) and observed (U_{obs}/a) in squeezing ground condition

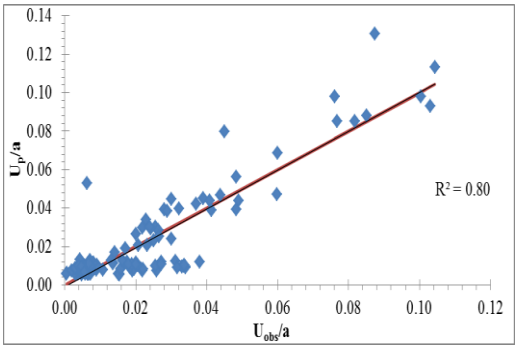

Fig. 90. Comparison between predicted (U_p/a) by Q approach and observed (U_{obs}/a) in squeezing ground condition

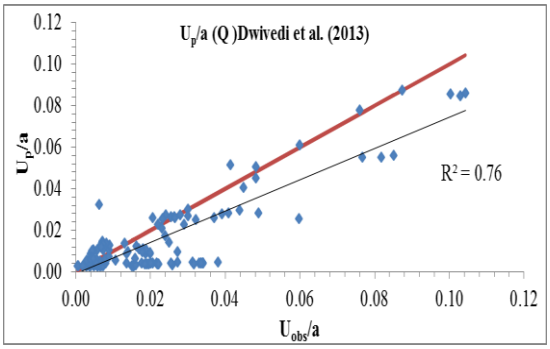

Fig. 91. Comparison between predicted (U_p/a) by Q approach (Dwivedi et al., 2013) and observed (U_{obs}/a) in squeezing ground condition

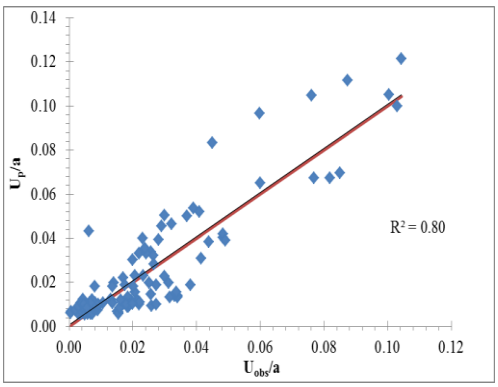

Fig. 92. Comparison between predicted (U_p/a) by Q approach and observed (U_{obs}/a) in squeezing ground condition

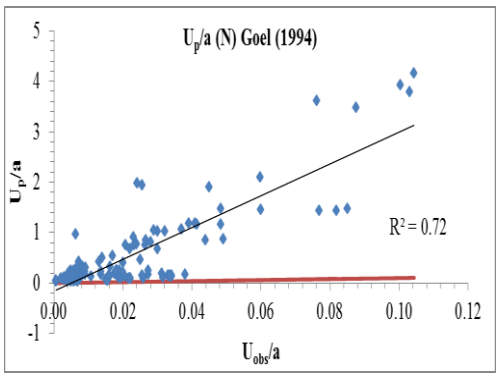

Fig. 93. Comparison between predicted (U_p/a) by N approach (Goel, 1994) and observed (U_{obs}/a) in squeezing ground condition

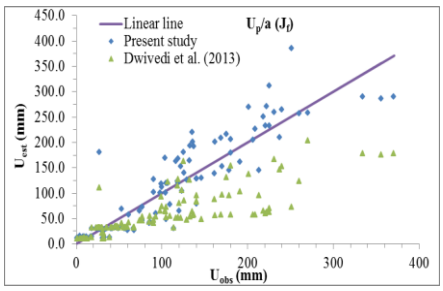

Fig. 94. Comparison of estimated deformation (using J_f) with observed deformation

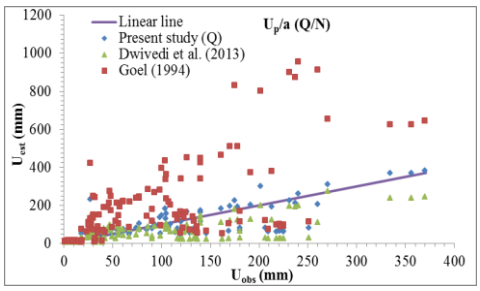

Fig. 95. Comparison of estimated deformation from various correlations with observed deformation

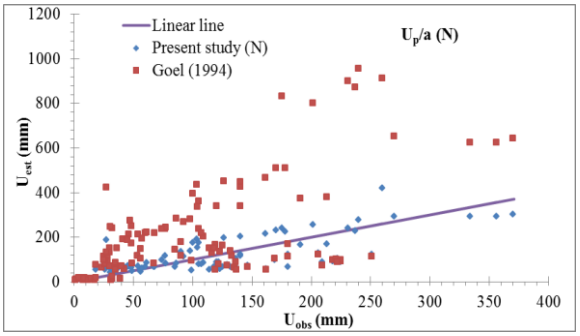

Fig. 96. Comparison of estimated deformation (using N) with observed deformation (Jain, 2019)

13 Impact and Blast Loads on Shallow Tunnels

The increase in population coupled with rapid growth and industrialization has increased the demand for infrastructural facilities. However, the limitation of space above ground has led to the use of underground space for a number of civil and military purposes such as subways, railways, highways, and water and sewage conveyance. A major application of underground space is for metro tunnels which has become a lifeline for cities. Underground structures are protected against air blast since air wave outruns ground shock. But with the progress of technology, there are innovation of missiles and projectiles which can penetrate the ground and then explode creating expanding craters. This may cause destruction to the surrounding underground structures fully/partly or may deform the same which may hinder functionality of the underground facilities and can threat lives of people inside it (Rao and Mishra, 2018).

However, recent events of terrorism related activities around the world have highlighted the vulnerability of underground structures. Europe and Asia are majorly disturbed places due to serial blasts and killings. India is also emerging as a lucrative target for the terrorists of late. Some of the strategically important targeted locations were marked on India map and its neighboring areas, are marked in Fig. 97 below. Due to brutal nature of terrorist attack, some of the most common examples of blasts in civil structures need a special mention like World Trade Centre attack, USA 2001; Madrid commuter train attacks, 2004; London underground metro bombing, 2005; and Moscow attack, 2009 (Fig. 97). Out of many factors, cover depth is reported to have a great influence on the stresses developed in the liner under impact loading. At shallow depth and low confinement, lining stresses are found to be large resulting in extensive damage (Liu, 2009).

The pattern of crack propagation has also been reported to be influenced by the overburden. Thus height of overburden is very essential to account for vibrations and crack propagation in the tunnel and surrounding rockmass. A great need is felt to visualize the effect of overburden on fracture and its propagation during static and dynamic loading. Dynamic loads due to explosions, result in strain rates of the order of 10^{-1} to 10^{3} s^{-1} which imply short time dynamic behavior of the materials involved, characterized mainly by a great over strength and increased stiffness, in comparison with normal, static properties. Fig. 98 shows strain-associated loading and various means available to characterize these materials under such strain rates. Thus, to arrive at a technically and economically feasible solution, it is important to carry out detailed investigations on strain rate behaviour of materials using appropriate techniques.

Generally degree of fracture and crack propagation due to change in in-situ stress under static/ impact loading for a given rockmass is directly dependent on the type of rock. Thus, in order to predict the extent of fracture, it is important to determine rockmass rating for given rock that is prone to blasting (Kaisar et al., 2000). Till now only limited research has been conducted so far to evaluate the impact resistance of different soft rock and tunnel passing through such rocks, with shotcrete as a lining material, although the results of some crude impact tests have been reported by ACI Committee 544, (1982); ACI Committee 506, (1984); Ramakrishnan, (1985) had monitored the effect of blast-induced vibration from adjacent tunnel on existing tunnel at Nanjing airport line, China. Tunnel lining material subjected to missile-impact at different depths in soft rock has not been studied and as such no strength criterion is available to predict the behavior of underground structures. Also, no such universal method is available to predict impact or penetration resistance for reinforced or unreinforced underground structures.

In order to protect these tunnels from ballistic threats and terrorist attack, physical modeling of simple static loading or low strain rate dynamic/impact tests were conducted on variety of geomaterials at different overburden depths with a view to predict the high strain rate blast induced deformations without performing any real blast test. For creating in-situ condition in the laboratory, a series of dynamic (impact) loading by means of drop hammer with varying weights of hammer and changing cover depth (C) and diameter of tunnel (D) ratio are planned. The samples prepared for testing comprises of tank (30cm x 30cm x 35cm) and a tunnel (5cm diameter and length 35cm) embedded in it. A total of 200 tests are conducted for determining crack propagation and fractures due to vibrations from impact in tunnel lining and surrounding rockmass as per the methodology shown in Fig. 99.

Fig. 97. Locations of major blast attacks in India from early 1990's and relative loss to property and mankind

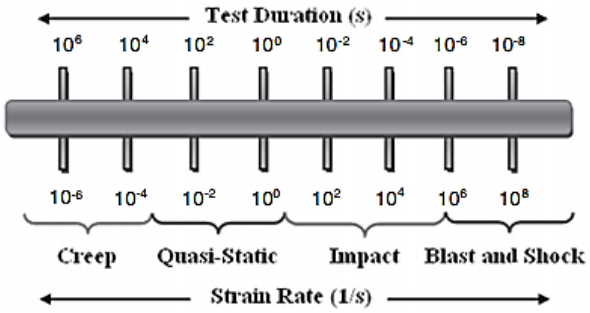

Fig. 98. Strain rate of different loading conditions (Goel and Matsagar, 2013)

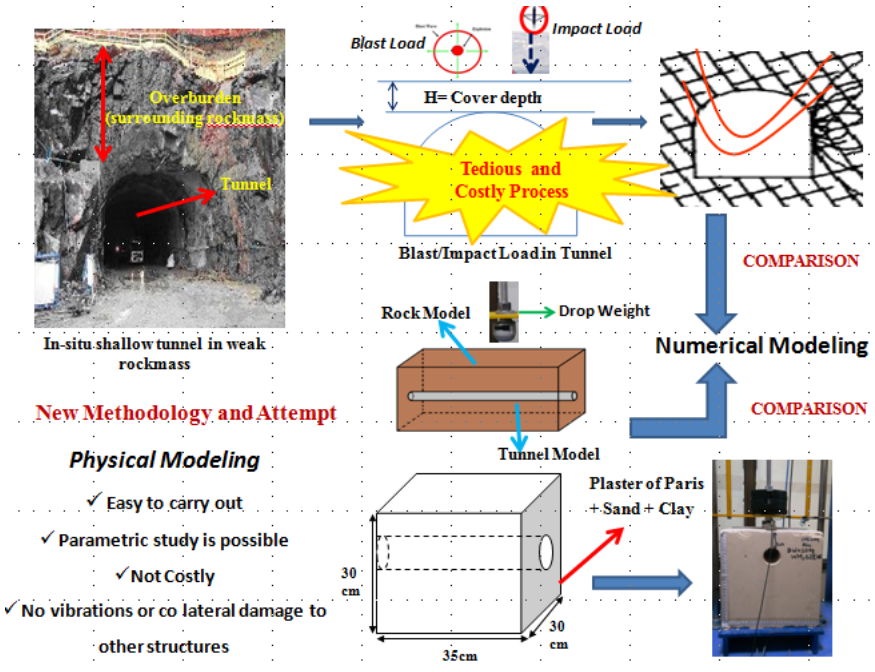

Fig. 99. Proposed methodology for dynamic response of tunnel lining

13.1 Material Characterization and Physical Modeling

At shallow depth normally soils and weathered rocks with compressive strength ranging between 1and 8 MPa are present. As most of the urban tunnels, subways and parking areas are constructed in such materials. Basic idea is to replicate the weathered and weak rockmass which is found at top few meters in natural green field conditions. A detailed parametric study of shallow tunnels subjected to impact and blast load is carried out.

The preliminary step of the study deals with the characterization of some new laboratory modeled synthetic rocks viz. GM1, GM2, and GM3. These rocks are formulated by mixing available geomaterials like kaolinite clay, Badarpur sand, PoP, mica in different proportions and water content. As per the Deere and Miller classification (1966), the laboratory modeled synthetic rockmass falls under 'EH' region representing low strength (E) with high modular ratio (H). The experimental investigations suggest that the peak strength, σ_1 varies non linearly with confining stress, σ_3 (Fig. 100 (a)). In this study a series of extensive small-scale physical tunnel models under simple gravity (1g) were modeled in the laboratory to assess the stability of shallow urban tunnels and their failure under imposed conditions.

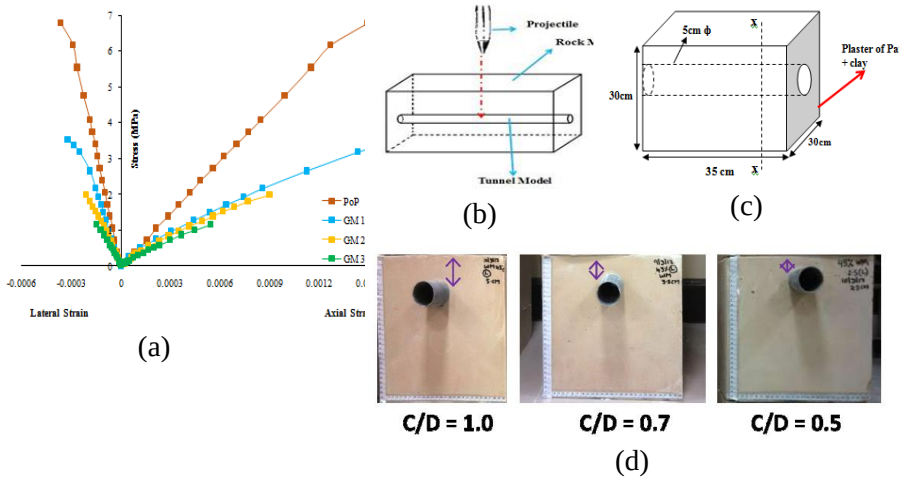

Fig. 100. Stress-strain curves of geomaterials and physical models with different cover depth

Such reduced physical model is shown in Fig. 100 (b). The geometry of the model is based on the testing area and the stress distribution around the circular opening in rockmass (Terzaghi and Richart, 1952; Ahmed and Iskander, 2011). The diameter of the circular opening is defined by the workability and feasibility. Tunnel rock model of selected geo-material is casted in the laboratory by using Perspex mould of dimensions 35cm x 30cm x 30cm, with circular holes on both the parallel plates along transverse axis of tunnel length (Fig. 100 (c)). Circular holes of diameter 5cm is extruded from both sides at different depth so as to prepare models with varying cover depths i.e. 2.5 cm, 3.5 cm, and 5 cm respectively as shown in Fig. 100 (d). The site of railway tunnel project at, T-48 Quazigund tunnel in Katra, Jammu was taken as a prototype, from where the properties of surrounding rockmass and tunnel lining is chosen for fixing the model specifications. In the study, selection of lining material and thickness of lining used for physical modeling is decided on the basis of proper scaling of the structural interaction of real field conditions. PVC hollow tubes are selected as a lining material for scaled studies. Lining thickness of tunnel is also fixed in the same manner.

13.2 Design and Development of Impact Facility

For determination of rockmass behaviour in real ground conditions, large scale physical modeling is conducted in the laboratory. For applying impact load of different intensities, Impact Testing Facility (ITF) is designed and developed (Fig. 101 (a)). A drop load of maximum 40 kg capacity can be impacted with the help of ITF facility. Maximum height of fall in the ITF facility is about 1.16 m. The working principle of the designed experimental setup (ITF) is based on the law of conservation of energy. In the study, a maximum of 25 kg load is impacted over rock tunnel model. Fig. 101 (b) shows the position of drop weight. Fig. 101 (c) presents the failure of the tunnel crown under impact load. The load cell and LVDTs are calibrated every time before the start of the experiment.

The ITF can test the sample of maximum size up to 350 mm x 300 mm x 300 mm. After the trial testing, it was concluded that locations at L/2, L/3, and 5L/12 distances from the end, are fixed and best suited for placing LVDTs to capture the strains along the tunnel length. It was observed that peak displacement captured for GM1 material is more than that of GM2 and GM3. A detailed parametric study is carried out in order to assess the crack initiation and fracture propagation in different rockmass under impact load.

13.3 Experimentation

Extensive experiments were carried out under different conditions. Some trial samples were tested before conducting the experiments on actual samples. A total of 27 test conditions have been considered for both lined and unlined tunnel models.

With dissipation of drop energy slowly, spalling started from inside. It is observed that as the C/D ratio increases; low deformations would occur in tunnels. Crack length decreases gradually with the increase in the depth of overlying strata.

Deformations at higher depth would only occur at very high impact load or drop energy. It was observed that the peak load exerted over tunnel for C/D ratio 0.5 is less than that of C/D ratio 0.7 and 1.0. Fragile rockmass like GM3 undergoes massive deformation as compared to GM1 and GM2 when the projectile hits the surface. The rockmass gets sheared at the upper inner face of the tunnel, while the lower inner tunnel surface remains unaffected. The extent of the tunnel length that gets affected depends on different factors like cover depth, intensity of drop loads, and mechanical strength of the surrounding rockmass. It is observed that when hammer strikes the top surface of the rock tunnel model, it started to penetrate the top surface up to a certain depth. Further, the rebound of the hammer is observed. In other words, the total impact energy imparted by drop hammer is equal to the difference between the kinetic energy of hammer before striking to that of kinetic energy of hammer after striking.

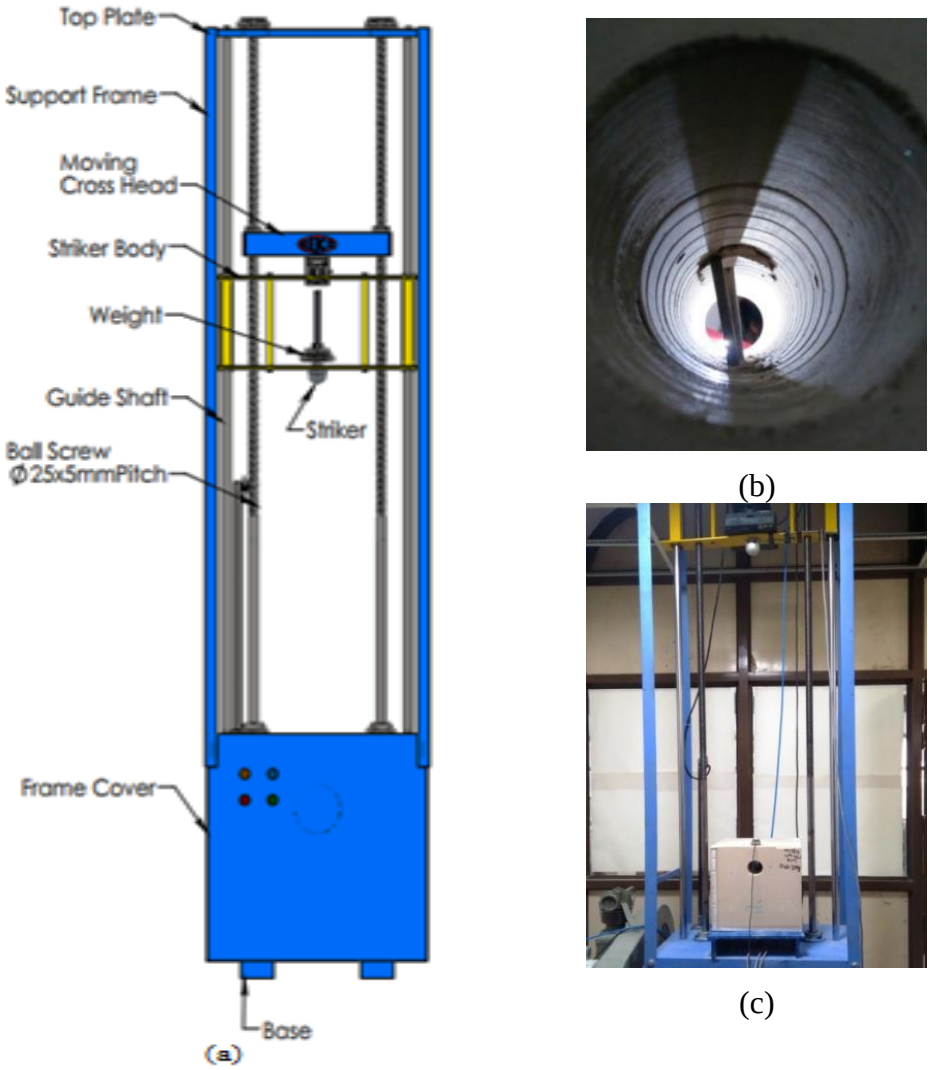

Fig. 101. Impact Testing Facility (ITF) (a) Nomenclature and 2D representation (b) ITF with rock tunnel model (c) Failed surface of tunnel portal (Mishra et al., 2018)

Deformation values are captured at the time of hitting and with every progressive movement of the hammer. Tunnel shows maximum deformation at the time of hitting and after some time it becomes constant and show the permanent deformation. Due to punching action at the point of loading, the surrounding rockmass gets detached from the inner surface of the tunnel at the crown. The lined models get failed with deformation less than that of the unlined tunnel for the same load as expected. But the zone of influence or deformation bulb is found to be large. This is because of the resistance offered by the lining in the direction of falling load as a result more area gets affected, but magnitude of deformation is less for lined tunnels as compared to unlined tunnels (Mishra, 2019).

13.4 Numerical Simulation and Settlement Profile

After carrying out extensive physical modeling, detailed numerical simulations are carried out and validated. It was observed that numerical analysis for small scale models are in good agreement with the experimentation. The dimensions of rock model are considered larger than the size of the tunnel in the study so as to minimize the reflection of the wave from the

boundaries. Once the models are created, properties are assigned for each unit i.e. for rockmass, tunnel, and hammer. Rockmass is assumed as homogeneous, isotropic and continuous material. Mohr-Coulomb plasticity model is chosen and defined to represent surrounding rockmass. While lining and hammer are assumed as elastic materials in the analysis. Global mesh size for hammer is 0.004, for rockmass taken as 0.008 and for lining it is chosen as 0.008. Schematic views of all the models and hammer is represented in Fig. 102 (a), (b), (c) and (d).

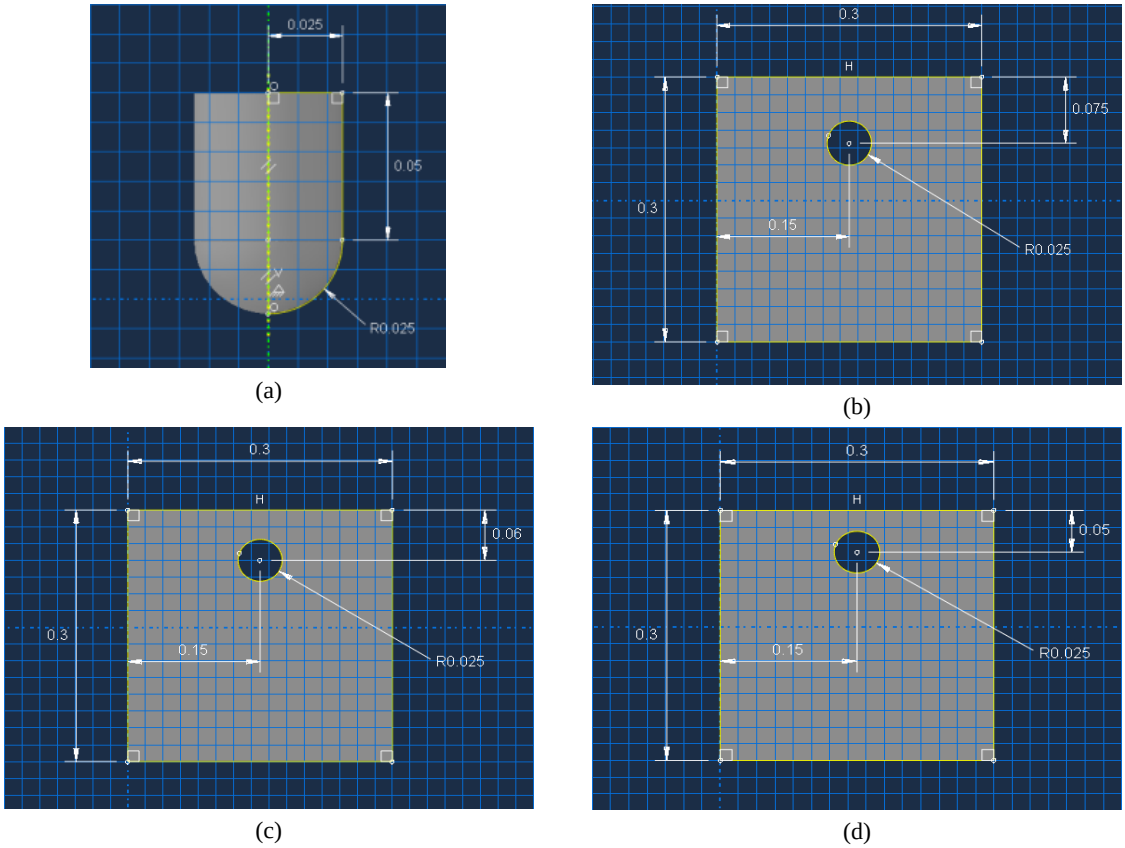

Fig. 102. Geometrical design of hammer and rock tunnel model(a) Hammer (b) Model with 0.05 m burial depth, (c) Model with 0.035m burial depth (d) Model with 0.025m burial depth (All dimensions in meter)

Mesh convergence and boundary convergence studies were performed to identify an appropriate mesh density and finally, higher mesh density with a minimum element size of 4 mm is used. The eight-node brick element (C3D8R) with reduced integration, hourglass control, and finite membrane strains are used in the FE mesh for rock model. The rockmass is modelled using Mohr-Coloumb plasticity model which allows the material to harden or soften isotropically. Contour plots of deformations for unlined tunnels are shown in Fig. 103. For different drop weights of 12.4, 15.0 and 20.0 kg, contours are plotted and it is clearly seen that the spread zone is less for unlined tunnels as compared to lined tunnels for C/D 1.0. Fig. 104 represents the deformation contours of lined tunnels obtained for C/D ratio of 1.0. It can be clearly observed that tunnels with more cover depth are not affected much laterally (vertically) rather than large area gets affected longitudinally (horizontally) because of the cushioning action. The behavior of top surface tunnel lining surrounded by different rockmass under varying impact loads are compared physically as well as numerically and the results obtained from both studies are critically analyzed. The displacement of the crown just below the loaded area is the highest. It is worth noting, that the pattern as well as the magnitude of vertical deformation computed from the numerical model is in good agreement with that of physical modeling for lined tunnels (Fig. 105 and Fig. 106).

While unlined tunnels reflect minuscule differences in predicting deformations experimentally and numerically. Numerical analysis predicts values on slightly higher side than the experimental predictions due to different assumptions on which analyses are based. Therefore, a deformation value obtained from numerical analysis for unlined and lined tunnels is considered as representative values for the study. It was found that, the fracture of rockmass under impact loads are mainly due to tensile and shear mechanisms. It is also concluded that the crack dimensions reduce as the brittleness of the material increases.

GM1 material is displaying more brittle behavior as compared to other materials such as GM2 and GM3, as depicted in Fig. 107. The peak of central deflection for GM3 material is more than GM1. This may be due to the presence of pores and fissures as GM2 and GM3 are representing weak weathered rockmass. They get deformed more and more as punching progresses until the maximum densification of fissures and voids is achieved. The difference in the experimental and numerical results is more prominent for cover depth of 25 mm as compared to 35 and 50 mm as shown in Fig. 108. This is because the deformation velocity at the crown is much higher for 25 mm as compared to other cover depths. It can be concluded that the effect of static material properties decreases with increase of cover depth.

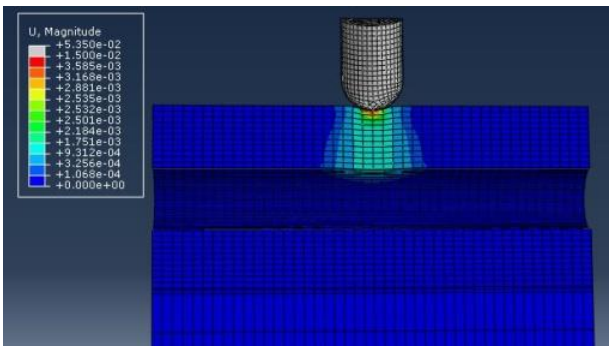

(a) Drop load = 12.4 kg

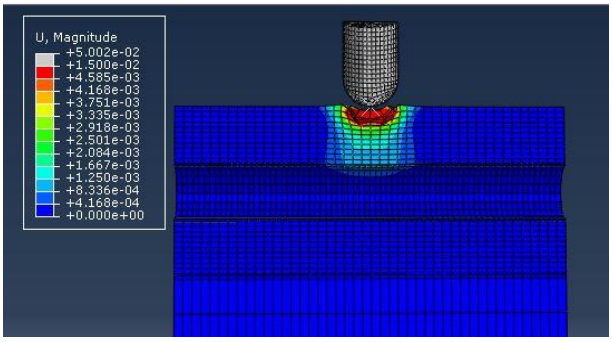

(a) Drop load = 17.6 kg

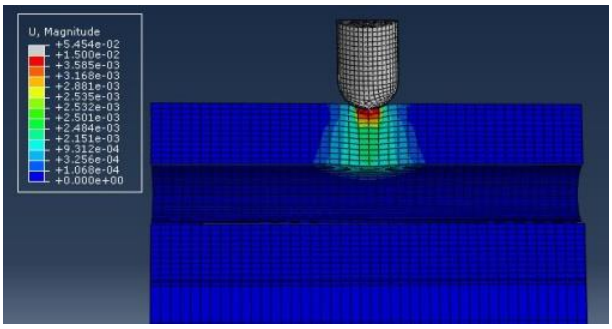

(b) Drop load = 15.0 kg

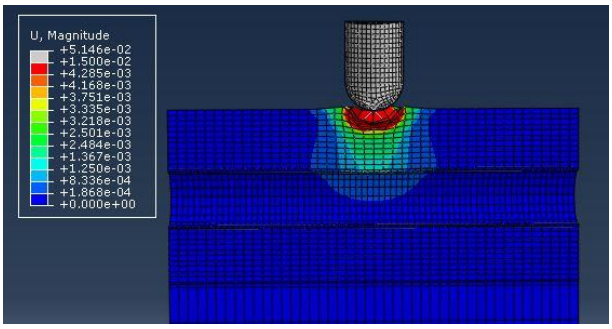

(b) Drop load = 20.0 kg

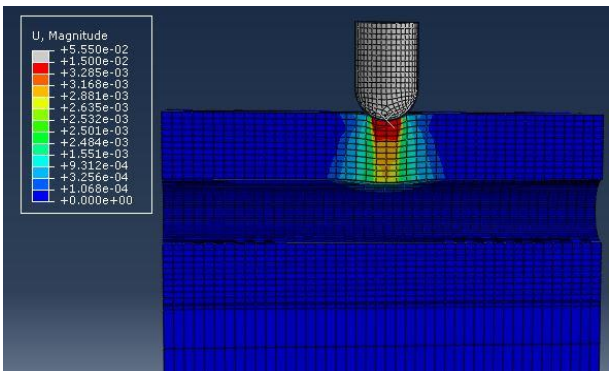

(c) Drop load = 20.0 kg

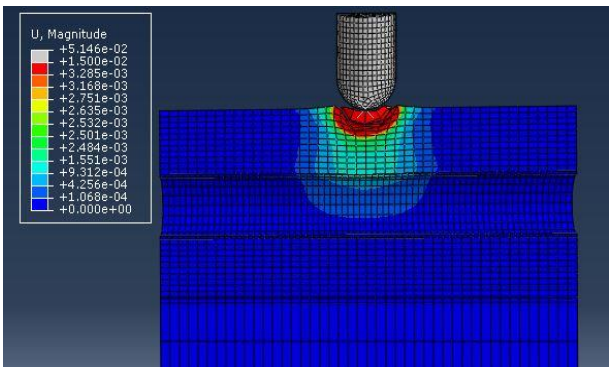

(c) Drop load = 25.0 kg

C/D = 1.0

Fig. 103. Deformation contours for unlined tunnels

Fig. 104. Deformation contours for lined tunnels

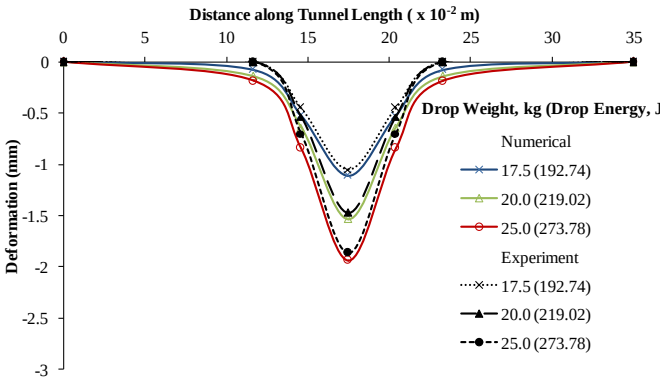

Fig. 105. Numerical validations for deformation in GM1 for lined tunnels (C/D = 1)

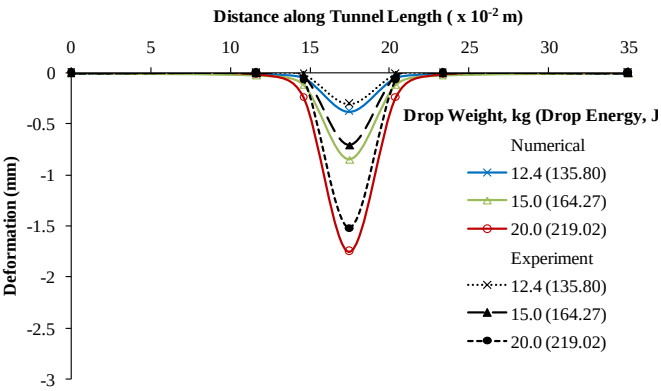

Fig. 106. Numerical validations for deformation in GM1 for un-lined tunnels (C/D = 1)

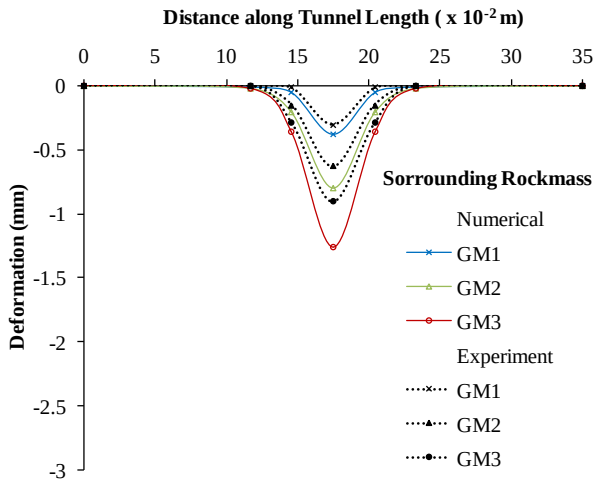

Fig. 107. Deformation profiles of lined tunnel for 10.0 kg drop weight (C/D = 1)

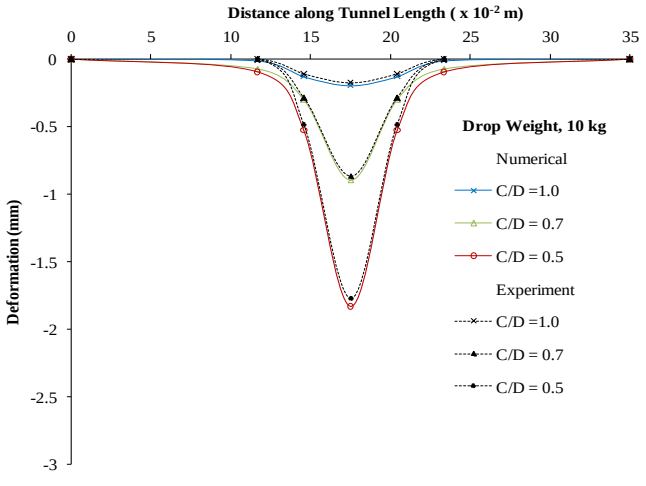

Fig. 108. Deformation profiles of unlined tunnel for 12.4 kg drop weight (for synthetic GM2 rock)

13.5 Impact and Blast Load Analysis in Prototype Models

Impact tests are conducted on a small-scale model in order to obtain the response characteristics of a geometrically similar full-scale prototype which is the actual purpose of interest. Chances of explosion inside an underground structure are very less because of sound technology that can detect the carrier of explosive material very easily inside the tunnel. On the contrary, external blasts are more prominent to occur and cause excessive destruction because of the difficulties in monitoring and preventing such activities.

In order to represent in-situ conditions, small models of laboratory are scaled up to predict field deformations of tunnels in weak or weathered rockmass. The response of a circular buried tunnel under dynamic loading of blast or sudden impact is analyzed. After adopting proper scaling laws, a 3D FE prototype model of surrounding rockmass and tunnel is modeled with dimensions 35 m x 30 m x 30 m using the Abaqus/CAE tool and the Langrangian elements. A 35 m long tunnel geometry with diameter of 5 m and thickness 150 mm have been prepared in rock domain of 35 m long and 30 m x 30 m cross section with the central axis of the tunnel placed at a depth of 5, 6 and 7.5m from the ground surface. In this study, four different TNT equivalents of 100, 250, 500 and 1000 kg is detonated at the surface where tunnel is passes at centerline, beneath the explosive charge under different cover depth with C/D ratio as 1.0, 0.7 and 0.5. In the numerical analysis, the small scaled models are scaled up to forecast deformation behavior of the lining as well as the pressure and velocity decay of the blast wave with time for real field in-situ condition. Pressure decay curve is plotted for different rockmasses (Fig. 109 (a)). From the Fig. 109 (b) it is observed that, immediately after surface detonation, shock waves are produced and attenuation started. A triangular blast pressure profile is analyzed. The area under the pressure time history curve is known as the impulse or the total work done by the blast waves. The positive time duration or positive impulse curve represents the permanent structural deformation and due to very small size of negative phase, it is neglected here.

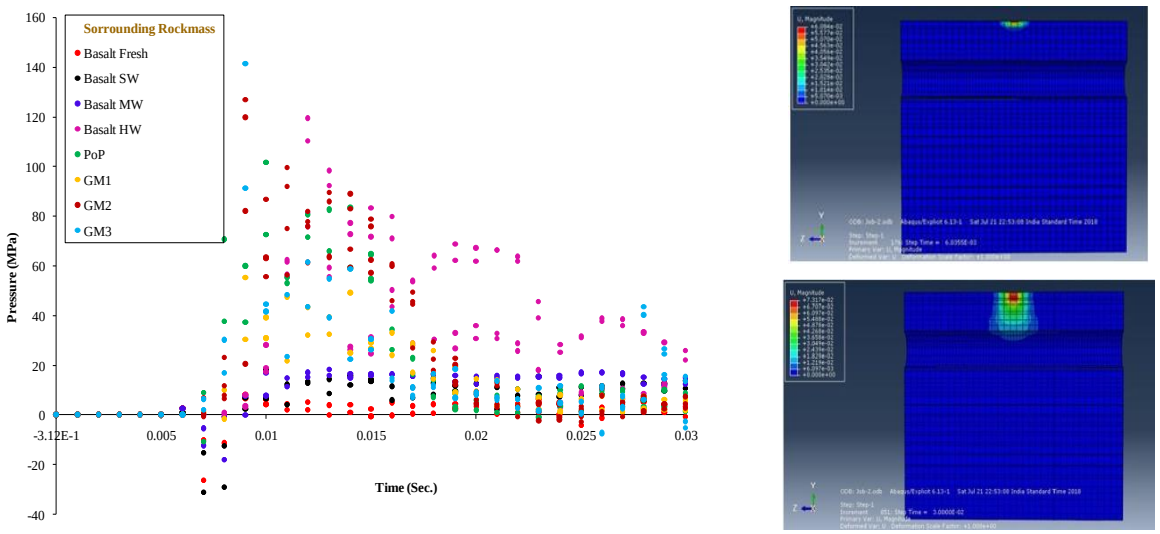

(a) (b)

Fig. 109. Pressure time history of geomaterials under surface blast with respective failure

Peak pressure for GM3 and other weak and weathered rockmass is high as compared to other strong rockmasses like Basalt (F), Basalt (SW), and GM1 etc. Apart from conducting detailed numerical modeling with varying parameters of shallow tunnels in soft rock, shape of the tunnel is also changed and dynamic response of lining is investigated for different cross-sections and impact and blast loads as shown in Fig. 110 (a), (b), (c) and (d). Fig. 110 (d) shows the comparison of experimental and numerical models for full deformed profile along the tunnel axis. From the analysis it has been concluded that deformation on the center of tunnel lining at 17.5 m distance along the tunnel length is maximum in case of D-shaped tunnel rather than circular shaped while in case of blast loads, deformation obtained on tunnel lining is maximum than impact loading in D-shaped tunnel and peak particle velocity of crown node increases as intensity of blast increases.

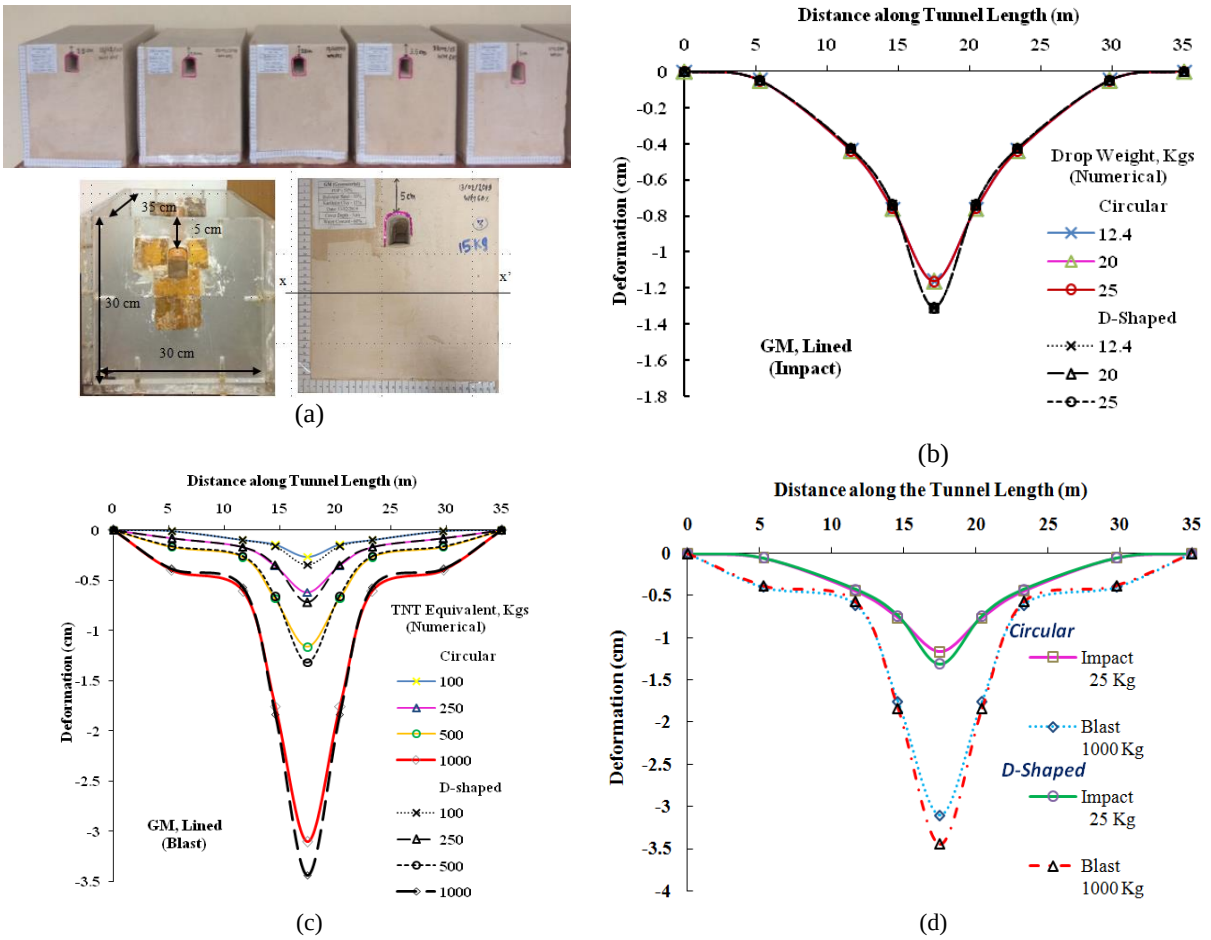

Fig. 110. D-shaped rock tunnel model subjected to impact and blast loads

13.6 Conclusions

13.6.1 Damage Profile

The deformations of lined and unlined tunnels are investigated and, it is observed that the tunnel deformation follows the Gaussian distribution along the length.

13.6.2 New Predictive Damage Model

The proposed new model is used for predicting deformation in the tunnel lining along the length, when tunnel gets impacted or hit by any drop weight at the surface or any surface detonation takes place. The correlation is presented as:

$$\frac{Ymax}{D} = \frac{\left(\frac{E'}{cD^3}\right)}{35.6}\left(\frac{1}{\frac{C}{D}}\frac{\frac{E}{c}}{10407}\right).012 \qquad (66)$$

where Y_{max} is the maximum deformation obtained at the point of impact loading (mm), D is diameter of tunnel (mm), C is cover depth (mm), E is elastic modulus (MPa), c is cohesion of surrounding rockmass (MPa) and E' is incident energy (J) which is equal to kinetic energy of drop hammer and is a function of mass of drop weight and velocity at the time of incident.

The proposed equation is in good agreement with experimental investigations and numerical simulations. Due to difficulty in undergoing gigantic experimental and numerical programme, the proposed equation provides an insight about the crown deformation in the tunnel and deformation to the surrounding rockmass. The empirical correlation is valid for all the weak and weathered rockmasses which are majorly found at the top cover.

13.6.3 Tunnel Crown Deformation with Cover Depth

Prototypes of rock tunnel assembly is created according to proper scaling laws and then subjected to both heavy impact loading and surface detonations. It is observed that the scaling of the velocity is very important to get the accurate results. It is found that the velocity of hammer in prototype is 2 times the velocity of hammer in the small scale model. It is also observed that the deformations of the tunnel crown in prototype are 100 times the deformations of the scaled model. The numerical investigation suggests that the deformation of the crown increases with increase in the blast loads. In this study, an exponential relation is developed to calculate the crown deformation under impact and blast loads. The proposed relation of U/C ratio with C/D ratio is expressed as:

$$\frac{U}{C} = Ae^{B\left(\frac{C}{D}\right)} \quad (67)$$

Where, U is crown deformation (mm), D is diameter of tunnel (mm), C is cover depth (mm), A and B are material parameters which depend on the type of loading. These parameters can be calculated by conducting the experimentation on the small scale models.

The results obtained from this study suggests that the proposed methodology in understanding the behavior of shallow tunnels in fragile ground conditions has the potential to provide useful information to the engineers before undergoing designing of blast resistant underground structures.

13.6.4 Shape of the Tunnel

It can be concluded that in case of impact as well as blast load, circular shaped tunnel is more stable than D-shaped tunnel as it undergoes less deformation observed on center part of lining by dropping a maximum impact load of 25 Kg and 1000 Kg blast load of TNT. Zone of influence and stress around the tunnel increase as impact energy increases.

13.6.5 Crack Pattern of Rock Tunnel Model

Due to punching action at the point of loading, the rockmass gets sheared at the upper inner face of the tunnel, while the lower inner tunnel surface remains unaffected. The extent of the tunnel length that gets affected depends on different factors like cover depth, intensity of drop loads, and mechanical strength of the surrounding rockmass. Tunnel shows maximum deformation at the time of hitting and after some time it becomes constant and shows the permanent deformation.

13.6.6 Validation of Numerical Simulations

It is worth to mention that for high cover depth of 50 mm and 35 mm, deformation values of experimental and numerical results are similar. For lined tunnels with varying surrounding rockmasses and drop energies, the difference between the ranges of deformations obtained numerically is 2 and 7% more than that of the deformations obtained experimentally. This difference is larger in the case of unlined tunnels. Particularly for unlined tunnels with C/D 1.0, in GM1 material difference varies from 10-15%. Similarly for C/D 0.7 and 0.5 this difference is 12-15 % and 15-25% respectively.

14 Case Studies

14.1 Stability Analysis of Jointed Rock Slopes of Chenab Bridge Abutments

Two iconic railway bridges were proposed to construct to cross River Chenab in the state of Jammu and Kashmir, India. Global stability of both the bridges was assessed and one of them is discussed herein. The Chenab Bridge, once it is constructed, would be the highest bridge in the World at a height of 359m from the river bed level. The 1,263 m long bridge consists of 950 m span steel arch over the river, in tandem with a 313 m long viaduct up to Salal road ‘B’ station. The bridge consists of total 18 piers. The loads exerted by these piers would affect the stability of the slopes. Apart from this, as the site falls under seismic zone V as per seismic zonation map of India, the seismic loads were also considered in the analysis from a site specific study. The hill slopes are carved due to the persistent geological processes with large nallahs and steep natural slopes. 2D and 3D analyses using UDEC and 3DEC were carried out for predicting the behaviour of the jointed rock slope of the abutments of the Chenab bridge. Extensive field and laboratory studies were also conducted for the physic-mechanical properties of rockmass.

The studies by Rao (2009) and Rathod et al. (2011, 2012) provide an illustration of how the geo-mechanical properties of a rockmass can be integrated in a discontinuum rock slope model. This model has helped to better understand the dynamics of the rockslide when subjected to static and dynamic loads.

14.1.1 Field Observations

Several field visits were made to the construction site to gather geological and structural observations. The sites where several direct shear and plate load tests were conducted in the drifts were also visited and specific observations were made on the failed rockmass. A special visit was also made to the riverbed in order to observe the geological nature of strata between toe and below the proposed arch foundation on both the abutments. The abutments of the proposed bridge across Chenab are shown in Fig. 111 (a) and the strata on right abutments in Fig. 111 (b).

(a) (b)

Fig. 111. (a) Abutments of proposed Chenab bridge (b) Strata on right abutments

14.1.2 Geological and Structural Features

The railway alignment passes through the Shiwaliks and Pre-Tertiary rocks overlain by unconsolidated sediments of recent to sub-recent periods. The primary lithological units are dolomitic limestone with different degree of fracturing and occasional weathering. Cherty, bouldery, brecciated and massive dolomite or dolomitic limestone of Sirban formations are mostly present in the area. The top layers are moderate to highly weathered but invariably the dolomite is fractured resulting into blocky mass. Mapping with reference to the alignment on the left and right abutments yielded that the strata are characterized by prominent sub-horizontal foliation joint and two sub-vertical joints which are very pronounced sets. Few random joint sets are also present occasionally. Foliation planes and other joint sets are very clear in the drifts made in the left and right abutments at expected arch foundation levels. Presence of minor shear zones was noticed and the fracturing was more in the right abutment. The close up view of the joints in dolomitic strata for left abutment is shown in Fig. 112. Extensive large scale direct shear tests along the 3 sets of joint planes and triaxial laboratory testing was carried out for appropriate parameters for the stability modelling studies.

Fig. 112. Close up view of the 3 sets of joints (J1, J2, J3) in Dolomitic rock on left abutment

14.1.3 Numerical Modelling

Since the height of slope is high and the site falls under very active seismic belt, it was decided to analyse the slope numerically to investigate the stability of slope which comprises of rockmass that could potentially slide under static and dynamic forces. The distinct element method (UDEC) simulates the progressive failure of slopes using an iterative calculation procedure (Rao, 2009). UDEC and 3DEC numerical codes utilizes a Lagrangian calculation scheme to model large movements and deformations of a blocky system, allows for modelling of complete detachment of rigid or deformable discrete blocks. The analysis was carried out in two stages. To simulate the prevailing rockmass conditions at the site first, an initial static loading is applied in the numerical model by introducing the joint sets in the rock slope. Then the pier and arch loads were applied on the existing model. For critical observations of displacements, stresses and velocity various monitoring points were installed in the model. The resultant values observed confirms the stability of the rock slope. Fig. 113 and Fig. 114 show the jointed slope models for UDEC and 3DEC for left abutments respectively. For dynamic calculations, user-specified velocity or stress waves can be input directly to the model either as an exterior boundary condition or interior excitation to the model.

14.1.4 Conclusions

The numerical analyses were carried out using UDEC and 3DEC considering joint sets and stiffness characteristics of large slopes of both abutments. Both static and dynamic analysis were carried out under various loading conditions. A critical observation was attempted at arch foundation. The dynamic cases were considered to be the most critical. The shear displacements, shear velocities, shear stresses, XX and YY stresses at all monitoring points, show that the slopes are stable in static

and dynamic conditions. The analyses revealed the slopes are stable with respective factor of safety under various loading conditions. A detailed long term stability measures including drainage system were suggested (Rao, 2009). Long term slope monitoring through surface and subsurface instrumentation programme during and post construction was recommended. The study cleared the way for the construction of world's highest Chenab Bridge.

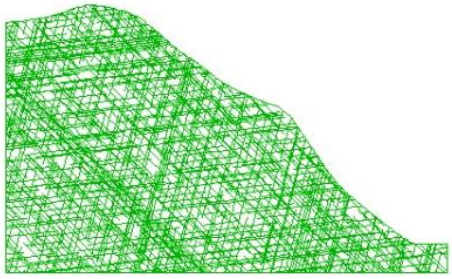

Fig. 113. UDEC model for left abutment

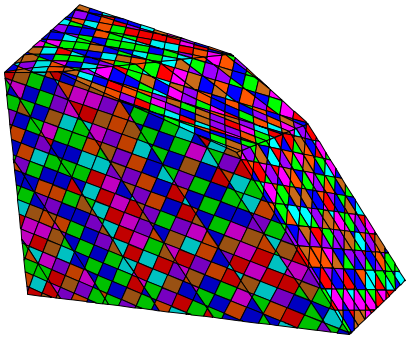

Fig. 114. 3DEC model for left abutment

14.2 Subansiri Power House Slope Stability

The Lower Subansiri Hydroelectric Project is a 2,000 MW project located in the states of Assam and Arunachal Pradesh, India. The project site falls in the very active seismic belt (zone V) of the Himalayas. The project envisages generating 2,000 MW (8 x 250 MW) of power utilizing 100 m of maximum gross head through a 133 m high concrete gravity dam.

The partly constructed and excavated power house slopes of Subansiri Lower Hydroelectric Project experienced extensive collapses through complex mode of failure. A detailed study was carried out by Rathod and Rao (2012) to understand the reasons for the failure and assess the stability of the existing constructed slopes using limit equilibrium and FEM solutions and also to propose modified design for rebuilding the slopes. To take into account the uncertainty associated with the rock-mass and soil properties, probability and reliability analyses were also carried out. Based on the field observations and stability analyses of the natural and cut slopes, suitable support and drainage system was proposed to meet the stability requirements.

14.2.1 Geology of the Area

The power house area comprises of fine to medium grained grey coloured sandstone of middle Shivalik formation. Occurrence of quartzite pebbles, coal patches and concretion of boulders and pebbles is also a significant property of the rock of this locality (Rao 2008). In this area, moderate to highly sheared and fractured rockmass is present, which is the continuation of the major slide plane in this area. The fresh sandstone is massive and compact but occasionally it is weathered to different degrees. Along with several sets of joint planes clay fillings and rock penetrative weathering also observed along the discontinuity planes. Several sets of major and minor joints and fractures are present in the rockmass. The joint planes are tight to partially open with occasional clay and carbonaceous filling. Apart from these joints, a major thick shear zone is also encountered at different elevations of the slope. The soft material, steep slopes, high water precipitation, several sets of prominent joints and presence of major shear zones culminated into a complex geological setting at the surface power house area.

14.2.2 Observed Failures and Reasons

In August 2006, some cracks were observed on the constructed slopes of the power house, which was alarming to the whole project. So, a keen monitoring programme was initiated to observe the load in rock anchors, displacements and pore pressure by installing load cells, multiple extensometers, inclinometers and piezometers. The slope of power house before failure is shown in Fig. 115 (a) and after failure in Fig. 115 (b). Deformation of the rockmass was monitored with an array of multiple-point borehole extensometer (MPBX) systems. Two sets of shear zones, one dipping along and the other against the slope were present and the slope failures were due to the shear zone inclined along the slope. The shear zone material was brownish and highly weathered condition.

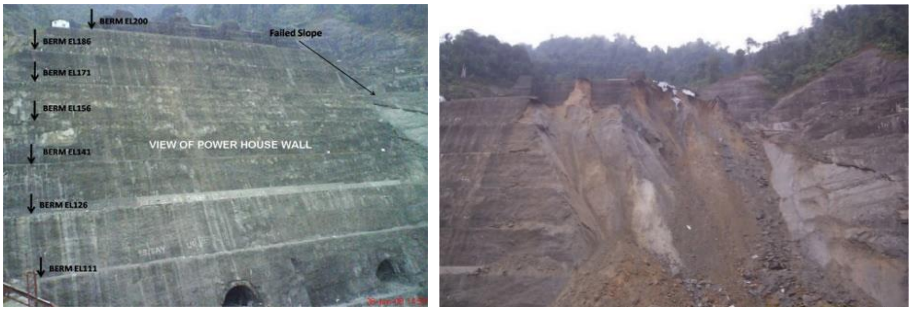

Fig. 115. A view of power house slopes (a) before failure and (b) after failure

14.2.3 Assessment of Slope Stability

Limit Equilibrium (LE) along with reliability analysis as well as Finite Element Method (FEM) have been used for the analyses. To take into account the heterogeneity of the rockmass and soil, probability and reliability analyses have also been carried out. A total of 8 sections of slopes at each power shaft (PS1 to PS8) were selected for the analysis. In the absence material properties, a back analysis has been carried out to decide the best suitable material properties reflecting the rockmass and shear zone in the field. Then the analyses were carried out separately on the existing and modified slope profiles with suitable support system (Rathod and Rao, 2012).

14.2.4 Proposed Design

Two out of eight slope sections were apparently stable, however, the analyses revealed that these two slopes are highly prone to failure. Hence, a new slope design was proposed for all slope sections. The support system was designed using grouted rock bolts, steel fibre reinforced shotcrete and weldmesh (Rao, 2008). The length and spacing of the bolts were fixed based on several trials to achieve the stability requirements. The details of all failed and modified slope sections are given in Fig. 116. Elaborate drainage control measures were also suggested for the long term stability of the modified power house slopes.

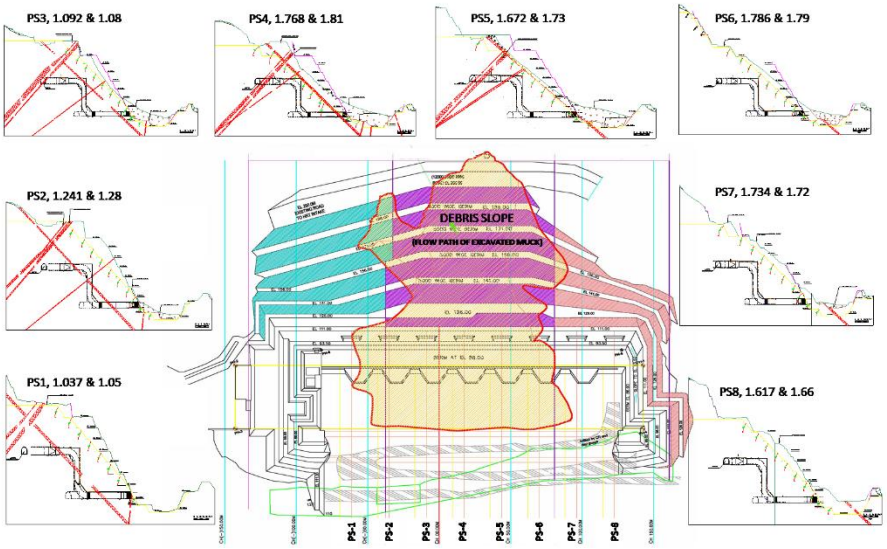

Fig. 116. Debris slope (Flow Path of Excavated Muck) and all slope sections with FoS (Mean) and SRF Values (Rathod and Rao, 2012)

14.3 Tindharia Landslide in Darjeeling Himalayas

The site (26°51'14.55" N & 88°20'13.12"E) is located along National Highway 55 (NH 55) in the Darjeeling district of West Bengal, within the upper most Shiva Khola catchment of Mahananda River. The World Heritage Derjeeling Himalayan Railway (DHR), built in 1880, runs along NH 55 with its' workshop at Tindharia. The site location is shown in Fig. 117.

Tindharia landslide was triggered by the 18th September 2011 Sikkim earthquake of Mw 6.9, having epicenter at Taplejung (27°21'0" N & 87°40'0"E) in Nepal. After the initial earthquake -induced slope failure, a series of slope failures triggered by heavy rainfall occurred on 27th September 2011 and on 28th September 2011. The slope failure also occurred in the next monsoon on 19th July 2012. Fig. 118 shows the site photographs after slope failure.

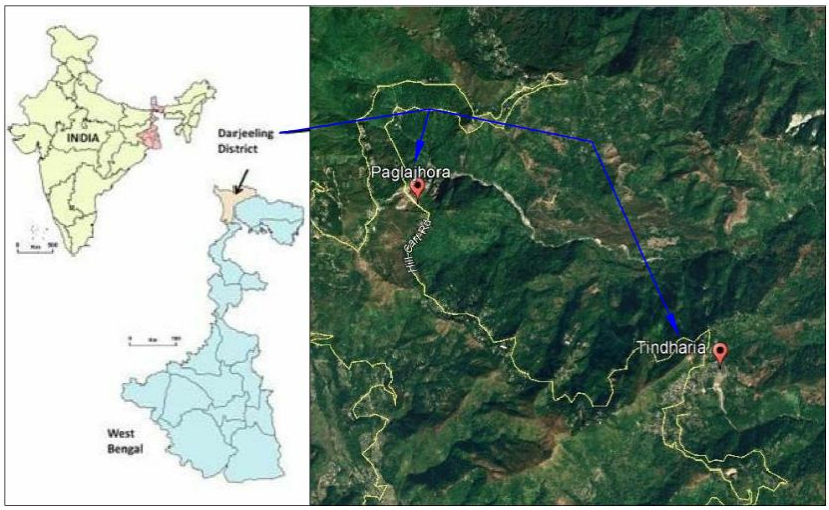

Fig. 117. Site location

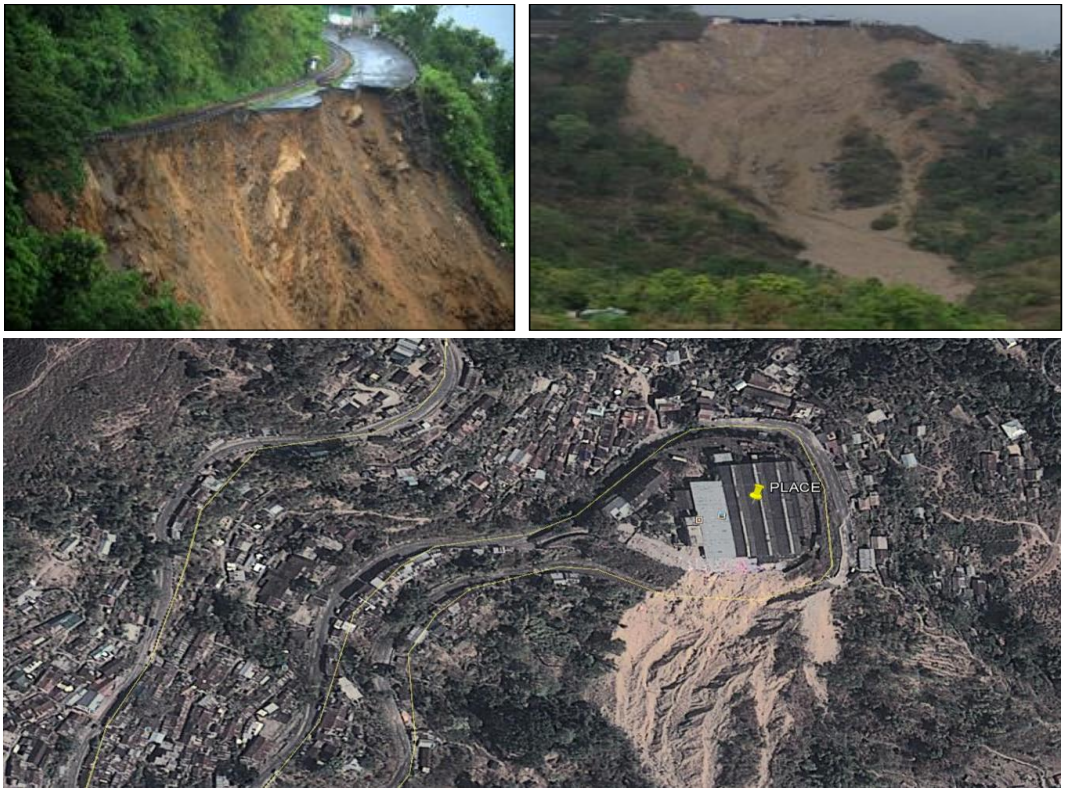

Fig. 118. Tindharia landslide site

14.3.1 Topography

The young mountain land slope in this region is characterized by steep slopes and narrow deep valley. In the lesser Himalayas towards south, the slope is gentler and in the undulating stretches, numerous streams and rivulets flow along the depressions and finally join with the trunk streams.

The topographic survey was carried out in the study area by using Total Station. Satellite Imagery of the study area was also collected to prepare DEM (Digital Elevation Modelling) and other maps like elevation and slope map (Fig. 119). The slope and elevation at the site vary from 30^0-45^o and 600-800m respectively. Fig. 120 shows the slope geometry before and after failure. The original ground profile before failure has been developed from Survey of India (SOI) topo-sheet of the study area (surveyed in 1964-65).

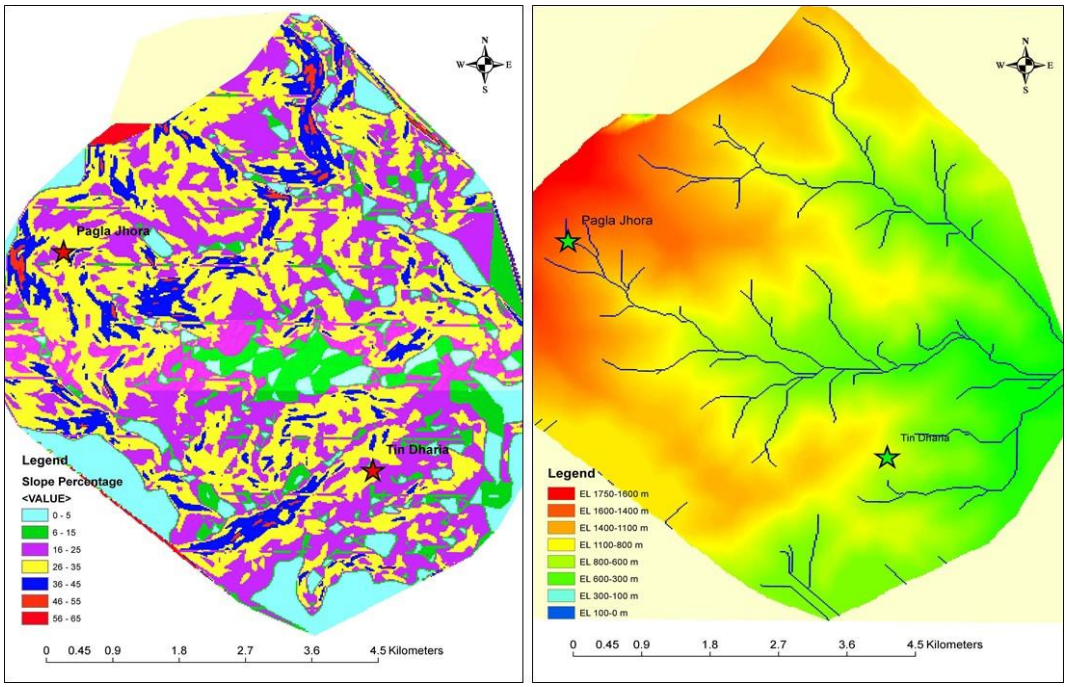

Fig. 119. Site topography (a) Elevation and (b) Slope map

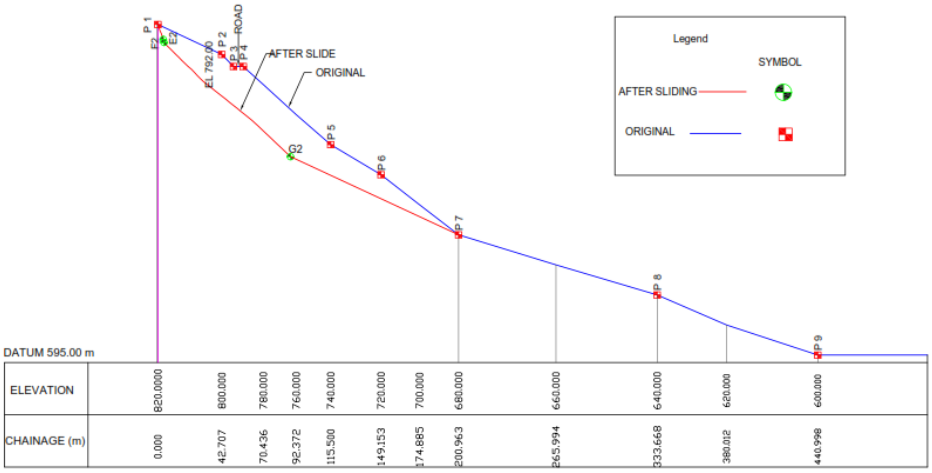

Fig. 120. Slope profile of Tindharia

14.3.2 Geological and Geotechnical Investigations

The slide scar is very steep (50°-60°) and undulatory depending upon the competency of rockmass exposed along the scar. Both the arms of the slide are conspicuous and represented by scarp faces. Mainly sandstone, shale, pebble bed with coaly shale of Gondwana Group are exposed at the slide scar. However, shale and coaly shale are exposed majorly at the bottom part of the slide. The bedding/ foliation of the rocks is N70W-S70E with dip 50° towards N20°E i.e. dipping into the hill. The exposed rockmass also contains three prominent joint planes. Geological sections are shown in Fig. 121. Geotechnical characterization of the site was also done by means of 10 boreholes to derive geotechnical properties of the slope material.

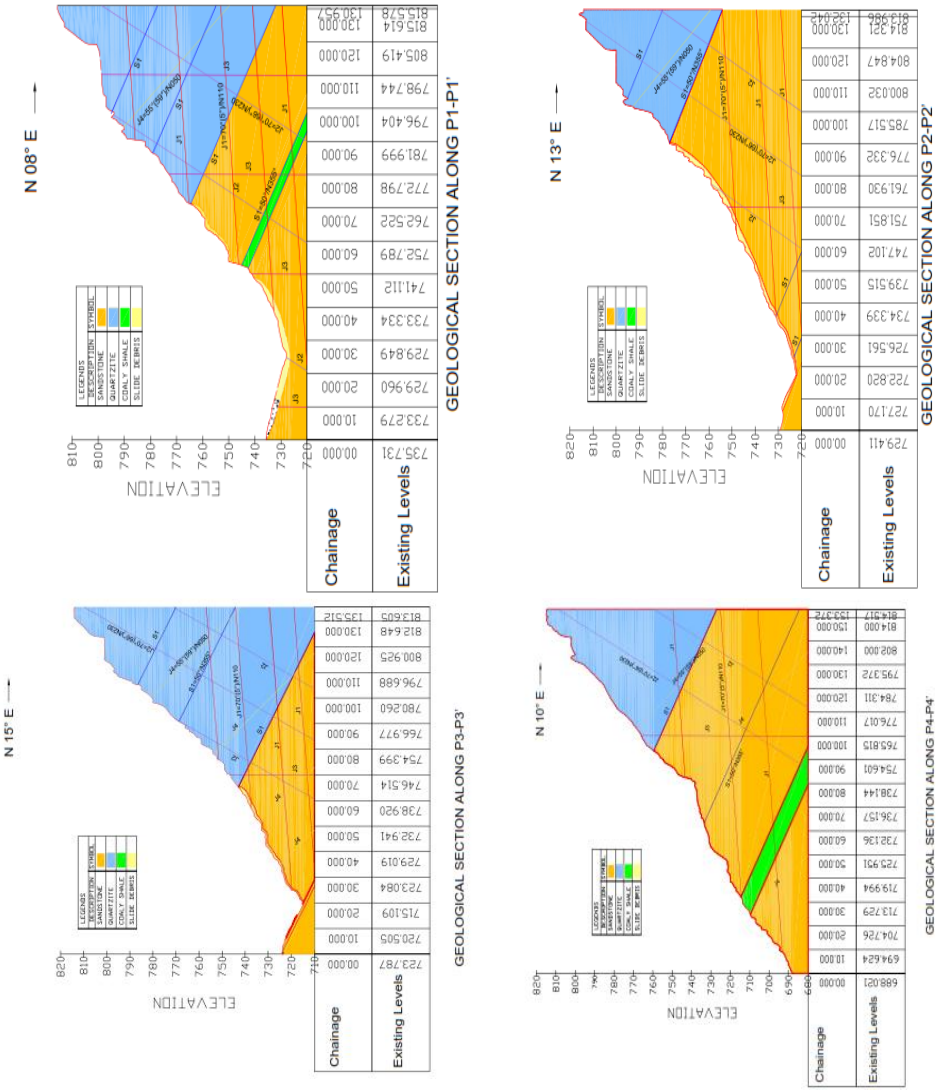

Fig. 121. Geological Sections of Tindharia Slide Area

14.3.3 Hydrological Studies

The study area receives heavy rainfall ranging from 2000mm to 4000 mm per year. Determination of design rainfall is an important requirement for the study of rainfall-induced landslide. Intensity-duration-frequency (IDF) analysis was carried out by using long term hourly rainfall data from IMD. The design rainfall intensities for 1-hour duration rainfall thus obtained are 53.4 mm and 92.5 mm respectively for return period of 1 year to 100 years.

Considering long monsoon with continuous rainfall, having frequent high intensity storms like cloud bursts, following aspects of rainfall has also been studied:

i. The effect of raindrop impact force in increasing the destabilizing force initiating landslides
ii. Generation of pore water pressure due to raindrop impact thus reducing shear strength of soil and causing liquefaction type failure.

Tipping bucket rain gauge and vibrating were piezometer were installed to continuously monitor rainfall and pore water pressure. For raindrop impact force measurements an equipment was designed and fabricated to continuously record, at desired frequency, the impact force in grams. The fluctuation in ground water level was monitored by measuring water level in standpipe using a water level indicator.

The study confirmed that antecedent rainfall plays an important role in landslides in this region. Ground water variation is negligible even after heavy rainfall. Perched water table is formed at the top surface, depth of which depends on rainfall intensity and soil permeability. High pore water pressure due to raindrop impact force was recorded within this perched water table, which is probably the cause for frequent shallow slides during intense rainfall.

14.3.4 Seismicity

The study area lies in the Darjeeling Himalayan region belonging to the unstable intercontinental plate system and falls in Zone IV of IS 1893 (Part I):2016. Considering very heavy and long monsoon in the eastern Himalayas along with high seismicity, there is high probability of earthquake when the soil is already saturated by continuous antecedent rainfall.

Site specific seismicity study has been done to derive the seismic design parameters. The PGA values for the site estimated at rock level for 475 years and 2475 years return periods are 0.15g and 0.26g, respectively. Dynamic pore water pressure due to earthquake has been evaluated duly considering sloping ground conditions and design earthquake magnitude.

14.3.5 Slope Stability Analysis

Geological profile, developed from geological and geotechnical investigations and as shown in Fig. 122, has been used in stability analysis (Kundu, 2019). The design parameters for various materials in the slope were obtained from extensive laboratory and field test results. Analysis has been performed by deterministic approach and results have been compared by both limit equilibrium and numerical methods of analysis. To investigate the causes of failure, analyses have been performed considering the geometry of original slopes before failure for dry, wet and saturated conditions, with and without earthquake. The summary of results is presented in Table 14.

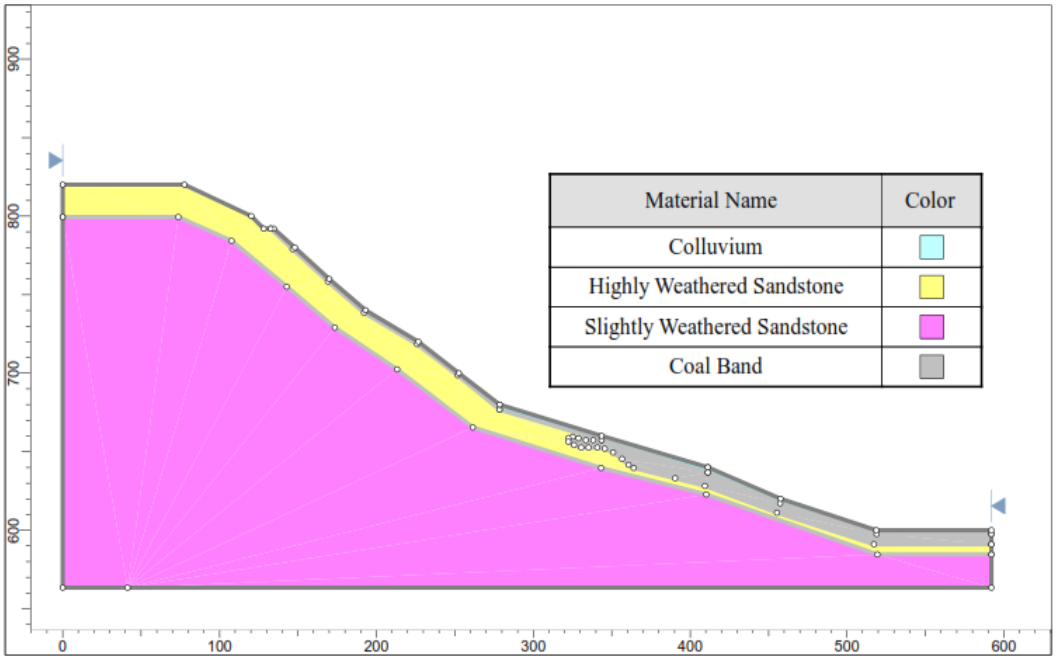

Fig. 122. Design slope profile of Tindharia

Table 14. Summary of analysis for Tindharia slope

Combination Type	FOS	
	Slide	Phase[2]
Wet Slope	1.42	1.37
Wet + Earthquake	1.18	1.10
Saturated Slope	0.86	0.81
Saturated Slope +Earthquake	0.67	0.73

The analysis confirmed that the failure was initiated by the Sikkim earthquake during which the softer coal band present at the toe of the slope failed, thus destabilizing the entire slope, which probably started moving thereby reducing the shear strength of the material to residual strength which subsequently failed during intense rainfall of 27th and 28th September. Cracks formed in the road bench accelerated the failure since it got filled with water adding to destabilizing force due to hydrostatic pressure. The overburden failure caused by intense rainfall propagated deep into the highly weathered rock. The failure surface was a combination of circular in overburden and planar and wedge in weathered rock.

14.3.6 Conclusions

A detailed study was carried out to understand the failure mechanism of earthquake and rainfall induced landslide in Darjeeling Himalayas. The study confirmed that antecedent rainfall and earthquake induced pore water pressure play important role in frequent landslides in the region. Drainage improvement and afforestation, instead of structural measures, are the most appropriate mitigation measures for such shallow landslides in that region during intense rainfall.

14.4 Evaluation of Bored Tunneling Practices in Rocks for Delhi Metro

Heavy Rail, Mass Rapid Transit system is being implemented in India at Delhi. For implementation of the full scheme, the project is being executed in different phases viz. Phase-I, Phase-II and Phase-III. The Phase-I of the project, consisting of 13.7 km of underground corridor with 47.5 km of elevated and 4.5 km on surface corridors. The underground metro corridor is from Vishwavidyalaya to Central Secretariat and from Connaught place to Mandi house. Kashmere gate, Delhi Main, Chawri bazar, New Delhi, Connaught place and Patel chowk are the other important stations situated in between Vishwavidyalaya and Central Secretariat stations (Fig. 123). These stations are linked either by cut and cover tunnels or by bored tunnels.

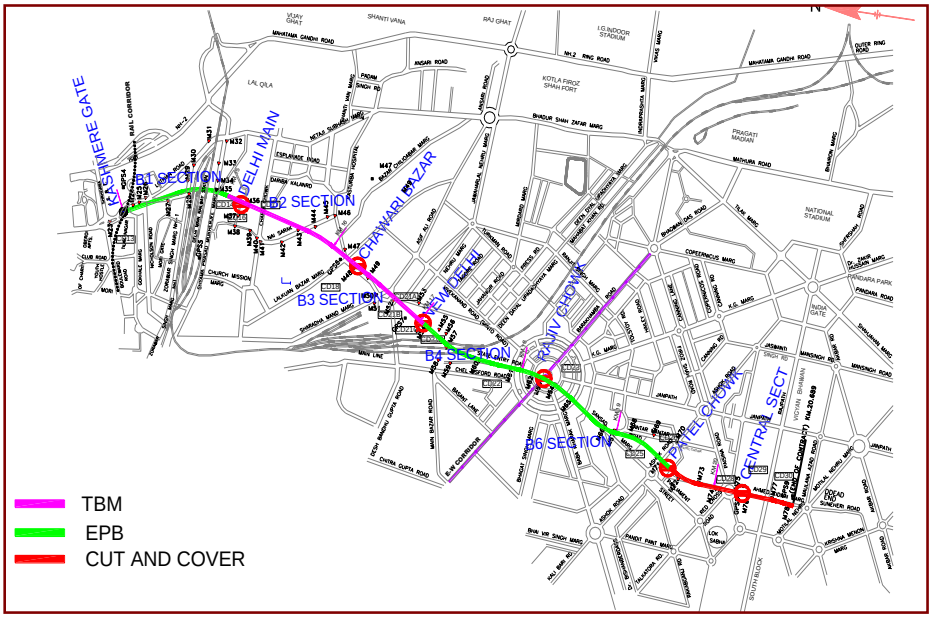

Fig. 123. Phase-1 Delhi metro project from Central Secretariat to Kashmere Gate

The Tunneling in rock by using Tunnel Boring Machine (TBM) has been carried out on the project between Delhi main and Chawri bazar. The schematic diagram of the area along with layout of end stations is shown in Fig. 124. The machine operation and grouting requirements were kept as these were being kept for the tunnels driven in alluvium. The experiences of tunneling with dual mode TBM in rocky strata is very limited. Therefore, design of TBM for the project was a difficult task. A detailed field and laboratory studies have been carried out in order to evaluate geological medium, the correlations suggested by various scientist between the properties of rock materials and rockmasses by using indices viz. RMR, GSI and weathering index (Rw) have been used to find out the strength and elastic parameters of rockmasses from laboratory test results.

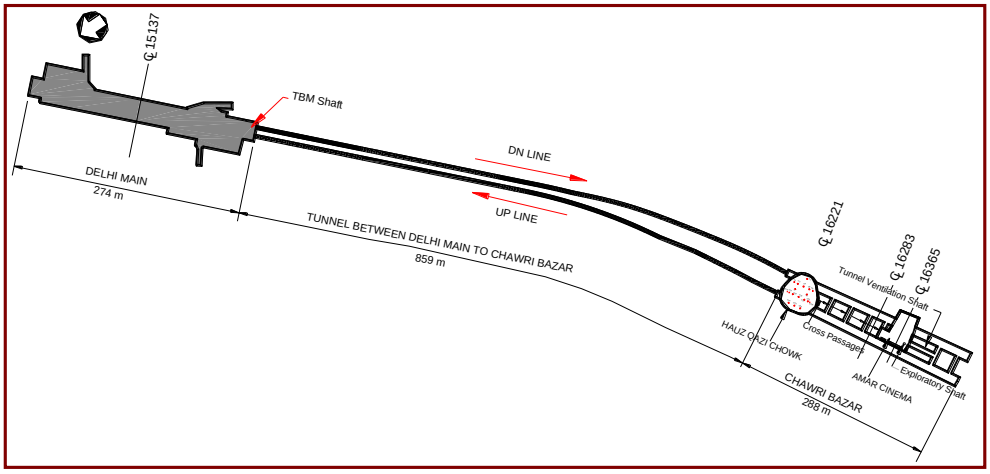

Fig. 124. Location map of Delhi main and Chawari bazar stations along with tunnels

A detailed analysis has been carried out on the basis of evaluated properties of rockmass in the area to study the response of the tunneling. The properties of alluvium (Delhi silt) have been adopted as reported for the project (DMRC, 2002). The tunneling operation can be reviewed particularly simultaneous grouting with advancement of machine. The review of tunneling operation in such conditions and evaluation of geological media are described below.

14.4.1 Geological Conditions

The analysis of tunnels in rocky strata is generally carried out by Distinct Element Methods by simulating joint geometry. In some cases the analysis is done by treating medium as continuum incorporating the effect of joints in the form of reduction factors for strength parameters. Detailed field study of rockmass encountered during excavations at Delhi Main and Chawri Bazar indicated that the rockmass is highly weathered and extensively jointed. The modeling of the tunnels in such media by Distinct Element Method was not found to be reasonable as simulation of joint geometry and its condition is very complex and difficult to simulate reasonably. Therefore, the only option left is to evaluate the media for engineering parameters of the continuum (rockmass) with the help of several test procedures developed by different researchers in the past to characterize the rock materials. Rockmass Rating (RMR) by Bieniawski (1989), Geological Strength Index (GSI) by Hoek and Brown (1997) and Weathering System (R_w) by Rao and Gupta (2001) are some of the useful methods for predicting the strength and deformation response of jointed and weathered rockmass.

14.4.2 General Geology and Hydrogeology

The general geology of the 1485 sq. km of Delhi is interesting on account of its being the end of exposed Precambrian Aravalli mountain ranges trending NE in this area (Fig. 125). The terrain is generally flat except for a low NNE-SSW striking Delhi ridge lying in the central portion of the region. The rocks of Delhi belong to the Delhi super group consisting of the Ajabgarh and the Alwar series. These rocks have undergone multiple folding and different phases of metamorphism (Rao, 2003).

The rocks, which outcrop in some parts of the city forming the ridge, comprise of quartzite and ortho-quartzite interbedded with thin intercalations of micaceous schist. The quartzitic rock has several sets of joints and exposed to different degree of weathering states. The general strike of the rock has been observed as N10°E with a dip ranging from 40°-80° towards both west and east directions. Though the fresh quartzite is grey in colour with weathering of iron oxides present. The rock becomes reddish in colour. The mica is sericitised and plastic in nature when mixed with water. At many places the quartzites are covered by recent alluvium. The water table in the area was very high, varying from 1-2 m below ground level.

Field Study

Comprehensive field study had been done for the rocks along the alignment for evaluation. For physical, elastic and strength parameters, a comprehensive laboratory testing has been carried out for the rockmasses of varying degree of weathering in the rock laboratory of IIT Delhi. The rockmasses have been exposed to different degree of weathering and jointing. Detailed joint mapping (scan line survey) which included observations related to orientation, spacing, condition, infilling etc. was carried out in different traverses. Five field parameters, viz. (i) discolouration and staining (ii) texture and fabric (iii) disintegration (iv) decomposition and (v) relative strength, has been used to recognise different weathering grades as suggested by Rao and Gupta (2001). The six weathering grades (W_0, W_1, W_2, W_3, W_4 and W_5) suggested by ISRM (1981) have been converted into three weathering grades viz. R_1, R_2 and R_3. These rockmasses are slightly to moderately, moderately to highly and highly to completely weathered quartzite respectively.

Based on data, it is found that there are four sets of joints/bedding planes present in the region. The orientation of the principle discontinuity set S_1 correlates with the general regional tectonic trend usually observed for the Alwar series, showing steep dips towards easterly directions. The joint sets viz. J_1, J_2 and J_3 is steeply dipping towards south. After careful study of

the core boxes and data of bore hole logs between Delhi main and Chawri bazar stations, the data has been processed in 'Data Mine' software in order to have wire frame, but the wire frame could not be prepared due to insufficient data.

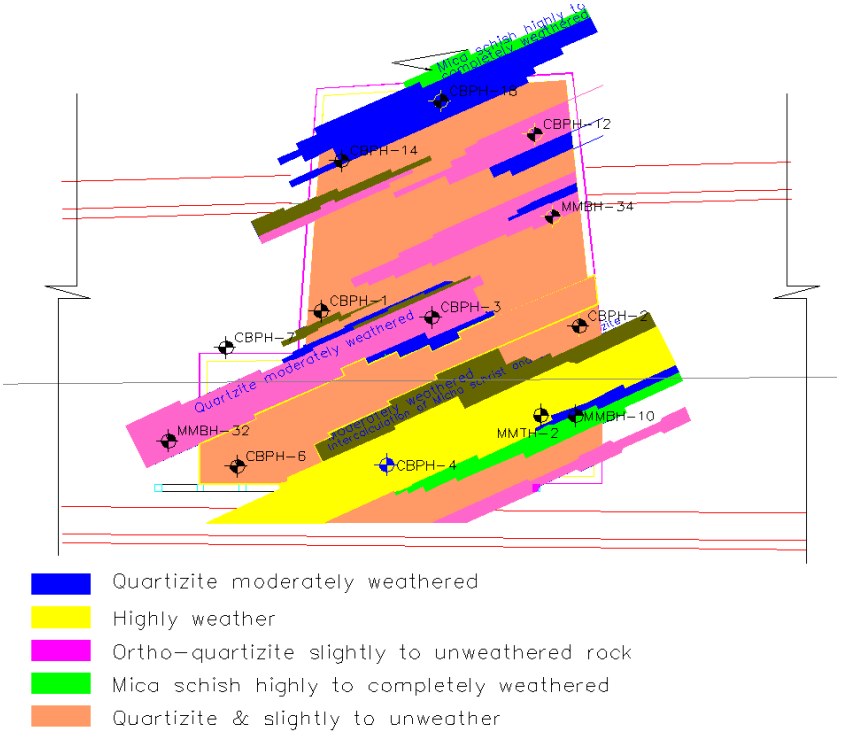

Fig. 125. Quartzite rock in different degree of weathering states at Chawari bazar station (Yadav, 2005)

14.4.3 Laboratory Studies

Physical Properties

The physical and mechanical properties were determined on samples of different degree of weathered quartzites. The strength indices gradually decrease with increasing degree of weathering. The Brazilian tensile strength (crib) values in dry and saturated conditions vary from 8.15 to 1.20 MPa and 7.45 to 1.08 MPa for R_1, R_2, R_3 and R_4 categories of quartzitic and mica schist rocks respectively.

The uniaxial compressive strength (rye) value for fresh to slightly weathered quartzite (R_1) is the highest with a value of 40 MPa followed by 28 MPa for R_2 and 10.50 MPa for R_3 category of rockmass. The lowest values of 2.5 MPa is observed for mica schist (R_4). The values of tangent modulus, (E_t) determined from the stress-strain curves (UC test) at 50% of the failure load in saturated and dry states for the rocks. The trend in variation in E_t values for different samples is similar to that observed for σ_c. Based on Deere and Miller (1966) classification the R_1, R_2, R_3 and R_4 rockmasses can be classified as CH, EH, EH and EM classes respectively.

It is clear that the failure strength increases with the increase of confuting pressure and the least weathered quartzitic rock (R_1) shows the highest values than more weathered ones at all σ_3 values. The a1 value gradually decreases with increase of weathering. The variation between al and σ_3 is observed to be non-linear and the rate of increase of al declines with increase in σ_3.

14.4.4 Classifications of Rockmasses

The rockmass rating (RMR) by Bieniawski (1984), Geological Strength Index (GSI) by Hoek and Brown (1997) and Weathering Classification System by Rao and Gupta (2001) have been considered more relevant in the prevailing site conditions for predicting the strength and deformation responses of jointed and weathered quartzitic rockmasses. The Ratings are evaluated for different classification systems (Yadav, 2005).

Strength and Elastic Parameters of Rockmasses

Evaluation of the strength and deformational behaviour of rockmass is very important for the design of tunnels in such masses. In this study, the strength prediction model suggested by Rao (1984) has been used. The material constants have been evaluated for the intact rock on the basis of triaxial test results. The material constants for rockmass were obtained from weathering index R_w, of Rao and Gupta (2001) correlations. Young's modulus (E_t) of rockmasses have been evaluated. The predicted values of modulus for R_1 and R_3 categories of rockmasses from Hoek and Brown (1997) and Rao and Gupta (2001) are same therefore, they are being recommended for these rockmasses. For R_2 category of rockmass the average value from both the methods has been adopted.

14.4.5 Analysis of Tunnels in Rock by Finite Difference Method

Finite Difference Method is perhaps the oldest numerical technique used for solution of sets of differential equations for given initial values and/or boundary values (Desai and Christian, 1977). In finite difference method every derivative in the set of governing equations is replaced directly by an algebraic expression written in terms of field variables (e.g., stress or displacement) at discrete points in space. These variables are undefined within elements. In contrast finite element method has a central requirement that the field variables (stress, displacement) vary throughout each element in a prescribed fashion using specific functions controlled by parameters. The formulation involves adjustment of these parameters to minimize error terms or energy terms. Both methods produce a set of algebraic equations to solve. Even though these equations are derived in quite different ways it is easy to show (in specific cases) that resulting equations are identical for the two methods. Wilkins (1964) presented a method of deriving difference equations for elements of any shape. The finite difference code developed by ITASCA (2000) on the basis of Lagrangian Analysis of Continua (commonly known as Fast Lagrangian Analysis of Continua, FLAC) has used this approach. In this study, the analysis of two-dimensional (ITASCA, 2000) code has been used.

Numerical Formulation in FLAC

FLAC's formulation is conceptually similar to that of dynamic relaxation (Otter et al., 1966) with adaptation for arbitrary grid shapes, large-strains and different damping types whereas finite difference method follows the approach of Wilkins (1964).

Analysis of Delhi Metro Tunnels in the Rock

The FLAC 2D analysis designated as primary (4,5,6 and 7) secondary (451, 452, 561, 562, 671 and 672) are considered for the analysis. Therefore, altogether ten reference lines have been identified for representative evaluation of response for the tunneling in the area. The analysis has been carried out for various values of face loss varying from 1.0 to 5.0 percent at sections corresponding to above mentioned primary and secondary reference lines. The results obtained from the analysis for the maximum ground surface settlements have been compared with observed values.

Quartzite with varying degree of weathering has been encountered during tunnelling in the area. The cover for these tunnels varies from 14.6 to 18.8 m and pillar width varies from 9.6 to 20.0 m between primary reference lines 4 and 7. The thickness of alluvium over the rocky strata is also varying from 3.0 to 7.0 m in the area between the above reference lines.

Analysis has been carried out for green-field condition i.e. Surface structures are not there. As simulation of densely non-engineered structures and manmade hidden cavities in the area is not practicable. The grid generated for the analysis consists of three portions in horizontal direction (along the x-axis of the model) viz. east, central and west and three portions in vertical direction (along the y-axis of the model) viz. upper, central and lower. The details of grid adopted for analysis are shown in Fig. 126.

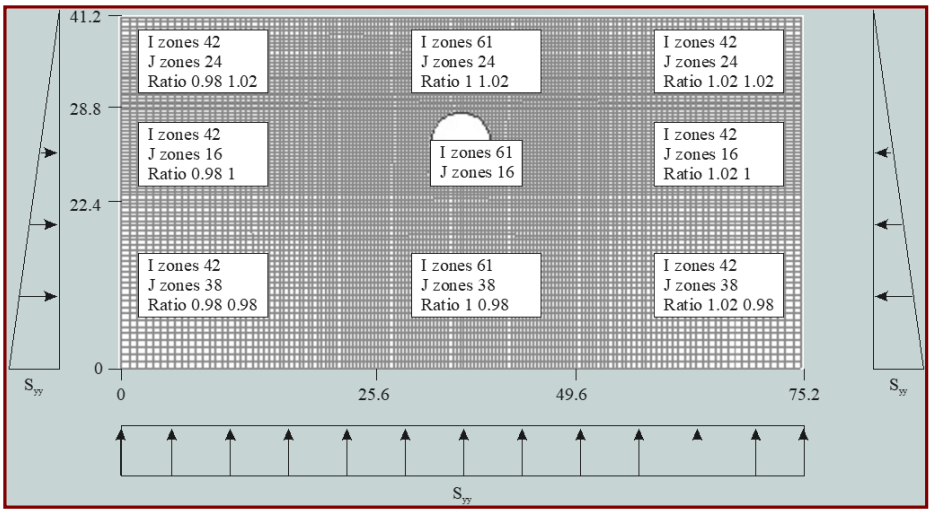

Fig. 126. Mesh adopted for analysis of tunnels in rocks

The annular space between the excavated boundary by cutter head and the liner is filled by the cement grout through the injection ports provided in the end of the TBM tail skin. The diameter of cutter head of the TBM was 6.53 m. The liner provided was of 0.28 m thickness for 5.70 m finished internal diameter of the tunnels. Therefore, the outer diameter of the liner is 6.26 m. The average of the cutter head diameter and external diameter of the liner comes out to be of the order of 6.40 m. The maximum annular gap left has been considered for the current work of the order of 50 percent of the maximum theoretical gap between the liner and excavated boundary i.e.70 mm. The simulation of the tunnel excavation has been carried out by assuming tunnels of 6.40 m diameter. The gap calculated for 5.0 percent face loss is of the order of 80 mm for the excavation diameter of 6.4 m. Hence, the maximum face loss considered for the analysis is 5.0 percent. The tunnels have been created in the model by a circle of 6.40 m diameter. The excavation of the tunnels has been simulated by assigning the

Null model to the regions marked by these circles. The excavation of the tunnels has been done sequentially. The face losses of 1.0, 2.0, 3.0, 4.0 and 5.0 percent have been taken for the analysis of tunnel sections at each reference line. The gap provided between the liner and excavated boundary is 16, 32, 48, 64 and 80 mm for the face loss simulation of 1.0, 2.0, 3.0, 4.0 and 5.0 percent respectively.

14.4.6 Results and Discussion

Analysis of tunnels for face loss and for drained condition.

The maximum settlement at the ground surface obtained from the drained analysis for the tunnel portion lying in the R_1, R_2 and R_3 type of rockmasses is of the order of 0.3, 0.9 and 2.0 mm respectively. The results of maximum ground surface settlement are same for the face losses 1, 2, 3, 4 and 5 percent for R_1, R_2 and R_3 rockmasses. The settlement trough at the ground surface for R_2 rockmass at monitoring line number 6 for a typical face loss of 3 percent is shown in Fig. 127.

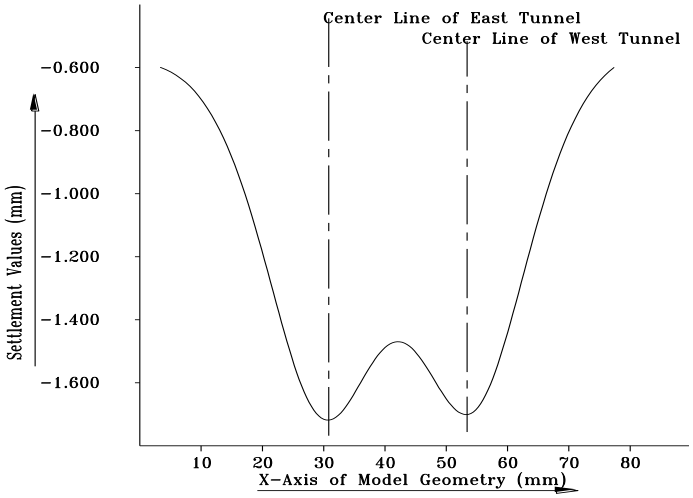

Fig. 127. Settlement trough (gap 48mm) for both tunnels at primary reference line 6

Field Measurements and Comparison with Analytical Results.

For the purpose of recording settlements in the area along the tunnel alignment, instrumentation scheme has been prepared by DMRC which mainly consists of settlement markers along the designated monitoring lines (primary reference lines). The total settlement values obtained from the analysis including consolidation of the overlaid alluvium are of the order of 1.0, 1.5 and 3.0 mm for R_1, R_2 and R_3 rocks respectively. For the face loss variation from 1 to 5 percent the maximum ground surface settlements are same for each type of rockmass i.e. R_1, R_2 and R_3. Therefore, before undertaking the detailed parametric study for these tunnels with respect to the geometric, elastic and strength parameters, the study for four different cases has been conducted just to visualize the actual behaviour of these tunnels with liner. Therefore the liners provided for the tunneling in between Delhi main and Chawri bazar are not being subjected to ground loading. Thus the face loss does not have any effect.

14.4.7 Conclusions

From the analysis of the Delhi Metro Tunnels in the weathered quartzite rockmass it has been observed that:

i. The tunnels remain in stable condition even without liners for R_1, R_2 and R_3 rockmasses. The liners provided therein with the TBM are not being subjected to the ground loading.
ii. For operational requirement, provision of liner cannot be ruled out of such machines. Primary grouting through tail skin can be dissociated with machine operation. This will save the construction time and cost for the tunnels driven using TBM in such type of weathered rockmasses for Metro tunnels.
iii. The grouting of annular space can be carried out through the grout holes provided in the segments of lining. This will dissociate the tunneling operation from the machine operation domain.

14.5 Coupled Hydro-Mechanical Modeling for the Slopes in Upper Beas Catchment, Himachal Pradesh

A landslide is a downslope movement of the rockmass, soil, debris or any mixture of these materials, of the sloping surface under the influence of the gravity. In mountainous regions, landslides are the most frequent natural hazards, causing tremendous loss of life, economy, property and creating a vast disturbance in the livelihood of the people. Complex geology and weak geological structures, rugged and steep terrain, high relief variations along with seasonal monsoon rainfall give rise to a high degree of fragility and instability in the whole mountain system. Thus, the detailed studies for material behavior, slope kinematics, rainfall frequency, assessment of landslide hazards and numerical modeling is of utmost importance to understand their behavior, deformation mechanisms leading to failure in varying conditions of stability. India, Nepal and China are the most affected due to neo-tectonic nature of Himalayas and frequent landslides.

It is well-known that water is one of the major triggers of landslides. Numerous landslide studies discuss different effects that water may have on slope stability: decreasing suction, rising groundwater table and subsequent increasing of pore water pressure, groundwater exfiltration from the bedrock, seepage erosion, hydraulic uplift pressure from below the landslide, and influence of water on the plasticity of the landslide (Fig. 128). The first objective of this study is to investigate the dominating controlling parameter for the landslide in UBC and to access the origin, flow paths and effect of rainfall in ten different slopes and landslides in UBC. The area is severely affected by the landslide issues and Fig. 129 shows some consequences of the landslide in the UBC.

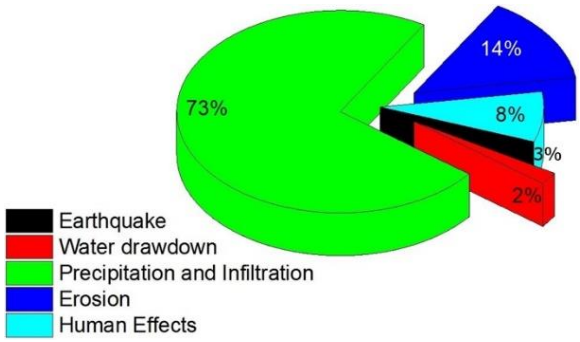

Fig. 128. Prevailing landslide causing factors in Himalayas and their percentages

Fig. 129. Some consequences of the landslide in the Himalayas, affected peoples, buried bodies and property loss

The geotechnical parameters e.g. physical and mechanical properties play a significant role in a precise forecast of rock behavior under such inconsistent conditions. The mechanical properties of rocks change with density, porosity, a variation of mineral assemblage, grain size and texture and effective pressures acting on them. A comprehensive study has been undertaken using three varieties of rocks obtained from the UBC in the Himalayan region. Attention has been paid to their petrographic and petrofabric analyses through SEM and thin sections studies. Uniaxial compressive strength, Brazilian tensile strength and triaxial strength tests are conducted on three different rock samples to understand the nature of failure patterns. Strength and deformation behavior of the rocks in both dry and saturated conditions are also defined and compared with various properties. The flowchart for the experimental program is shown in Fig. 130.

Laboratory testing of the collected samples has been performed using ISRM (2007-14) suggested methods of rock characterization to evaluate shear strength parameters. For the assessment of the natural stability of rock slopes, kinematic analysis technique is extensively used. This technique makes use of dominant discontinuity planes within slope mass to forecast the probability of sliding, wedging and falling. As rock slope surface is either concave or convex shaped, its changing strike also plays a significant role in the kinematic analysis. These slopes will have two or more planar surfaces and are termed as multi-faced slopes (MFS). The details of kinematic analysis performed on these MFS and gives the stability index for these slopes with the change in strike direction. The adopted methodology for the kinematic analysis is presented in Fig. 131.

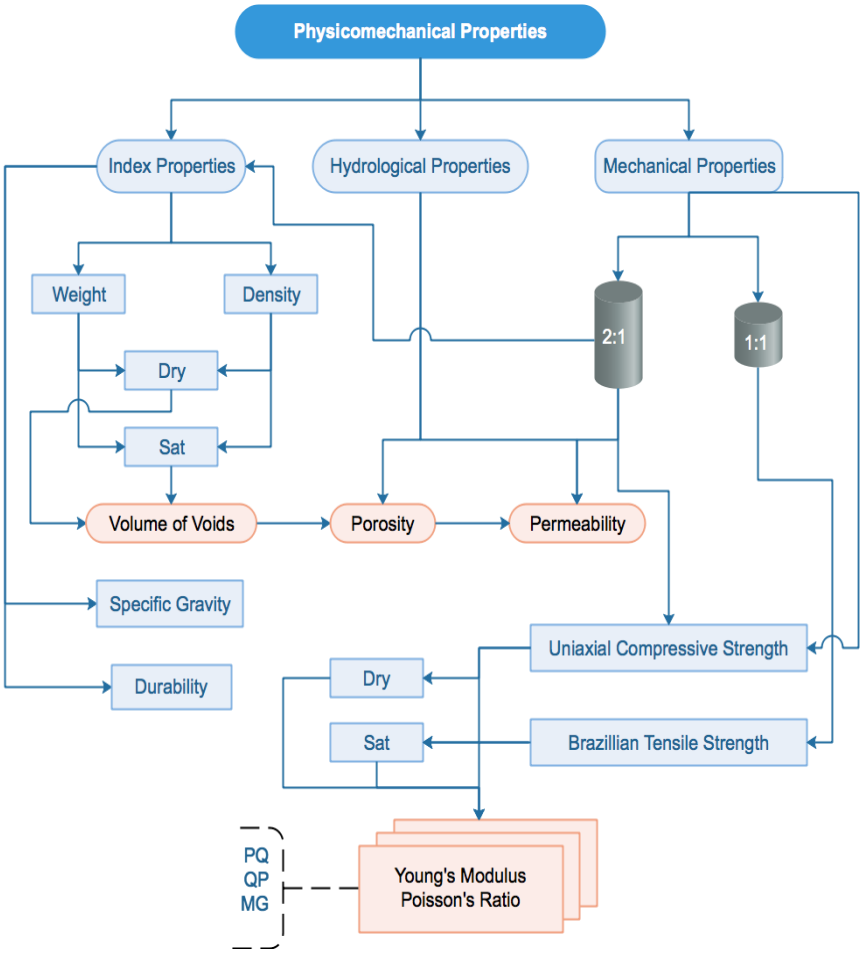

Fig. 130. Flowchart for the physico-mechanical experimentation program (Singh, 2018b)

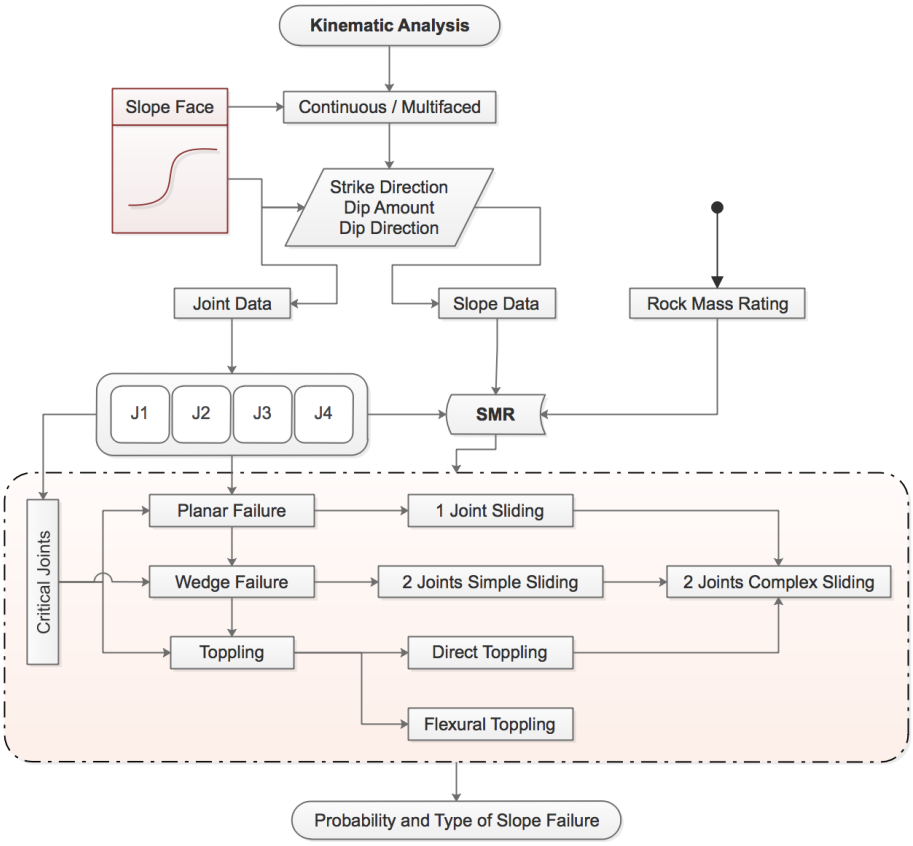

Fig. 131. Algorithm for Kinematic analysis (Singh. 2018b)

Three cases are used for further analysis. Case 1 (Planar sliding), when the failure is based on only one joint set and is planar in nature. Case 2 (Double plane sliding / Wedging), when wedge block is formed and sliding is along both planes, formed by either, the intersection of dominant joint sets or by two slope surfaces. Case 3 (Toppling), when the block topples, either showing flexural toppling or direct toppling. Results of the cases study are presented.

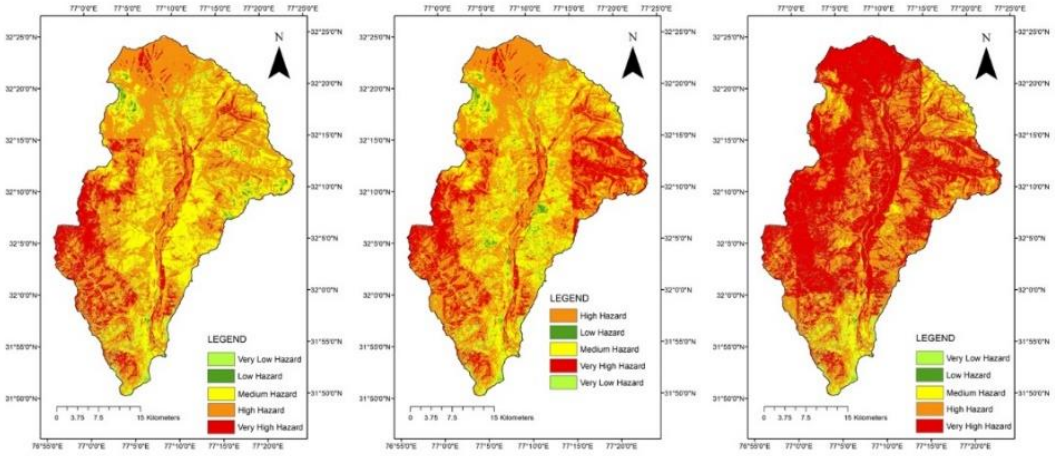

Fig. 132. Rainfall based LHZ for 20, 50 and 100 years for the UBC (Singh. 2018b)

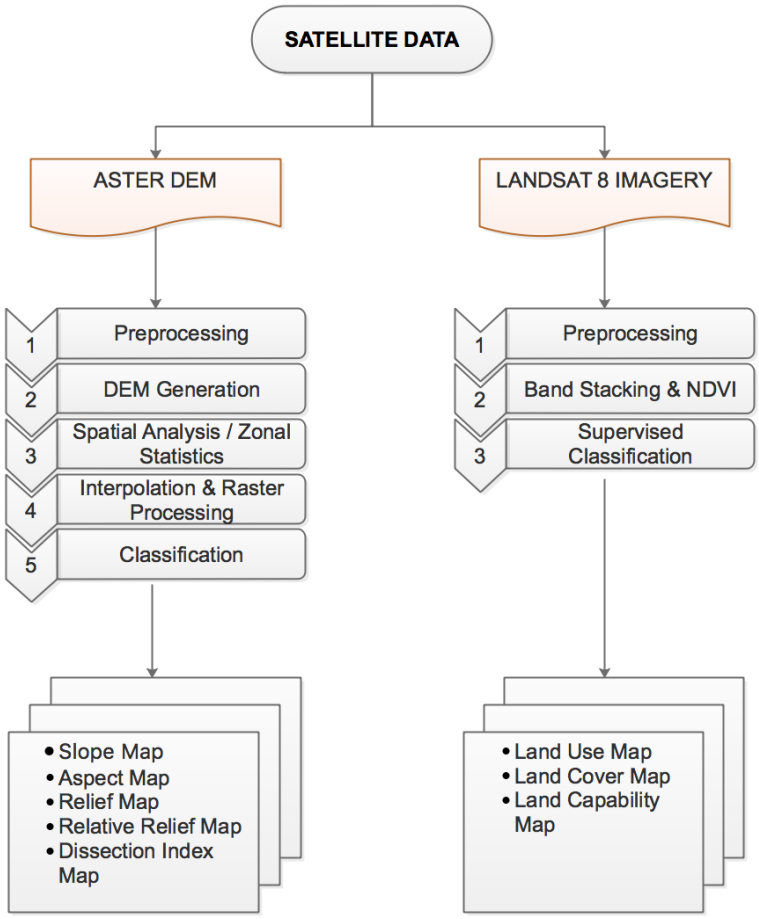

Fig. 133. Algorithm to predisposing parameters for landslide hazard (Singh. 2018b)

For the information regarding long-term trends, variability, extreme events etc. of the rainfall over a catchment are accessed through Indian Meteorological Data. For the accurate prediction of rainfall diurnal and spatial variation, and amount of rainfall at the slightest scale, a new high resolution gridded rainfall database is created. This database is used to study the orogenic effect on rainfall and to predict the 10, 20, 50 and 100-year rainfall return period. Isohyet maps are created at monthly and annual scale for 113 years (1901-2013) representing variability over UBC. For determining the susceptible areas to slope failure, a multiparametric landslide hazard zonation is performed in ArcGIS Environment at the catchment scale. The effect of rainfall in changing the percentage of area under a particular hazard (very low to the extreme) is determined by overlying the isohyet maps for rainfall return period with the developed LHZ maps. The developed LHZ for the rainfall return

period of 20, 50 and 100 years are shown and compared in Fig. 132. This new approach of wet LHZ is compared with available landslide inventory, which shows high correlation factor over dry LHZ. The methodology adopted for the development of rainfall based Landslide Hazard Zonation system is presented in Fig. 133.

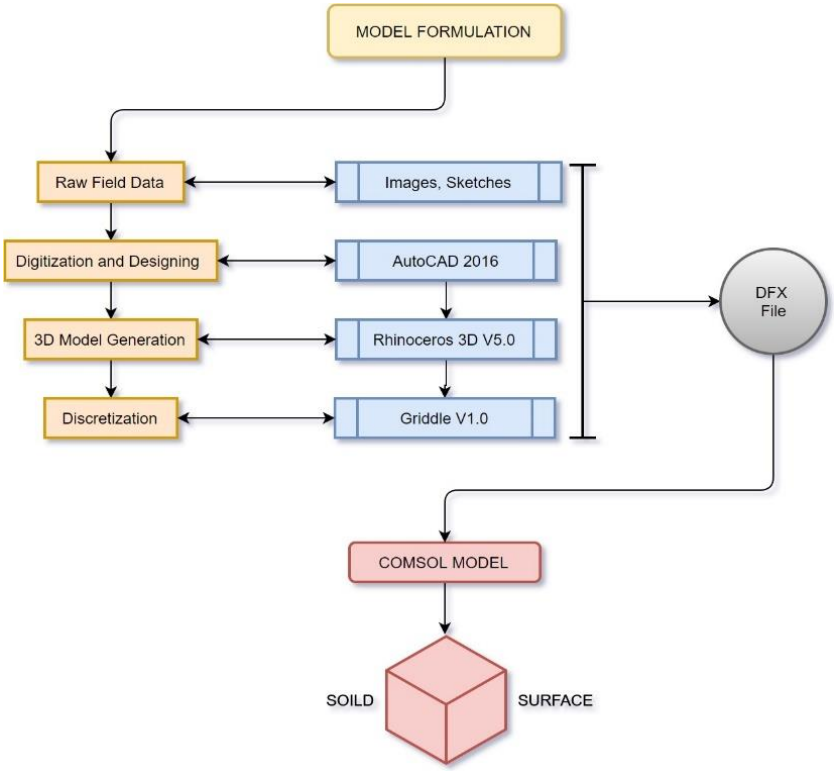

Fig. 134. Algorithm for the development of Numerical model (Singh. 2018b)

For the preferential flow paths, such as cracks, macropores, fissures, pipes etc. are common features of heterogeneous slopes. During intense rainstorms, the preferential flow has a significant influence on subsurface flow and slope stability. Dual-permeability models are widely used to simulate preferential flow but have not been incorporated into hydro-mechanical models. In this study, the COMSOL Multiphysics software is used to couple a dual-permeability model with a mechanics model for landslide stability evaluation. Detailed information is provided on how to incorporate current hydrological and mechanics theories into COMSOL. A total of ten slopes are modeled in 3D and variation of the factor of safety, pore water pressure, the degree of saturation and deformation over the course of 113 years is recorded. The results are further analyzed to elucidate the implications of rainfall data for determining and predicting the arising instability within slope masses. The algorithm adopted for the development of COMSOL model is presented in Fig. 134.

14.5.1 Conclusions

This study demonstrated that by using rainfall, rock parameters, site geology, and slope geometry, the hydro-mechanical analysis is capable of accurately predicting the failure, timing, and deformation of unsaturated slopes under transient seepage conditions. Moreover, hydro-mechanical analysis can be effectively used to identify the underlying mechanism of the effects of rainfall infiltration on slope instability.

The sensitivity of slope to rainfall is accessed through coupled hydro-mechanical finite element based modeling, establishing the variation in pore water pressure at top and bottom, degree of saturation, stresses, displacement of toe and crown and other basic parameters.

15 Concluding Remarks

Strength and deformation behavior of intact, anisotropic, weathered and jointed rockmass under different stress state is modelled through physical, analytical and numerical approaches. As the physical modelling requires sensitive and robust experimental facilities, we designed and developed large scale uniaxial, biaxial and polyaxial testing equipment, servo controlled static and cyclic direct shear equipment, Impact testing facility, Creep testing unit, Servo controlled high pressure triaxial testing facility, Profilometer for 3D joint mapping, Rain fall impact gauges and High temperature chamber, Rock salt leaching setup to mention a few, which allowed us to pursue a large range of research areas over the years. The sustained approach yielded significant new contributions, methods and criteria to understand rock and rockmass in totality. This clarity enabling us to provide effective solutions to the numerous ground engineering problems and serving the industry.

Acknowledgements

I would like to thank the Indian Geotechnical Society for the kind invitation to deliver this 41st Annual Lecture. I also thank the IGC 2019 for bringing the lecture in print.

I thank all my senior and present colleagues who mentored and allowed me to find my moorings and grow. In the process we could create the best Rock Mechanics Laboratory in India.

Most of the work highlighted in this lecture is drawn from the doctoral works of my students, Prof Mahendra Singh, Prof R P Tiwari, Prof AK Shrivastava, Prof Nasseri, Prof H Noferesti, Dr HR Yadav, Dr Ganesh Rathod, Dr SMM Niktabar, Dr Ankesh Kumar, Dr Swapnil Mishra, Dr PK Kundu, Dr Tarun Singh, Dr Aditya Singh, Dr Chandan Kumar, Dr Chala Endalu, Dr Zaei Mahin, Dr AP Singh, Dr B Sandeep, and Dr Ashwani Jain. Several seminal research contributions are also made by my postgraduate students. I thank all of them for their painstaking work without which it would not be possible to understand the complex behavior of rockmass. I also thank my other researchers of Seismic hazard and Microzonation group who are making excellent contributions.

I thank the present doctoral students Nirbhay, Venkat, Shipra, Abdullah, Ankit and Arpan for their help in preparing the document.

Indian National Committee on Geotechnical Engineering, Min. of Water Resources, Govt. of India, Department of Science and Technology, CMPDI, Coal India and IIT Delhi provided the financial support. I thank them all for the same.

I also thank Mr. Jattinder Singh, Managing Director, M/s Hydraulic and Engineering Industries for the fabrication and other instrumental support for the research.

Many Public and Private Sector organizations engaged us for professional services which gave us opportunity to vet the theory into practice.

My special indebtedness to my wife Sita for her encouragement, patience and forbearance and to Aditya and Gayatri for their love and affection.

To all mentioned above and to many who have not been mentioned, I wish to express my gratitude.

References

1. Abaqus (2011) Explicit User's Manual, v6.13, Dassault Systemes Simulia Corporation, Providence.
2. ACI Committee 544 (1982) Impact resistance of steel fibre reinforced lightweight concrete. International Journal of Cement Composites and Lightweight Concrete 4.4:209-220.
3. ACI Committee 506 (1984) State-of-the-art report on fiber reinforced shotcrete. International Journal of Cement Composites and Lightweight Concrete 6.12:15-27.
4. Ahmed M and Iskander M (2011) Analysis of tunneling induced ground movements using transparent soil models. ASCE Journal of Geotechnical and Geo Environmental Engineering 137.5: 525-535.
5. Al-Ajmi AM and Zimmerman RW (2005) Relation between the Mogi and the Coulomb failure criteria. International Journal of Rock Mechanics and Mining Sciences 42:431-439.
6. Alam MS, Chakraborty T, Vasant M, Rao KS, Sharma P and Singh M (2015) Characterization of kota sandstone under different strain rates in uniaxial loading. Geotechnical and Geological Engineering.
7. Arikan F, Ulusay R and Aydin N (2007) Characterization of weathered acidic volcanic rocks and a weathering classification based on a rating System. Bulletin of Engineering geology and the environment 66: 415-430.
8. Aydan O, Akagi T and Kawamoto T (1993) The squeezing potential of rocks around tunnels; theory and prediction. Rock Mechanics and Rock Engineering 26.2: 137-163.
9. Aydan Ö, Akagi T and Kawamoto T (1996) The squeezing potential of rock around tunnels: Theory and prediction with examples taken from Japan. Rock Mech Rock Engng, 29(3), 125-143.
10. Baar CA (1977) Applied salt-rock mechanics: The in-situ behavior of salt rocks. Elsevier, p. 302.
11. Bandis S, Lumsden AC and Barton NR (1981) Experimental studies of scale effects on the shear behavior of rock joints. International Journal of Rock Mechanics and Mining Sciences and Geomechanics Abstracts 18: 1-21.
12. Barth TFW (1952) Theoretical petrology. Wiley New York.
13. Barton N (1971) Estimation of in situ shear strength from back analysis of failed rock slopes Rock fracture. Proc Int Symp Rock Mech Nancy 2: 27.
14. Barton N (1973) Review of a new shear strength criterion for rock joints. Engineering Geology 7.4: 287–332.
15. Barton N and Choubey V (1977) The shear strength of rock joint in theory and practice. Rock Mech 10:1-54.
16. Behrestaghi MHN (1992) strength and deformation response of schistose rocks. PhD Thesis, IIT Delhi.
17. Behrestaghi MHN, Rao KS, Ramamurthy, T (1996) Geological and geotechnical response of schistose rocks from dam projects in India. Engineering Geology 44:183-201.
18. Behrestaghi MHN, Rao KS, Ramamurthy T (1997) failure mechanism in schistose rocks. Int J Rock Mech Min Sci 34.3-4: 219-e1.
19. Behrestaghi MHN, Rao KS, Ramamurthy T (2003) Anisotropic strength and deformational behaviour of Himalayan schists. Int J Rock Mech Min Sci 40.1:3-23.
20. Bhardwaj S (2019) Physical and numerical modelling of shear behaviour of natural rock joints. PhD Thesis, IIT Delhi.
21. Bieniawski ZT (1967) Mechanics of brittle fracture of rocks. Part I, II and III. International Journal of Rock Mechanics and Mining Sciences 4: 395-430.
22. Bieniawski ZT, Denkhaus HG and Vogler UG (1969) Failure of fractured rock. International Journal of Rock Mechanics and Mining Sciences 6: 323-341.
23. Bieniawski ZT (1973) Engineering classification of jointed rock masses. Trans S AfrInstCivEng 15:335–344.

24. Bieniawski ZT (1984) The design process in rock engineering. Rock Mech Rock Engg, 17(3), 183-190.
25. Bieniawski ZT (1989) Engineering rock mass classifications. John Wiley and Sons, New York 251.
26. Blair SG and Cook NGW (1998) Analysis of compressive fracture in rock using statistical techniques: Part II. Effect of microscale heterogeneity on macroscopic deformation. International Journal of Rock Mechanics and Mining Sciences 35: 849-861.
27. Blake William (1863) Poems, ed. Dante Gabriel Rossetti.
28. Bobet and Einstein (1998) Fracture coalescence in rock-type materials under uniaxial and biaxial compression. International Journal of Rock Mechanics and Mining Sciences 35.7: 863-883.
29. Bowen NL (1915) Crystallisation-differentiation in silicate liquids. American Journal of Science 39: 175-191.
30. Brantmark J and Stille H (1996) Prediction of squeezing pressure on the Uri Project, Kashmir, India. Proceedings. ISRM International symposium, Eurock, Turin, 96 2:1025-1032.
31. Carranza-Torres C and Fairhurst C (2000) Application of the convergence- confinement method of tunnel design to rock masses that satisfy the Hoek-Brown failure criteria. Tunnelling and Underground Space Technology, 15.2: 187-213.
32. Ceryan S, Tudes S and Ceryan N (2008) A new quantitative weathering classification for igneous rocks. Environmental Geology 55: 1319-1336.
33. Chakraborty A and Rao KS (2015) Water Ingress Assessment in Tunnels-An overview. J Engineering Geology Sp Pub:1020-1043.
34. Chala ET and Rao KS (2017) Influence of weathering on engineering behavior of rocks under triaxial loading conditions. ASCE Geotechnical frontiers, Orlando, Florida, GSP280, pp. 570-578.
35. Chala ET (2018) Geomechanical characterization and classification of weathered volcanic rocks for rock engineering. PhD Thesis, IIT Delhi.
36. Cook NGW (1965) The failure of rock. International Journal of Rock Mechanics and Mining Sciences 2: 389-403.
37. Deere DU and Miller RP (1966) Engineering classification and index properties for intact rock. Technical Report No AFNL-TR-65-116 Air Force Weapons Laboratory New Mexico.
38. Desai CS and Christian JT (1977) Numerical methods in geotechnical engineering. McGRAW-HILL.
39. Drucker DC and Prager W (1952) Soil mechanics and plastic analysis or limit design. Quarterly of Applied Mathematics 9.2:157-165.
40. Duncan Fama, ME (1993) Numerical modelling of yield zones in weak rocks. In: Hudson, J. A. (ed.), Comprehensive Rock Engineering, Pergamon Press, Oxford 2: 49-75.
41. Dwivedi RD, Singh M, Viladkar MN and Goel RK (2013) Prediction of tunnel deformation in squeezing grounds. Engineering Geology 161: 55-64.
42. Dwivedi RD, Singh M, Viladkar MN and Goel RK (2014) Estimation of support pressure during tunnelling through squeezing grounds. Engineering Geology 168: 9-22.
43. Feng F, Li X, Rostami J, Peng D, Li D and Du K (2019) Numerical investigation of hard rock strength and fracturing under polyaxial compression based on Mogi-Coulomb failure criterion. International Journal of Geomechanics, 19(4).
44. GhoshRoy M, Rao KS, Singh T (2018) Strength behavior of middle Siwalik sandstone under uniaxial and triaxial conditions. Geomechanics and Geodynamics of Rockmasses, ISRM Symposium, EUROCK-2018, St Petersburg, Russia, pp. 1155-1164.
45. GhoshRoy M (2019) Static and cyclic behavior of the Himalayan rocks. PhD Thesis, IIT Delhi.
46. Gioda G and Cividini A (1996) Numerical methods for the analysis of tunnel performance in squeezing rocks. Rock Mechanics and Rock Engineering 4.29: 171-193.
47. Goel MD and Matsagar VA (2013) Blast-resistant design of structures. Practice Periodical on Structural Design and Construction, 19(2) 04014007
48. Goel RK (1994) Correlations for predicting support pressures and closures in tunnels. PhD thesis, Nagpur University, India.
49. Gokceoglu C, Zorlu K, Ceryan S and Nefeslioglu HA (2009) A comparative study on indirect determination of degree of weathering of granites from some physical and strength parameters by two soft computing techniques. Materials Characterization 60: 1317-1327.
50. Goodman RE (1974) The mechanical properties of joints. Proc 3rd Congr ISRM Denver 1A: 127-140.
51. Gupta AS and Rao KS (1996) Index tests for the assessment of weathered rock. journal of engineering geology 25:57-62.
52. Gupta AS (1997) Engineering behaviour and classification of weathered rocks. PhD Thesis, IIT Delhi.
53. Gupta AS and Rao KS (1998) engineering characterization of weathering in rock mass through rating concept. IGC Golden Jubilee Conf. New Delhi, 1:323-326.
54. Gupta AS and Rao KS (2000) Weathering effects on strengths and deformational behaviour of crystalline rocks under uniaxial compression state. Int Jour Engg Geology 56: 257-274.
55. Gupta AS and Rao KS (2001) Weathering indices and their applicability for crystalline rocks. Bulletin of Engineering Geology and the Environment 60: 201-221.
56. Haimson B and Chang C (2000) A new true triaxial cell for testing mechanical properties of rock and its use to determine rock strength and deformability of Westerly granite. Int J Rock Mech Min Sci 37.1-2: 285-296.
57. Heidbach O, Tingay M, Barth A, Reinecker J, Kurfe D and Müller B (2009) World stress map, II edition. Helmholtz Centre Potsdam - GFZ German Research Centre for Geosciences, Commission for the Geological Map of the World.
58. Hoek E and Brown ET (1980) Empirical strength criterion for rock masses. J. Geotechnical Engineering Division ASCE: 1013–1025.
59. Hoek E (1983) Strength of jointed rock masses. 23rd Rankine Lecture Geotechnique 33.3: 187-223
60. Hoek E and Brown ET (1997) Practical estimates of rock mass strength. International Journal of Rock Mechanics and Mining Science and Geomechanics Abstracts. 34.8:1165-1186.
61. Hoek E and Marinos P (2000) Predicting tunnel squeezing problems in weak heterogeneous rock masses. Tunnels and Tunnelling International 32.11: 45-51.
62. Indraratna B, Haque A and Aziz N (1998) Laboratory modelling of shear behavior of soft joints under constant normal stiffness condition. Journal of Geotechnical and Geological Engineering 16:17-44.
63. Indraratna B, Welideniya HS and Brown ET (2005) A shear strength model for idealised infilled joints under constant normal stiffness. Geotechnique 55.3: 215–226.

64. Indraratna B, Oliveira DAF, Brown ET and Assis APD (2010) Effect of soil–infilled joints on the stability of rock wedges formed in a tunnel roof. Int J Rock Mech Min Sci 47:739–751.
65. Indraratna B, Premadasa WN and Oliveira D (2012) Physical modeling of soil infilled discontinuities. ASCE Geo Congress 2312-2321.
66. Indraratna B, Premadasa WN and Brown ET (2013) Shear behavior of rock joints with unsaturated infill. Geotechnique 63.5:1356–1360.
67. Irfan TY and Powell GE (1985) Engineering geological investigations for pile foundations on a deeply weathered granitic rock in Hong Kong Bulletin of Inernational Association of Engineering Geology 32: 67-80.
68. ISRM (1978) Suggested methods for the quantitative description of discontinuities in rock masses.
69. ISRM (1979) Suggested method for determining the uniaxial compressive strength and deformability of rock materials.
70. ISRM (1981) Suggested methods for determining tensile strength of rock materials.
71. ISRM (1983) Suggested methods for the determining the strength of rock materials in triaxial compression.
72. Itasca Consulting Group, Inc. (2000) FLAC — Fast Lagrangian Analysis of Continua, Minneapolis: Itasca.
73. Itasca Consulting Group, Inc. (2004) UDEC — Universal Distinct Element Code, Minneapolis: Itasca.
74. Jain A (2019) Analyses of underground structures under squeezing rock conditions. PhD Thesis, IIT Delhi.
75. Jethwa J L, Singh B and Singh Bhawani (1984) Estimation of ultimate rock pressure for tunnel linings under squeezing rock conditions- a new approach. Proceedings ISRM Symposium on Design and Performance of Underground Excavations, Cambridge, U.K.
76. Jiang Y, Xiao J, Tanabashi Y and Mizokami T (2004) Development of an automated servo-controlled direct shear apparatus applying a constant normal stiffness condition. International Journal of Rock Mechanics and Mining Sciences 41: 275–286.
77. Kaiser PK, Diederichs MS, Martin CD, Sharp J and Steiner W (2000) Underground works in hard rock tunneling and mining. ISRM International Symposium. International Society for Rock Mechanics.
78. Kim DY, Chun BS and Yang JS (2006) Development of a direct shear apparatus with rock joints and its verification tests. Geotechnical Testing Journal 29(5):1-9.
79. Kovari K and Staus J (1996) Basic considerations on tunnelling in squeezing ground. Rock Mechanics and Rock Engineering 29.4: 203-210.
80. Kovari K (1998) Tunneling in squeezing rock. Tunnel 5/98:12-31.
81. Kovari K (2000) Mastering of squeezing rock in the Gotthard base. Tunnels and Tunnelling International 234-238.
82. Kumar A, Manna B and Rao KS (2013) Dynamic response of block foundations resting on soil-rock, rock-rock system under vertical excitation. Indian Geotechnical Journal 43.1:83-95.
83. Kumar A, Manna B and Rao KS (2013) Effect of vertical vibration on block foundation resting on homogeneous and layered medium. Int J Engineering Research 2.7: 452-456.
84. Kumar A (2019a) Engineering behaviour of oil shales under high pressure and temperature. PhD Thesis, IIT Delhi.
85. Kumar C (2019b) Experimental characterisation of rock salt for underground structures. PhD Thesis, IIT Delhi.
86. Kumar R (2007) Testing and constitutive modelling of the strain-softening behaviour rocks. PhD Thesis, IIT Delhi.
87. Kundu PK (2019) Effect of rainfall and earthquake on landslides of Darjeeling Himalayas. PhD Thesis, IIT Delhi.
88. Ladanyi B and Archambault G (1970) Simulation of shear behavior of a jointed rock mass. Rock Mechanics; Theory and Practice (Somerton WH ed) 105–125.
89. Lambe TW (1960) A mechanistic picture of shear strength in clay. Proc. ASCE Research Conf. on Shear Strength of Cohesive Soils, Vol. 437.
90. Liu E, Huang R and He S (2012) Effects of frequency on the dynamic properties of intact rock samples subjected to cyclic loading under confining pressure conditions. Rock Mechanics and Rock Engineering, 45(1), 89–102.
91. Liu H (2009) Dynamic analysis of subway structures under blast loading. Geotechnical and Geological Engineering ASCE 27.6: 699 – 711.
92. Maksimovic M (1996) The shear strength components of a rough rock joint. Int J Rock Mech Min Sci and Geomech Abst 33: 769–783.
93. Malik A, Chakraborty T, Rao KS and Kumar D (2017) Experiments to determine static and dynamic tensile strength of Deccan trap rocks, India. EUROCK 17, Ostrava, Procedia Engineering 191: 946-953.
94. Malik A, Chakraborty T and Rao KS (2018) Strain rate effect on the mechanical behaviour of basalt: observations from static and dynamic tests, Thin-Walled Structures 126:127-137.
95. Martin D, Griffiths W and Campbell IH (1987) Compositional and thermal convection in magma chambers. Contrib Mineral Petrol 96: 465–475.
96. Mishra S, Rao KS and Gupta NK (2017) Damage to shallow tunnels under static and dynamic loading. Implast, Procedia Engineering 173:1322-1329.
97. Mishra S, Rao KS, Gupta NK and Kumar A (2018) Damage to shallow tunnels in different geomaterials under static and dynamic loading. Thin-Walled Structures 126: 138-149.
98. Mishra S (2019) Physical and numerical modelling of tunnels under impact and blast loads. PhD Thesis, IIT Delhi.
99. Mogi K (1971) Fracture and flow of rocks under high triaxial compression. Journal of Geophysical Research 76:1255–1269.
100. Momeni AA, Khanlari GR, Heidari M, Sepahi AA and Bazvand E (2015) New engineering geological weathering classifications for granitoid rocks. Engineering Geology, Vol. 185, 43-51.
101. Mukesh K, Goel MD, Matsagar VA and Rao KS (2015) Response of semi-buried structures subjected to multiple blast loading considering soil-structure interaction. Indian Geotech J 45: 243-253.
102. Niktabar SMM, Rao KS and Shrivastava AK (2015) Shear Behaviour of Rock Joints under Cyclic Condition. J Engineering Geology Sp Pub: 277-286.
103. Niktabar SMM (2016) Shear strength behaviour of jointed rock under dynamic loads. PhD Thesis, IIT Delhi.
104. Niktabar SMM, Rao KS and Shrivastava AK (2017) Effect of rock joint roughness on its cyclic shear behavior. Journal of Rock Mechanics and Geotechnical Engineering 9.7:1071-1084.

105. Niktabar SMM, Rao KS and Shrivastava AK (2018) automatic static and cyclic shear testing machine under constant normal stiffness boundary conditions. ASTM Geotechnical Testing Journal, 41(3) 508-525.
106. Noferesti H and Rao KS (2006) Physical simulation of brittle failure in rocks. In Proceedings of the Indian Geotechnical Conference Chennai, 373-76.
107. Noferesti H (2007) Simulation of brittle failure in crystalline rocks. PhD Thesis, IIT Delhi.
108. Noferesti H and Rao KS (2010) New observations on the brittle failure process of simulated crystalline rocks. Rock mechanics and rock engineering 43.2: 135-150.
109. Noferesti H and Rao KS (2011) Role of crystal interlocking on the strength of brittle rocks. Rock mechanics and rock engineering 44.2: 221-230.
110. Obert L, Brady BT and Schmechel FW (1976) The effect of normal stiffness on the shear resistance of rock. Rock Mech 8.2: 57-72.
111. Ooi LH and Carter PJ (1987) A constant normal stiffness direct shear device for static and cyclic loading. Geotechnical Testing Journal 10.1: 3-12.
112. Otter JRH, Cassell AC, Hobbs RE and Poisson (1966) Dynamic Relaxation. Proceedings of the Institution of Civil Engineers, 35(4), 633-656.
113. Papanastasiou P and Durban D (1996) Elastoplastic analysis of cylindrical cavity problems in geomaterials. Int J Numer Anal Methods Geomech 21:133–149.
114. Patton FD (1966) Multiple modes of shear failure in rock and related materials. Dissertation, University of Illinois.
115. Philpotts AR (1990) Principles of igneous and metamorphic petrology. Prentice-Hall, London, p 498.
116. Ramakrishnan V (1985) Steel fiber reinforced shotcrete: A state of the art report. Proceedings of US Sweden Joint Seminar on Steel Fibre Concrete Stockholm 7-24.
117. Ramamurthy T, Rao GV and Rao KS (1985) A strength criterion for rocks. Proceeding of the Indian Geotechnical Conference, Vol. 1, pp. 59-64.
118. Ramamurthy T and Rao KS (1987) Geotechnical response of dolomite of salal dam project. Irrigation and Power Journal 1:25-40.
119. Ramamurthy T, Rao GV and Singh J (1988) A strength criterion for anisotropic rocks. In Fifth Australia-New Zealand Conference on Geomechanics: Prediction Versus Performance; Preprints of Papers (p. 253) Institution of Engineers, Australia.
120. Ramamurthy T, Rao GV and Singh J (1993) Engineering behaviour of phyllites. Engineering Geology, 33(3), pp. 209-225.
121. Ramamurthy T and Arora VK (1994) Strength prediction for jointed rocks in confined and unconfined states. Int J Rock Mech Min Sci Geomech Abstr 31.1: 9–22.
122. Rao KS and Raymahashay BC (1981) Influence of clay minerals and iron oxides on selected properties of two lateritic soils. Indian Geotechnical Journal 11.3: 255-266.
123. Rao KS, Rao GV and Ramamurthy T (1981) Effect of moisture moisture on strength of intact rocks, Proceedings of GEOMECH-81, Hyderabad, Vol. 1, pp. 245-254.
124. Rao KS (1984) Strength and deformation behaviour of sandstones. PhD Thesis, IIT Delhi.
125. Rao KS, Rao GV and Ramamurthy T (1986) a strength criterion for anisotropic rocks. Indian Geotechnical Journal 16.4: 317-333.
126. Rao KS, Rao GV and Ramamurthy T (1987) A comparative evaluation of rock strength measures. Int Rock Mech Min Sci Geomech 24.3: 93-196.
127. Rao KS, Rao GV and Ramamurthy T (1987) Strength of sandstones in saturated and partially saturated conditions. J Geotechnical Engineering 18.1: 99-127.
128. Rao KS, Mukherje C and Ramamurthy T (1988) geotechnical properties of the antarctic rocks. 5th Indian Expedition to Antarctica Scientific Publication 5: 157-167.
129. Rao KS, Rao GV and Ramamurthy T (1988) strength and deformation behaviour of sandstones. Journal of Institution of Engineers 68:181-186.
130. Rao KS and Gupta AS (1997a) Assessment of parameters for rock weathering classification: it case study on Malanjkhand copper project. India, Proc. 1st Asian Rock Mechanics Symposium 2: 661 - 666 Seoul Korea Balkema Pub.
131. Rao KS and Gupta AS (1997b) Engineering classification of weathered rockmass. Int Tunneling Asia, New Delhi, 97: 21-28.
132. Rao KS and Gupta A (1998) Index properties of weathered rocks: interrelationships and applicability. Bulletin of Engineering Geology and the Environment. 57.2:161-172.
133. Rao KS and Tyagi AK (1999) Behaviour of jointed model material under compression, Int. Symp. on slope stability engineering, Shikoku, Japan, Balkema, 11: 805-808.
134. Rao KS and Gupta AS (2001) A quantitative rock weathering classification for geotechnical engineering practice. Proc National Workshop on Application of Rock Engg In Nation's Development 1: 101- 127.
135. Rao KS, Gupta KK and Neelima SD (2001) Effect of structural planes on rock foundations, IGC 2002, 19-21 December 2002, Allah-abad, India, 1: 454-460.
136. Rao KS and Gopichand T (2002) Analysis and design of underground rock tunnels by boundary element method for Delhi metro project. IGC 2002, 19-21 December 2002, Allahabad, India, 1: 513-520.
137. Rao KS and Tiwari RP (2002) Physical simulation of jointed model materials under biaxial ad true-triaxial stress states. Report, IIT Delhi.
138. Rao KS, Tiwari RP, Kapoor N, Reddy V and Kamlakar KVR (2002a) Strength response of jointed model materials under biaxial stress condition. IGC 2002, 19-21 December 2002, Allahabad. India, 1: 451-454.
139. Rao KS, Shrivastava VK, Tiwari RP and Vermeer PA (2002b) Excavation induced stress and deformation analyses of Osterfeld tunnel using plaxis-3d - a case study. IGC 2002, 19-21 December 2002, Allahabad, India, 2:767-775.
140. Rao KS (2003) Geotechnical aspects for Delhi metro. Proceeding of National Seminar on Developmental Geotech. Methods, DGMFE-3, Invited Lecture.
141. Rao KS, Tiwari RP and Singh J (2003) Development of a true-triaxial system (TTS) for rock mass testing. IGC 2003, 18-20 December 2003 IIT Roorkee, India, 219-226.
142. Rao KS and Tiwari RP (2004) Physical modelling of jointed rockmass under true triaxial stress state, SINOROCK 2004, China.

143. Rao KS (2008) Slope stability assessment and support measures for Subansiri lower hydroelectric project. Technical Report. Indian Institute of Technology Delhi, India.
144. Rao KS and Noferesti H (2008) Brittle failure in heterogeneous crystalline rocks. Defense Science Journal 58.2: 285-294.
145. Rao KS and Tiwari RP (2008) A polyaxial system for testing of jointed rock mass models. Geotechnical Testing Journal 31.4: 285-294.
146. Rao KS (2009) Slope stability analysis of Chenab bridge abutments in Katra Dharam section of USBRL project, J&K. Technical Report. Indian Institute of Technology Delhi, India.
147. Rao KS and Noferesti H (2009) New observations on the brittle fracture of simulated crystalline rocks. International Journal of Rock Mechanics and Rock Engineering 43.2:135-150.
148. Rao KS, Shrivastava AK and Singh J (2009) Development of an automated large-scale direct shear testing machine for rock. IGC Guntur, India, 238-244.
149. Rao KS and Noferesti H (2011) Crystal interlocking effects on strength of brittle rocks. Tropical Problems in Solids and Fluid Mechanics, Invited Contribution: 301-317.
150. Rao KS and GhoshRoy M (2015) Analysis of creep behaviour of soft rocks in tunnelling. J Engineering Geology, Engineering Geology in new millennium ISEG, International Golden Jubilee Conference, IIT Delhi, Sp Pub: 332-344.
151. Rao KS and Jain A (2015) Approaches for assessment and analysis of squeezing phenomenon in underground structure. Journal of Engineering Geology Sp. Pub.: 584-600.
152. Rao KS and Kumar A (2015) Geological and engineering behavior of oil shales. Journal of Engineering Geology Sp. Pub: 319-331.
153. Rao KS and Mishra S (2015) Fracture propagation of rocks under dynamic regime. J Engineering Geology Sp Pub: 345-358.
154. Rathod GW, Shrivastava AK and Rao KS (2011) Distinct element modelling for high rock slopes in static and dynamic conditions: a case study. ASCE GSP 224: 484-492.
155. Rathod GW and Rao KS (2012) finite element and reliability analysis for slope stability of Subansiri lower hydroelectric project: a case study. Journal of Geotechnical and Geological Engineering 30.1: 233-252.
156. Rathod GW, Varughese A, Shrivastava AK and Rao KS (2012) 3 Dimensional stability assessment of jointed rock slopes using distinct element modelling. ASCE GSP 225: 2382-2391.
157. Raymahashay BC, Bhavana PR, Rao KS and Mehta VK (1984) Ion exchange properties of lateritic soil from Calicut, Kerala. Journal Geological Society of India 25.7: 466-470.
158. Raymahashay BC, Bhavana PR, Rao KS and Mehta VK (1987) Mineralogy and geochemistry of lateritic soil profiles. Chemical Geology 60: 327-330.
159. Salencon J (1969) Contraction quasi- statique d'une cavite a symetrie spherique ou cylindrique dans un milieu elasto-plastique. Annales Des Ponts et Chaussees, 139(4), 231–236.
160. Sana Z and Rao KS (2014) Assessment of cyclic triaxial behavior of Shivalik sandstone. International Journal of Research in Engineering and Technology 3:61-67.
161. Shrivastava AK and Rao KS (2009) Shear behavior of jointed rock: a state of art. IGC 2009, Guntur, India, 245-249.
162. Shrivastava AK and Rao KS (2010) Estimation of contact area undergoing shearing for the rock mass. IGC 2010, IIT Guwahati, India, 891-894.
163. Shrivastava AK and Rao KS (2011) Shear behavior of non-planar rock joints. 14th ARC on Soil Mechanics and Geotechnical Engineering, Hong Kong China, 296-147.
164. Shrivastava AK (2012) Physical and numerical modelling of shear behavior of jointed rocks under CNL and CNS boundary conditions. PhD Thesis, IIT Delhi.
165. Shrivastava AK, Rathod GW and Rao, KS (2012) Numerical simulation of direct shear test on rock sample. ASCE, Geotechnical Special Publication.
166. Shrivastava AK and Rao KS (2013) Development of a large-scale direct shear testing machine for unfilled and infilled rock joints under constant normal stiffness conditions. Geotechnical Testing Journal 36.5: 670-679.
167. Shrivastava AK and Rao KS (2015) Shear behavior of rock joints under CNL and CNS boundary conditions. Int J of Geotech Geol Engg 33.3: 1205-1220.
168. Shrivastava AK and Rao KS (2018) Physical modelling of shear behaviour of infilled rock joints under CNL and CNS boundary condition. Rock Mechanics and Rock Engineering 51: 101-118.
169. Singh A, Rao KS, Chandan K, Kannan G and Ayothiraman, R (2017) Rheological behaviour of rock salt under uniaxial compression. Implast 2016, Procedia Engineering 173: 639-646.
170. Singh A, Rao KS and Ayothiraman R (2017) Effect of intermediate principal stress on cylindrical tunnel in an elasto-plastic rock mass. Procedia Engineering 173:1056-1063.
171. Singh A (2018b) Closed-form solutions for circular cavity in brittle and ductile rocks using true triaxial strength criteria under plane strain. PhD Thesis, IIT Delhi.
172. Singh A, Chandan K, Kannan G, Rao KS and Ayothiraman R (2018) Estimation of creep parameters for rock salt from uniaxial compression test. Int J Rock Mechanics and Mining Sciences 107: 243-248.
173. Singh A, Kumar A and Rao KS (2018) Strength behaviour of anisotropic rock under true triaxial stress state. ISRM International Symposium-10th Asian Rock Mechanics Symposium International Society for Rock Mechanics and Rock Engineering.
174. Singh A, Kumar C, Kannan LG, Rao KS and Ayothiraman R (2018) Engineering properties of rock salt and simplified closed-form deformation solution for circular opening in rock salt under the true triaxial stress state. Engineering Geology 243: 218-230.
175. Singh A, Rao KS and Ayothiraman R (2018) Study on Mohr-Coulomb based three-dimensional strength criteria and the application in the stability analysis of vertical borehole. Arabian Journal of Geosciences 12.18: 578-596.
176. Singh A, Rao KS and Ayothiraman R (2019a) A closed form analytical solution for a circular opening using Drucker-Prager. Indian Geotechnical Journal 49.4: 437-454.
177. Singh A, Rao KS and Ayothiraman R(2019b) An analytical solution to wellbore stability using Mogi-Coulomb failure criterion. Journal of Rock Mechanics and Geotechnical Engineering, https://doi.org/10.1016/j.jrmge.2019.03.004.

178. Singh AP, Bhandari T, Ayothiraman R and Rao KS (2017) Numerical analysis of rock socketed piles under combined vertical-lateral loading. EUROCK 17,Procedia Engineering 191:776-784.
179. Singh AP (2019) Behaviour of rock socketed piles under inclined loading. PhD Thesis, IIT Delhi (Submitted).
180. Singh B, Jethwa JL, Dube AK and Singh M (1992) Correlation between observed support pressure and rock mass quality. Tunnelling and Underground Space Technology 7.1: 59-74.
181. Singh B, Goel RK, Meherotra VK, Garg SK and Allu MR (1998). Effect of intermediate principle stress on strength of anisotropic rock mass. Tunneling and Underground Space Technology 13.1: 17-79.
182. Singh J (1988) Strength prediction of anisotropic rocks. PhD Thesis, IIT Delhi.
183. Singh M (1997) Engineering behavior of jointed model materials. PhD Thesis, IIT Delhi.
184. Singh M, Rao KS and Ramamurthy T (1999) Assessment of strength and deformational behavior of jointed block mass. 11th Asian Regional Conference, Seoul, South Korea, 1: 325-328.
185. Singh M and Rao KS and Ramamurthy T (2002) Strength and deformational behavior of a jointed rockmass. Rock Mech and Rock Engg. 35.1: 45-64.
186. Singh M, Rao KS and Ramamurthy T (2004) Engineering behavior of jointed rockmass. Indian Geotechnical Journal 34.2:164- 198.
187. Singh M and Rao KS (2005) Physical and constitutive modelling to simulate jointed rock mass under uniaxial stress state. Journal of Rock Mechanics and Tunneling Technology, 11.2:111- 131.
188. Singh M and Rao KS (2005a) Bearing capacity of shallow foundations in anisotropic non-Hoek-Brown rock masses. Journal of Geotechnical and Geo-environmental Engineering, ASCE 131.8:1014-1023.
189. Singh M and Rao KS (2005b) Empirical methods to estimate the strength of jointed rock masses. Engineering Geology 77.1:127-137.
190. Singh M and Rao KS (2007) Response to the discussion on bearing capacity of shallow foundations in anisotropic non-Hoek-Brown rock masses. Journal of Geotechnical and Geo-environmental Engineering, ASCE 133.2: 241-242.
191. Singh T (2018b) Coupled hydro-mechanical slope stability model for upper beas catchment region. PhD Thesis, IIT Delhi.
192. Singh T and Rao KS (2017) Physico-mechanical behavior of metamorphic rocks in rohtang tunnel, Himachal Pradesh, India. Procedia Engineering. 191: 419-425.
193. Sridharan A (1968) Some studies on the strength of partly saturated clays. PhD Thesis, Purdue University, Lafayette, Indiana.
194. Terzaghi K (1936) The shearing resistance of saturated soils and the angle between the planes of shear. Proceedings of the 1st International Conference on Soil Mechanics and Foundation Engineering, Harvard University, Cambridge, Mass., vol. 1, pp. 54–56.
195. Terzaghi K (1946) Rock defects and load on tunnel supports, Introduction to rock tunnelling with steel supports. R.V. Proctor and T.C. White, Youngstown, Ohio, USA.
196. Terzaghi K and Richart FE (1952) Stresses in rock about cavities. Geotechnique 3.2: 57-90
197. Tiwari RP (2004) Rockmass modelling in polyaxial stress state. PhD Thesis, IIT Delhi.
198. Tiwari RP and Rao KS (2004) Physical modeling of a rock mass under a true triaxial stress. International Journal of Rock Mechanics and Mining Sciences 41.3:1–6.
199. Tiwari RP and Rao KS (2006a) Deformability characteristics of a rock mass under true triaxial stress compression. Geotech Geol Engg J 24.4:1039- 1063.
200. Tiwari RP and Rao KS (2006b) Influence of intermediate principle stress on strength and modulus of rock mass. J Southeast Asian Geotech Society 38: 29-41.
201. Tiwari RP and Rao KS (2006c) Post failure behaviour of a rock mass under the influence of triaxial and true triaxial confinement. Engineering Geology 84(3-4):112-29.
202. Tiwari RP and Rao KS (2007) response of an anisotropic rock mass under polyaxial stress state. J Materials in Civil Engineering, ASCE 19.5: 393-403.
203. von Karman (1911) T über den mechanismus des widerstandes den ein bewegter körper in einer flüssigkeit erfährt. Nachrichten von der Gesellschaft der Wissenschaften zu Göttingen Mathematisch-Physikalische Klasse, 509-517.
204. Vutukuri VS, Lama RD and Salija SS (1974) Handbook on mechanical properties of rocks, Vol. I-IV, Trans. Tech Publications.
205. Wilkins ML (1964) Calculation of elastic-plastic flow. In: B. Alder (Ed.), Methods in Computational Physics, Vol. 3, Academic Press, New-York, 211-263.
206. Xie H and Pariseau WG (1992) Fractal estimate of joint roughness coefficients. Proc Int Conf on Fractal and Jointed Rock Masses Lake Tahoe California USA June 1992, 125-131.
207. Yadav HR (2005) Geotechnical evaluation and analysis of Delhi metro tunnels. PhD Thesis, IIT Delhi.
208. Zaei ME (2019) Petro-physico and mechanical behaviour of oil reservoir rocks under static and dynamic conditions. PhD Thesis, IIT Delhi.
209. Zhou XP, Bao XR, Yu MH and Xie Q (2010) Triaxial stress state of cylindrical openings for rocks modeled by elastoplasticity and strength criterion. Theoretical and Applied Fracture Mechanics 53:65-73.